

AD-A252 979



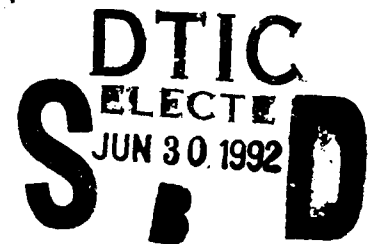
WL-TR-92-4006

**HIGH STRAIN RATE BEHAVIOR OF METALS,
CERAMICS, AND CONCRETE**

**A.M. Rajendran
University of Dayton Research Institute
300 College Park
Dayton, Ohio 45469-0120**

April 1992

Final Report for Period September 1986 - September 1991



Approved for public release; distribution is unlimited.

92 6 22 0213

**MATERIALS DIRECTORATE
WRIGHT LABORATORY
AIR FORCE SYSTEMS COMMAND
WRIGHT-PATTERSON AIR FORCE BASE, OHIO 45433-6533**

92-17033

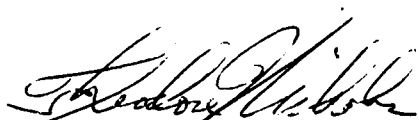


NOTICE

When Government drawings, specifications, or other data are used for any purpose other than in connection with a definitely government-related procurement, the United States Government incurs no responsibility or any obligation whatsoever. The fact that the government may have formulated or in any way supplied the said drawings, specifications, or other data, is not to be regarded by implication or otherwise in any manner construed, as licensing the holder or any other person or corporation; or as conveying any rights or permission to manufacture, use, or sell any patented invention that may in any way be related thereto.

This report is releasable to the National Technical Information Service (NTIS). At NTIS, it will be available to the general public, including foreign nations.

This technical report has been reviewed and is approved for publication.



THEODORE NICHOLAS
Project Engineer
Materials Behavior Branch
Metals and Ceramics Division



KATHERINE A. WILLIAMS
Technical Area Manager
Materials Behavior Branch
Metals and Ceramics Division



ALLAN W. GUNDERSON, Chief
Materials Behavior Branch
Metals and Ceramics Division

If your address has changed, if you wish to be removed from our mailing list, or if the addressee is no longer employed by your organization, please notify WL/MLLN, Wright-Patterson AFB OH 45433-6533 to help us maintain a current mailing list.

Copies of this report should not be returned unless return is required by security considerations, contractual obligations, or notice on a specific document.

REPORT DOCUMENTATION PAGE			Form Approved OMB No. 0704-0188	
<small>Public reporting burden for this collection of information is estimated to average 1 hour per response, including the time for reviewing instructions, searching existing data sources, gathering and maintaining the data needed, and completing and reviewing the collection of information. Send comments regarding this burden estimate or any other aspect of this collection of information, including suggestions for reducing this burden, to Washington Headquarters Services, Directorate for Information Operations and Reports, 1215 Jefferson Davis Highway, Suite 1204, Arlington, VA 22202-4302, and to the Office of Management and Budget, Paperwork Reduction Project (0704-0188), Washington, DC 20503.</small>				
1. AGENCY USE ONLY (Leave blank)		2. REPORT DATE April 1992		3. REPORT TYPE AND DATES COVERED Final / Sep 86 - Sep 91
4. TITLE AND SUBTITLE High Strain Rate Behavior of Metals, Ceramics, and Concrete			5. FUNDING NUMBERS C F33615-86-C-5064 PE 62102F PR 2418 TA 04 WU 50	
6. AUTHOR(S) A.M. Rajendran			8. PERFORMING ORGANIZATION REPORT NUMBER UDR-TR-91-122	
7. PERFORMING ORGANIZATION NAME(S) AND ADDRESS(ES) University of Dayton Research Institute 300 College Park Dayton OH 45469-0120			10. SPONSORING/MONITORING AGENCY REPORT NUMBER WL-TR-92-4006	
9. SPONSORING/MONITORING AGENCY NAME(S) AND ADDRESS(ES) T. Nicholas (513) 255-1347 Materials Directorate (WL/MLLN) Wright Laboratory Wright-Patterson AFB OH 45433-6533				
11. SUPPLEMENTARY NOTES				
12a. DISTRIBUTION / AVAILABILITY STATEMENT Approved for public release; distribution is unlimited.			12b. DISTRIBUTION CODE	
13. ABSTRACT (Maximum 200 words) This report summarizes the major results obtained during the contractual period between September 1986 through December 1990. During this period, high strain rate behavior of various metals and ceramics was investigated through a combined experimental and computational approach. The experiments include quasi-static, split Hopkinson bar, rod-on rod, plate-on-rod, and plate impact test configurations. Three-dimensional, loading history dependent, and internal state variable based constitutive models for metals and ceramics were developed. Damage, in terms of microvoids/cracks nucleation and growth, was treated as an internal state variable. The model constants for several metals and AD85 ceramic were determined and applied successfully to several impact problems				
14. SUBJECT TERMS impact, constitutive equation, failure, model, high strain rate, metals, ceramics, concrete, computer code			15. NUMBER OF PAGES 165	
			16. PRICE CODE	
17. SECURITY CLASSIFICATION OF REPORT Unclassified	18. SECURITY CLASSIFICATION OF THIS PAGE Unclassified	19. SECURITY CLASSIFICATION OF ABSTRACT Unclassified	20. LIMITATION OF ABSTRACT UL	

Abstract

This report summarizes the major results obtained during the contractual period between September 1986 through December 1990. High strain rate behavior of various metals and ceramics are evaluated through a combined experimental and computational approach. The experiments include quasi-static, split Hopkinson bar, rod-on-rod, plate-on-rod, and plate impact test configurations. Three-dimensional, loading history dependent, and internal state variable based constitutive models for metals and ceramics are developed. Damage, in terms of microvoids/cracks nucleation and growth, is treated as an internal state variable. The model constants for several metals and AD85 ceramic are determined and applied successfully to several impact problems.

Accession For	
NTIS GRA&I	<input checked="checked" type="checkbox"/>
DTIC TAB	<input type="checkbox"/>
Unannounced	<input type="checkbox"/>
Justification	
By _____	
Distribution/	
Availability Codes	
Dist	Avail and/or Special
A-1	



Contents

<u>Section</u>	<u>Page</u>
1 INTRODUCTION	1-1
2 HIGH STRAIN RATE TEST RESULTS	2-1
2.1 Split Hopkinson Bar Data	2-1
2.1.1 Metals	2-1
2.1.2 Ceramics and Concrete	2-2
2.2 Plate Impact Data Experiments	2-12
2.2.1 Metals	2-16
2.2.2 Ceramics	2-17
2.3 Plate-on-Bar Impact Data	2-17
2.3.1 Metal Bars	2-20
2.3.2 Ceramic Bars	2-20
2.4 Bar-on-Bar Impact Test	2-22
3 DUCTILE FAILURE MODEL FOR METALS	3-1
3.1 Constitutive Equations	3-2
3.2 Degradation of Shear and Bulk Moduli	3-4
3.3 Equation of State for the Aggregate	3-4
3.4 Model Parameters	3-6
3.5 Modeling of Double Flyer Plate Impact	3-14
3.6 RDG Model Applications	3-23
3.6.1 Tensile Necking	3-24
3.6.2 Rod Penetration	3-48
3.6.3 Spall in a Solid Cone Target	3-61
4 IMPACT DAMAGE MODEL FOR CERAMICS	4-1
4.1 Constitutive Equations	4-2
4.2 Damaged Stiffness Tensor	4-6
4.3 Microcrack Damage Evolution	4-10
4.3.1 Microcrack Nucleation	4-11
4.3.2 Microcrack Growth	4-13
4.3.3 Microcrack Coalescence	4-14
4.4 Numerical Solutions of Equations	4-15
4.4.1 Uniaxial Stress	4-15
4.4.2 Plate Impact Simulation	4-17
4.5 Bar-on-Bar Impact Simulation	4-27
4.6 Long Rod Penetration Simulation	4-31
5 SUMMARY AND CONCLUSIONS	5-1
5.1 RDG Model Summary	5-1
5.2 Ceramic Model Summary	5-3

Contents (Continued)

<u>Section</u>	<u>Page</u>
5.3 Recommendations	5-4
5.3.1 Metals	5-4
5.3.2 Ceramics	5-4
REFERENCES	6-1

<u>Appendix</u>	<u>Page</u>
A SPLIT HOPKINSON BAR AND PLATE IMPACT DATA	A-1
A.1 Split Hopkinson Bar (SHB)	A-1
A.2 Plate Impact Experiments	A-3
A.3 Materials Data	A-4
A.4 References	A-4
B JOHNSON-COOK AND BODNER-PARTOM MODELS	B-1
B.1 Johnson-Cook Model	B-1
B.2 Bodner-Partom Model	B-3
B.3 References	B-5
C SOLUTION SCHEME	C-1
C.1 Numerical Solution of the Governing Equations in Sections 3 and 4	C-1
C.2 References	C-3
D DIAGONALLY IMPLICIT RUNGE KUTTA SCHEME	D-1
D.1 References	D-2
E MODIFIED TCK MODEL FOR CERAMIC MATERIALS	E-1

Figures

<u>Figure</u>	<u>Page</u>
2.1	Silicon Nitride Compressive Strength Variation with Respect to Strain Rate . . . 2-3
2.2	Effect of Strain Rate on the Compressive Strength of Concrete 2-4
2.3	Schematic of Splitting Tension Geometry 2-5
2.4	Schematic of the Split Hopkinson Bar in Splitting Tension Mode 2-6
2.5	Silicon Nitride Tensile Strength Variation with Respect to Strain Rate 2-7
2.6	Strain History during Elastic Impact on Concrete 2-9
2.7	Photographs Highlighting Locations of Crack Initiation in Concrete 2-10
2.8	Stress History Corresponding to the Test in Figure 2.7 for Concrete 2-10
2.9	Effect of Strain Rate and Specimen Size on the Tensile Strength of Concrete . 2-11
2.10	Strain Rate Sensitivity of Tensile Strength Normalized With Respect to Static Strength for Concrete 2-13
2.11	Typical Free Surface Velocity of the Target Measured Using VISAR 2-14
2.12	A Schematic of Plate-on-Bar Impact Test Configuration 2-19
2.13	Oscilloscope Records from Experiments on AD-998 Rods. Scales for All Records are 0.2 V/div. and 0.5 μ s/div 2-21
2.14	High Speed Photograph of AD-998 Fracturing Due to Steel Plate Impact 2-23
2.15	A Schematic of Bar-on-Bar Impact Test Configuration 2-24
2.16	High Speed Photograph of AD-998 Fracturing Due to AD-998 Bar-on-Bar Impact 2-25
2.17	High Speed Photograph of Soda Lime Glass Fracturing Due to Soda Lime Glass Bar-on-Bar Impact 2-26
3.1	Comparison between Model and Experimental Free Surface Velocity Histories (OFHC Copper) 3-8
3.2	(a) Comparison between Model and Experimental Stress Histories (HY100 Steel), (b) Numerical Simulation of the Stress History at the Spall Plane (HY100 Steel) 3-9
3.3	Comparison between RDG Model Generated and Experimental Stress Gauge Signals for Different Metals 3-11
3.4	Comparison between RDG Model Generated and Experimental Stress Gauge Signals for Different Metals 3-12
3.5	Comparison of Spall Modeling for HY100 Steel using BP and JC Models. Spall Process is Described by the RDG Model 3-13
3.6	Comparison between the Spall Signals Generated using JC and BP Models for Different Values of RDG Model Constants 3-15
3.7	Comparison between Model Prediction and the Measured Stress History (OFHC Copper) 3-16
3.8	Experiment Configuration for Double Flyer Impact Experiment 3-18
3.9	Stress History Comparison for Original RDG Model 3-19
3.10	Stress History Comparison for Modified RDG Model, with a Critical Void Volume Fraction of 5% for Complete Collapse 3-20

Figures (Continued)

Figure		Page
3.11	Comparison of Simulated Stress Histories from Double Flyer Impact Configuration, with and without Void Growth	3-21
3.12	X-T Diagram for the Double Flyer Impact Experiment, Assuming No Void Growth	3-22
3.13	Shallow-Notched Tensile Specimen Geometry	3-25
3.14	Finite Element Mesh for Shallow-Notched SHB Specimen. The Velocity Loading History is Shown in the Inset	3-26
3.15	Stress Triaxiality (P/Y) at (a) $t=40$ and (b) $t=60$ microseconds	3-28
3.16	Damage (Void Volume Fraction) Contours at (a) $t=0$, (b) $t=20$, (c) $t=50$, and (d) $t=60$ microseconds	3-29
3.16	Damage (Void Volume Fraction) Contours at (a) $t=0$, (b) $t=20$, (c) $t=50$, and (d) $t=60$ microseconds (concluded)	3-30
3.17	Time Histories of Effective Plastic Strain and Void Volume Fraction for Elements 82 (Uniform Section) and 382 (Local Section)	3-31
3.18	Time History Plots for the Stress Components and Void Volume Fraction	3-32
3.19	Stress-Strain Response for Elements 82 and 382, along with the Variation of f with Respect to Effective Plastic Strain. Note that $f=0$ for Element 82	3-34
3.20	Time History Plot of Mean Stress for Elements 82, 182, 282, and 382	3-35
3.21	Measure of Triaxiality with Respect to Time for the Uniform (82) and Local (382) Sections. The Dashed Line Represents the Uniaxial Stress State	3-36
3.22	Loading Paths with Respect to Pressure Dependent Yield Surfaces in Elements 82, 182, 282, and 382	3-37
3.23	Radial Distribution of Void Volume Fraction at Three Different Positions along the Specimen Length	3-39
3.24	Normalized Effective Stress (σ_{eff}/Y_m) Distribution along the Radius for Different z Positions and Times	3-40
3.25	Comparison of Strains in Element 82 for Tensile Necking with and without Voids. The Solid Line Without Symbols is an Average Measure of Strain Based on the Pull Velocity	3-42
3.26	Comparison of σ_{eff} versus ϵ_{eff}^p in Element 382 for Tensile Necking with and without Voids	3-43
3.27	Radial Distributions of ϵ_{eff}^p for Cases with and without Voids at $t=60$ μs , Plotted for Uniform ($z=1.61$) and Local ($z=0.0$) Sections	3-45
3.28	Radial Distributions of Triaxiality (P/σ_{eff}) for Cases with and without Voids at $t=60$ μs , Plotted for Uniform ($z=1.61$) and Local ($z=0.0$) Sections	3-46
3.29	Pressure Contour Plot for Void-Growth Influenced Necking Process at $t=60$ μs . The Shaded Region is under Tensile Loading, and the Rest of the Region Experiences Compressive Loading	3-47
3.30	Initial (Dotted Line) and Final (Solid Line) Shapes of the Shallow Notch Tensile Specimen	3-49

Figures (Continued)

Figure		Page
3.31	Finite Element Mesh for the Rod Penetration Problem	3-50
3.32	Time Histories of Triaxiality (Mean Stress/Aggregate Effective Stress) and Void Volume Fraction for Element 736	3-52
3.33	Effect of Void Volume Fraction, f (Porosity) on the Aggregate Strength in Element 736. The Matrix Strength (Y_m) is Independent of f	3-53
3.34	The Loading Path (Solid Line) in Element 736, with Respect to the Pressure Dependent Yield Surfaces	3-55
3.35	Radial Distributions of Aggregate Strength (Y_a) and Void Volume Fraction (f) Inside the Target at a Depth of 0.8 Inches for $t = 5 \mu s$ and $20 \mu s$	3-56
3.36	Damage Contours at Various Stages in the Rod Penetration	3-58
3.37	Comparison of Aggregate Yield Strengths (Y_a) with and without Voids in Element 736. Y_m is the Matrix Strength of the Void Containing Material. Note that $Y_m = Y_a$ when $f = 0$	3-59
3.38	Deformed Configurations of the Rod Penetration at $20 \mu s$, with and without Void Growth	3-60
3.39	(a) Schematic Two-Dimensional Sketch of a Flyer Plate Impact on the Base of a Right Solid Cone. (b) Recovered and Sectioned Solid Cone Revealing the Complex Spall Zones	3-62
3.40	Void Contours ($\geq 10\%$) in Cone, from RDG Model Simulation	3-63
3.41	Effective Plastic Strain Contours ($\geq 10\%$) in Cone, from RDG Model Simulation	3-64
3.42	Code Generated Spall Planes in Cone, from RDG Model Simulation	3-65
3.43	Effective Plastic Strain Contours ($\geq 10\%$) in Cone, with Void Growth Suppressed	3-67
4.1	Stress-Strain Curves for AD-85 Ceramic at Different Strain Rates and Confining Pressures	4-16
4.2	Effects of Dynamic Cracking and Viscoplastic Flow on the Compressive Strength of AD-85	4-18
4.3	Effect of Confining Pressure on Strength of AD-85	4-19
4.4	Manganin Stress Gauge Data and Model Simulation for Single Flyer Impact on Alumina Plate at Velocity 570 m/sec	4-21
4.5	VISAR Data and Model Simulation for Double Flyer Impact on Alumina Plate at Velocity 293 m/sec	4-22
4.6	Manganin Stress Gauge Data and Model Simulation for Single Flyer Impact on TiB_2 Plate at Velocity 719 m/sec	4-23
4.7	Low Velocity (175 m/s) Plate Impact Test with Si_3N_4 Target. (a) Comparison Between Model and Gauge Signal, (b) Model Generated Stress (Solid Line) and Damage (Dashed Line) Histories Inside the Target . . .	4-25

Figures (Continued)

Figure		Page
4.8	High Velocity (800 m/s) Plate Impact Test with Si_3N_4 Target. (a) Comparison Between Model and Gauge Signal, (b) Model Generated Stress (Solid Line) and Damage (Dashed Line) Histories Inside the Target . . .	4-26
4.9	Configuration of AD-85 Bar-on-Bar Impact Experiment	4-28
4.10	Stress History from Elastic (No Microcracking) Simulation of AD-85 Bar-on-Bar Impact Experiment	4-29
4.11	Model Generated Stress History with Microcrack Growth Rate Parameters (n_1^+ , n_2^+ , n_1^- , and n_2^-) Equal to 1.0 (Excessive Crack Growth) for AD-85 Bar-on-Bar Impact Experiment	4-30
4.12	Model Generated Stress History with New Set of Constants for AD-85 Bar-on-Bar Impact Experiment	4-32
4.13	A Long Tungsten Rod Penetration into a Confined Ceramic Target	4-33
4.14	Element Locations (Inside Ceramic Plate) in Rod Penetration Simulation . . .	4-34
4.15	Microcrack Damage Contours at (a) 8 μs , (b) 10 μs , (c) 12 μs , and (d) 20 μs .	4-36
4.15	Microcrack Damage Contours at (a) 8 μs , (b) 10 μs , (c) 12 μs , and (d) 20 μs (concluded)	4-37
4.16	Mesh Plot of the Pulverized (Darker Region) Ceramic	4-38
4.17	Time History Plots for Element 3665: (a) Pressure, and (b) Maximum Principal Stress (Solid Line) and Damage (Dashed Line)	4-39
4.18	Time History Plots for Element 6402: (a) Pressure, and (b) Maximum Principal Stress (Solid Line) and Damage (Dashed Line)	4-40
4.19	Time History Plots for Element 9083: (a) Pressure, and (b) Maximum Principal Stress (Solid Line) and Damage (Dashed Line)	4-41
A.1a	A Schematic of the Split Hopkinson Bar Setup	A-2
A.1b	SHB Tensile Specimen Configuration	A-2
A.2	A Schematic of the Plate Impact Test Configuration	A-2
A.3	Stress (Strength) versus Strain Rate for MAR-M 300 Steel	A-5
A.4	Stress (Strength) versus Strain Rate for 3003 Aluminum	A-6
A.5	Stress (Strength) versus Strain Rate for Inconel 600	A-7
A.6	Stress (Strength) versus Strain Rate for Inconel 718	A-8
A.7	Stress (Strength) versus Strain Rate for AF1410 Steel	A-9
A.8	Stress (Strength) versus Strain Rate for Vanadium	A-10
A.9	Stress (Strength) versus Strain Rate for HL Aluminum	A-11
A.10	Stress (Strength) versus Strain Rate for 7017 Aluminum	A-12
A.11	Stress (Strength) versus Strain Rate for 6016-T6 Aluminum	A-13
A.12	Stress (Strength) versus Strain Rate for 1044 Steel	A-14
A.13	Stress (Strength) versus Strain Rate for 7039-T64 Aluminum	A-15
A.14	Stress (Strength) versus Strain Rate for OFHC Copper	A-16
A.15	Stress (Strength) versus Strain Rate for HY100 Steel	A-17
A.16	Stress (Strength) versus Strain Rate for 1020 Steel	A-18

Figures (Concluded)

<u>Figure</u>		<u>Page</u>
A.17	Stress (Strength) versus Strain Rate for C1008 Steel	A-19
A.18	Stress (Strength) versus Strain Rate for Plates A and B, DU1 and DU2	A-20
A.19	Stress (Strength) versus Strain Rate for 2024-T7 Aluminum	A-21
A.20	Stress (Strength) versus Strain Rate for Tungsten	A-22
A.21	Stress (Strength) versus Strain Rate for Nickel	A-23
A.22	Stress (Strength) versus Strain Rate for Inconel 625 and Pure Tantalum	A-24
A.23	Stress (Strength) versus Strain Rate for 52125 Steel and Armco Iron	A-25
A.24	Stress (Strength) versus Strain Rate for D-6AC Steel	A-26
A.25	Stress (Strength) versus Strain Rate for MAR-M 200 Steel	A-27
A.26	Gauge Stress-Time History for Tungsten (90%) Plate Impact Test	A-28
A.27	Gauge Stress-Time History for 1215 Steel Plate Impact Test	A-29
A.28	Gauge Stress-Time History for 4340 Steel Plate Impact Test	A-30
A.29	Gauge Stress-Time History for 46100 Steel Plate Impact Test	A-31
A.30	Gauge Stress-Time History for MAR-200 Steel Plate Impact Test	A-32
A.31	Gauge Stress-Time History for MAR-250 Steel Plate Impact Test	A-33
A.32	Gauge Stress-Time History for Tungsten (98%) Plate Impact Test	A-34
A.33	Gauge Stress-Time History for Tantalum Plate Impact Test	A-35
A.34	Gauge Stress-Time History for HY100 Steel Plate Impact Test	A-36
A.35	Gauge Stress-Time History for 1020 Steel Plate Impact Test	A-37
A.36	Gauge Stress-Time History for Armco Iron Plate Impact Test	A-38
A.37	Gauge Stress-Time History for C1008 Steel Plate Impact Test	A-39
A.38	Gauge Stress-Time History for AD-85 Plate Impact Test	A-40
A.39	Gauge Stress-Time History for AD-90 Plate Impact Test	A-41
A.40	Gauge Stress-Time History for AD-995 Plate Impact Test	A-42
A.41	Gauge Stress-Time History for Titanium Diboride Plate Impact Test	A-43
A.42	Gauge Stress-Time History for Titanium Diboride Plate Impact Test	A-44
A.43	Gauge Stress-Time History for Silicon Nitride Plate Impact Test	A-45
A.44	Gauge Stress-Time History for Silicon Nitride Plate Impact Test	A-46
A.45	Gauge Stress-Time History for Silicon Nitride Plate Impact Test	A-47

Tables

<u>Table</u>		<u>Page</u>
2.1	Plate Impact Experiments on Metals	2-16
2.2	HEL for Metals	2-17
2.3	Plate Impact Experiments on Ceramics	2-18
2.4	HEL for Ceramics	2-18
3.1	RDG Model Constants	3-7
4.1	Model Constants for AD-85 Ceramic	4-31
B.1	Strength Model Constants For Johnson-Cook Model	B-2
B.2	Bodner-Partom Model Constants	B-6

Preface

This work was conducted under USAF Contract No. F33615-86-C-5064 for Wright Laboratory's Materials Directorate. The Contract Monitor was Dr. Theodore Nicholas (WL/MLLN), whose many helpful comments and guidance during the execution of the research program are greatly appreciated. Dr. William H. Cook of WL/ MNW at Eglin Air Force Base, FL, provided the main source of funding on the modeling activities. The author greatly appreciates the technical interaction and participation of Mr. Cook, especially during the ceramic model developmental activities.

Mr. Robert K. Garrett (code RS32) of Naval Surface Warfare Center (NSWC), White Oaks, MD, supported the high strain rate characterization of pure tantalum, Mar 250, Mar 300, and AF1410 steels. His enthusiastic participation and suggestions during the execution of the research program are appreciated by the author.

This project was performed by the University of Dayton Research Institute primarily by personnel from the Structural Integrity Division and from the Impact Physics Laboratory. Dr. A.M. Rajendran of the Structural Integrity Division was the Principal Investigator. Dr. Joseph P. Gallagher, Supervisor of the Structural Integrity Division, was the Project Manager for the University of Dayton. The author greatly appreciates Dr. Gallagher's encouragement and administrative help during the execution of the program.

Dr. Stephan J. Bless and Dr. N. S. Brar of the Impact Physics Laboratory are the main contributors to the experimental portion of the research program. The SHB tests were conducted by graduate students, Mr. Tarabay Antoun and Mr. Robin Banerjee, under the guidance of Dr. A. M. Rajendran and Dr. Reji John. The undergraduate student, Ms. Julie Dominic, supported the SHB test data processing activities. Dr. John was responsible for the splitting tension tests on silicon nitride and concrete.

Success of this program would not have been possible without the participation of many additional staff members. Dr. A. M. Rajendran guided Dr. Mark A. Dietenberger and Mr. David J. Grove towards the development of the constitutive/failure models for metals and ceramics. Mr. Dietenberger also suggested improved numerical algorithms for the implementation of the models in EPIC-2/3 finite element codes. Mr. Grove was solely responsible for implementing, debugging, and validating the advanced mathematical models into the codes. The author also greatly appreciates Dr. Miles Rubin and Prof. S. R. Bodner of Technion, Israel, for enthusiastically discussing and contributing towards the evaluation of the numerical algorithm for the implementation of the Bodner-Partom model in explicit hydrocodes.

The author is grateful to Ms. Karen Reynolds, secretary, and Mr. R. Kandasamy, graduate student, for their help in assembling this report.

This work was also supported in part by a grant from the Ohio Supercomputer Center in Columbus, Ohio.

Section 1

Introduction

Material response under impact loading conditions is very complex. Most often, the impact loading induces compressive shock under one-dimensional strain; however, later, the reflected waves from the lateral stress free boundaries generate intense tensile loading. In many applied engineering problems, the stress and strain states are three-dimensional and the strain rates are extremely high. The material deformation and failure processes are greatly influenced by these loading conditions. The initially intact material develops microvoids and/or microcracks, which lead to a loss of stiffness. The coalescence of these defects ultimately leads to complete failure of the material under high velocity impact. Mathematical models describing these fundamental damage processes are important tools in the analysis of target and warhead designs using advanced, shock-wave-based, finite element/difference computer codes. With the advent of supercomputers, it has become feasible to use computationally demanding, but physically based constitutive models as predictive tools in impact engineering calculations.

This report summarizes the development of advanced, three-dimensional, constitutive/damage models for metals and ceramics. These models are suitable for a variety of dynamic loading conditions. The model development philosophy was to (1) describe most of the physical processes that operate in the material, (2) minimize the mathematical complexity, (3) keep the number of model constants to a minimum, and (4) devise an efficient numerical scheme to implement into any general purpose shock-wave-propagation based computer code.

Under this program, a new dynamic model (the RDG model) to describe void nucleation, growth, and coalescence in ductile metals was developed by Rajendran, Dietenberger, and Grove [1]. This three-dimensional constitutive model, based on a pressure dependent yield criterion for compressible plastic flow, is strain rate and loading history dependent. A detailed description of the RDG model as well as the constants determined for several metals are reported in Section 3. The model was incorporated into the EPIC-2 code and several example problems were successfully simulated. The results of these simulations are also summarized in Section 3. A

impact response of such altered material. In hydrocode calculations, a simple linear relationship between the strength and pressure is assumed for the powdered ceramic.

Characterizing the impact behavior of ceramic materials involved the following impact experimental techniques: (1) split Hopkinson bar (SHB), (2) plate impact, (3) plate impact on a bar, and (4) bar-on-bar impact. In these experiments, strain gauges, stress gauges, and high speed cameras were used to measure strain, stress, displacement, and deformed shapes. The results of these experiments were used to calibrate the material constants in the model.

In addition to the development of the metal and ceramic models, this program involved extensive material characterization under dynamic loading. Much of this information was obtained in support of the model development. The high-strain-rate-test data obtained under this program for several metals and ceramics are summarized in Section 2.

Both the fragmentation-based and microphysical-based models have been incorporated into the EPIC-2 code. Laboratory impact experiments on AD85 ceramics were simulated. Using the advanced microphysical model, a sample calculation of a long rod penetration into a confined ceramic plate was also performed. The results of the numerical simulations as well as a complete description of the ceramic model are presented in Section 4.

The summary and recommendations are discussed in Section 5. Appendix A summarizes the SHB and plate impact test data. The Bodner-Partom [13] and Johnson-Cook [14] strength models are presented in Appendix B. The numerical algorithm and the solution technique to solve the RDG model are discussed in Appendices C and D, respectively. The modified TCK model used to describe the impact damage in ceramics is presented in Appendix E.

Section 2

High Strain Rate Test Results

The two main objectives of the high strain rate testing are (1) to determine the dynamic properties, such as the variation of strength with respect to strain rate, Hugoniot elastic limit (HEL), spall strength, and initial yield strength, and (2) to obtain the dynamic deformation and stress characteristics from high speed photographs of dynamically deforming (metal) and fracturing (ceramics) specimens using a high speed camera, and stress-time history data from stress gauges.

For this purpose, several impact test configurations were considered: (1) split Hopkinson bar, (2) plate impact, (3) flyer plate impacting a long bar, and (4) short bar impacting a long bar. In this section, no attempt is made to describe the test techniques or the data analysis; however, brief descriptions of split Hopkinson bar and plate impact tests and a summary of data are provided in Appendix A.

2.1 Split Hopkinson Bar Data

The split Hopkinson bar (SHB) experiments provide stress-strain data for metals over a strain rate range of 500 - 2000/sec. This apparatus is also useful to determine the compressive strength of unconfined ceramics under uniaxial stress condition.

2.1.1 Metals

The SHB test data provide variation of strength with respect to strain rate under uniaxial stress. Appendix A provides the SHB data for the various metals tested under this program. Using these data, the Bodner-Partom viscoplastic constitutive (strength) model [13] constants were determined. Detailed discussion of the modeling is given in Section 3.

The IMACON high speed camera was employed to obtain data for ductile necking evolution in copper, Maraging 250 steel, and pure tantalum. Rajendran and Bless [15] described the use of such data to correct the engineering stress-strain relationship beyond the onset of necking. The measured radius of curvature of the neck profile and the minimum radius from the high speed photographs are used to calculate the Bridgman correction factors. Using the

Bridgman relationship, the SHB stress-strain curves beyond the onset of necking can be constructed.

2.1.2 Ceramics and Concrete

The compressive strength of brittle ceramics and concrete materials is an important mechanical property for the design of impact resistant structures. Compressive strength data can be obtained from the SHB tests. The data from the SHB tests are also useful for evaluating the effects of strain rate on the strength of unconfined brittle materials. We performed SHB tests on both silicon nitride and concrete. The results for concrete which were reported previously by Antoun [16] and John et al. [17] are summarized in this section. The compressive strength variation with respect to strain rate for silicon nitride and concrete was determined and the results are presented in Figures 2.1 and 2.2, respectively. Both the ceramic and concrete exhibited significant rate dependency. For concrete, data from other sources are also included for comparison. The data shown in Figures 2.1 and 2.2 are important in the constitutive model development.

The tensile strength of brittle materials can be determined from 'splitting tension' tests using the test specimen shown in Figure 2.3. Quasi-static and dynamic tests were conducted using a servo-hydraulic testing machine and a split Hopkinson bar (SHB), respectively. A schematic of the SHB setup is shown in Figure 2.4. Using the equation in Figure 2.3, the splitting tensile strength is calculated at the peak load as measured by the strain gauge on the SHB's transmitter bar. The strain rate in the specimen is computed using the peak stress, Young's modulus, and time to peak, assuming elastic behavior [18]. The compressive loading results in a uniform lateral (σ_x) tensile stress in the middle of the specimen along the loading axis. In tension-weak brittle materials such as ceramic and concrete, tensile failure can be expected to occur with the crack initiating near the center of the disk. The data obtained for silicon nitride are plotted in Figure 2.5. As one can see in this figure, the tensile strength is highly strain rate sensitive.

The concrete used in this study consisted of Type I ordinary portland cement, river gravel (maximum size = 0.16 in.) and water in the ratio 1:2.5:0.5 by weight. The 3 in. diameter x 6 in. cylinders were cast in cardboard molds and cured for 14 days in water followed by 14 days in laboratory air. The splitting tension specimens were prepared from some of these cylinders.

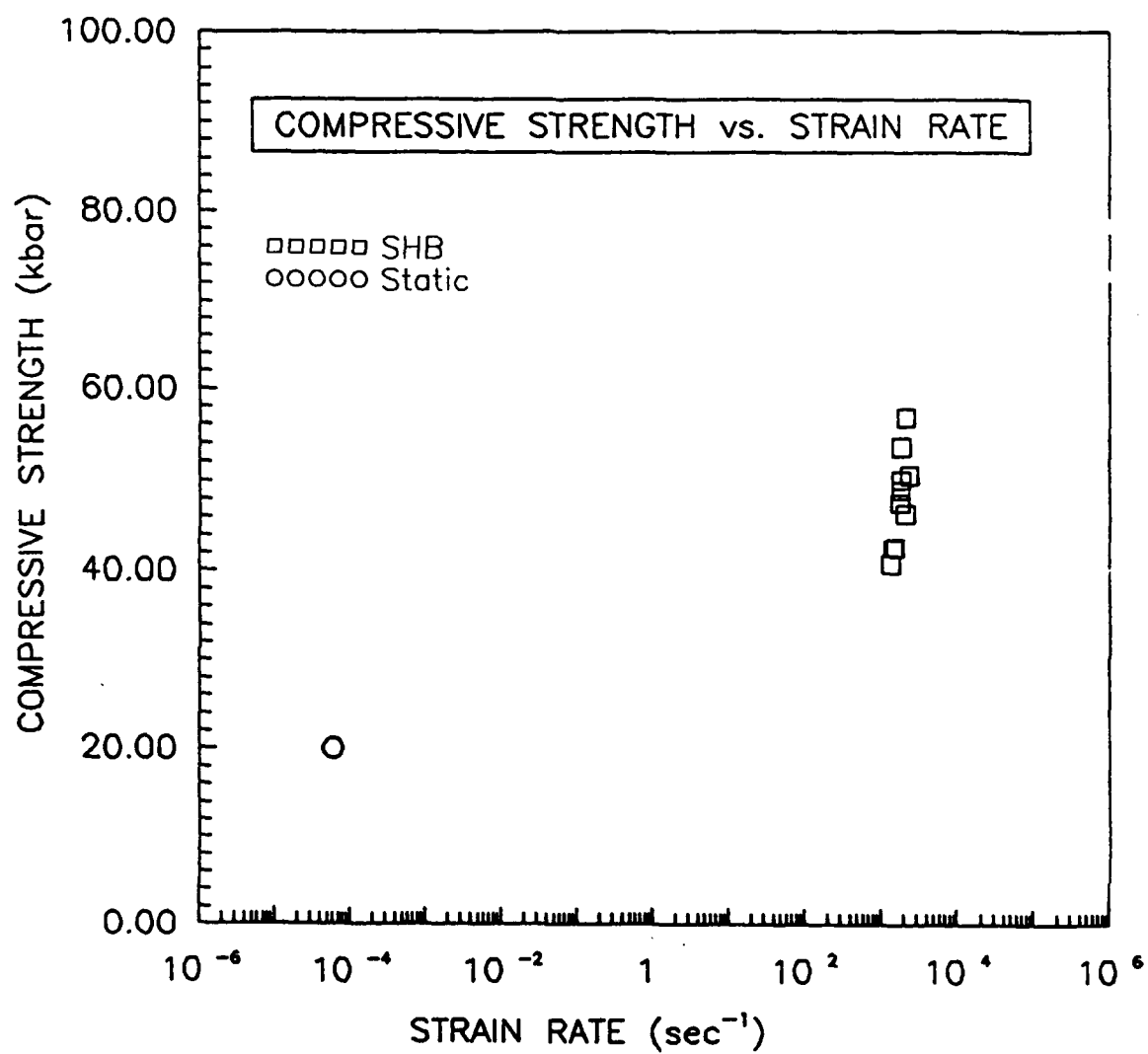


Figure 2.1. Silicon Nitride Compressive Strength Variation with Respect to Strain Rate.

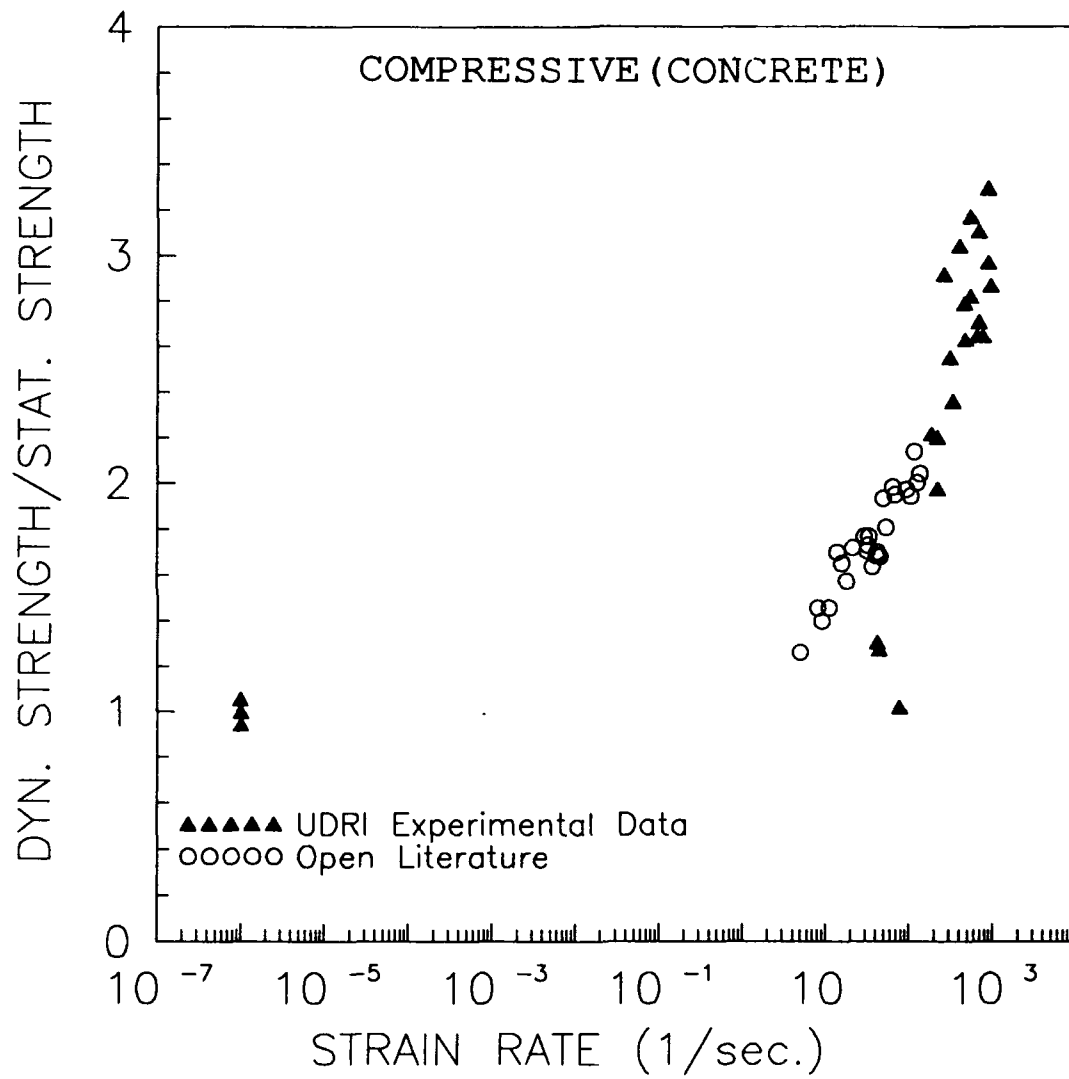


Figure 2.2. Effect of Strain Rate on the Compressive Strength of Concrete.

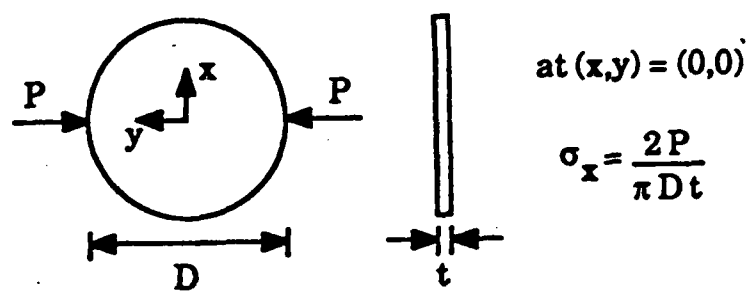


Figure 2.3. Schematic of Splitting Tension Geometry.

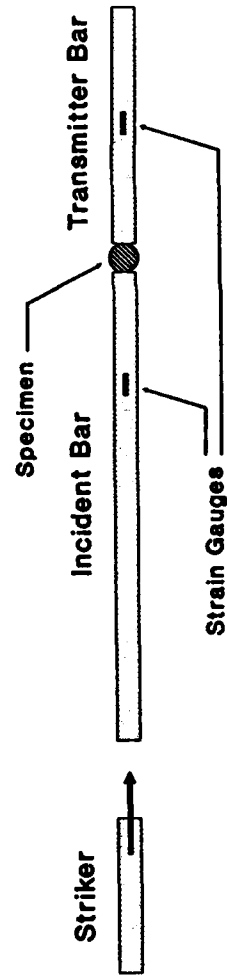


Figure 2.4. Schematic of the Split Hopkinson Bar in Splitting Tension Mode.

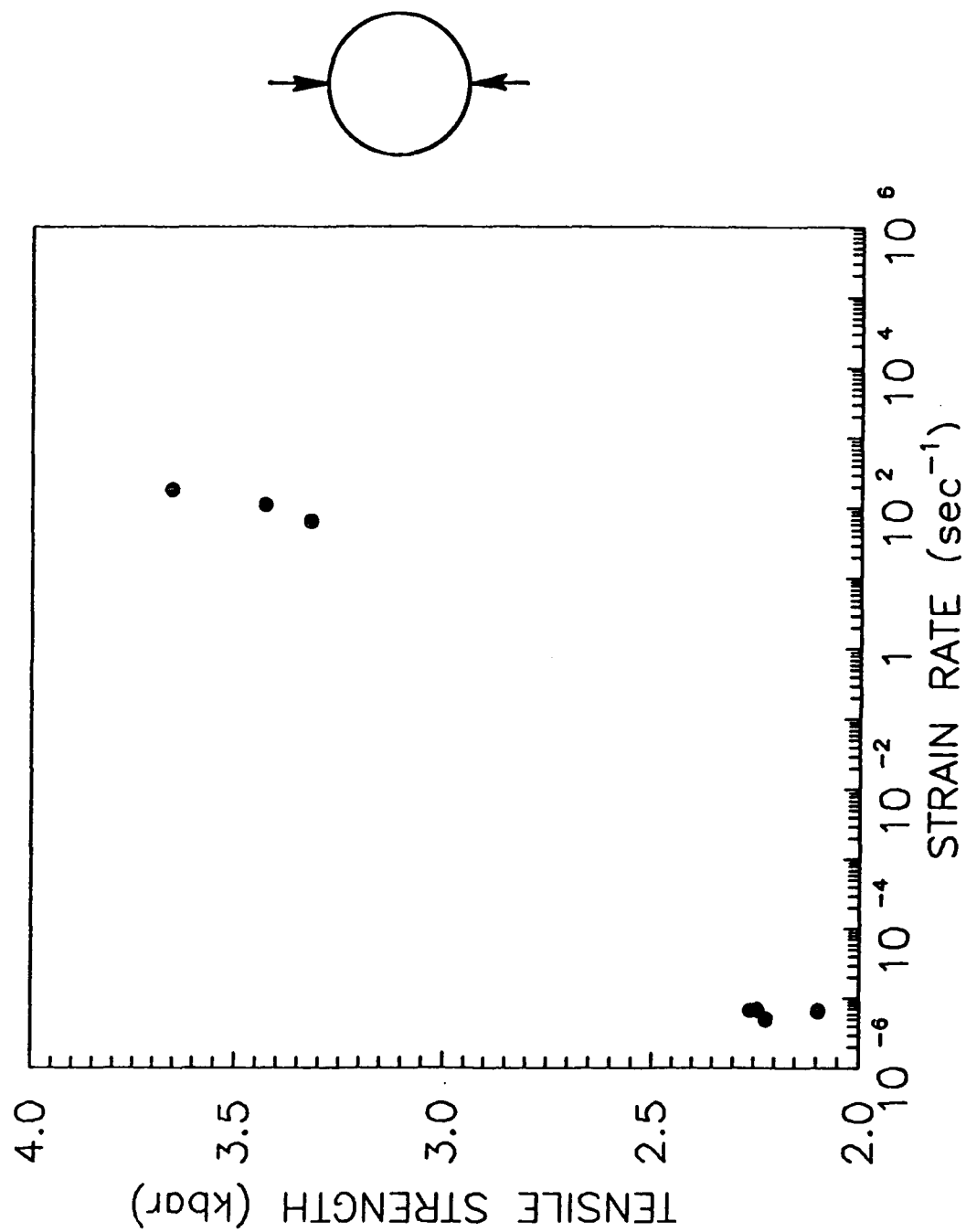


Figure 2.5. Silicon Nitride Tensile Strength Variation with Respect to Strain Rate.

Disk specimens with diameters of 0.5, 1.0 and 2.0 in. and thicknesses of 0.25 and 0.50 in. were prepared. The other 3x6 in. cylinders were used for the quasi-static compression tests. The average compressive strength, Young's modulus (E), and Poisson's ratio are equal to 8357 psi, 4.25×10^6 psi and 0.21, respectively.

For the elastic verification tests, a 2.0 in. diameter x 0.5 in. thick concrete specimen was instrumented with strain gauges at the center on both sides. This specimen was first loaded within the elastic limit at the quasi-static rate to determine the Young's modulus and Poisson's ratio. The same specimen was then subjected to low velocity impact in the SHB. The tensile strain measured during the impact event is shown as a dotted line in Figure 2.6. Assuming that the deformation was elastic, the tensile strain at the center of the disk was predicted from the output of the gauge on the SHB. The predicted strain was then time-shifted and plotted as a solid line in Figure 2.6. The gauge measurements on the SHB correlate well with the average specimen response. The oscillations in the strain response are due to the wave reflections within the specimen. The average time period of the oscillation is 30 μ s which is equal to the time taken by the wave to traverse twice the diameter of the specimen, assuming that the Young's modulus of concrete is rate-independent.

In the disk shown in Figure 2.3, there are two possible locations of crack initiation, namely (1) the point of load application due to high compressive stresses and (2) at or near the center of the disk due to tensile stresses. To determine the location of crack initiation, high speed photography tests were conducted. The concrete specimens were painted black to emphasize the cracks. During the impact, the photographs were taken at 1.0 μ s intervals. Two frames highlighting the crack initiation event and the corresponding stress versus time plot are shown in Figures 2.7 and 2.8, respectively. The first frame, at a time equal to 32 μ s, shows that crack initiation occurred in the constant tensile stress region. Hence this is a valid splitting tension test. The average crack velocity calculated from these tests was 880 ft/s ($\approx 0.12 \times$ Rayleigh wave speed).

The results of the quasi-static and dynamic tests are plotted in Figure 2.9 [16,17]. The splitting tensile strength of concrete is shown to be strain-rate sensitive as was also observed by Ross et al. [18]. The maximum ratio of the dynamic to quasi-static strength is 4.5 at a strain rate of 73 per second. As shown in Figure 2.9, the strain rate sensitivity is independent of thickness.

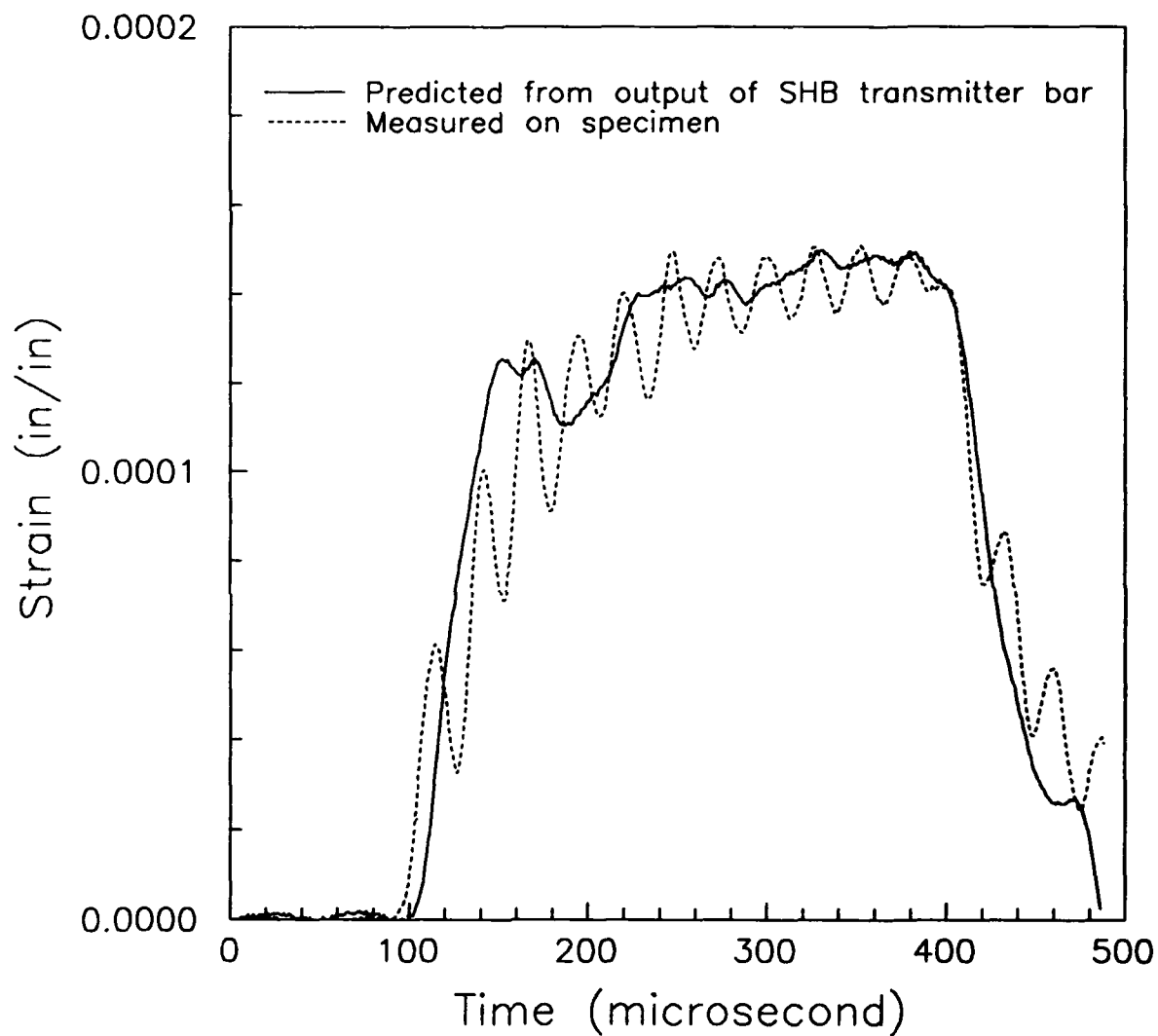


Figure 2.6. Strain History during Elastic Impact on Concrete.

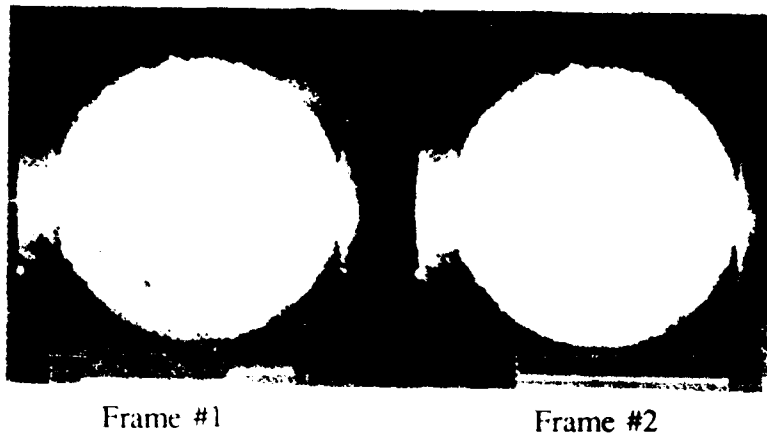


Figure 2.7. Photographs Highlighting Locations of Crack Initiation in Concrete.

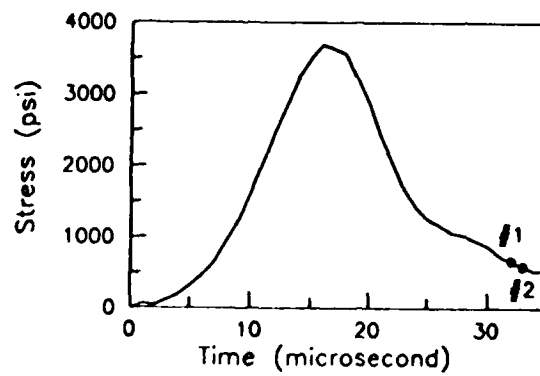


Figure 2.8. Stress History Corresponding to the Test in Figure 2.7 for Concrete.

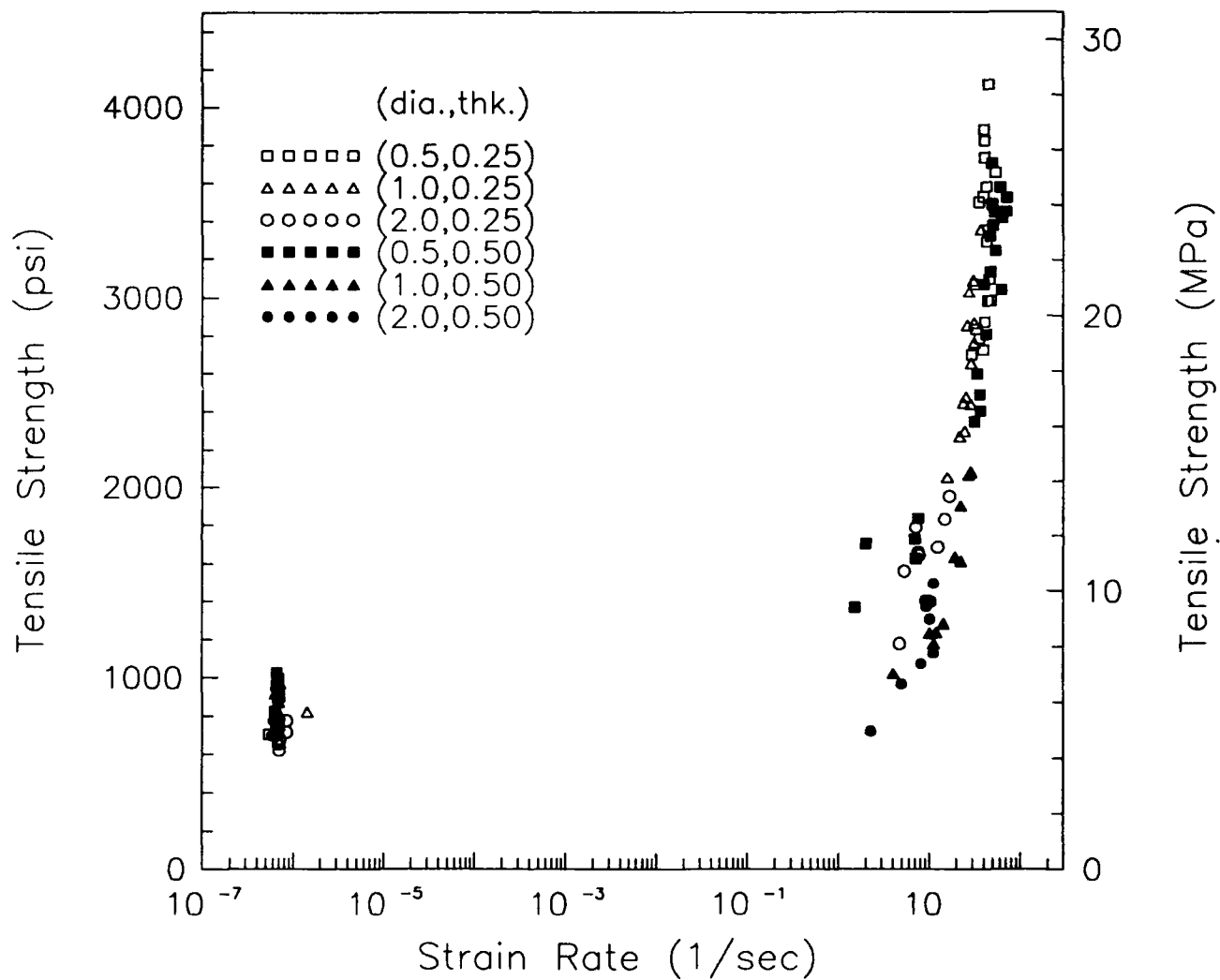


Figure 2.9. Effect of Strain Rate and Specimen Size on the Tensile Strength of Concrete.

The quasi-static strength decreased with increasing diameters as also shown by other investigators [18,19]. The tensile strength from the 2.0 in. diameter specimen was equal to about one-tenth the compressive strength.

The dynamic tensile strength data was normalized with respect to the quasi-static strength for the same size specimen and replotted with the results of other investigators [18-21] in Figure 2.10. The data from our study confirm the steep increase in dynamic tensile strength in the strain rate regime from 1.0 to 100 per second.

In summary, dynamic splitting tension tests were conducted using the SHB apparatus to investigate the influence of specimen size on the dynamic tensile strength of concrete. The validity of the SHB data was confirmed through high speed photographs of the concrete specimen under dynamic deformation. The thickness of the concrete specimens had negligible effect on the splitting tensile strength. The strength decreased with increasing specimen diameter under quasi-static and dynamic loading. But the ratio of dynamic to quasi-static strength was observed to be size-independent. For strain rates greater than 1.0 per second, the splitting tensile strength exhibited significant strain-rate dependency. At a strain rate of 73 per second, the ratio of dynamic to quasi-static strength was about 4.5.

2.2 Plate Impact Experiments

The plate impact experiment is the most commonly used configuration for studying dynamic tensile (spall) failure in materials at very high strain rates. In the plate impact test, a flat flyer plate is made to impact against a target plate at a high velocity. The diagnostic measurements usually involve a VISAR to measure the particle velocity history or piezo-resistive stress gauges to measure the stress history at the target and back plate interface. This configuration is schematically shown in Appendix A. The flyer and target may be of the same or different material. Compressive stresses are produced and transmitted immediately from the plane of impact to the adjacent stress free areas of the material in the form of a stress pulse. A typical free surface velocity history is shown in Figure 2.11. The portion of the velocity history indicated by the letter *E* represents the arrival of an elastic shock wave from the impact plane. The material particles are compressed elastically ($E-E'$) until the relatively slow moving plastic shock wave arrives at the free surface. Typically, both the shape and time duration of the portion

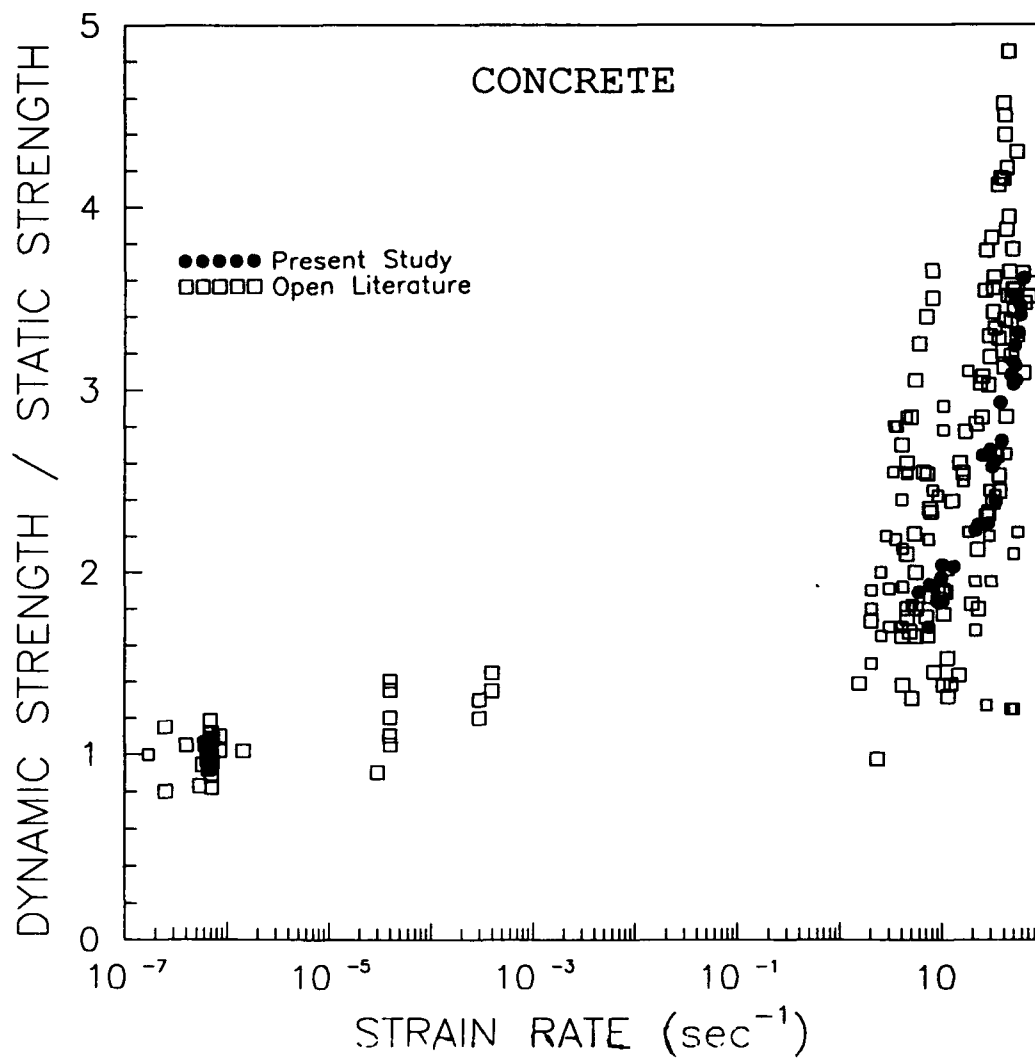


Figure 2.10. Strain Rate Sensitivity of Tensile Strength Normalized With Respect to Static Strength for Concrete

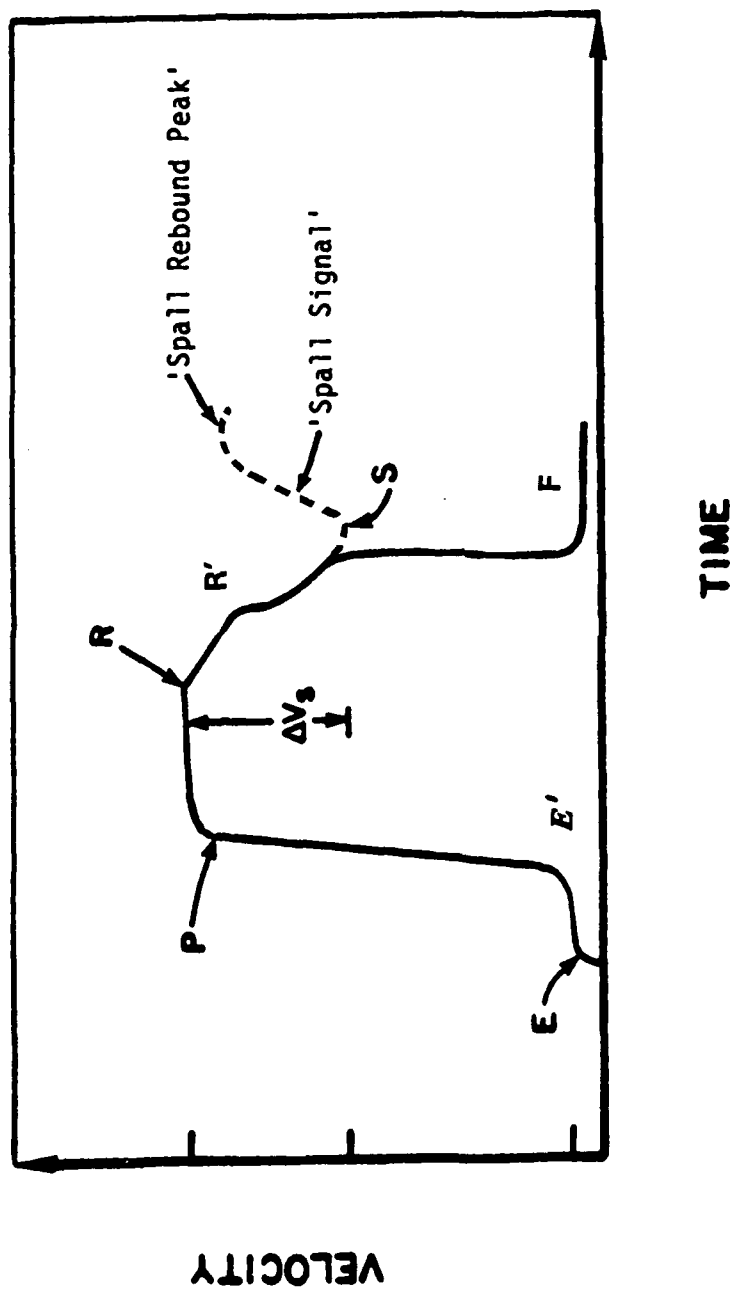


Figure 2.11. Typical Free Surface Velocity of the Target Measured Using VISAR

$E-E'$ depend on the strain rate sensitivity of the material and thickness of the target plate. For engineering calculations, the average velocity level between the points E and E' is usually defined as the velocity at the HEL, V_{HEL} . Using this experimental value, the stress at the HEL (σ_{HEL}) is calculated from the relationship $\sigma_{HEL} = \frac{1}{2}\rho c V_{HEL}$, where ρ is the material density, c is the elastic sound wave speed, and V_{HEL} is the velocity at the HEL measured at the target's free surface. This expression is valid only under symmetric impact conditions, that is, when the target and flyer are of the same material. The high strain rate yield strength, Y_o , can then be calculated as $Y_o = \sigma_{HEL} / [\frac{K}{2G} + \frac{2}{3}]$, where G is the shear modulus and K is the bulk modulus.

When the plastic shock wave arrives at the target's free surface, this wave takes the particle velocity to the peak level defined between points P and R . Later, the elastic release wave from the back surface of the flyer plate arrives at point R , and the velocity drops to R' . The plastic release wave from the flyer reaches the target's free surface and drops the velocity further to F . In general, in modeling, the level $E-E'$ and the wave structure around the HEL are sensitive to the constitutive relations (strength models); however, the slopes and peak of the VISAR signal depend primarily on the pressure-volume relationship (equation of state).

Depending on the severity of the impact, the bulk material (target) can spall and a stress-free fracture surface (spall plane) is created in the target. When the spall plane separates inside the target, the stresses relax to zero, and hence, a compressive shock wave is generated. This shock wave arrives at point S , as shown in the typical VISAR signal. The material particle velocity history follows the dashed line (recompression). The signal beyond point S is often denoted as the "spall signal." This spall signal is most often used in the estimation or calibration of failure model parameters.

The experimental data from the plate impact experiments for several metals and ceramics are given in Appendix A.

2.2.1 Metals

We performed plate impact experiments on several steels, aluminum alloys, copper, pure tantalum, and tungsten. The details of the tests are given in Table 2.1. The stress gauge measured stress histories at the interface of the target and the back plate are given in Appendix A. The measured stress history is often used in the spall model calibration. The Hugoniot elastic limits (HEL) for these various metals were determined and tabulated in Table 2.2.

TABLE 2.1
PLATE IMPACT EXPERIMENTS ON METALS

Shot Number	Flyer Plate		Target Plate		Impact Velocity (m/sec)
	Material	Thickness (mm)	Material	Thickness (mm)	
7-538	Copper	2.0	Copper (98%)	9.0	185
7-1070	Copper	2.0	Tungsten (98%)	4.0	188
7-1071	46100 Steel	2.65	46100 Steel	6.0	310
7-1244	Copper	6.4	Tungsten (90%)	5.6	292
7-1250	2519 Al	4.0	2519 Al	8.0	324
7-1267	Copper	4.0	1215 Steel	10.6	634
7-1268	1020 Steel	3.9	1020 Steel	7.8	572
7-1288	Copper	2.0	Copper	4.1	512
7-1298	Copper	3.0	Armco Iron	6.0	470
7-1299	Copper	3.0	HY100 Steel	6.0	489
7-1300	Copper	3.0	C1008 Steel	6.0	462
7-1302	Copper	2.0	Tantalum	6.0	735
7-1305	Copper	3.0	4340 Steel	8.0	665
7-1454	MAR-250 Steel	3.0	MAR-250 Steel	6.0	575
7-1455	MAR-200 Steel	3.0	MAR-200 Steel	6.0	508
7-1523	AF1410 Steel	4.5	AF1410 Steel	9.0	678

TABLE 2.2
HEL FOR METALS

MATERIAL	HEL (kbar)	Y (kbar)
Tantalum	27.0	13.5
Tungsten	82.0	51.0
46100 Steel	38.0	19.0
1215 Steel	14.4	7.2
4340 Steel	20.0	10.0
MAR-200 Steel	26.0	13.0
MAR-250 Steel	21.0	10.5
1020 Steel	7.4	3.7
C1008 Steel	11.0	5.5
AF1410 Steel	36.0	18.0
HY100 Steel	16.0	8.0

2.2.2 Ceramics

We performed a limited number of plate impact tests on AD85, AD90, AD95, pure alumina (99.8%), Silicon Nitride, Boron Carbide, and Titanium Diboride. The details of the experiments are given in Table 2.3. The HEL values for various ceramics are summarized in Table 2.4. The corresponding measured stress histories are given in Appendix A.

2.3 Plate-on-Bar Impact Data

In this configuration, a thick flyer plate impacts onto a long slender bar. An aspect ratio (length to diameter) of twelve was used for the bar. In Figure 2.12, a schematic of the plate-on-bar test is shown. For diagnostic measurement, a piezo-resistive stress gauge is imbedded into the bar at a distance several diameters away from the impact end. This technique was described in detail by Rosenberg and Bless [22].

TABLE 2.3
PLATE IMPACT EXPERIMENTS ON CERAMICS

Shot Number	Flyer Plate		Target Plate		Impact Velocity (m/sec)
	Material	Thickness (mm)	Material	Thickness (mm)	
7-1108	Copper	2.6	AD-90	---	181
7-1109	Copper	2.6	AD-99.5	8.4	551
7-1136	Copper	2.6	TiB ₂	12.7	719
7-1154	Copper	2.0	B ₄ C	10.0	1121
7-1215	Copper	3.0	Si ₃ N ₄	11.4	1009
7-1218	Copper	3.0	Si ₃ N ₄	11.4	1110
7-1295	AD-85	5.0	AD-85	8.0	237
7-1332	Copper	3.0	Si ₃ N ₄	11.4	770

TABLE 2.4
HEL FOR CERAMICS

MATERIAL	HEL (kbar)	Y (kbar)
Alumina (AD-85)	55	39
Alumina (AD-90)	70	52
Alumina (AD-99.5)	83	59
Alumina (Hot Pressed, 99.8% Pure)	123	82
Silicon Nitride	120	78
Silicon Carbide	140	107
Aluminum Nitride	94	64
Titanium Diboride	75	66
Boron Carbide	180	146
Sodalime Glass	64	39

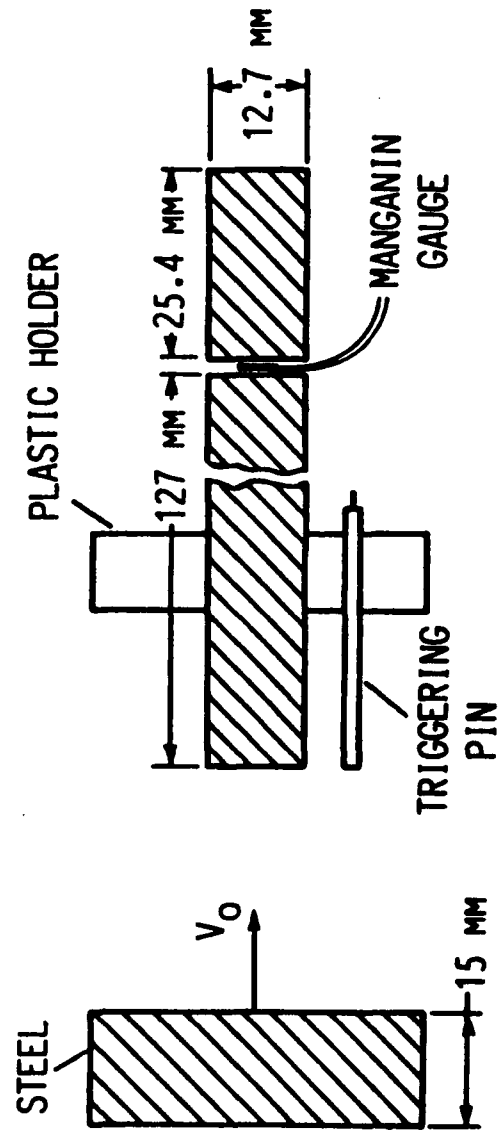


Figure 2.12. A Schematic of Plate-on-Bar Impact Test Configuration.

2.3.1 Metal Bars

While the stress state near the impact end is multiaxial, it is uniaxial at the gauge location. At high velocities, metals plastically flow near the impact end. However, the stress wave that passes through the gauge is essentially an elastic wave and its amplitude is a measure of yield strength at medium strain rates (about 500/sec). This measurement is useful, especially when the SHB test does not provide accurate measurements of the initial yield strength due to spurious wave reflections at small strains (< 0.03).

Grove and Rajendran [23] performed a numerical simulation of a 15mm thick 1020 steel plate impacting a 152mm long, 12.7mm diameter C1008 steel bar. The calculated initial yield stress (maximum amplitude of the elastic wave) matched well with the gauge data. Such numerical simulations are useful in the evaluation of constitutive models.

2.3.2 Ceramic Bars

The plate-on-bar experimental technique was initially employed to measure stresses in metal bars. However, under the Air Force contract, we extended the technique to characterize deformation and fracture in ceramic bars. Several articles were prepared and published by Brar et al. [24], Rosenberg et al. [25], Brar and Bless [26], Grove and Rajendran [27], and others [28,29].

Brar et al. [24] conducted plate-on-bar experiments on Coor's AD-998 (almost pure aluminum oxide) and AD94. Ten experiments, at impact velocities in the range 96-560 m/s, were performed using a 50 mm gas/powder gun. Steel impactors, 15 mm thick, were used in all the experiments. In these experiments, when the impact stress was below the compressive yield strength, a constant amplitude stress wave was produced in the bar. When the impact stress exceeded the yield strength, the stress level in the bar decayed with distance and time. This stress decay is consistent with lateral release involving dilatancy.

These types of impact tests can be used to measure dynamic yield strength. The measured dynamic strength in AD998 and AD94 ceramics did not differ significantly from static strengths. Typical oscilloscope records from experiments at impact velocities of 102, 125, and 551 m/s respectively on AD998 (99.8 % pure alumina) bars are shown in Figure 2.13. The

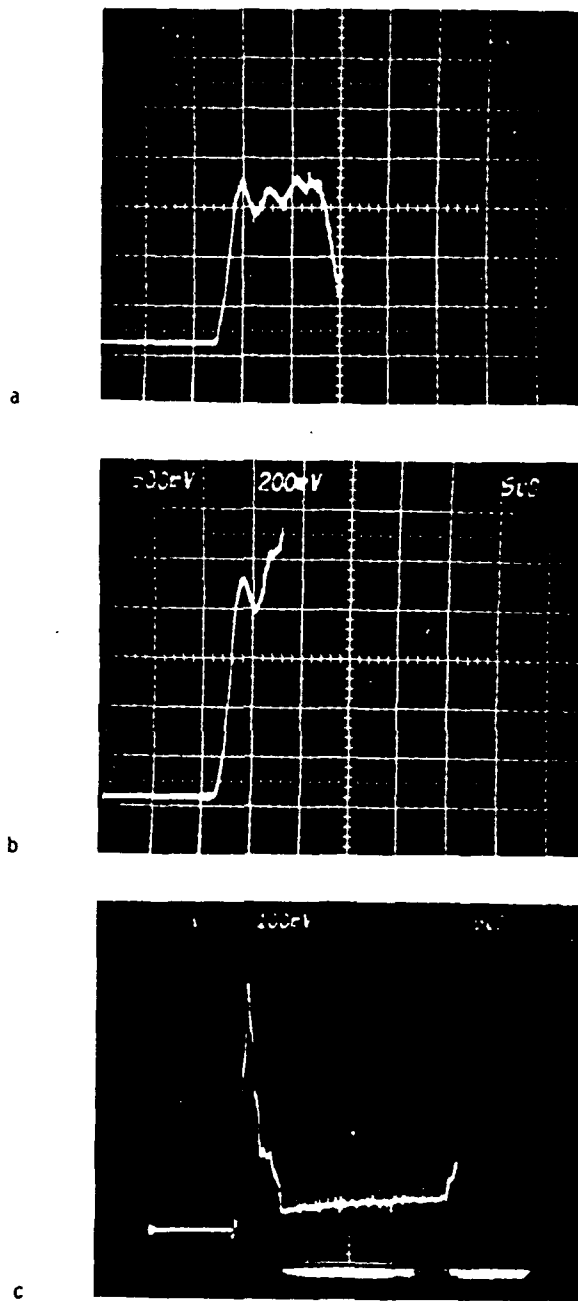


Figure 2.13. Oscilloscope Records from Experiments on AD-998 Rods. Scales for All Records are 0.2 V/div. and 0.5 μ s/div.

corresponding peak stresses were 18, 21.5, and 92 kbars. Detailed interpretations of these plate-on-bar experiments can be found in Reference [24].

The serial high speed photographs of the fracturing AD998 bar are shown in Figure 2.14. The frames are read from top to bottom and left to right. The first frame (top left) is at time zero and successive frames are taken every 10 microseconds. In the experiment, the bar was painted black to observe the fracture patterns. The bar laterally expands due to pulverization at the impact end. Later, splitting cracks emanate from the impact end and propagate towards the other end of the bar. The fracture of the bar is indeed extremely complex due to fracturing under a multiaxial stress state. At present, no definitive understanding or modeling of this failure process is available.

2.4 Bar-on-Bar Impact Test

Failure of ceramics can be studied with instrumented bar impacts and high speed photography. Brar and Bless [26] summarized their results in detail. In the bar-on bar impact configuration (see Figure 2.15), a short ceramic bar impacts onto a long ceramic bar having an aspect ratio of 4~5. Both bars are made of the same material. The strain rates are in the range of $10^3 \sim 10^4/\text{sec}$. Manganin gauges were embedded at several diameters away from the impact end. The rod projectiles were launched using a lexan sabot in a 50 mm gas/powder gun. The bar targets were aligned for a planar impact using a special fixture. An Imacon 790 high speed camera was used to photograph the fracture of the rods. Alumina bars were painted black so that the cracks and faults could be distinguished. The bar fracturing was photographed every 10 microseconds. The recording time duration is usually about 140 microseconds. The photographs of the fracturing ceramics indicate three types of fracture; pulverization of the bar at the impact plane, axial splitting (or faulting), and a propagating destruction (fracture) wave. The material behind this wave is pulverized and the measurements from the pictures indicate that the fracture wave propagates faster than the interface velocity.

In alumina AD-998, a splitting type of crack pattern can be seen from Figure 2.16. However, in soda lime glass bars the splitting type fracture was not observed in the high speed photographs shown in Figure 2.17. A compressive fracture front propagates from the impact end. This fracture pattern is more of a pulverization type than a few cracks running into the bar as with splitting cracks. Upon impact, a compressive shock wave travels into the bar and reflects

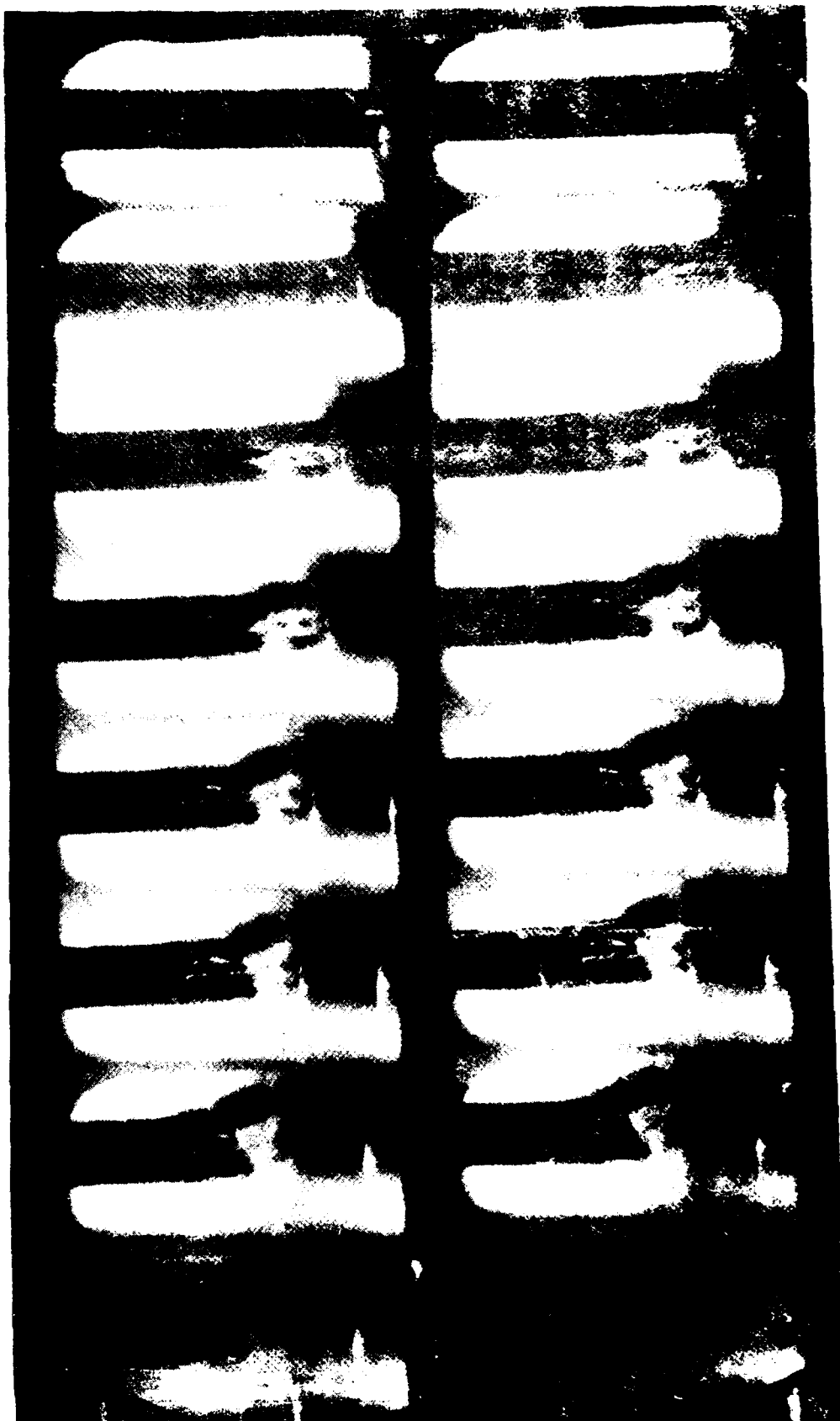


Figure 2.14. High Speed Photograph of AD-998 Fracturing Due to Steel Plate Impact.

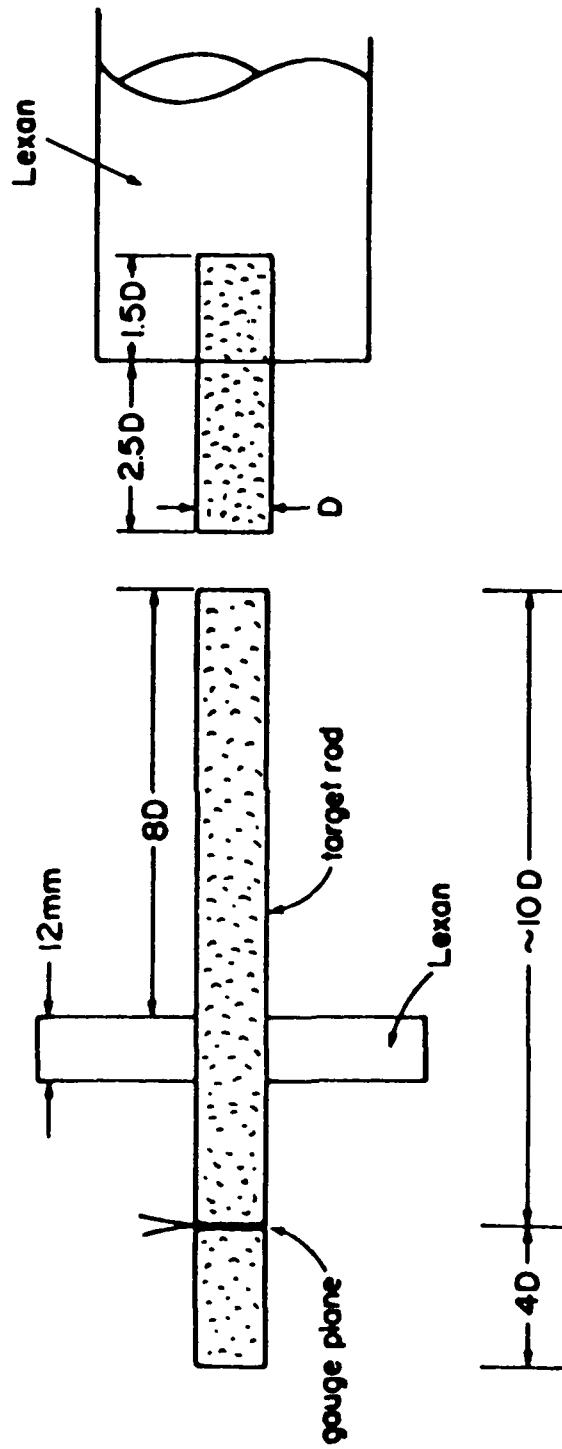


Figure 2.15. A Schematic of Bar-on-Bar Impact Test Configuration.

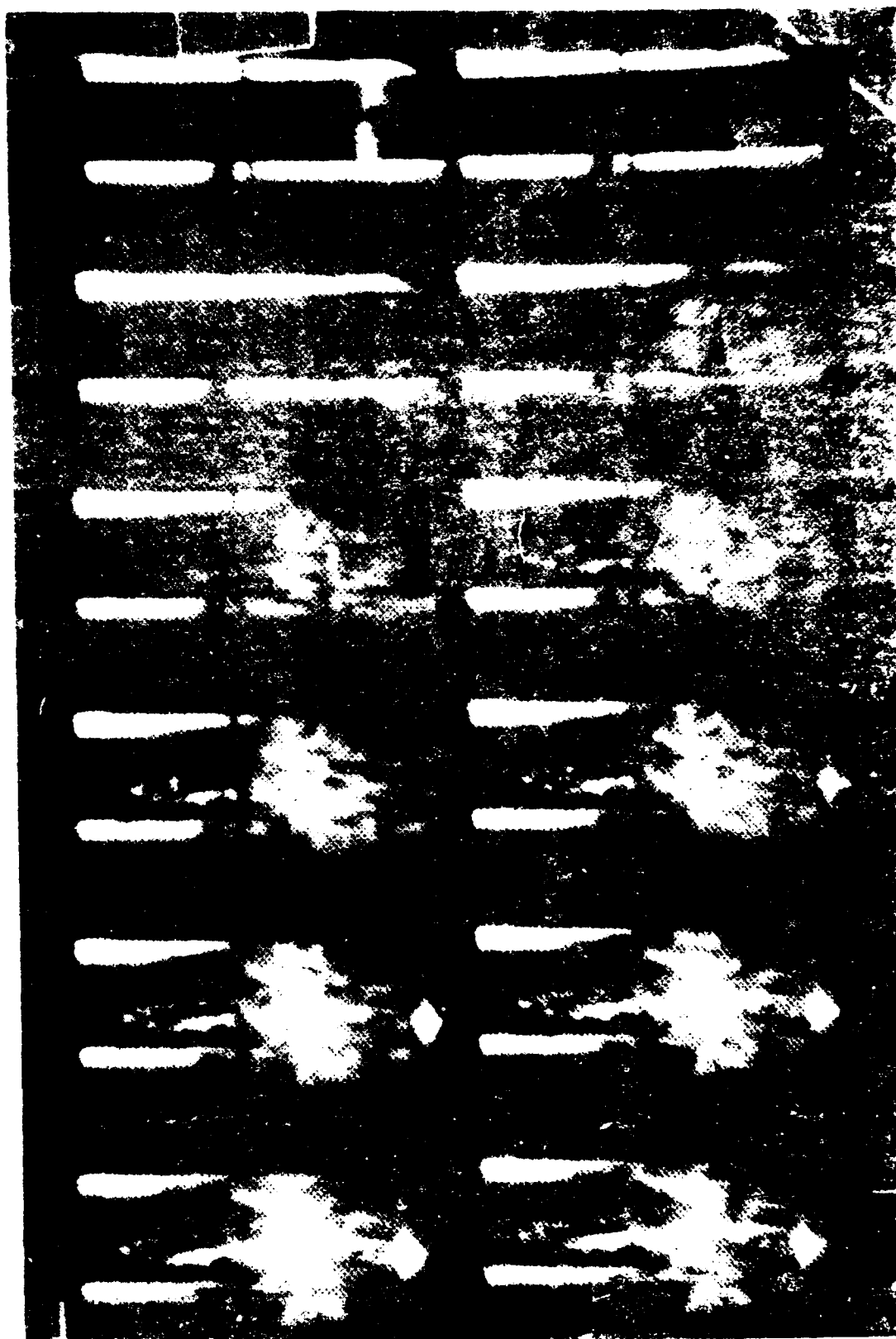


Figure 2.16. High Speed Photograph of AD-998 Fracturing Due to AD-223 Bar-on-Bar Impact.

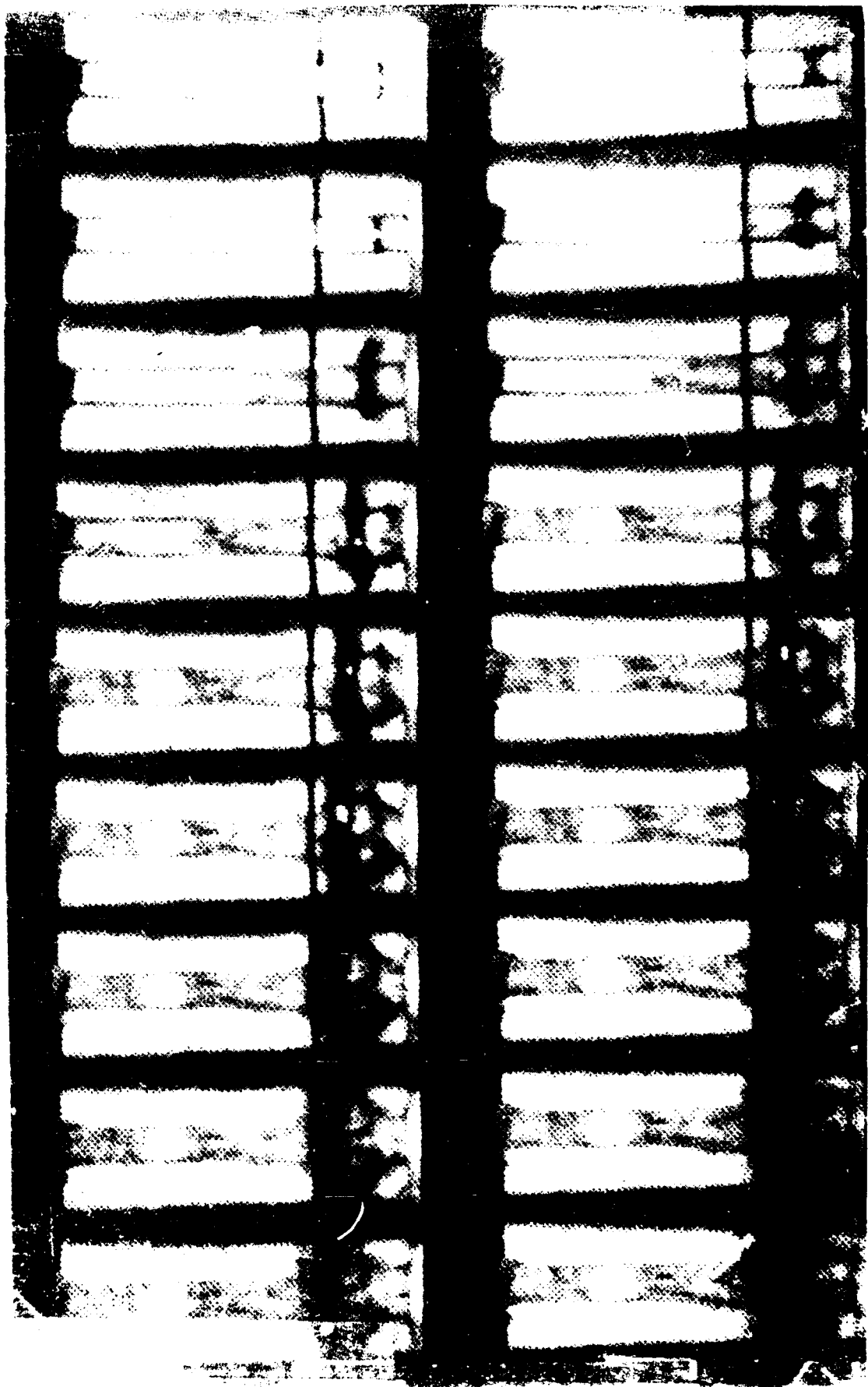


Figure 2.17. High Speed Photograph of Soda Lime Glass Fracturing Due to Soda Lime Glass Bar-on-Bar Impact.

as a tensile wave. This tensile wave, along with release waves from the lateral surface, initiates fracture at the free end of the bar. The tension-initiated fracture front propagates towards the fracture front arriving from the impact end of the bar.

This tensile wave, which propagates faster than the fracture front, encounters the compressive fracture front and reflects back as a compressive wave of lesser amplitude. This trapped wave decays and, as one can clearly see in Figure 2.17, leaves a small length of the bar unbroken. These types of diagnostic photographs should be useful to model builders in validating ceramic failure models.

Section 3

Ductile Failure Model for Metals

Three of the main features in a dynamic ductile failure model are the following: (1) the initial intact (void-free) material requires a constitutive description which will include strain rate and temperature effects; (2) a mathematical description of the void nucleation and growth process; and (3) pressure dependent plastic flow equations for the porous (void-containing) aggregate. There could be several other features in the failure modeling. For instance, depending on the level of voids, the stiffness of the aggregate may significantly be reduced; therefore, models to degrade the stiffness will be required for the realistic description of the material behavior. The final process of voids coalescence may also be important. Another aspect of the failure model is the equation of state for the porous aggregate.

In this section, a brief description of a ductile failure model developed under this program is presented. Previously, a detailed description of this RDG model was presented by Rajendran [8], and Rajendran, Dietenberger, and Grove [1]. This three-dimensional, continuum-mechanics based, dynamic failure model (RDG Model) is capable of describing spallation under two-dimensional stress (long rod impact on a thick plate) and one-dimensional strain (plane plate impact). The RDG model considered a viscoplastic constitutive description for the matrix and the porous aggregate materials. The stress and strain based void nucleation process was modeled through a Gaussian distribution. The RDG model proposed a new pressure dependent yield function for describing plastic flow in the porous aggregate. There are four phases in the model. In the first phase, the intact material is described by the Bodner-Partom viscoplastic model [13]. The void nucleation is introduced in the second phase. The void-contained aggregate is described in the third phase using an associated plastic flow rule derived from a pressure dependent yield function. The last phase of modeling is the coalescence of voids leading to complete failure. In the RDG model, separate modeling of the coalescence process is not needed. The void growth law is such that the growth rate is rapidly increased as the damage approaches its critical value.

3.1 Constitutive Equations

A pressure dependent yield-criterion-based approach has been considered in the constitutive model formulation. For randomly distributed voids or microcracks contained in the aggregate, the yield behavior will be influenced not only by the second invariant of the deviatoric stress (J_2) but also by the pressure or mean stress (I_1). The following form of the yield function has been considered:

$$\Phi = (2 + \rho^2) J_2 + \frac{1 - \rho^2}{3} I_1^2 - \delta(\rho) Y_m^2 = 0 \quad (1)$$

where,

$$\delta(\rho) = \frac{g(\rho) - g(\rho_{cr})}{g(1) - g(\rho_{cr})} \quad (2)$$

and

$$g(\rho) = \left(\kappa - \frac{N}{|N|} (1 - \rho) \right)^N \quad (3)$$

where Y_m is the effective yield stress in the matrix material, κ and N are model constants, and ρ is the relative density. A negative value of N makes Equation (3) a hyperbolic power function.

Numerical simulations of a plate impact test configuration were performed to evaluate the effects of the δ function on the spall signal. In these simulations, the initial slope of $\delta(\rho)$ at $\rho=1$ greatly influenced the slope of the spall signal. Consequently, the parameter $\beta (= \delta'(1))$ was introduced. With β , N , and ρ_{cr} as model constants, the corresponding value of κ can be solved by a simple iterative scheme. An idealistic value of zero can be assumed for ρ_{cr} .

The viscoplastic strain rates, $\dot{\epsilon}_{ij}^p$ in the aggregate can be calculated using the flow rule derived from the yield function given by Equation (1). An expression for σ_{ij} can be obtained from Hooke's law (elastic stress-strain relationship) by defining the elastic strain rate as the difference between total and plastic strain rates,

$$\sigma_{ij} = E_{ik} (\dot{\epsilon}_{kj} - \dot{\epsilon}_{kj}^p) \quad (4)$$

The evolution laws for the void content f (void volume fraction, $f = 1-\rho$) are given by the nucleation and growth equations. Rajendran et al. [1], described the evolution laws in detail. For completeness, the salient equations are given:

$$\dot{f} = \dot{f}_n + \dot{f}_g \quad (5)$$

where, for the void volume fraction nucleation law we use

$$\dot{f}_n = F_\sigma (\dot{Y}_m + \dot{P}) + F_\epsilon \dot{D}_m^p \quad (6)$$

with

$$F_\sigma = \frac{f_1}{s_1 \sqrt{2\pi}} e^{-\frac{1}{2} \left(\frac{Y_m + P - \sigma_N}{s_1} \right)^2} \quad (7)$$

and

$$F_\epsilon = \frac{f_2}{s_2 \sqrt{2\pi}} e^{-\frac{1}{2} \left(\frac{D_m^p - e_N}{s_2} \right)^2} \quad (8)$$

where Y_m is the effective stress in the matrix, P is the pressure in the aggregate, D_m^p is the equivalent plastic strain in the matrix, and σ_N and e_N are the mean equivalent stress and strain, respectively, around which the nucleation stress and strain are distributed in a Gaussian manner. The terms s_1 and s_2 are the standard deviations of these distributions. These two parameters control the ranges of stress or strain over which most of the voids can be nucleated. The terms f_1 and f_2 define the maximum allowable void volume fractions due to stress and strain nucleation, respectively.

The growth law can be directly related to the dilatation due to growth of voids in the aggregate. By definition, the void growth rate is given by,

$$\dot{f}_g = \rho \dot{e}_{ii}^p \quad (9)$$

where repeated index means summation, $\dot{\epsilon}_{ii}^p$ are the plastic strain rates in the three principal directions, and $\rho (=1-f)$ is the relative density.

To complete the formulation, an evolution equation for the matrix effective stress is required. For the intact matrix material, either the Bodner-Partom [13] (BP) or Johnson-Cook [14] (JC) model can be employed. These models are described in Appendix B. A strain rate dependent relationship between Y_m and the equivalent plastic strain rate in the matrix material is provided by these models.

3.2 Degradation of Shear and Bulk Moduli

The shear and bulk moduli (K and G , respectively) are degraded using Mackenzie's formula [30]. Mackenzie derived an approximate analytical expression for the reduction of elastic stiffness based on the elastic-plastic flow around a spherical void in an infinite, incompressible matrix material. The RDG model [1] employed the corresponding expression for the degraded moduli \bar{K} and \bar{G} as,

$$\frac{\bar{K}}{K} = \frac{(1-f)}{(1 + 3K\frac{f}{4G})} \quad (10)$$

and,

$$\frac{\bar{G}}{G} = (1-f) \left\{ 1 - \frac{6K+12G}{9K+8G} f \right\} \quad (11)$$

where K and G are the bulk and shear moduli of the intact material. Appendices C and D outline the solution scheme to solve the governing equations.

3.3 Equation of State for the Aggregate

The equation of state for the solid (intact) material has been routinely determined from the experimentally obtained Hugoniot data for steel, aluminum, copper, and other metals. However, once the initially intact solid develops voids upon tensile loading, the equation of state (EOS) of the original solid material is no longer valid during the subsequent compressive loading. For this purpose, the EOS parameters have to be modified.

The simple approach used in the RDG model is an extension of Mackenzie's procedure. The EOS for the intact solid is described by the Mie-Gruneisen equation as

$$P_s = (\beta_1\mu + \beta_2\mu^2 + \beta_3\mu^3) (1 - \Gamma \frac{\mu}{2}) + \Gamma (I - I_0) \quad (12)$$

where β_1 , β_2 , β_3 , and Γ are EOS constants. μ is the volumetric compressible strain of the intact solid, $(\frac{V_s}{V} - 1)$, and I is the specific internal energy of the solid material. To account for the voids, Mackenzie's formulation is implemented as follows. A volumetric elastic strain of the aggregate is first defined as,

$$\mu_{ag} = [\frac{(1+\mu)}{(1-f)} - 1] \quad (13)$$

to replace μ in the right side of Equation (12). Then the right side expression of Equation (12) is multiplied by the Mackenzie correction term, $\frac{\bar{K}}{K}$, to obtain the aggregate pressure, P . Thus a voided material undergoing compression will load along a degraded bulk modulus at the aggregate compressible strain. At high enough stress levels, the void will collapse ($f=0$), and thus the modified EOS will reduce to Equation (12).

The various governing equations can be rearranged and numerically integrated. The RDG model along with the choice of BP or JC model was implemented into the EPIC-2 finite element code [31]. Special purpose subroutines have been developed successfully. The corresponding numerical scheme is given in Appendices C and D.

The strength model (BP or JC) constants are determined using the stress - strain data from split Hopkinson bar (SHB) tests. These data may comprise data from quasi-static tensile, SHB tensile, compressive, and torsional tests. Rajendran et al. [32] described a combined experimental and numerical scheme for evaluating BP model constants. They also included the HEL (Hugoniot Elastic Limit) data in the scheme. Johnson and Holmquist [33] provided a methodology to obtain JC model constants. The BP and JC model constants for various metals are given in Appendix B.

Determining failure model constants requires plate impact test data in terms of either velocity history or stress history at the back of the target. Rajendran et al. [1] determined the failure model constants using the velocity history obtained from a plate impact test on OFHC copper.

3.4 Model Parameters

The BP model was employed for the intact material description. The corresponding model parameters are given in Appendix B. For establishing a standard procedure to calibrate the failure model constants, two plate impact experiments (7-538 and 7-1299) were considered. (See Table 2.1.) Experiment 7-538 was first employed in the failure model parameter evaluation. In this experiment, a 2 mm copper flyer was impacted against a 9 mm OFHC copper target at an impact velocity of 185 m/s, and the target's free surface velocity history was obtained using a VISAR (velocity interferometer). The second experiment (7-1299) consisted of a 3 mm copper flyer impacting a 6 mm HY100 steel target at a velocity of 489 m/s; in this experiment, the diagnostic was a manganin gauge measured stress history. These two experiments were simulated using the EPIC-2 code. The special purpose subroutines describing the RDG model were used to model the spall process in both OFHC copper and HY100 steel. Using the suggested procedure, the model constants for these two as well as several other metals were determined. The corresponding constants are given in Table 3.1.

The comparison between the model simulation and the experimental velocity history data for OFHC copper is shown in Figure 3.1. Since the HEL of OFHC copper is extremely low compared to the shock stress, the BP model predicted HEL (knee at A in Figure 3.1) did not match well. However, for copper, the HEL value is not considered critical because plastic yielding occurs at a (uniaxial) stress below 1 kbar. The matching beyond point S is controlled by the RDG model constants. In general, the overall match between the simulation and the data is very good. This demonstrates the ability to calibrate the model constants using plate impact test data as well as the RDG model capability to accurately reproduce the spall signal.

TABLE 3.1
RDG MODEL CONSTANTS

Material	Nucleation			Yield Function	
	f_1	σ_N (GPa)	$s(=\sigma_N/4)$ (GPa)	β	N
OFHC Copper	0.01	1.6	0.4	65	-2.4
HY100 Steel	0.035	3.6	0.9	30	-1.0
C1008 Steel	0.02	1.2	0.3	100	-2.0
MAR-200 Steel	0.01	4.8	1.2	40	-5.0
Armco Iron	0.05	2.0	0.5	70	-0.5
Tantalum	0.003	4.8	1.2	10	-3.0
1020 Steel	0.01	2.4	0.6	1	-0.5
MAR-250 Steel	0.01	3.2	0.8	50	-3.0
AF1410 Steel	0.01	5.6	1.4	20	-4.0

To further verify the model constant calibration scheme using data from a plate impact test, spall in HY100 steel was considered. In this case, a manganin gauge recorded stress history provided the experimental data. Recall that the failure model constants for OFHC copper were obtained using the velocity history. The experimental data were obtained only for a time duration of 4 microseconds. (In this experiment, release waves from the edges of the flyer plate arrived at the gauge location at around 4.2 microseconds.) The model constants were obtained by matching the experimental stress signal until this time. The corresponding match is shown in Figure 3.2a. The excellent comparison between model and experiment before the spall signal indicates that the BP model constants reproduced the HEL data well. Also, the strain rate sensitivity of HY100 steel seemed to be modeled correctly as one can interpret from the shape of the simulated signal around the stress peak. Rajendran et al. [32] modeled the SHB test accurately using the same BP model constants for HY100 steel. The ability to model both the SHB and plate impact tests indicates the generality of the model constants. In Figure 3.2b, the computed stress history at the spall plane is shown. The compressive stress is shown as positive, and the tensile stress is shown as negative. The material experiences a compressive stress of

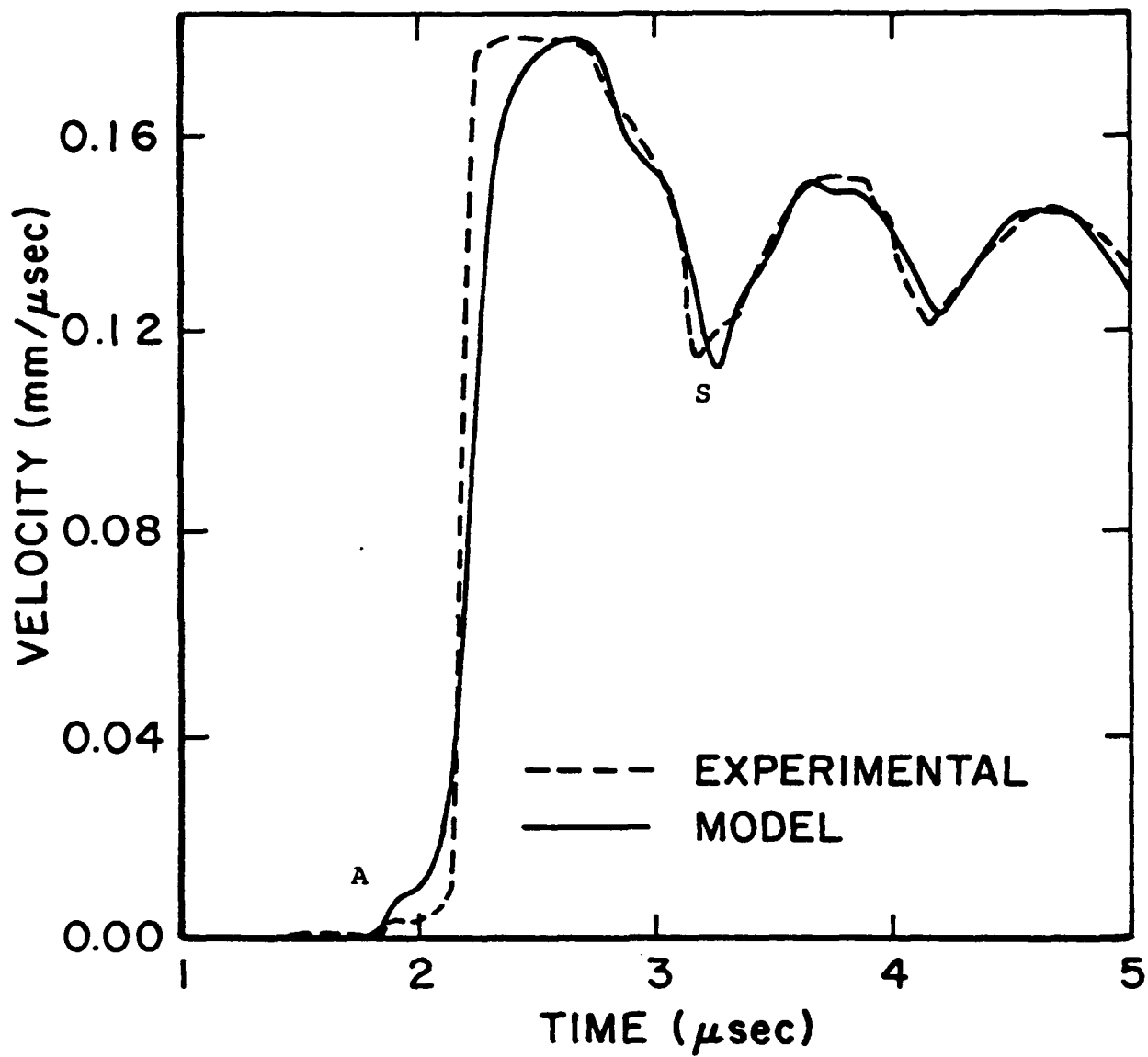


Figure 3.1. Comparison between Model and Experimental Free Surface Velocity Histories (OFHC Copper).

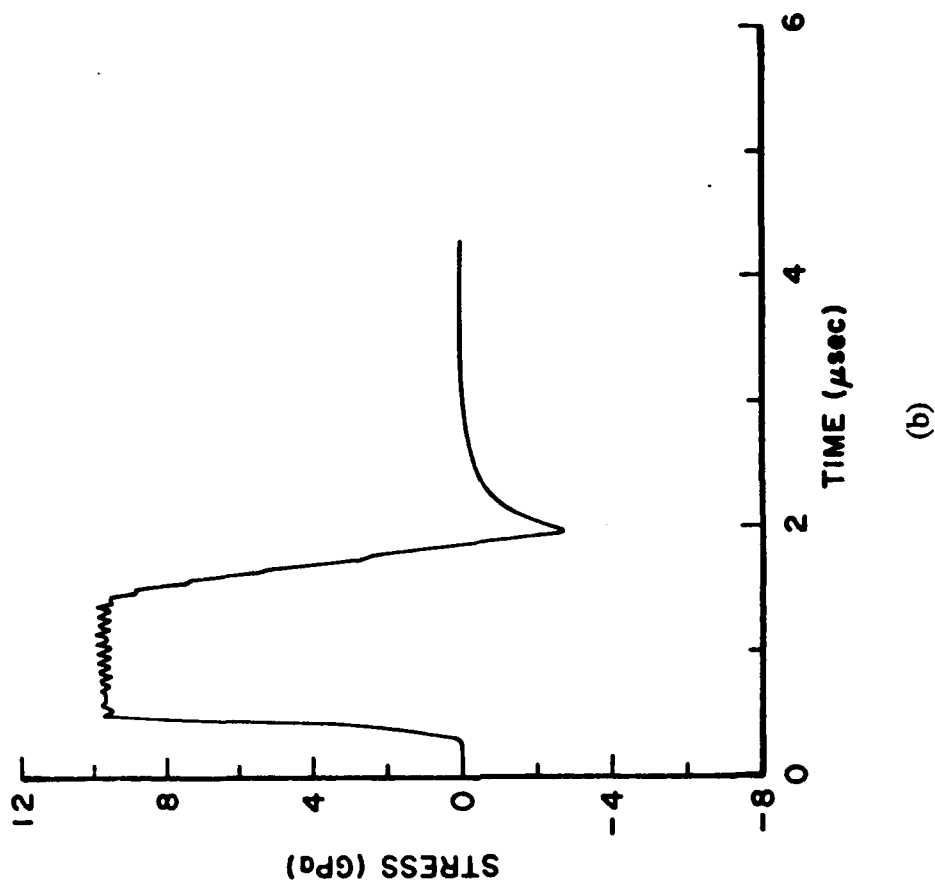
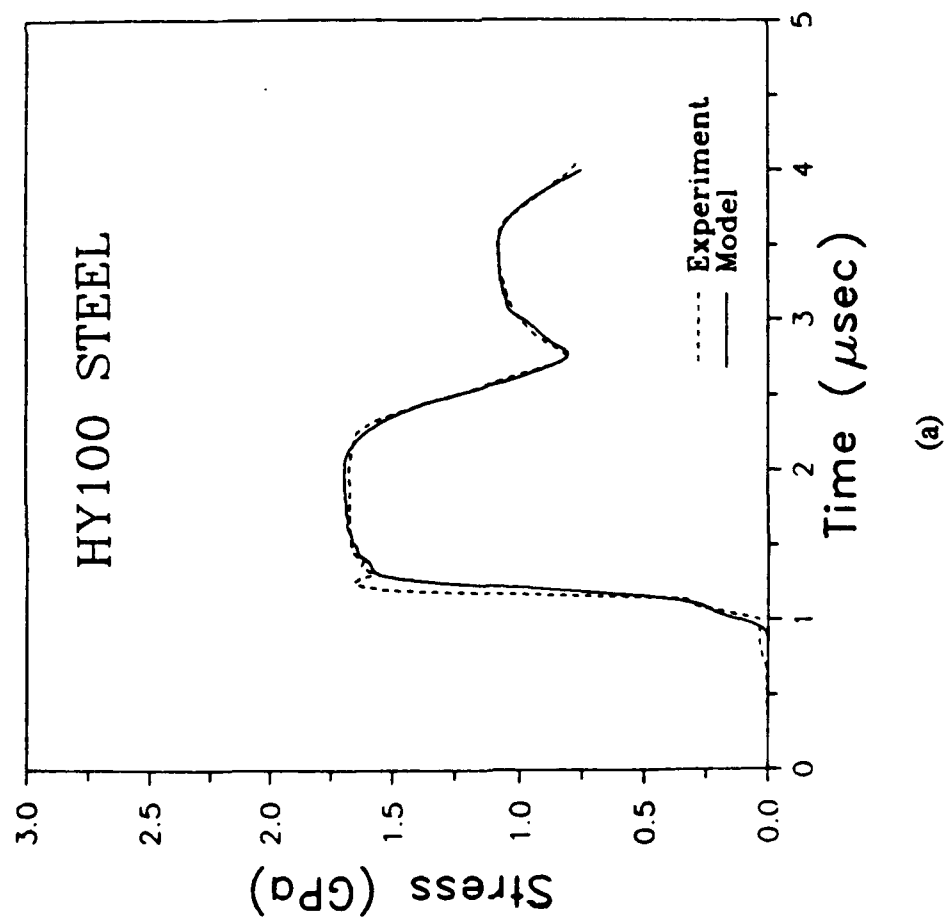


Figure 3.2. (a) Comparison between Model and Experimental Stress Histories (HY100 Steel).
(b) Numerical Simulation of the Stress History at the Spall Plane (HY100 Steel).

around 10 GPa. When the material goes into tension, the stress peak only reaches 2.8 GPa. This reduction in stress under tension is due to void softening. The stress relaxes to zero as the material spalls. Modeling of this time dependent stress relaxation is the most important feature of the RDG model.

The failure model constants were accurately determined as can be seen from the excellent comparison between the model simulation and the experimental data in Figure 3.2a. Since the BP model constants for the intact material and the RDG model constants for the void-containing aggregate were accurately determined, the entire stress history could be reproduced accurately. Of course, this statement assumes that the equations of state for the flyer, target, and the PMMA are accurately modeled in the computer code simulation. The ability of the model to reproduce the entire spall signal clearly demonstrates that the nucleation and growth models follow the physical processes realistically.

RDG model constants were also determined for 1020, C1008, MAR-250, AF1410, and MAR-200 steels, Armco Iron, and pure tantalum by matching the experimental data as shown in Figures 3.3 and 3.4. The ability of the RDG model in modeling the spall failure is truly outstanding. The RDG model generated spall signal for tantalum matched extremely well with the data up to 3.4 microseconds. The difference between the model and experiment could be due to the uncertainty in the experimental data. In this test (7-1302), the plate impact configuration was such that the spall plane location was very close to the manganin gauge (about one millimeter).

In the simulations, behavior of the intact material can also be described by the JC model instead of the BP model. Using the JC and RDG models, the plate impact test 7-1299 on HY100 steel was resimulated. The JC constants for the HY100 steel were obtained by Johnson and Holmquist [33] using torsional SHB test data. Initially, the RDG model constants used were those that had been previously determined for HY100 steel in conjunction with the BP model. Figure 3.5 compares the stress histories obtained from (1) the test data, (2) the simulation using the BP model with the RDG model, and (3) the simulation using the JC model with the RDG model. In the simulation using the JC model, the spall signals did not match exactly. This slight difference could be attributed to the material characterizations of HY100 steel using different experimental configurations and sources. In other words, the descriptions of HY100 steel by the

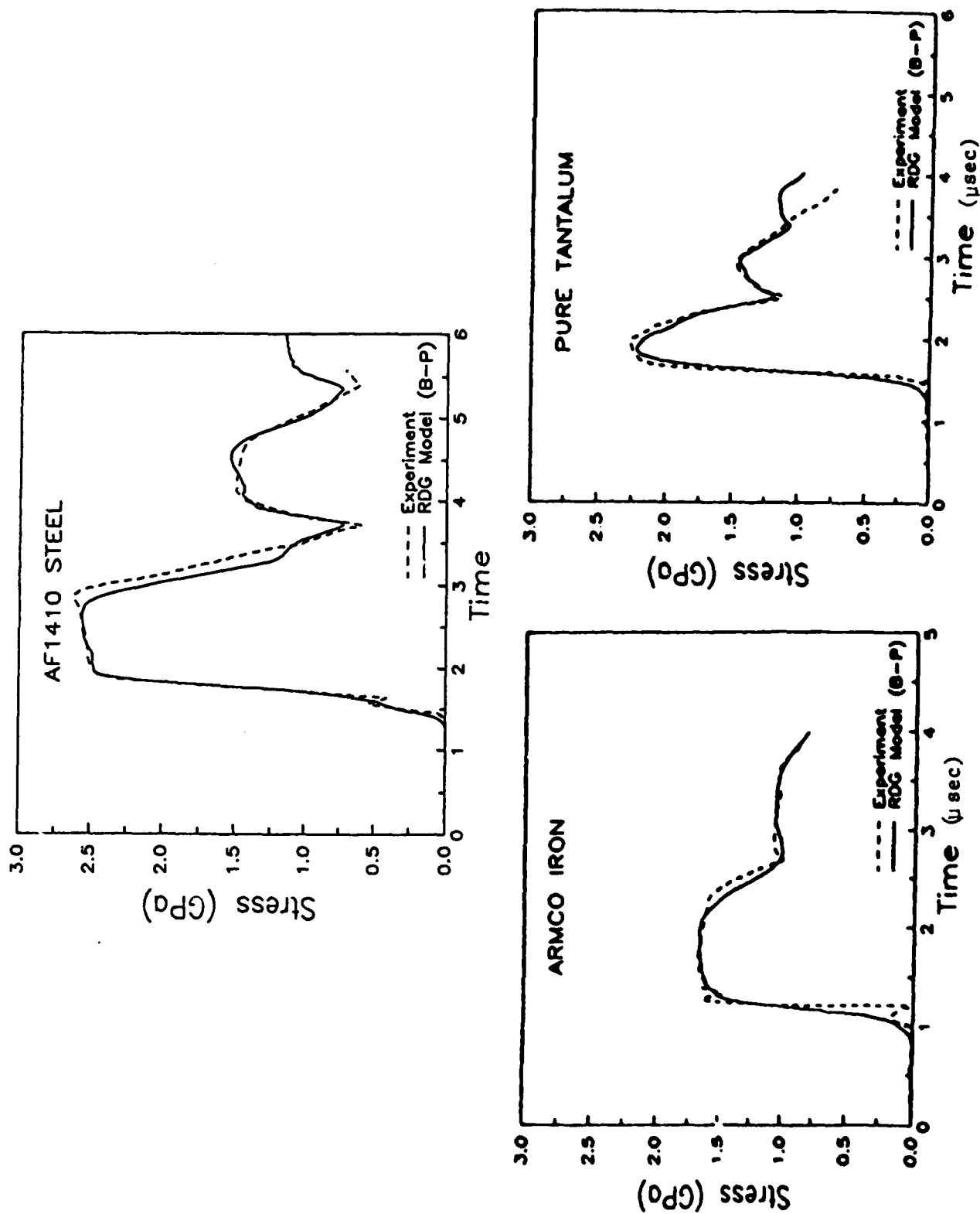


Figure 3.3. Comparison between RDG Model Generated and Experimental Stress Gauge Signals for Different Metals.

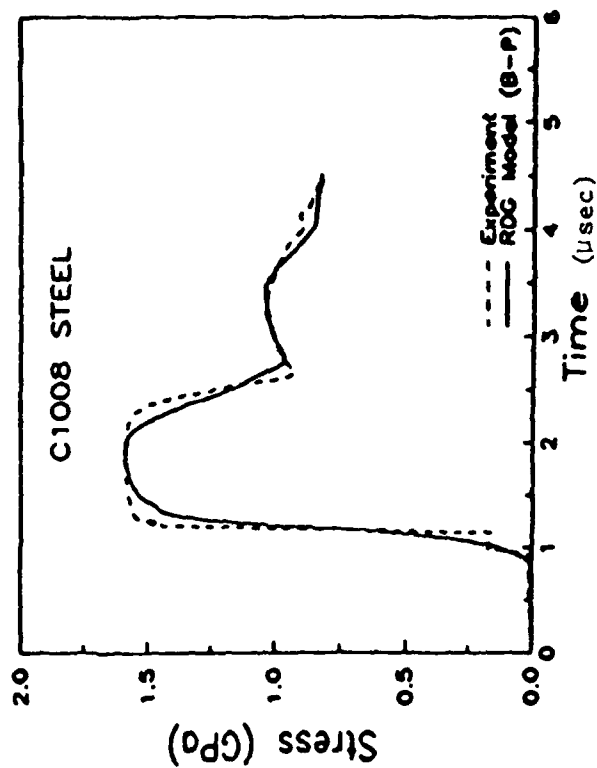
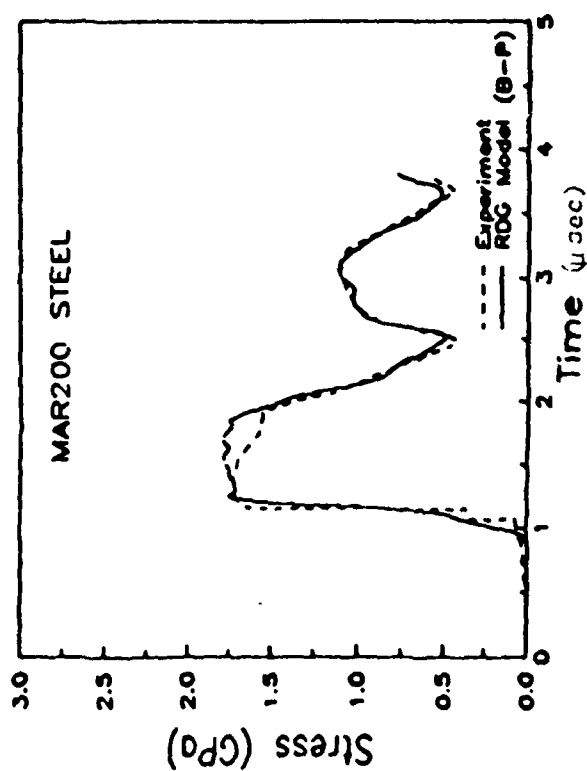
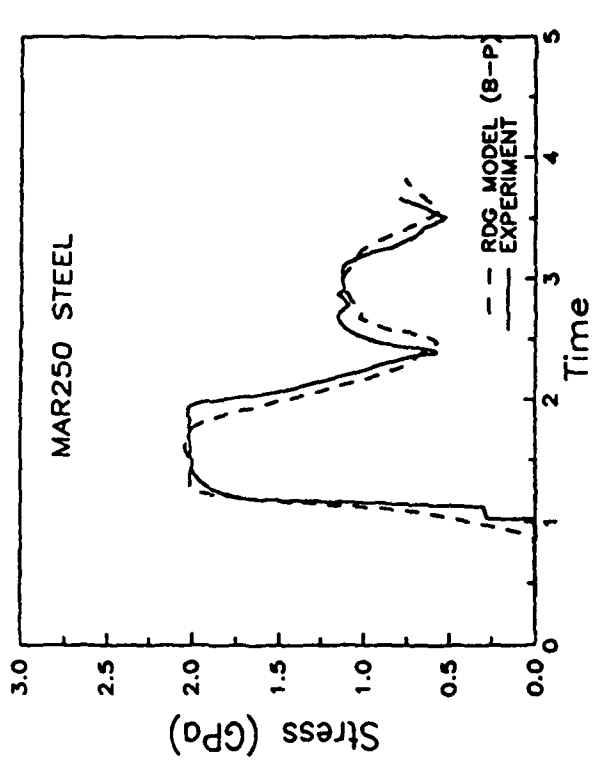
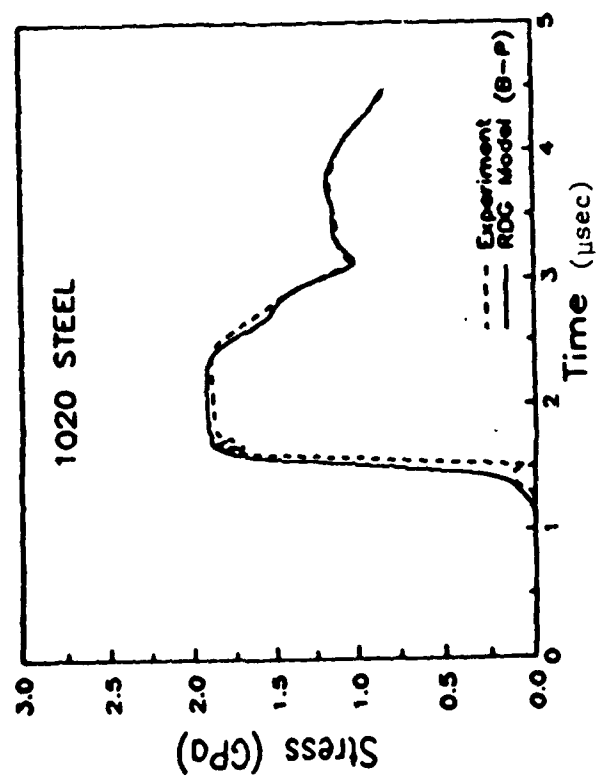


Figure 3.4. Comparison between RDG Model Generated and Experimental Stress Gauge Signals for Different Metals.

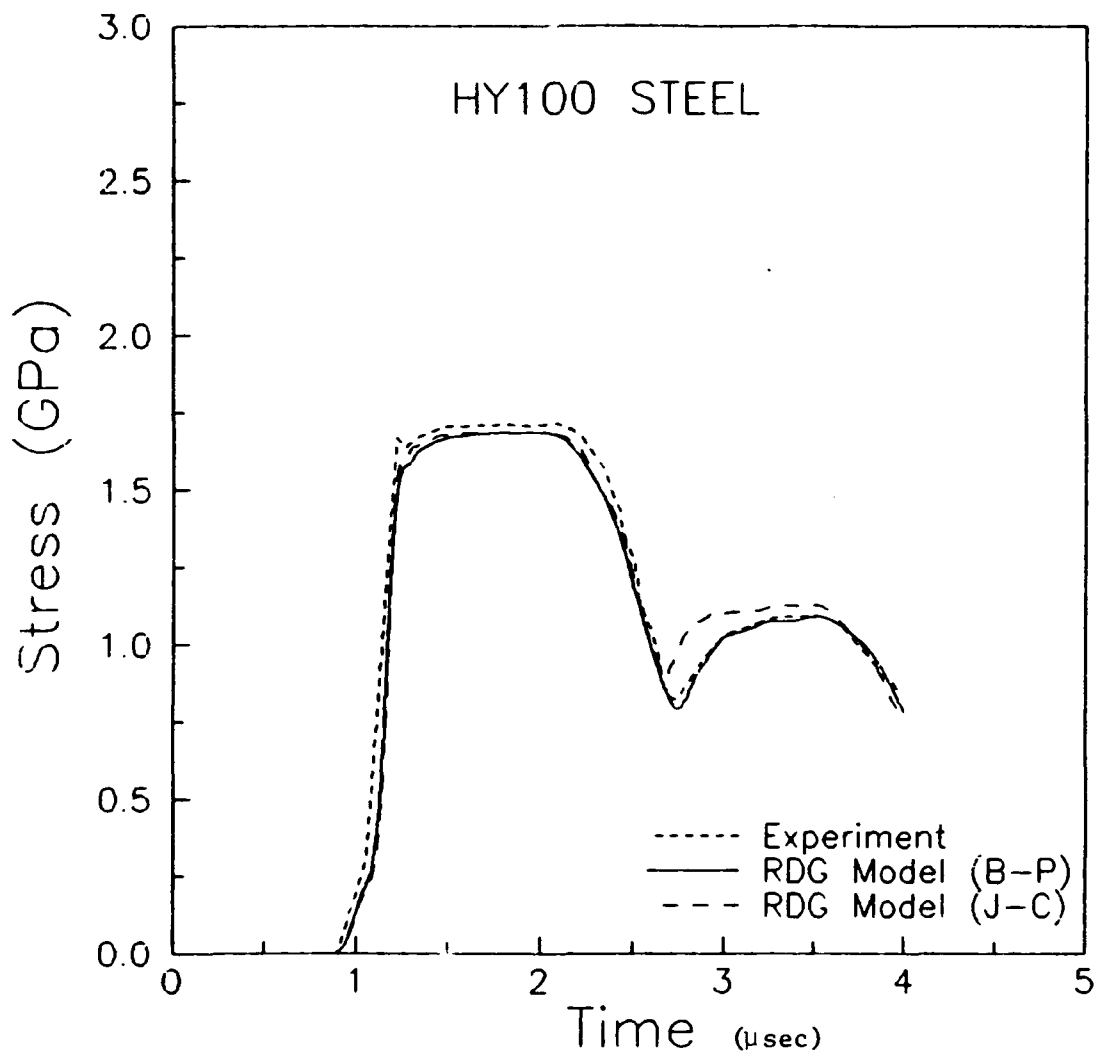


Figure 3.5. Comparison of Spall Modeling for HY100 Steel using BP and JC Models. Spall Process is Described by the RDG Model.

BP model and the JC model are slightly different; because of this, accurate modeling of spallation using the JC model required minor adjustments to the RDG model constants. To determine the RDG model constants that correspond to the use of the JC model for the intact material, plate impact simulations were made and the constants were determined. An adjustment to the f_1 from 0.035 to a value of 0.01 led to a better fit between the failure model and the test data. It can be seen from Figure 3.6 that the spall signal is matched extremely well by both BP and JC models with the use of appropriate RDG model constants.

An important aspect of the modeling is the model's ability to reproduce an experiment which was not used for determining the model constants. Also the model's ability to reproduce a failure process in some other stress-strain configuration is important. To check this aspect, a new experiment (7-1288) on OFHC copper was considered. In this experiment, the stress history at the interface of the target and the back plate was measured using a manganin gauge. The target thickness and the impact velocity were both different than in experiment 7-538. To check the model's ability to predict the measured stress history, the new experiment 7-1288 was simulated using the same model constants that were determined using experiment 7-538. In Figure 3.7, a comparison between the model prediction and the data is shown. The model reproduced the measured spall signal extremely well as can be seen from this figure.

3.5 Modeling of Double Flyer Plate Impact

In application problems, dealing with projectile penetration into a target, explosively compacted metal operations, etc., the loading conditions often lead to multiple shocking in the material. Under these conditions, both void growth and void collapse may occur. The dynamic properties of the shocked material are modified due to loading history effects. To simulate such conditions and to further evaluate the RDG model, a double flyer plate impact experiment was simulated with the EPIC-2 finite element code [31]. Previously calibrated RDG model parameters were used in the simulation. The computed stress history was compared with the experimentally measured stress history. A simple void collapse criterion, based on a critical void volume fraction, was employed to obtain a better fit to the experimental data.

Yaziv [34] and Yaziv et al. [35] introduced double flyer plate impact techniques for examining the dynamic properties of shock damaged materials. This technique differs from a

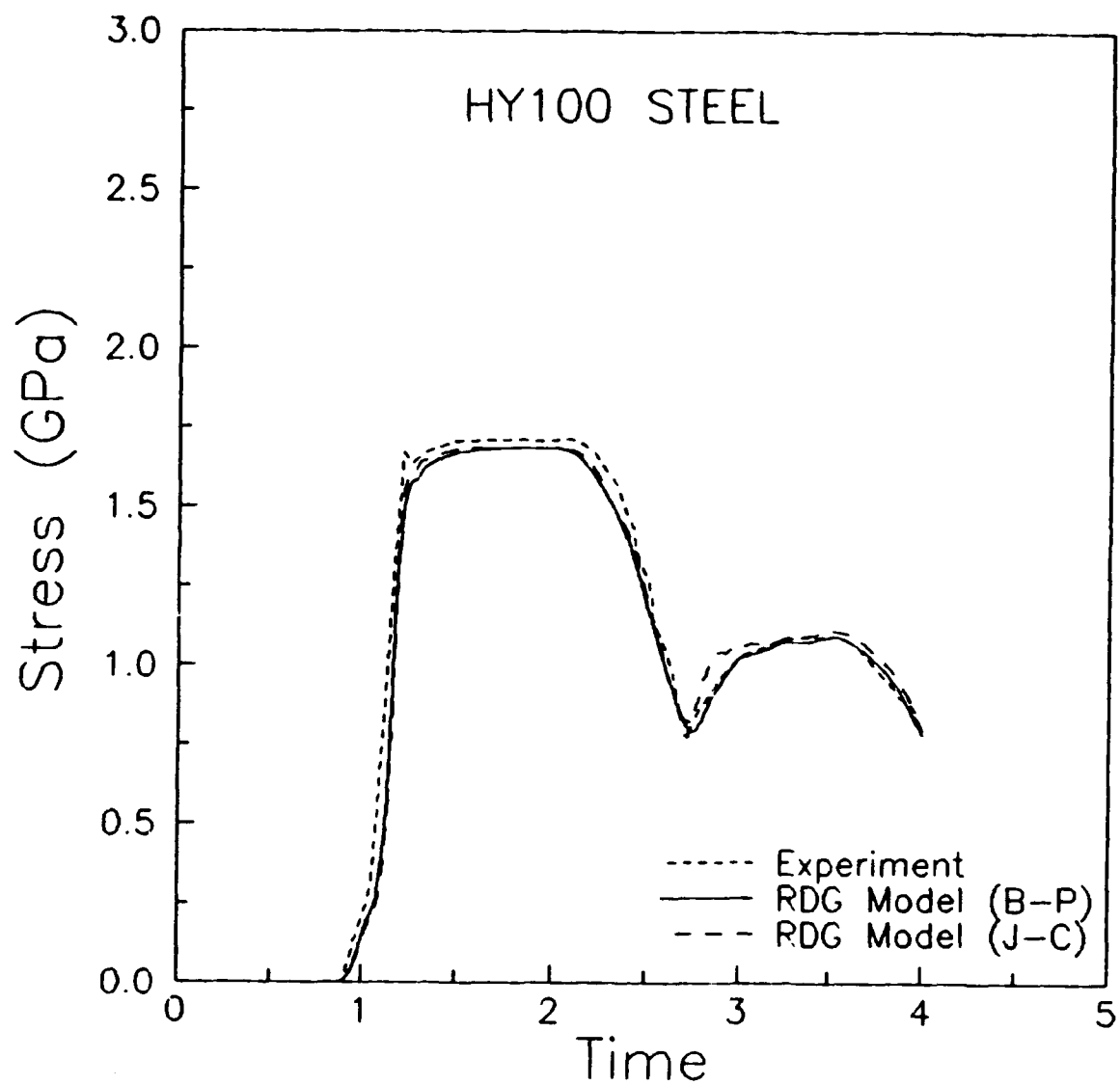


Figure 3.6. Comparison between the Spall Signals Generated using JC and BP Models for Different Values of RDG Model Constants.

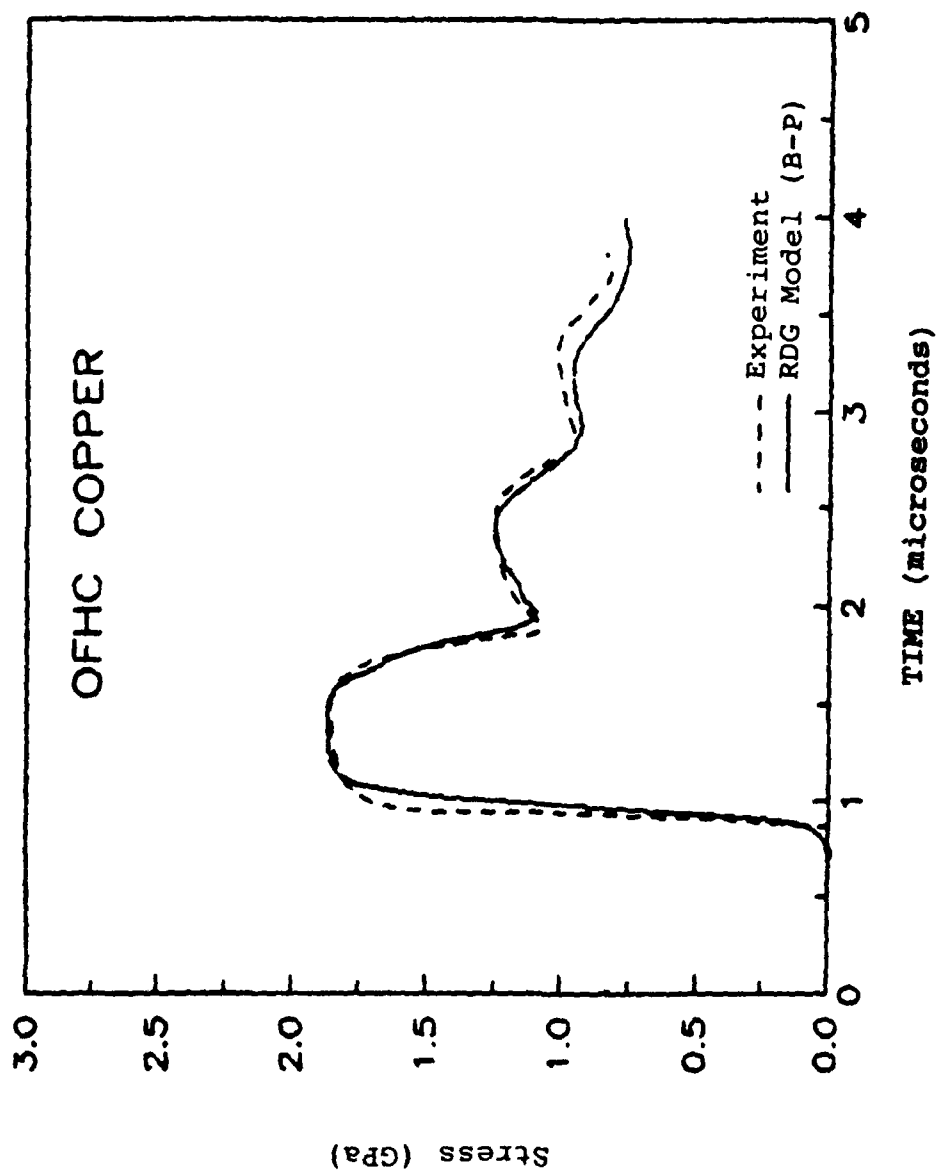


Figure 3.7. Comparison between Model Prediction and the Measured Stress History (OFHC Copper).

conventional plate impact experiment in that two flyer plates are used, separated by a small gap, as shown schematically in Figure 3.8. The first flyer has a lower shock impedance than the second flyer. When the first flyer impacts the target plate, microvoid nucleation and growth occur in a localized area of maximum tensile stress in the target. The reshocking by the second flyer reverses the damage by closing the microvoids.

Grove et al. [5] simulated an experiment (829) in which the first flyer was a 2 mm thick aluminum plate and the second flyer was a 3 mm thick copper plate. The spacing between the flyers was 0.25 mm, and the impact velocity was approximately 336 m/s. The target was a 4 mm thick OFHC copper plate with a PMMA backing. The stress history at the interface of the target and PMMA was measured with a manganin stress gauge.

The double flyer plate impact experiment was simulated using the EPIC-2 finite element code. EPIC-2 material models were used to describe both flyers and the PMMA. The PMMA was modeled as a rate independent elastic-perfectly plastic material with a yield strength of 0.18 GPa. The RDG model was used to describe the plastic flow and dilatation in the OFHC copper target plate. The previously determined RDG model parameters for OFHC copper were used in this simulation.

In the first simulation of the double flyer plate experiment, the RDG model predicted the initial spall signal reasonably well but was unable to accurately reproduce the experimental recompaction signal, as indicated by Figure 3.9. The plastic wave slope of the simulated reshocking exhibited ramping with a long rise time indicating that the predicted pore collapse, described by the same equations as void growth, was unrealistically slow and required modification. Grove et al. [5] introduced a complete collapse of the microvoids in a particular element if that element's dilatation rate was negative and its void volume fraction was less than or equal to some critical value. Figure 3.10 shows the excellent fit to the experiment obtained when the critical void volume fraction for complete collapse was five percent.

The double flyer plate experiment without void growth was also simulated so that the microvoids effect on the reshock signal could be investigated. Figure 3.11 compares the two simulations, with and without void growth. It is interesting to note that the dip at point *F* occurs at the same time in both curves, indicating that this feature is directly related to the experimental configuration. Figure 3.12 shows an x-t (distance-time) diagram for the double flyer plate impact

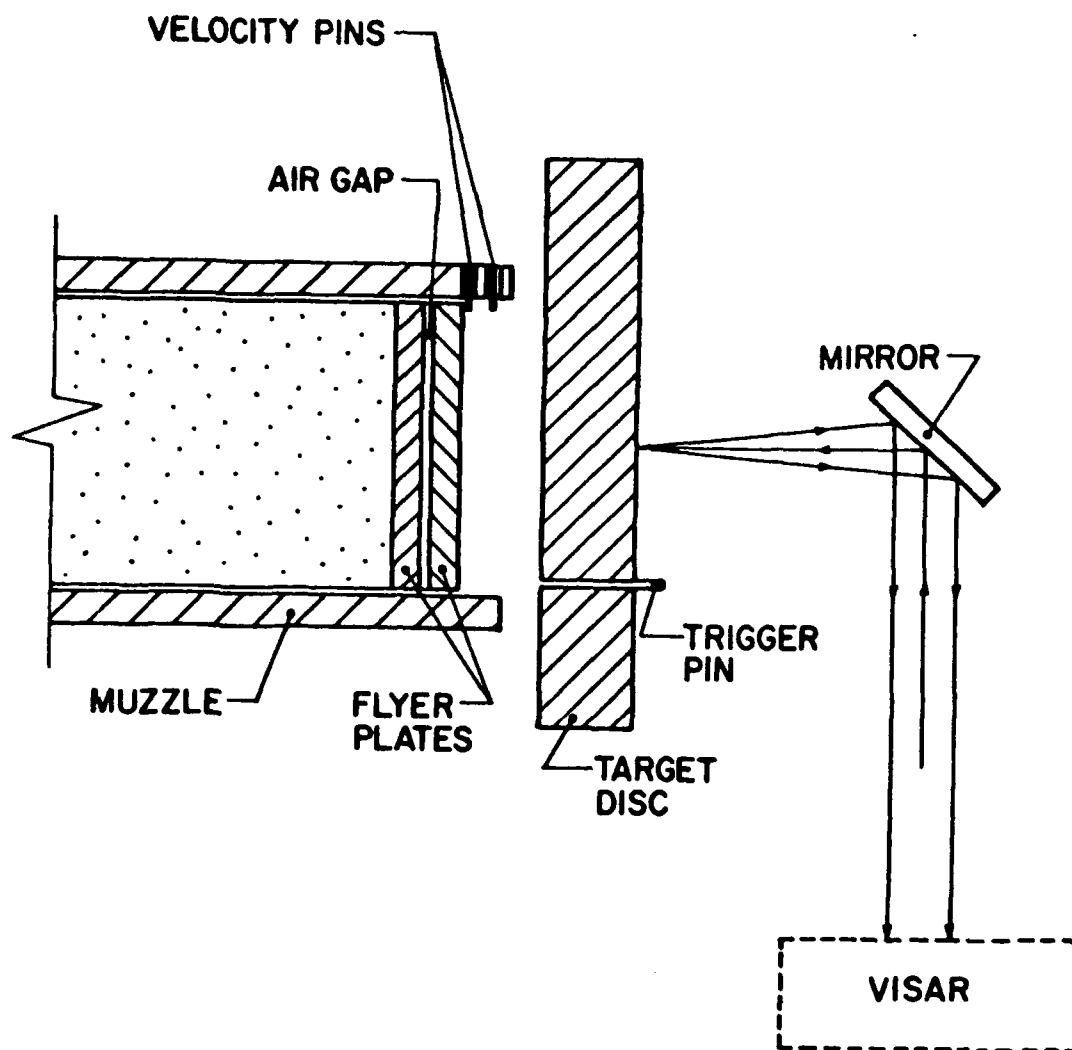


Figure 3.8. Experiment Configuration for Double Flyer Impact Experiment.

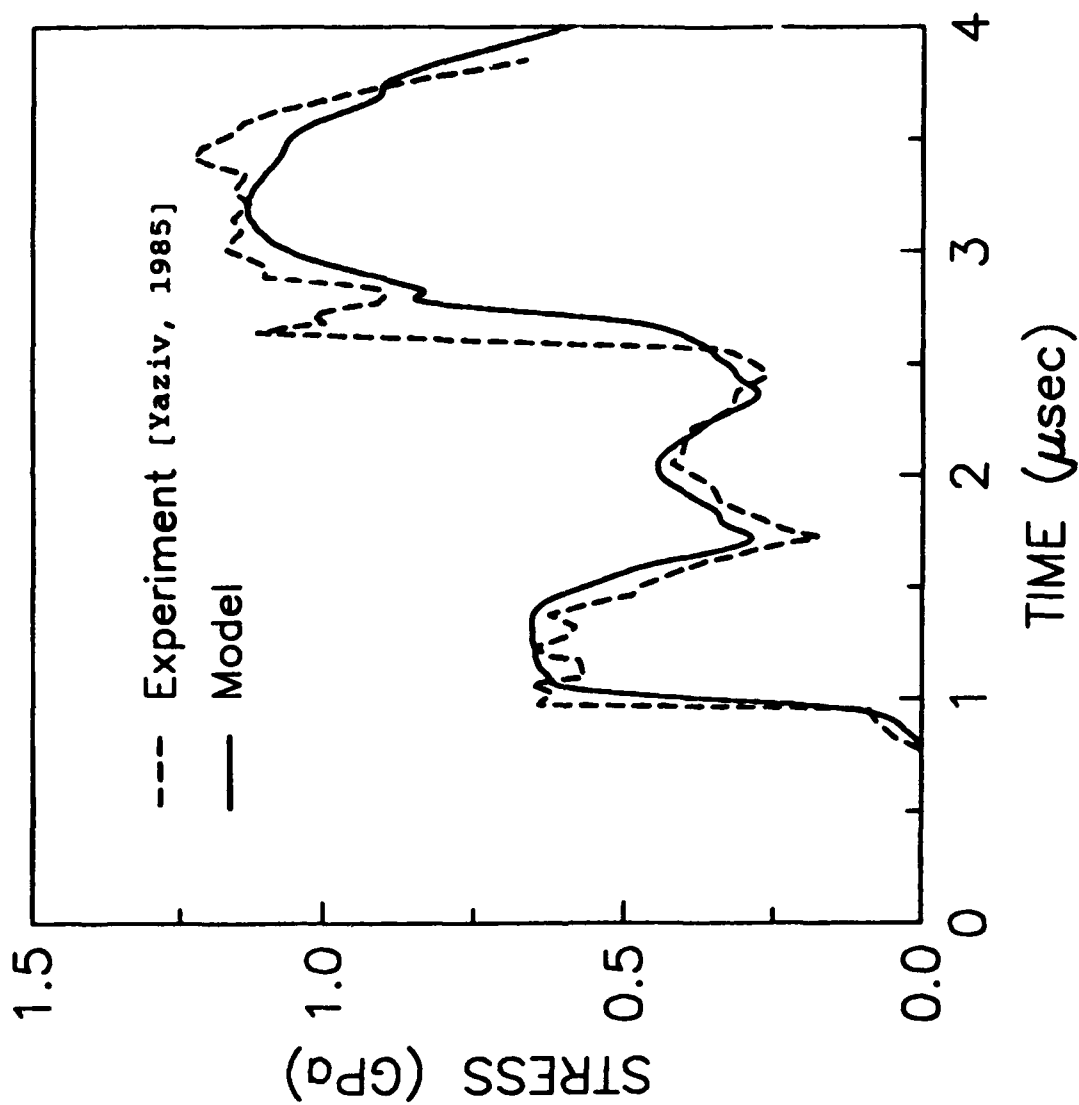


Figure 3.9. Stress History Comparison for Original RDG Model.

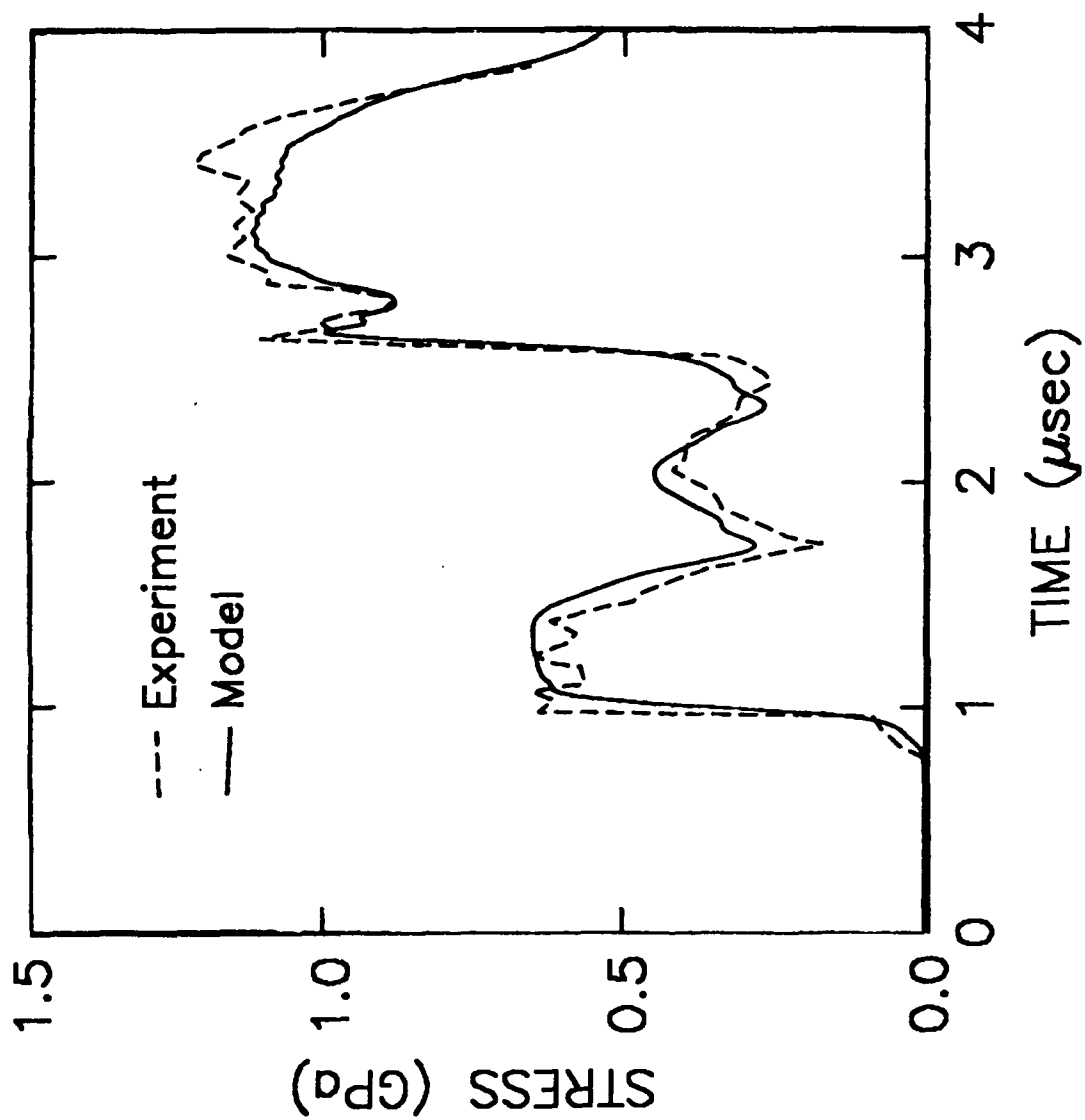


Figure 3.10. Stress History Comparison for Modified RDG Model, with a Critical Void Volume Fraction of 5% for Complete Collapse.

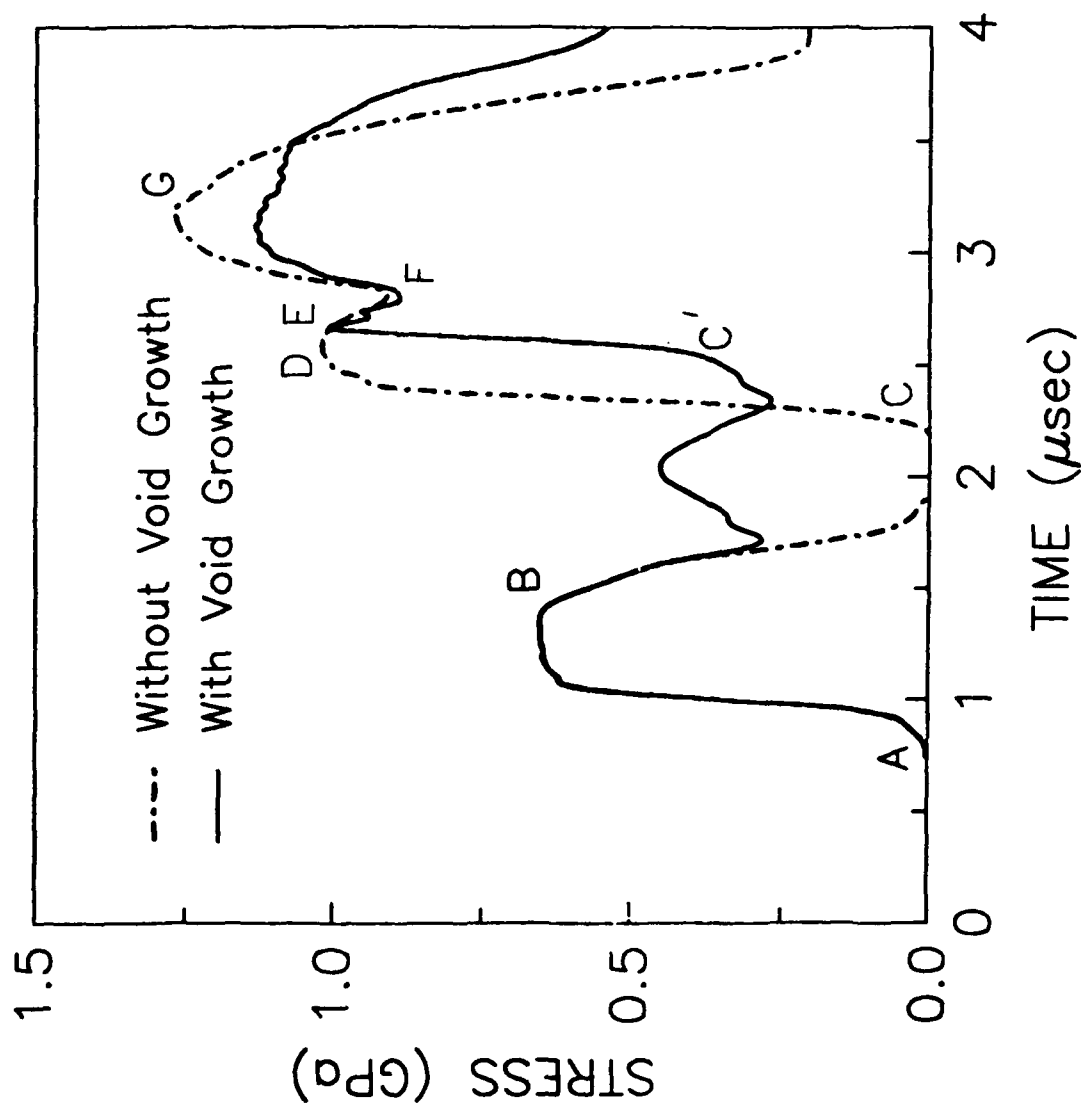


Figure 3.11. Comparison of Simulated Stress Histories from Double Flyer Impact Configuration, with and without Void Growth.

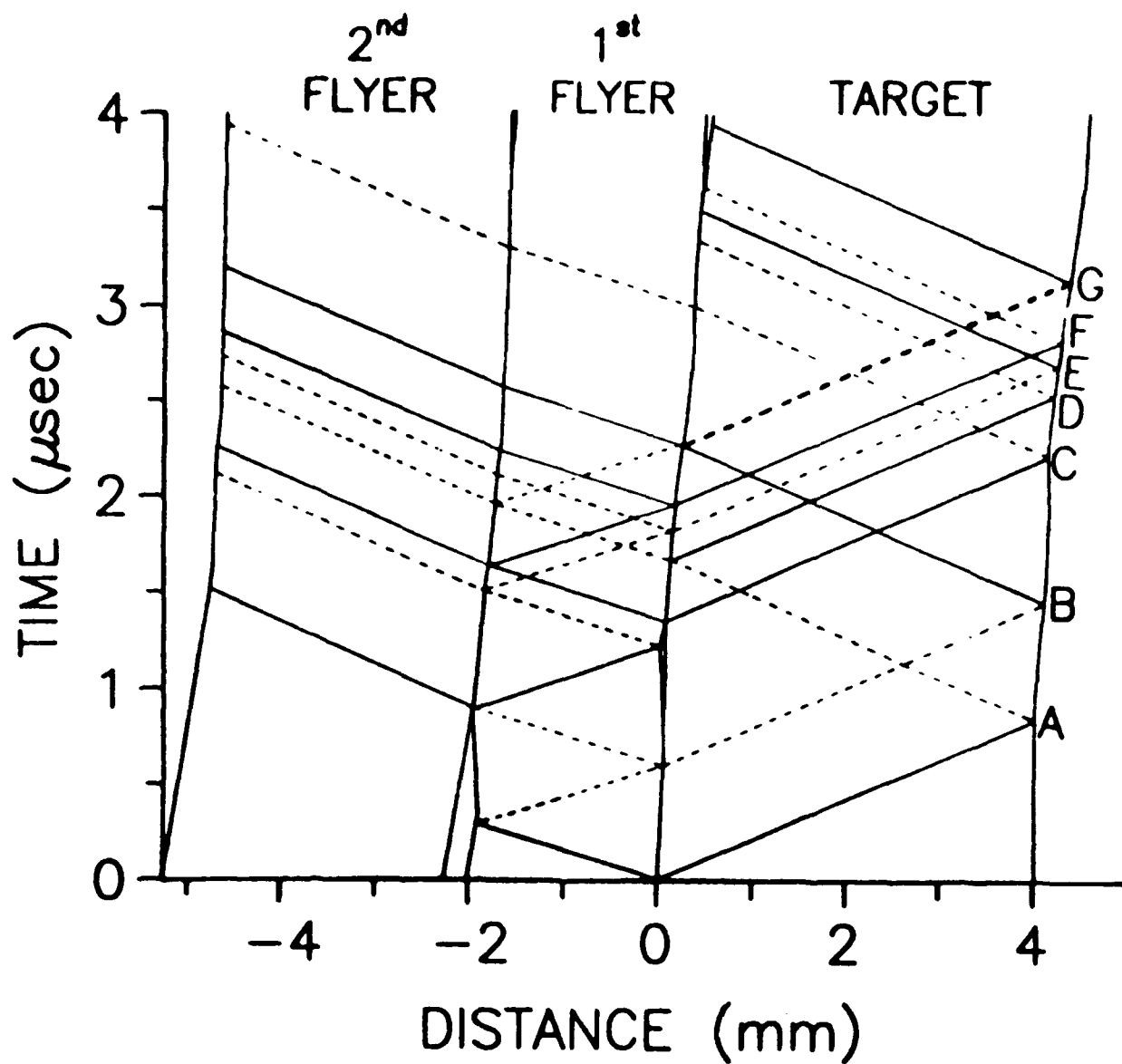


Figure 3.12. X-T Diagram for the Double Flyer Impact Experiment, Assuming No Void Growth.

experiment, assuming no void growth. In this figure, the solid and dashed lines represent shock and release waves, respectively. The release and shock waves that arrive at points *E* and *F* are solely due to the impedance mismatch between the first flyer and the target. Because the first flyer has a lower impedance than the target, it separates from the target at about 0.75 microseconds. As Figure 3.12 indicates, the initial shock wave from the second flyer reflects off the free surface of the first flyer as a release wave because of the gap formed between the first flyer and the target. This release wave can be traced to point *E*. When the first flyer impacts the target again, another shock wave is produced, and this shock wave can be traced to point *F* in the x-t diagram.

In the absence of microvoid nucleation and growth, the shock wave from the second flyer would arrive at point *C*. When void growth occurs, however, this signal is delayed because of the reduced wave speed in the porous region of the target. Arrival of this signal at point *C'* (in Figure 3.11) signifies that the microvoids have completely collapsed. Since the release and shock waves at points *E* and *F* arrive after point *C'*, it appears that they are unaffected by the void growth phenomenon.

In summary, a double flyer plate impact experiment was successfully simulated using the RDG model. Using previously calibrated constants, the RDG model was able to reproduce the initial spall signal, but the reshock signal did not compare as well with the experimental stress history. The RDG model was then modified to include a simple void collapse criterion in which the microvoids were forced to completely collapse below a critical void volume fraction when the dilatation rate was negative. Microvoid collapse in OFHC copper was successfully modeled using precalibrated RDG model constants and a critical void volume fraction for complete collapse of 5 percent. Thus, the RDG model has been extended to describe microvoid collapse as well as a history dependent failure process.

3.6 RDG Model Applications

Dynamic ductile failure also occurs in other types of configurations. Tensile necking in a split Hopkinson bar test specimen, spallation in a target plate impacted by a rod penetrator, and spallation in a solid cone impacted by a thin plate are a few examples. These configurations are investigated in the following subsections.

3.6.1 Tensile Necking

To further demonstrate the capability of the RDG model, several two-dimensional axisymmetric configurations were considered. The first case considered the problem of dynamic tensile necking. The main objective of this two-dimensional analysis was to examine the stress states, evolution of necking, void growth as influenced by the plastic deformation, and ductility. To initiate necking, a shallow-notched copper specimen of the geometry described in Figure 3.13 was considered. The length and uniform diameter of the specimen are 8.9 mm and 3.2 mm, respectively. The minimum diameter at the notch is 2.7 mm. The length represents the actual gauge length of a standard SHB tensile specimen.

The shallow notched specimen was modeled using the quadrilateral element option in the EPIC-2 code. Due to specimen symmetry, it is sufficient to model only one quarter of the specimen as shown in Figure 3.14. The Bodner-Partom (BP) model was used to describe the high strain rate behavior of the copper specimen. The BP model constants for copper are given in Appendix B. A typical experimentally measured SHB velocity history was applied to the specimen in the simulation. The velocity was linearly increased from zero to 50.8 m/sec (2000 inches/sec) for 40 microseconds, and afterwards, it was kept constant.

The RDG model was used to describe the necking evolution. A mean effective plastic strain based Gaussian distribution, as described by Equation (8), was used for void nucleation. Since the stress level under a uniaxial stress state is considerably lower than the level under uniaxial strain conditions (plate impact test), the void nucleation was assumed to occur entirely due to large plastic flow around the inclusions and oxide particles. In a uniaxial tensile test, the necking often progresses under significant plastic flow and a moderate triaxial stress state.

In the analysis, the time histories of effective stress, effective plastic strain, void volume fraction, and triaxiality of the stress state (ratio of pressure to effective stress) were evaluated for elements 82, 182, 282, and 382 which are shown in Figure 3.14. Variation of pressure, stress components, strength, and other variables along a radius for different time intervals have also been considered in the analysis.

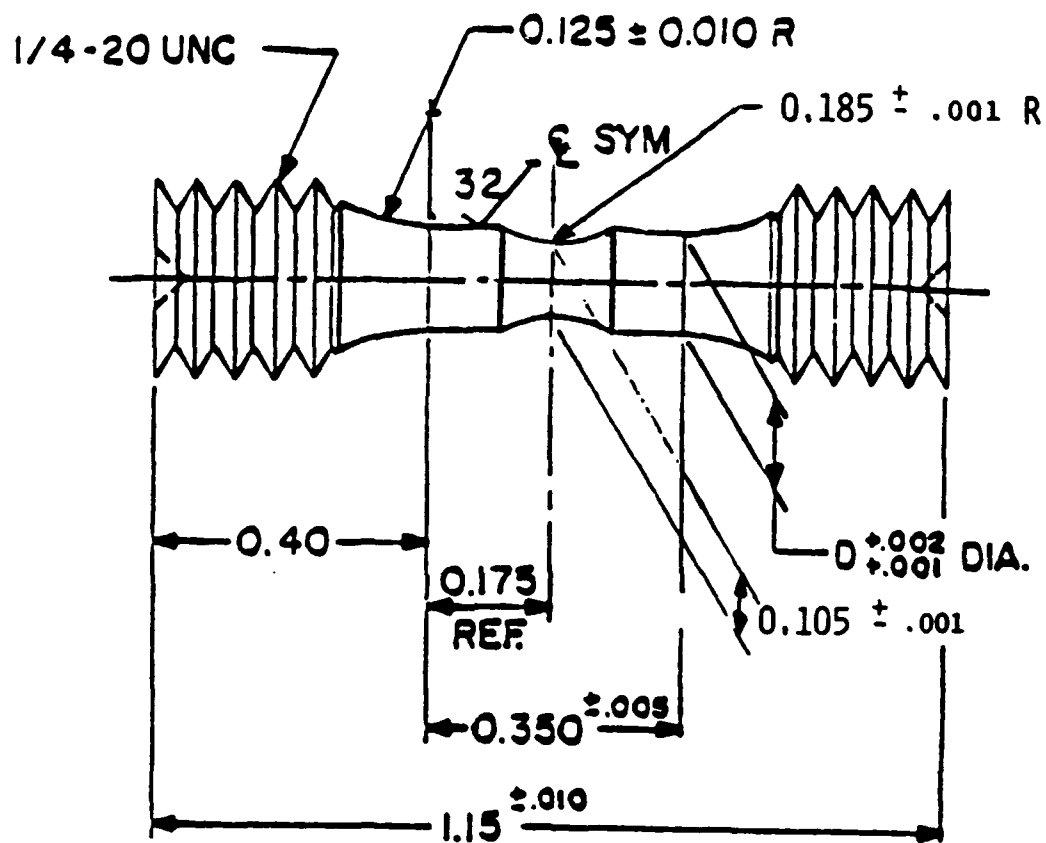


Figure 3.13. Shallow-Notched Tensile Specimen Geometry.

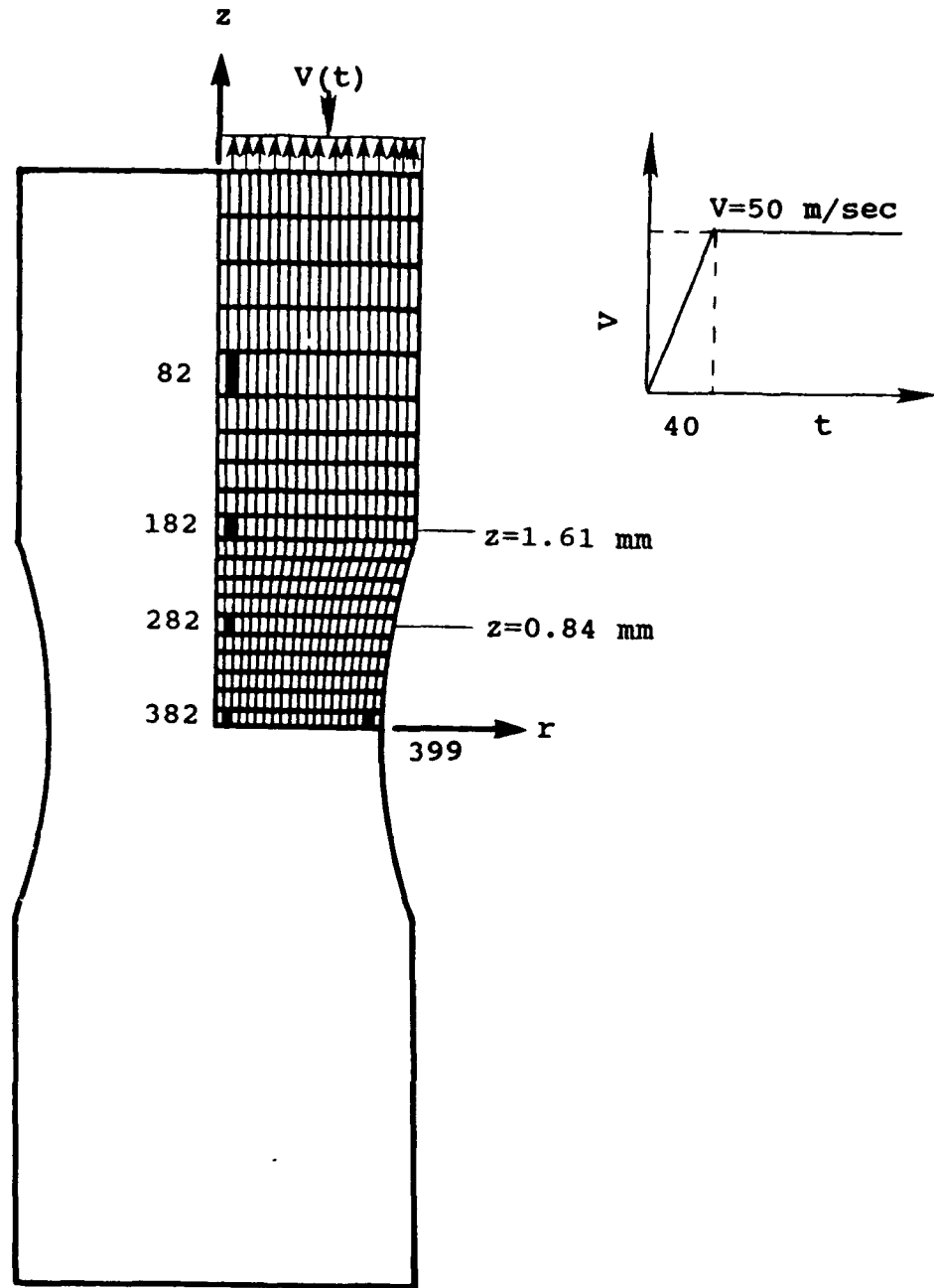


Figure 3.14. Finite Element Mesh for Shallow-Notched SHB Specimen. The Velocity Loading History is Shown in the Inset.

The stress triaxiality parameter (P/Y) contours are plotted in Figure 3.15. While this parameter is increasing at the specimen center, the stress state is uniaxial (P/Y is around $1/3$) in the uniform region. The triaxiality ratio becomes negative (compressive) within region *A* as can be seen from Figure 3.15b. The unloading of the uniform section (region *B*) and the compressive loading at *A* make the interpretation of the triaxiality contours complicated. In the presence of increased triaxiality, the void growth also increases as shown in Figure 3.16. The void volume fraction contours at $t=0, 20, 50$, and 60 microseconds are shown. Initially, a small amount of voids nucleate near the stress-free notch surface. The void distribution spreads toward the specimen center with increasing necking. By about 50 microseconds, the void content at the center region increases rapidly to 3 to 4 percent. Due to increasing triaxial tensile state, rapid void growth occurs during the next 10 microseconds; by $t=60$, the necked region is filled with voids, over 40 percent located at the center (see Figure 3.16d). Although the voids nucleate near the surface, the failure initiation eventually occurs at the center of the specimen. Hancock and Brown [36] provided the physical evidence to support failure initiation at the center in notched tensile specimens for various notch geometries under quasi-static loading conditions.

The time history plots of effective plastic strain and void volume fraction for regions near the neck (local, element 382) and away from the neck (uniform, element 82) are given in Figure 3.17. Initially, the plastic strains are identical at both regions. However, the local strain at the center of the specimen starts deviating from the uniform strain slowly due to enhanced void growth. The void nucleation process occurs during the first 40 microseconds, and rapid growth initiates around $t=50$. Beyond this time, while the local strain continues to increase due to void growth, the uniform strain at element 82 (see Figure 3.17) reaches a maximum value of 20 percent and stops increasing. This is due to unloading of the sections away from the local necking region.

The stress-time histories for the local and uniform regions are shown in Figure 3.18. Also shown in this figure is the void volume fraction history for elements 82 and 382. Since these two elements are very close to the axis of symmetry, the hoop and radial stresses are similar (Figure 3.18). For the uniform element (82), the hoop and radial stresses are zero as one would expect. However, the stress state in the local element 382 begins almost uniaxial and becomes triaxial due to necking. The hoop and radial stresses increase as the void growth occurs in the local region generating a high local triaxial stress state. Between 40 and 50 microseconds,

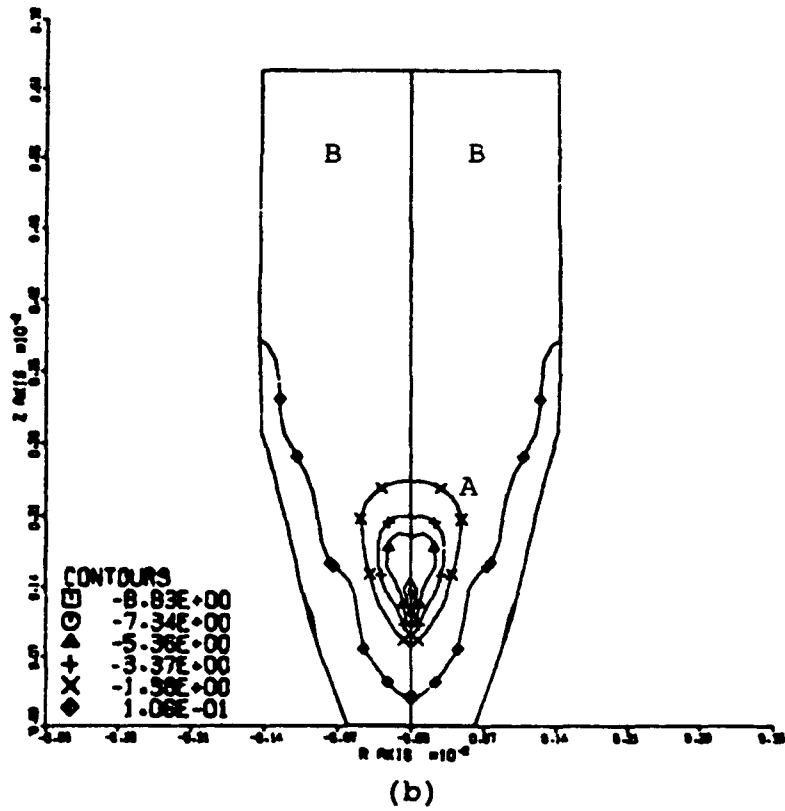
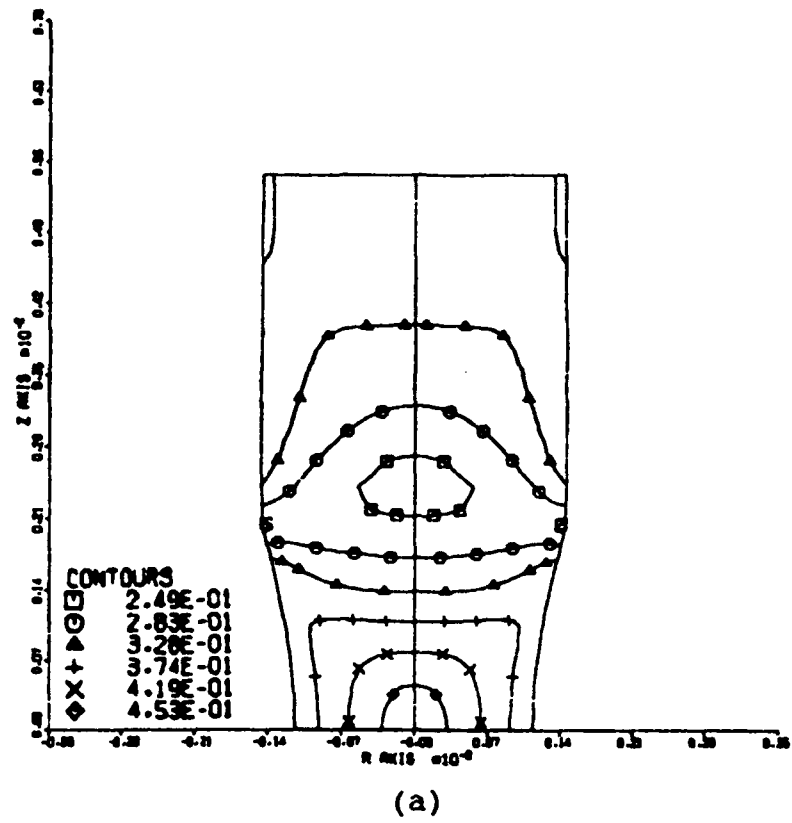


Figure 3.15. Stress Triaxiality (P/Y) at (a) $t=40$ and (b) $t=60$ microseconds.

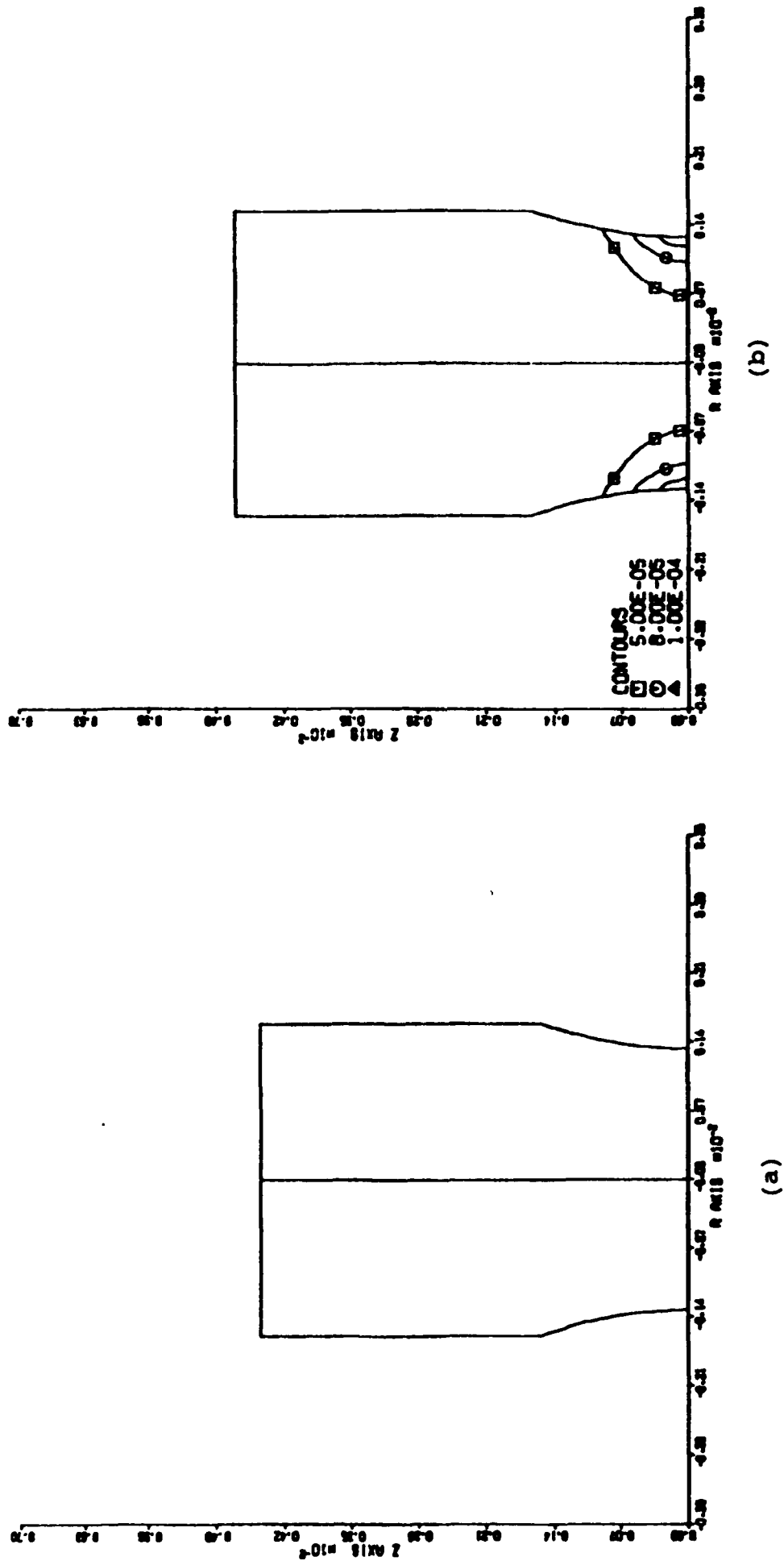
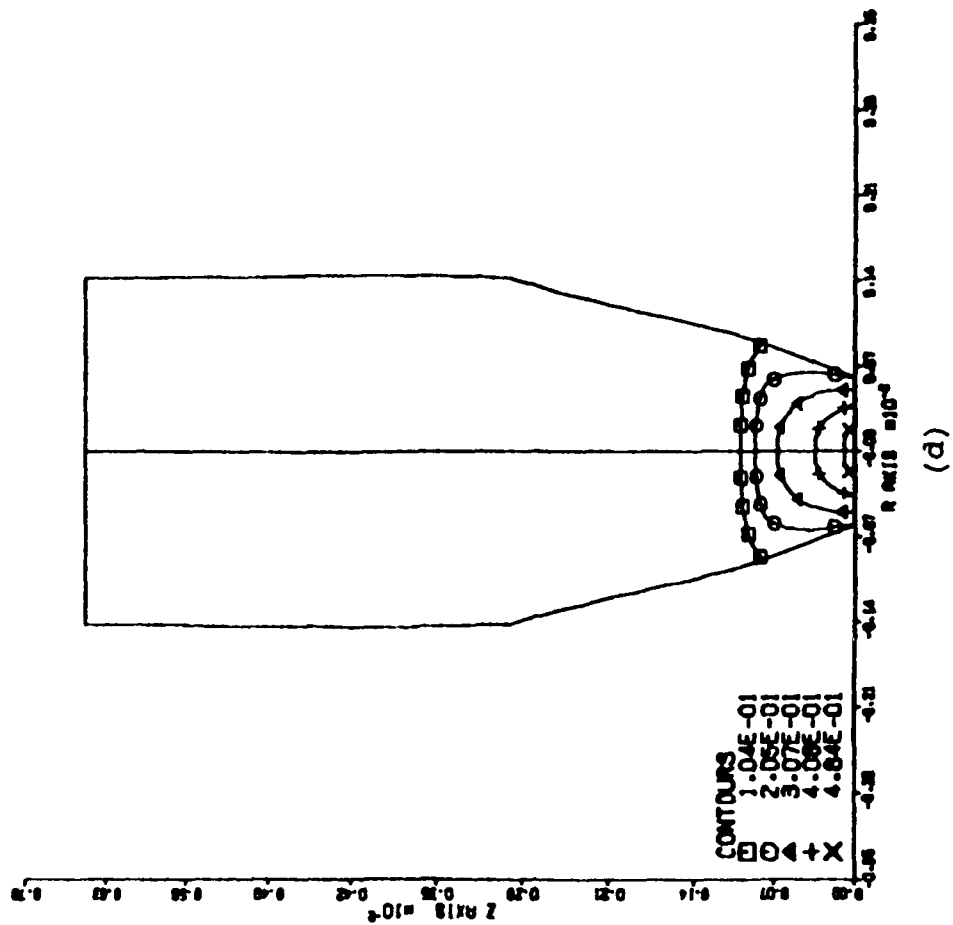
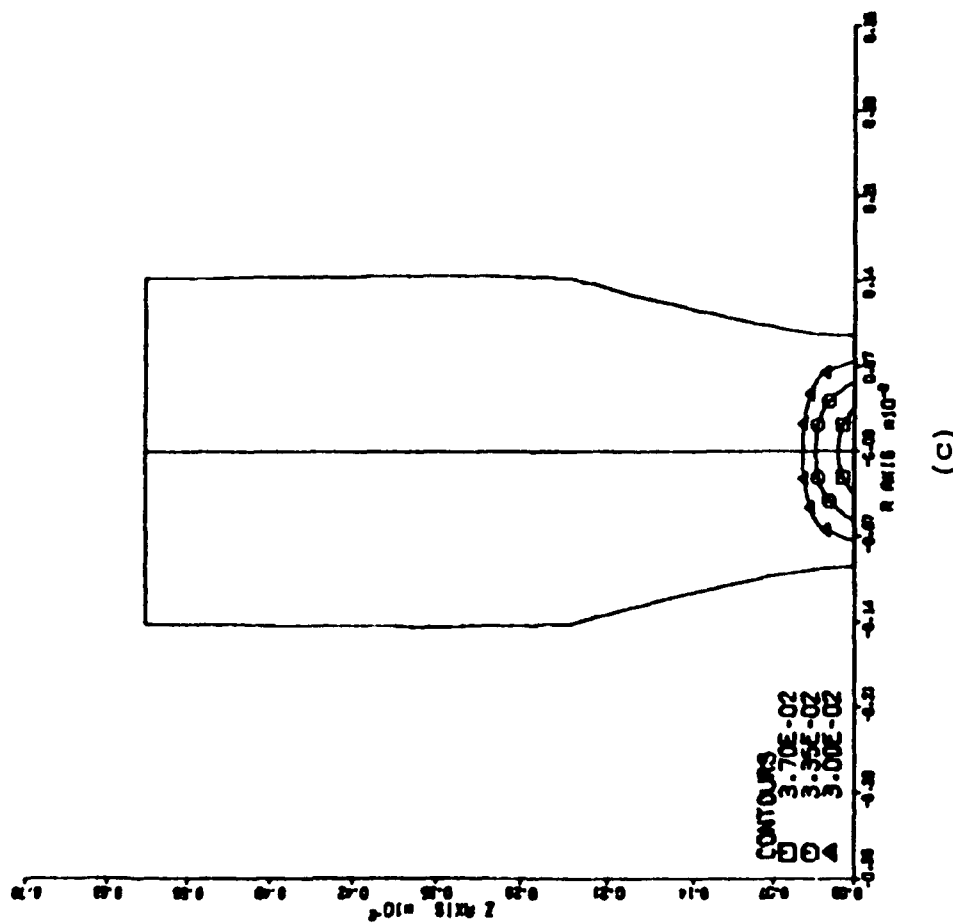


Figure 3.16. Damage (Void Volume Fraction) Contours at (a) $t=0$, (b) $t=20$, (c) $t=50$, and (d) $t=60$ microseconds.



(c)



(d)

Figure 3.16. Damage (Void Volume Fraction) Contours at (a) $t=0$, (b) $t=20$, (c) $t=50$, and (d) $t=60$ microseconds (concluded).

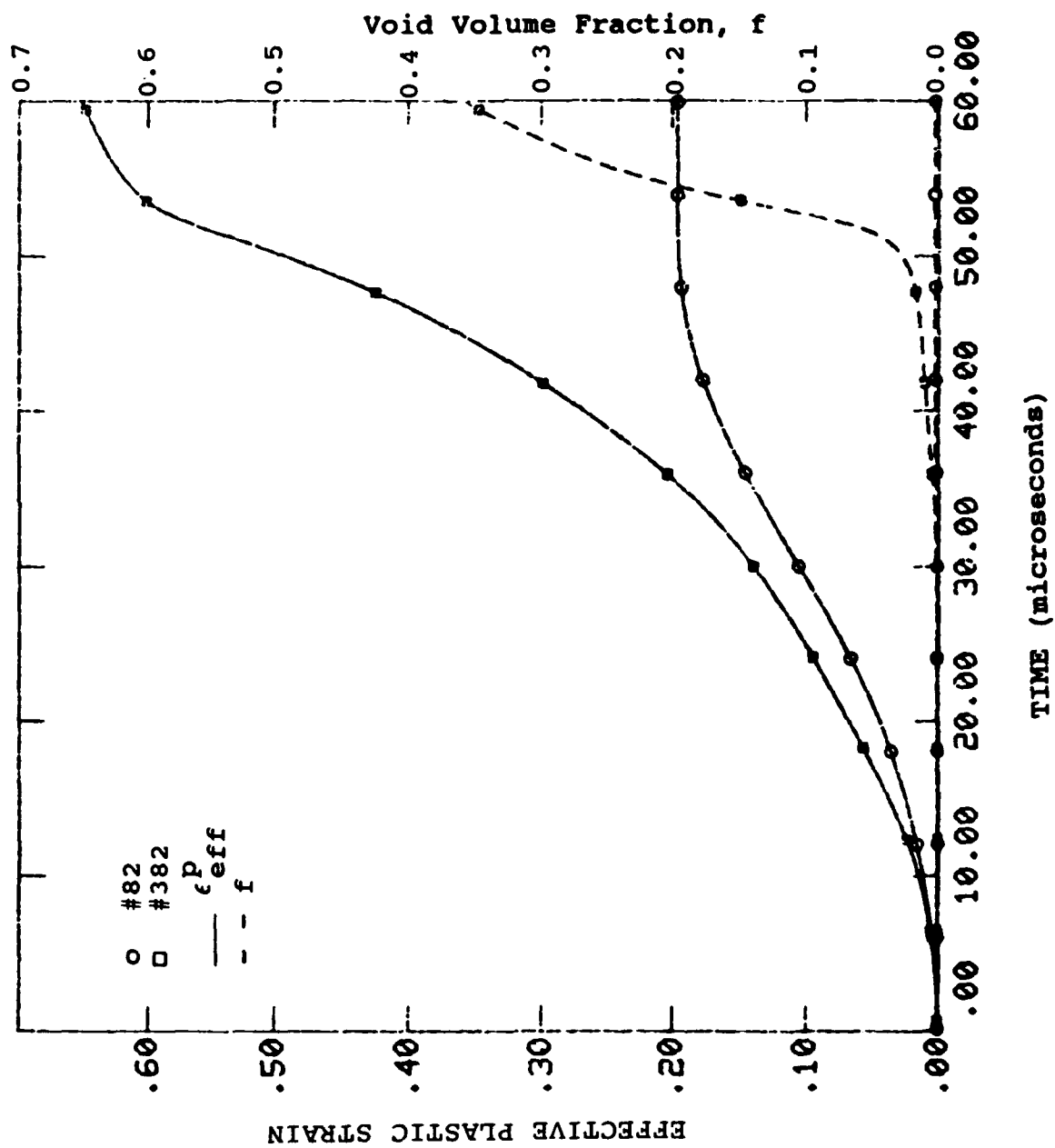


Figure 3.17. Time Histories of Effective Plastic Strain and Void Volume Fraction for Elements 82 (Uniform Section) and 382 (Local Section).

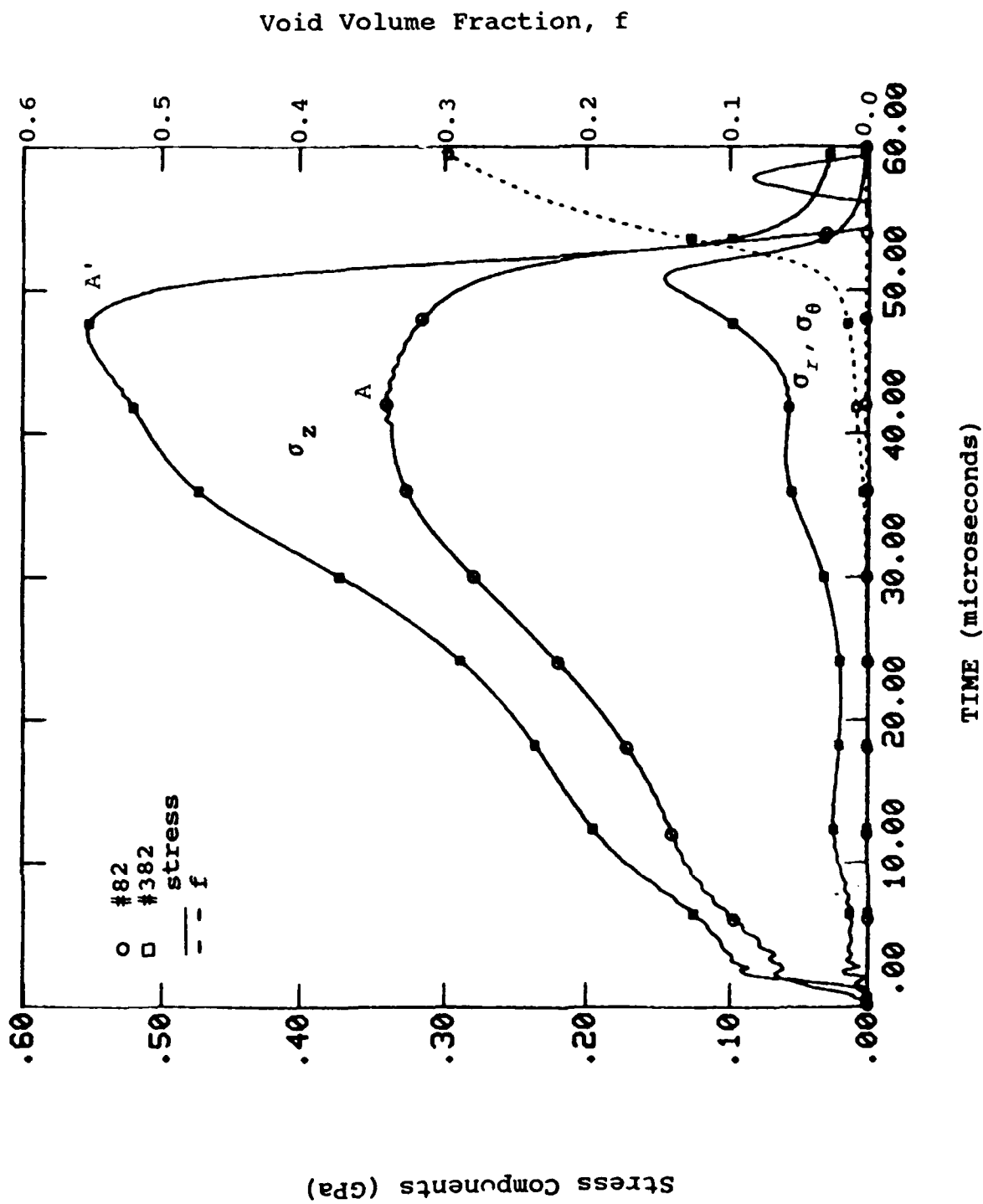


Figure 3.18. Time History Plots for the Stress Components and Void Volume Fraction.

this stress state accelerates the necking process. As rapid void growth occurs at 50 microseconds, the axial as well as hoop and radial stresses relax (at point A') in local element 382. The word 'relax' indicates that the stresses decrease with increasing plastic strains. However, the axial stress actually unloads in uniform element 82 (at point A in Figure 3.18) due to rapid localization of the deformation. Since no void growth occurs in this uniform region, the decreasing stresses are only due to unloading. In regions away from the neck, the material is intact without any voids, and, therefore, the possibility of any strength degradation leading to stress relaxation does not exist. To further demonstrate these aspects, the effective stress versus effective plastic strain behavior for the two locations is shown in Figure 3.19. The void volume fraction history has also been included. The stress (strength degradation) relaxation beyond point A can be seen in this figure. The plastic strain continually increases because of the void growth induced plastic flow. As the void volume fraction increases, the strength continues to decrease.

The mean stress (pressure) histories at various locations are plotted in Figure 3.20. As mentioned earlier, 82 represents the uniform region and 382 represents the local region. Elements 282 and 182 represent the intermediate regions (see Figure 3.14). The stress triaxiality (defined as the ratio of mean stress and effective stress) due to the initial notch leads to a higher mean stress level in the local region before the occurrence of necking. When necking initiates around 40 microseconds, the regions (82 and 182) away from the neck start unloading. While the pressure decreases because of unloading in these regions, the mean stress also relaxes due to void growth in the local regions.

The stress triaxiality is plotted with respect to time for elements 82 and 382 in Figure 3.21. The uniform region experiences behavior close to a uniaxial stress state. The ratio of mean stress to effective stress was almost $1/3$, as one would expect. The slight deviation from this value before 20 microseconds is numerical, and later this ratio remains close to $1/3$. For the element in the local region, the stress triaxiality is initially greater than $1/3$ due to the notch. However, as necking occurs between 40 and 50 microseconds, the local triaxiality rapidly increases as shown in Figure 3.21. Beyond point B , rapid void growth leads to strength degradation and failure initiation. To further understand the loading conditions, the loading paths are shown at different locations with respect to the pressure dependent yield surfaces in Figure 3.22. The loading path for each element (82, 182, 282, and 382) is described by plotting the ratio of effective stresses of the aggregate and the fully dense matrix (σ_{eff}/Y_m) versus the ratio

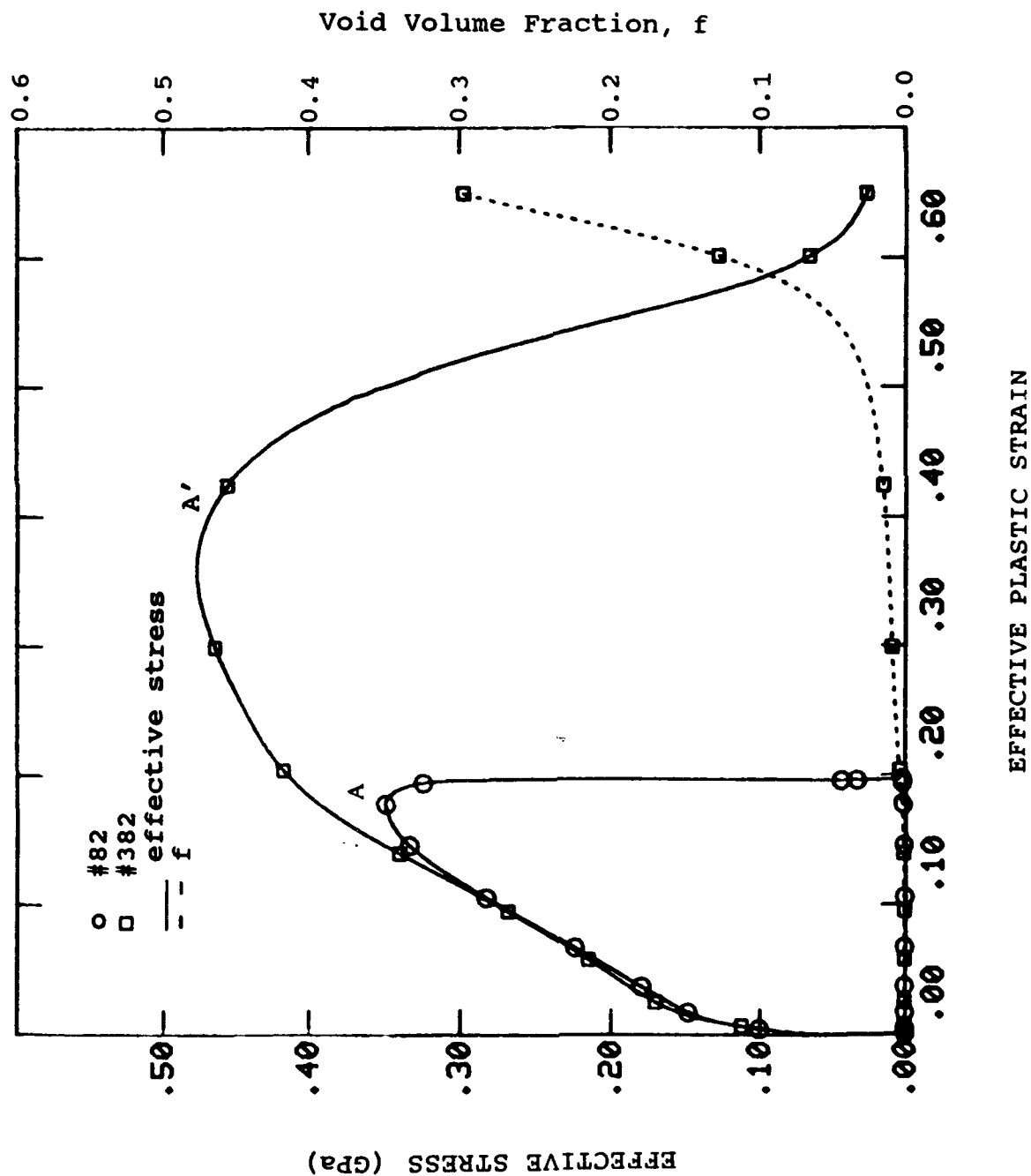


Figure 3.19. Stress-Strain Response for Elements 82 and 382, along with the Variation of f with Respect to Effective Plastic Strain. Note that $f=0$ for Element 82.

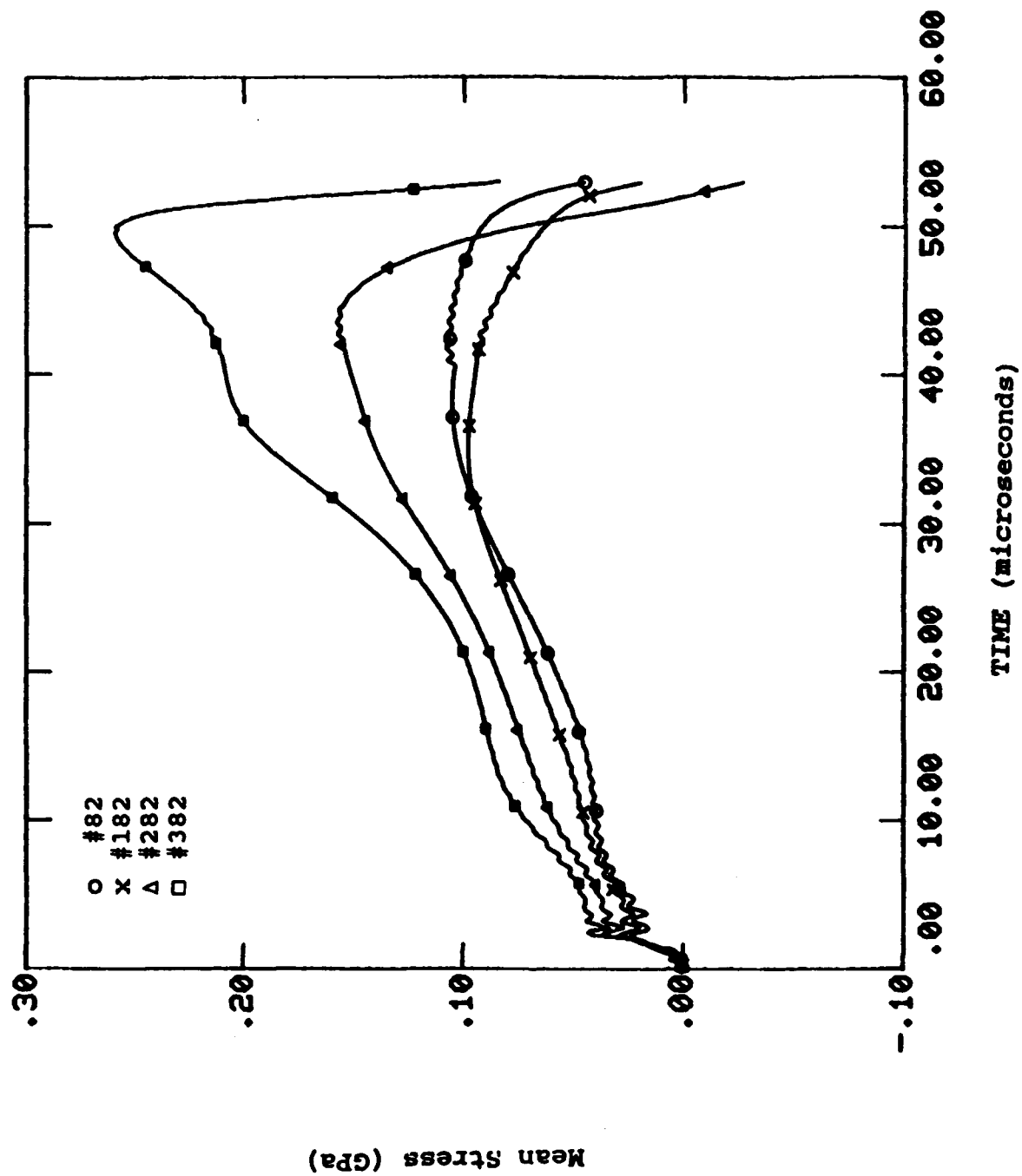


Figure 3.20. Time History Plot of Mean Stress for Elements 82, 182, 282 and 382.

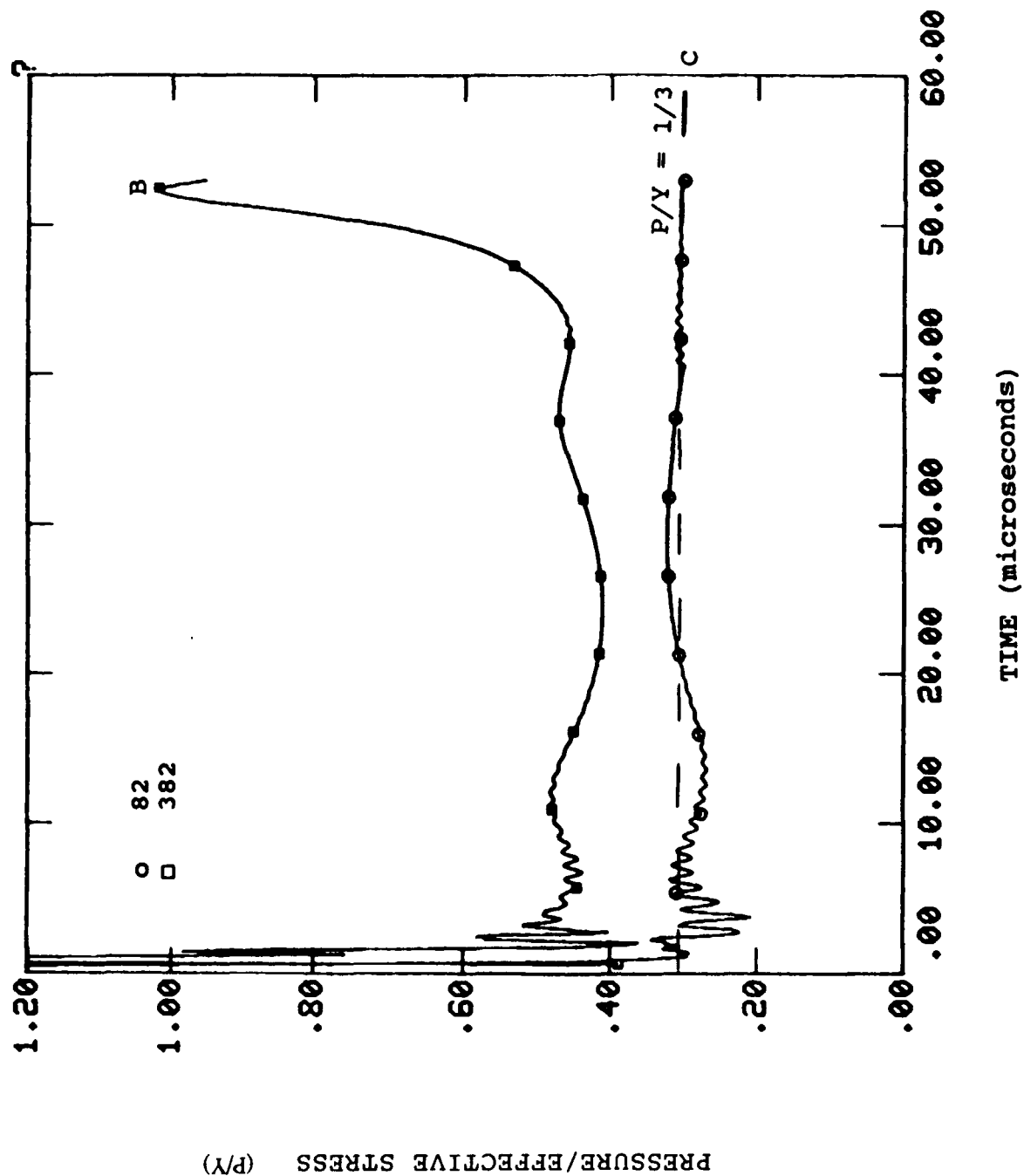


Figure 3.21. Measure of Triaxiality with Respect to Time for the Uniform (82) and Local (382) Sections. The Dashed Line Represents the Uniaxial Stress State.

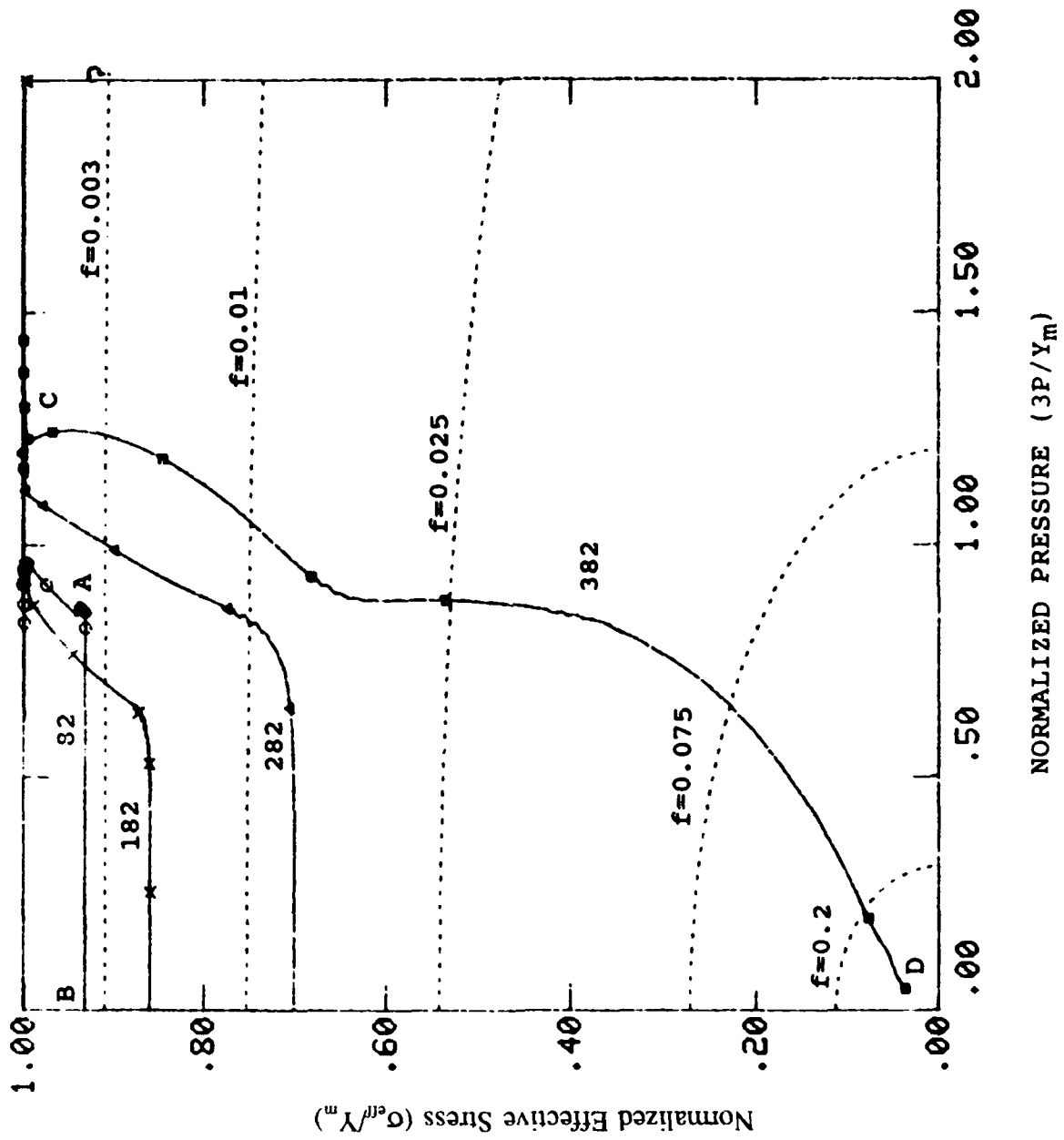


Figure 3.22. Loading Paths with Respect to Pressure Dependent Yield Surfaces in Elements 82, 182, 282, and 382.

of aggregate mean stress and matrix effective stress ($3P/Y_m$). Since the material is initially void-free, the plastic yielding is pressure independent and the loading path starts at $\sigma_{eff}/Y_m = 1$, as shown in Figure 3.22. The dotted lines represent the elliptical yield surfaces for various levels of porosity. In element 82, a limited amount of voids nucleate initially and grow very little. The corresponding loading path is shown between points *A* and *B*. The loading remains on the yield surface for void volume fractions less than 0.3 percent. In a similar manner, the loading path for element 182, which is away from the notch zone, is confined to a yield surface corresponding to $f = 0.005$. Because of enhanced void growth in the local regions, a significant amount of void growth occurred, especially in element 382 as between points *C* and *D* in Figure 3.22. As the loading path proceeds along the shrinking yield surfaces, the material strength degrades to less than 80 to 90 percent of the original intact material, indicating failure of the material.

To complete the discussion of the RDG model capabilities as applied to the dynamic necking problem, additional analyses in terms of snapshots and additional contour plots are presented. The snapshots are plots that describe the distribution of a variable with respect to position (for example, radial distance from the axis-of-symmetry). In Figure 3.23, void volume fraction snapshots at three different *z* positions (see Figure 3.14) are plotted. The *z* position describes the axial distance (along the specimen length) from the minimum cross section (*c/s*) of the shallow notched tensile specimen. Therefore, $z=0$ represents the minimum cross section. Since the triaxiality is largest at the center of the specimen ($r=0$ and $z=0$), the void volume fraction is maximum at the center and decreases toward the free surface. The present analysis is for a dynamically stretched tensile specimen with a loading duration on the order of microseconds. Interestingly, these numerical results are very similar to those of a statically deformed specimen. These analyses compared qualitatively well with the results reported by Norris et al. [37]. They analyzed quasi-static necking deformation using a dynamic finite difference computer program. However, in the present work, the problem is considered to be inherently dynamic and has been treated as a shock wave propagation problem. Due to several reverberations of the shock waves, the deformation is homogeneous, and the problem is dominated by inertial loading rather than the shock wave effects.

Snapshots of normalized effective stress in the voided aggregate are given in Figure 3.24. At $t=20$ microseconds, the effective stresses of the matrix and the aggregate are almost the same due to insignificant void growth; therefore, the stress ratio (σ_{eff}/Y_m) is one. When the void

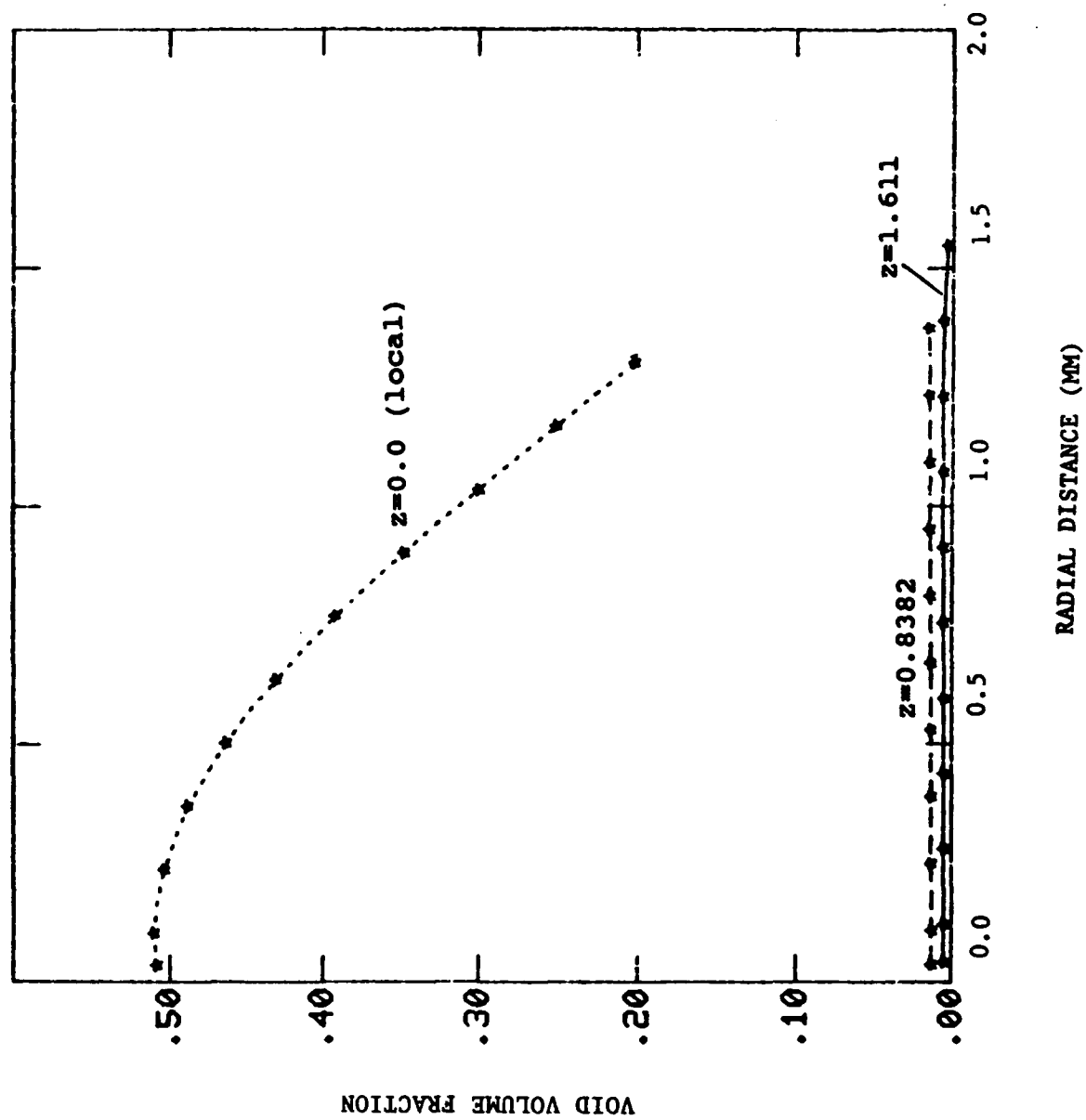


Figure 3.23. Radial Distribution of Void Volume Fraction at Three Different Positions along the Specimen Length.

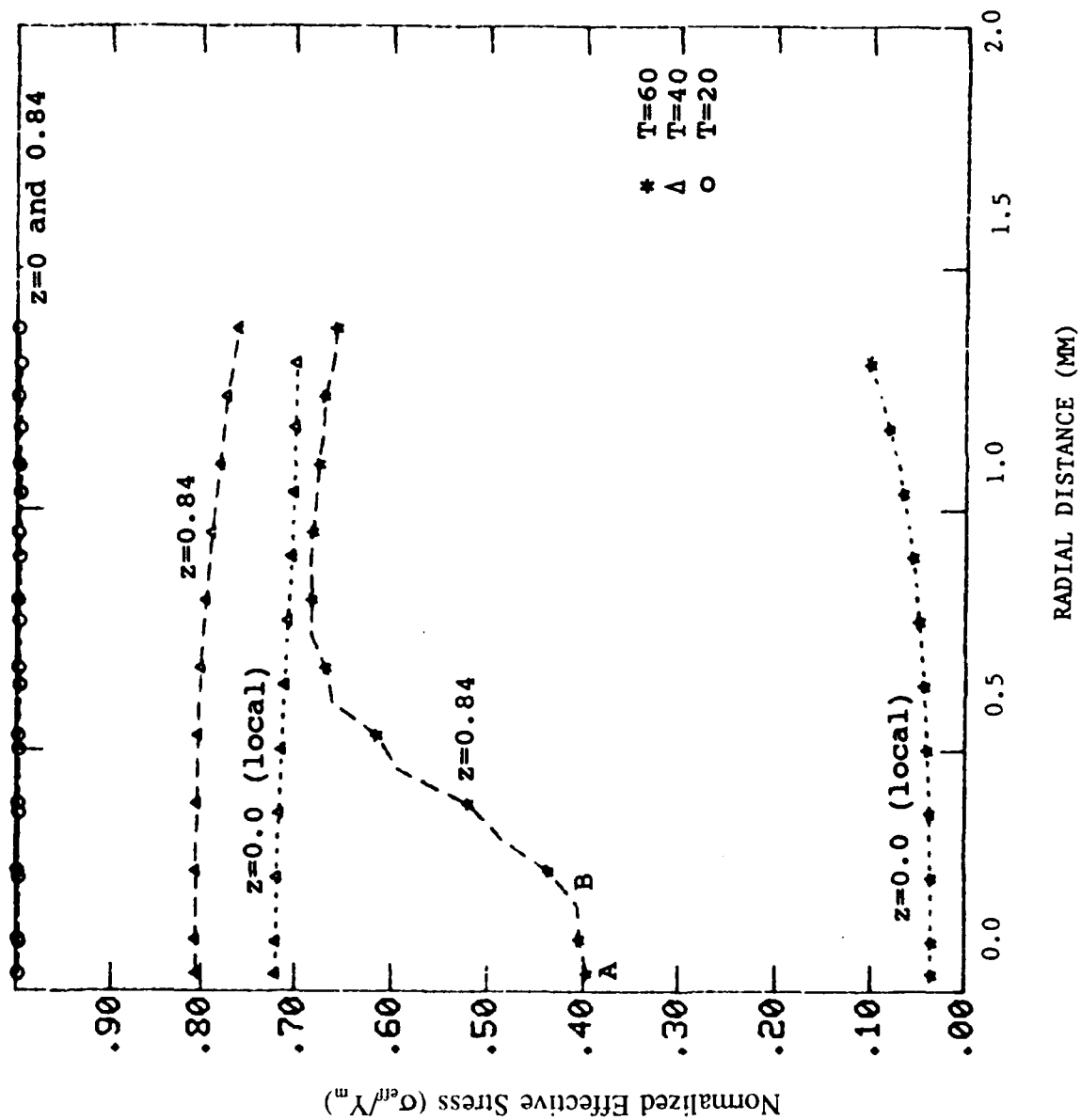


Figure 3.24. Normalized Effective Stress (σ_{eff}/Y_m) Distribution along the Radius for Different z Positions and Times.

growth occurs, the aggregate strength degrades and the stress ratio becomes less than one. By 40 microseconds, the c/s at $z=0.84$ mm and the minimum c/s have developed significant voids. The $z=0$ c/s degrades faster than the section at 0.84 mm. Since the void volume fraction is initially evenly distributed across the c/s (not shown in the figure), the reductions in strength are almost uniform. Between 40 and 60 microseconds, non-uniform void growth in the intermediate section leads to rapid strength degradation near the axis ($r=0$), as shown between *A* and *B* in Figure 3.24. However, because of a lack of stress triaxiality, the void growth near the surface (for the $z=0.84$ c/s) is not significant; correspondingly, the strength near the surface does not significantly degrade. By 60 microseconds, due to enhanced void growth and void coalescence, the aggregate strength at the minimum c/s ($z=0$) has decreased by more than 90 percent. This indicates failure initiation leading to total separation of the material.

For comparison, the necking process was also simulated without voids; this simulation will be referred to as case 2 below. As before, the Bodner-Partom model was used to describe the material behavior, and the solution was conducted for 60 microseconds. Since the boundary conditions for the two simulations were the same, the top section was moved (pulled) identically. Therefore, at any given instant, the specimen length was the same for both cases. Figure 3.25 compares the following strains from the two simulations: (1) ratio of current length and original length, (2) uniform effective plastic strain in element 82 for the void-free material (case 2), and (3) uniform effective plastic strain in element 82 for the void-containing material (case 1). As expected, the average strain based on the overall specimen length was larger than the uniform strains in element 82 for the two cases. While in case 2 the uniform section continues to deform at 60 microseconds, deformation no longer occurs in case 1 due to the void growth controlled necking process. For this reason, the final strains in the uniform region were significantly reduced in the presence of void growth.

Plots of effective stress versus effective plastic strain in the local element (382) are shown in Figure 3.26 for both cases (with and without voids). In the void-free case, since material degradation does not occur, the effective stress (strength) follows the true stress-strain curves generated by the BP model for OFHC copper. In the void-growth influenced necking case, the decreasing portion of the stress-strain curve (between points *A* and *B*) is due to strength degradation. Even though the loading (increasing plastic strain) increases beyond point *A*, the stress continually drops, indicating void-softening of the material.

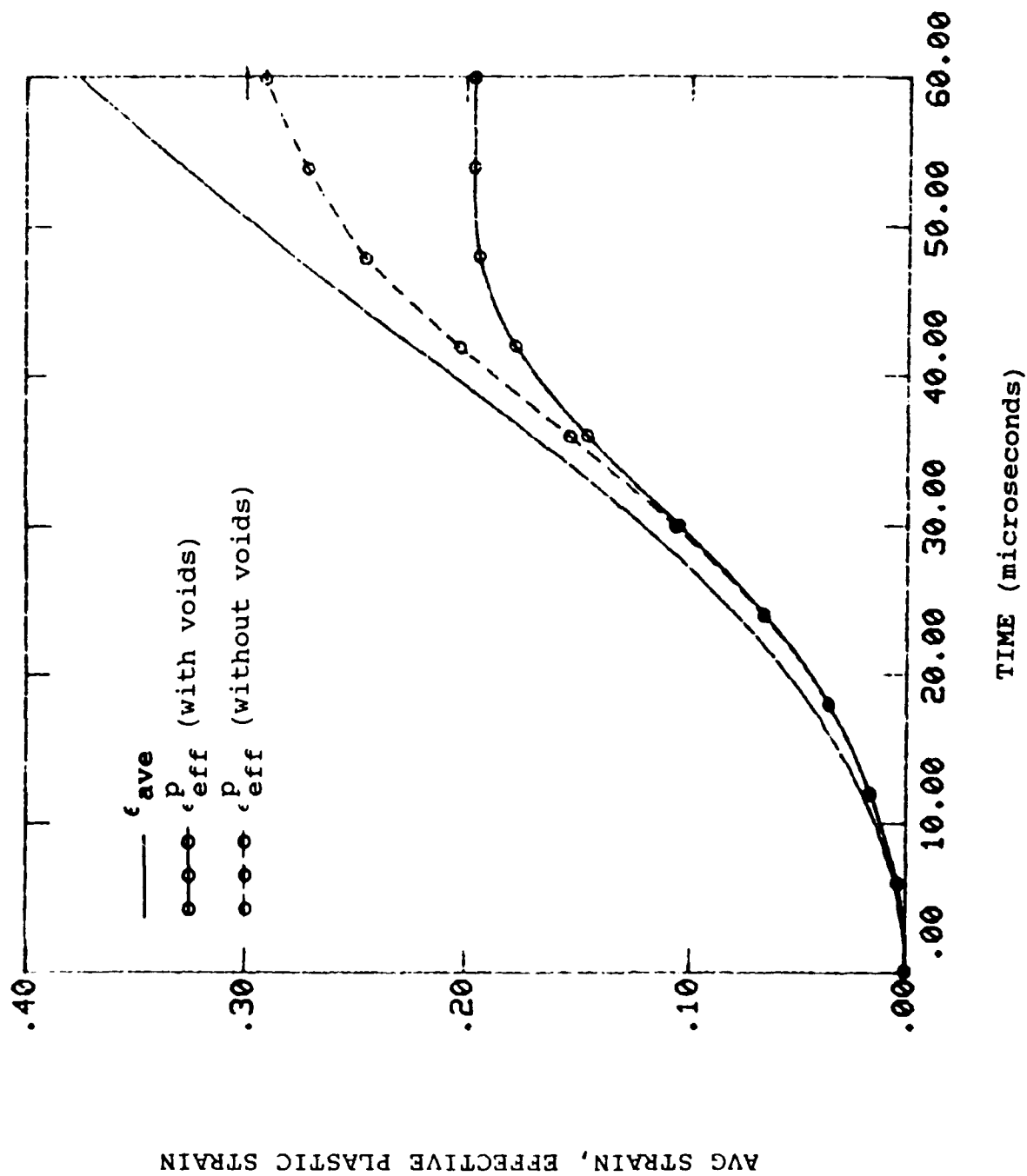


Figure 3.25. Comparison of Strains in Element 82 for Tensile Necking with and without Voids. The Solid Line Without Symbols is an Average Measure of Strain Based on the Pull Velocity.

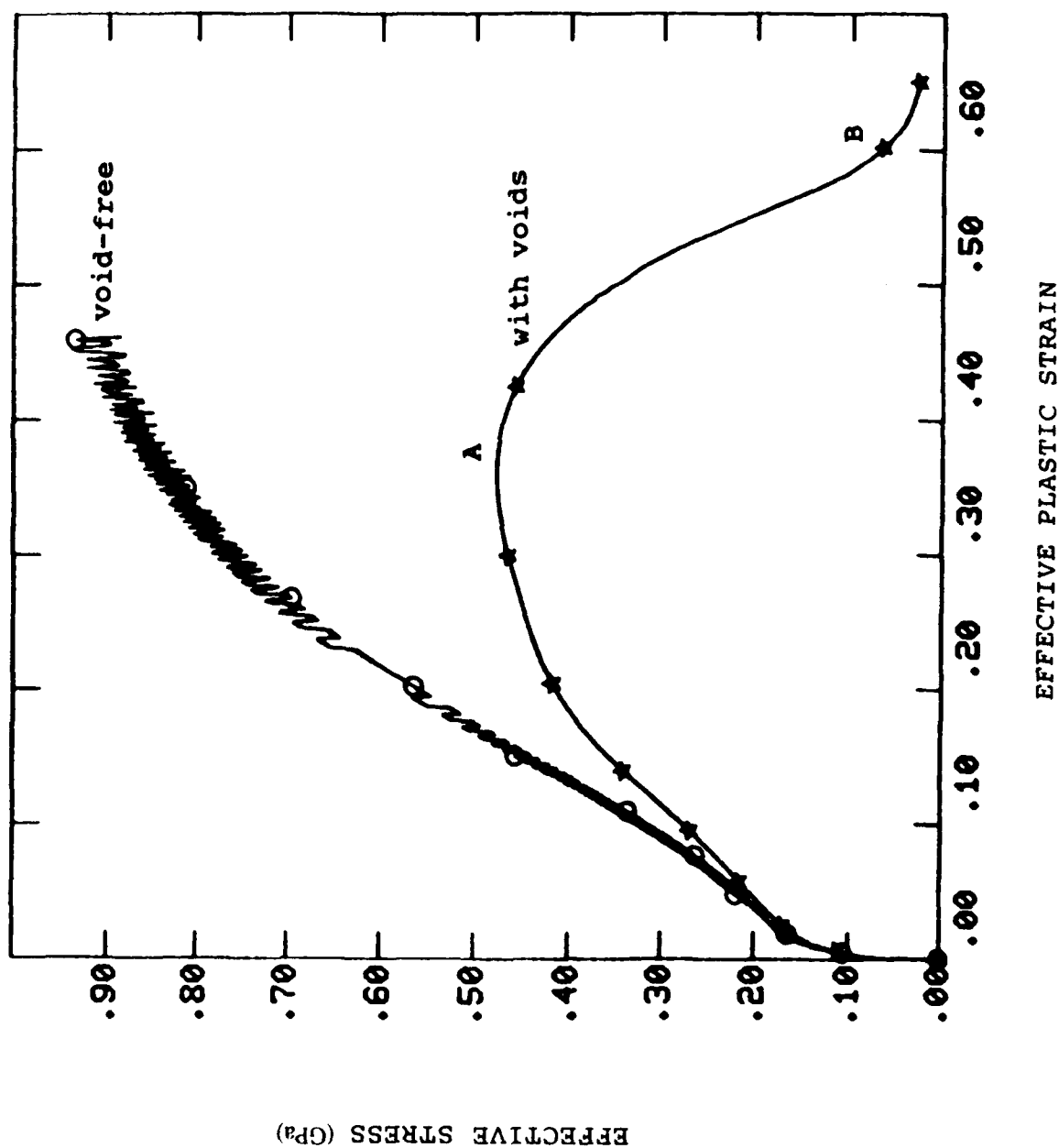


Figure 3.26. Comparison of σ_{eff} versus ϵ_{eff}^p in Element 382 for Tensile Necking with and without Voids.

The effective plastic strain variations along a radius for the necking process with and without voids are shown in Figure 3.27. The variation along the minimum radius (local region) indicates that the strain reached a maximum near the surface and not at the axis for both cases. These results differ from the tensile simulation results reported by Norris et al. [37] in which the plastic strain reached a maximum at the axis. They considered a quasi-static necking problem in which the inertial effects were neglected. Since the present necking analysis considers the inertial effects, the difference in the effective plastic strain distribution is attributed to the inertial loading. Also, the stress-strain response was modeled as an isothermal process. In the simulations, the effects due to the adiabatic process are not considered.

The local plastic strain levels in the void-growth case are larger than those in the void-free case. The obvious reason is that void growth and pressure-dependent yielding enhance the plastic flow. While loading continues in the local region, the uniform section unloads because of the enhanced necking process due to void growth. In the void-free case, since the necking is not very severe, the loading continues in the uniform section, as shown earlier in Figure 3.26. Because of this, the effective plastic strain also continues to increase in the uniform section.

Snapshots of stress triaxiality for the two cases are plotted in Figure 3.28. In the void growth case, the triaxiality was maximum at the local (minimum radius) section, especially near the axis ($r=0$) as can be seen from the figure. Other investigators [37-39] have observed similar behavior under quasi-static loading conditions, with and without void growth. The triaxiality levels are relatively low near the surface, as expected. In the void-free case, the stress triaxiality is equal to about 0.3 in the uniform section. However, in the uniform section of the void-growth case, the triaxiality is actually lower than 0.3. The reason for this can be explained by Figure 3.29. This figure shows a mean stress contour plot for the void-growth case. The material under compression is shown by the region which is not shaded. The contour was plotted for the final solution time (60 microseconds). Failure initiation has occurred due to a large void content near the central portion of the tensile specimen. This final phase in the failure process results in unloading of the uniform section and further loading under compression. In the void-free case (not shown in the figure), the uniform section unloads completely but does not go into compression. If calculations were performed beyond 60 microseconds, compressive loading

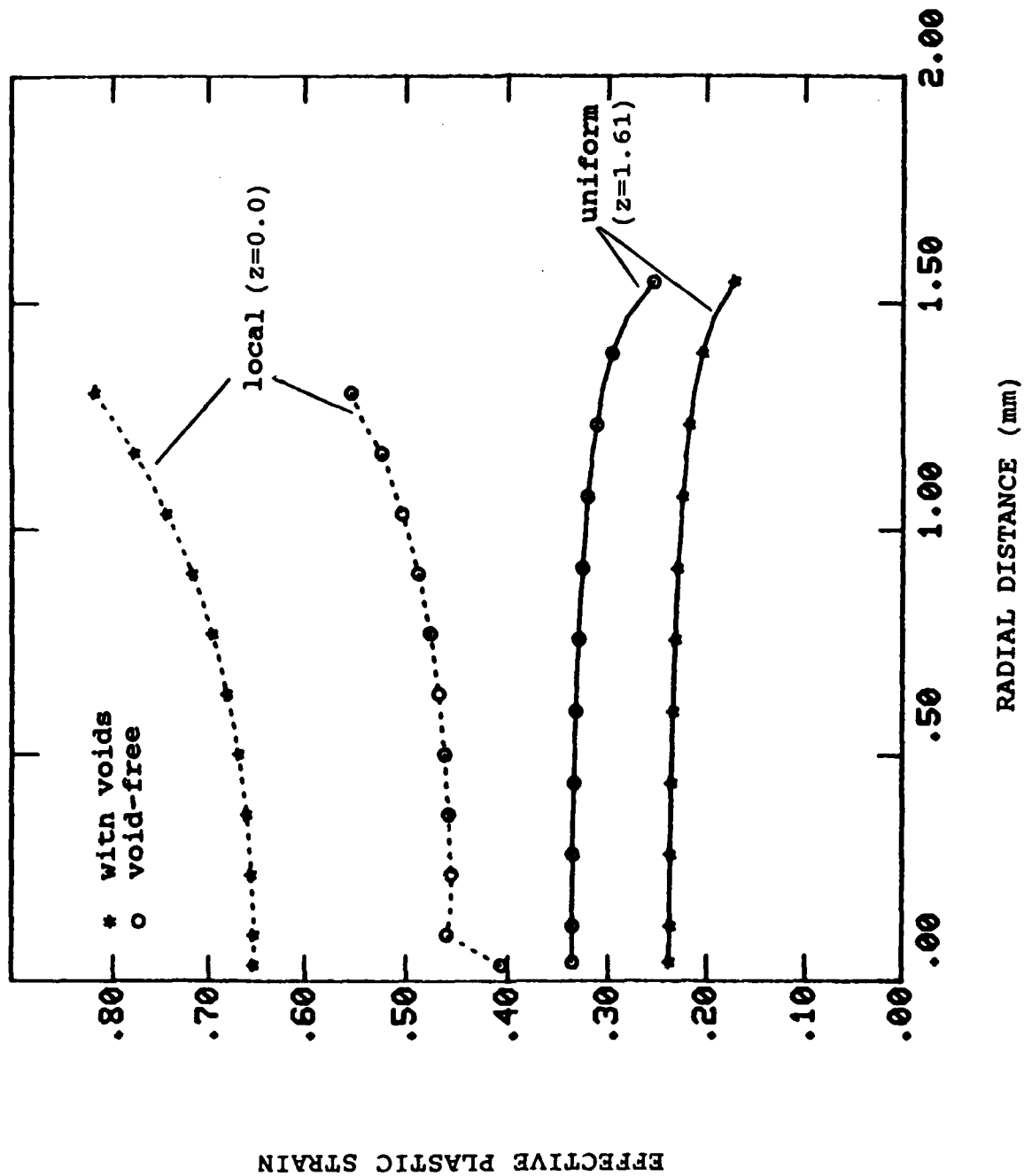


Figure 3.27. Radial Distributions of e_{eff}^p for Cases with and without Voids at $t=60 \mu s$, Plotted for Uniform ($z=1.61$) and Local ($z=0.0$) Sections.

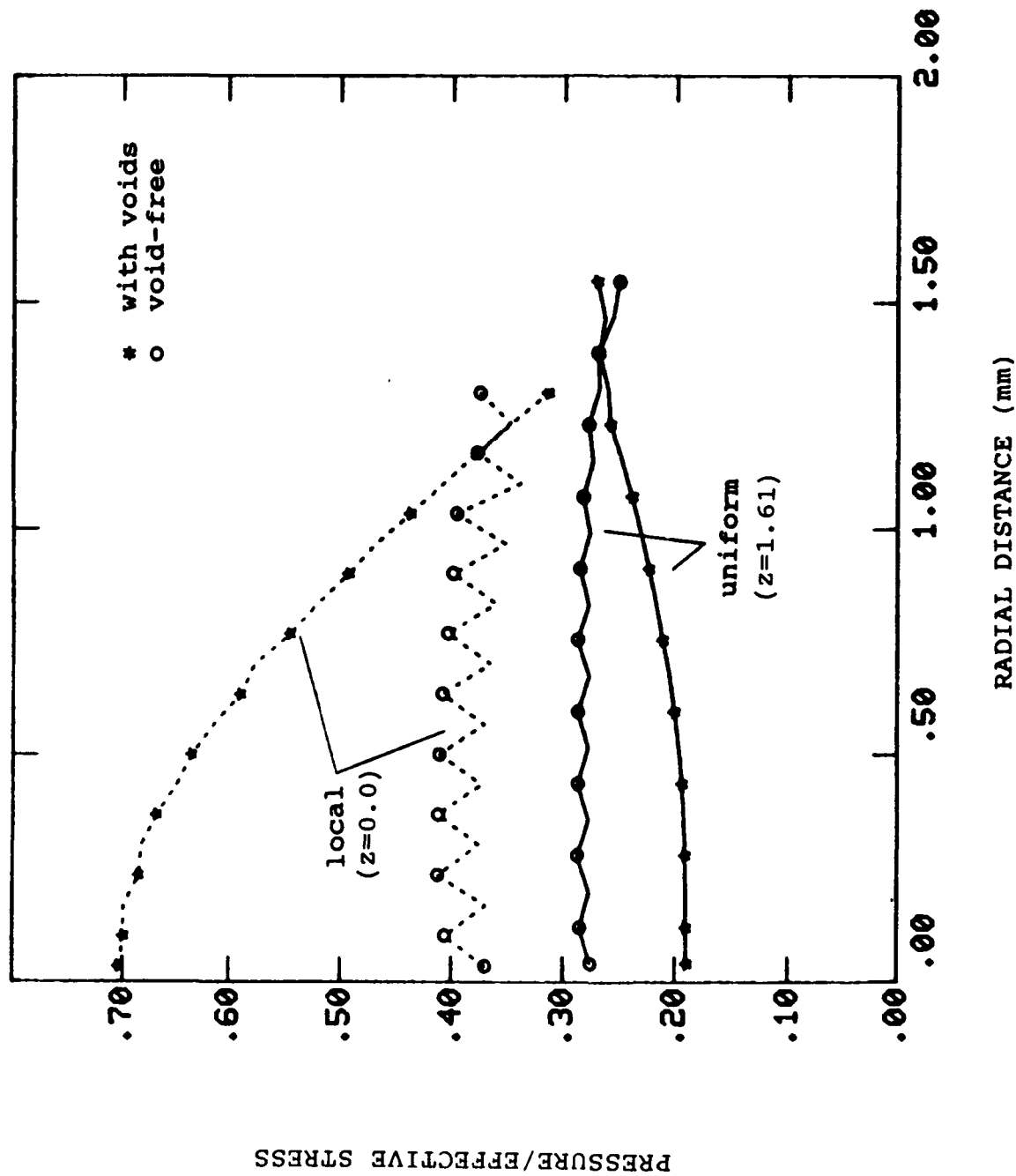


Figure 3.28. Radial Distributions of Triaxiality (P/σ_{eff}) for Cases with and without Voids at $t=60 \mu s$, Plotted for Uniform ($z=1.61$) and Local ($z=0.0$) Sections.

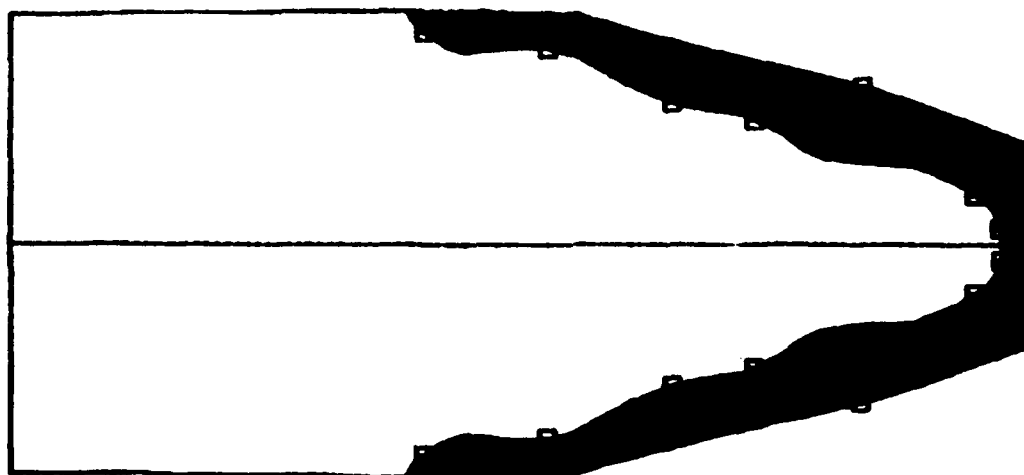


Figure 3.29. Pressure Contour Plot for Void-Growth Influenced Necking Process at $t=60 \mu s$. The Shaded Region is under Tensile Loading, and the Rest of the Region Experiences Compressive Loading.

might also occur in the void-free case. However, Norris et al. [37], in their numerical analysis of quasi-static tensile necking, observed compressive zones away from the local region.

The deformed configurations of the shallow notched tensile specimen for the cases with and without void growth are shown in Figure 3.30. Only one half of the specimen is shown for each case for comparison. Also included is the initial geometry, shown by the dotted line. In the void-free case, the neck profile retained the original notch shape, while in the void-growth case, the profile resulted in a sharp localized notch at the $z=0$ c/s.

In the present application, the material was modeled as strain rate dependent and highly strain hardening. Additional exercises with different material behaviors such as perfectly plastic, strain-rate independent, and thermal softening, with and without voids, will shed additional light on the evolution of necking.

3.6.2 Rod Penetration

The main objective of this simulation was to show the spall evolution in a target using the RDG ductile failure model. As shown above, the model successfully describes the spallation phenomenon in the plate impact configuration and the behavior of void-growth enhanced tensile necking problems.

An EPIC-2 code simulation of a 2 inch long, 1 inch diameter solid copper rod impacting a 6 inch diameter, 1 inch thick HY100 steel plate target at an impact velocity of 8333 ft/sec was considered. The corresponding finite element mesh is shown in Figure 3.31. Material behavior was modeled using the Johnson-Cook (JC) constitutive model for the copper rod and the RDG model (with the Bodner-Partom (BP) constitutive model) for the HY100 steel plate. The constants for the BP, JC, and RDG models are given in Appendix B and in Table 3.1.

The numerical solution was obtained for 20 microseconds. For analysis, an element (736) near the axis of symmetry of the target and at a distance of about 0.8 inches from the impact point was examined. Time histories of pressure, stress components, effective stress, and damage (void volume fraction) in this element were stored for post-processing. Snapshot plots were also used to display the distributions of these variables along the target radius at different depths for various times. Finally, damage contours were plotted at different times to examine the evolution of a spall zone inside the target.

with void void-free

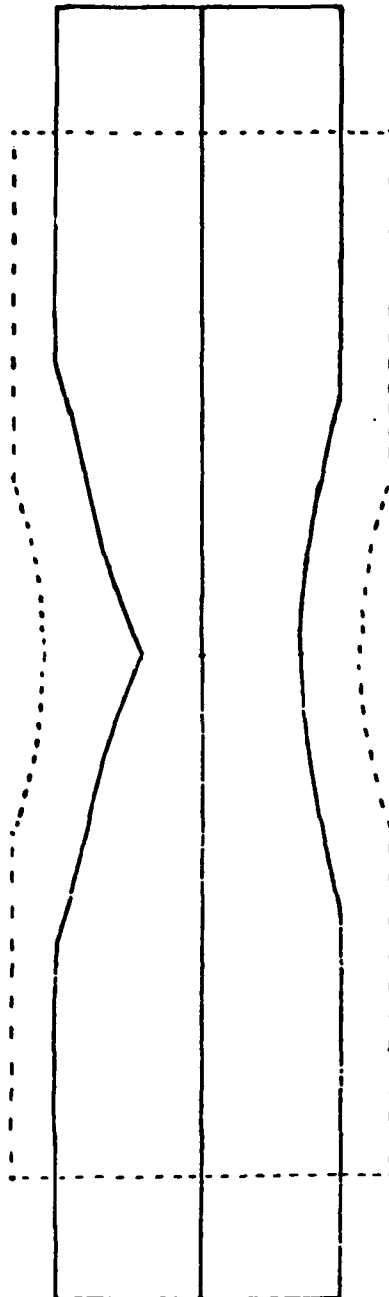


Figure 3.30. Initial (Dotted Line) and Final (Solid Line) Shapes of the Shallow Notch Tensile Specimen.

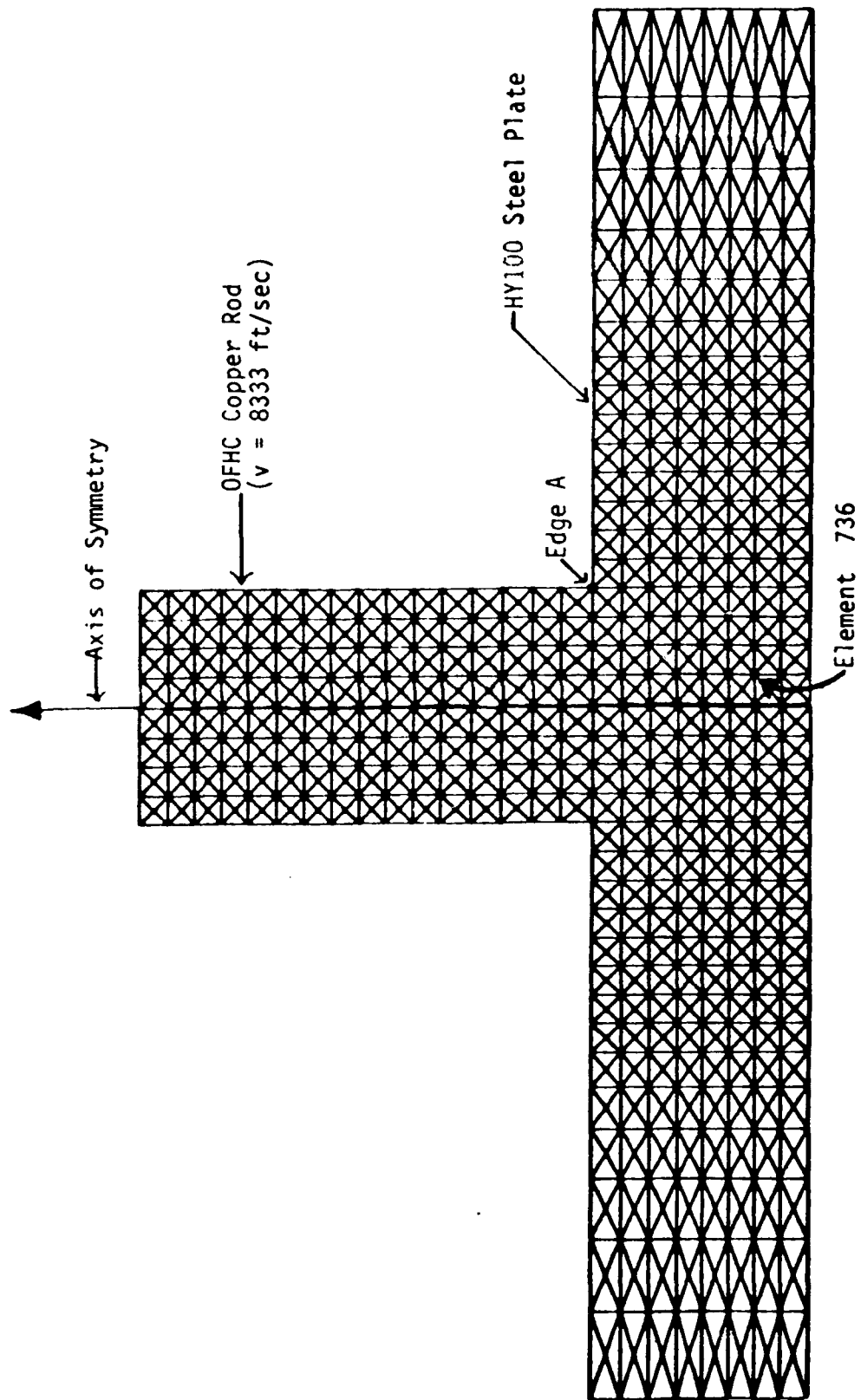


Figure 3.31. Finite Element Mesh for the Rod Penetration Problem.

In Figure 3.32, the normalized pressure (mean stress/aggregate strength) is plotted with respect to time for element 736 in the target. The evolution of damage in terms of void volume fraction is also shown. The normalized pressure is a measure of the triaxiality of the stress state. A negative normalized pressure indicates that the material is under compression, and void growth cannot occur. To generate voids in an intact ductile metal, a high triaxial stress state under tension is required. The derivations of Rice and Tracey [39] and McClintock [40], and the quasi-static experiments of Hancock and MacKenzie [41] support the concept that a high triaxial tensile state enhances void nucleation and growth. The RDG model, which is based on this concept, was able to model the void growth accordingly as can be seen from Figure 3.32. In a tensile test, before the onset of necking, the triaxiality ratio is $1/3$. However, in a penetration experiment configuration, the triaxiality can become large enough to generate spallation in the target. In this particular simulation, the tensile triaxiality became extremely high (>10 in Figure 3.32).

In element 736, the release wave from the edge (point A in Figure 3.31) arrives at about 4 microseconds and releases the compressive pressure. Note that the distance of this element from the edge A in Figure 3.31 is around 0.9 inches, and the wave speed in HY100 steel is about 0.23 inches/microsecond. Then, at about 5 microseconds, the release wave from the stress free back surface of the target reaches element 736. (Note that the initial shock wave will reflect as a tensile wave.) This tensile wave puts the element under a high triaxial stress state leading to void nucleation and growth. The void volume fraction increases while the tensile stress state prevails. As the material degrades due to voids, the pressure as well as the strength relaxes, as shown in Figure 3.32.

The strengths of the matrix material (intact HY100 steel) and the porous aggregate (HY100 steel with porosity) for element 736 are shown in Figure 3.33 with respect to time. For further understanding and evaluation of the RDG model capabilities, the evolution of void volume fraction (damage) has also been included in the plot. Initially, the material is intact; therefore, the aggregate and matrix strengths are the same, and the curves between points A and B are identical. Void nucleation occurs at around $t = 4.9$ microseconds. Subsequent void growth degrades the aggregate strength, as shown by the sudden drop of the effective stress (Y_a) to point C, and the aggregate strength remains significantly lower than the matrix strength (as shown by the dotted line).

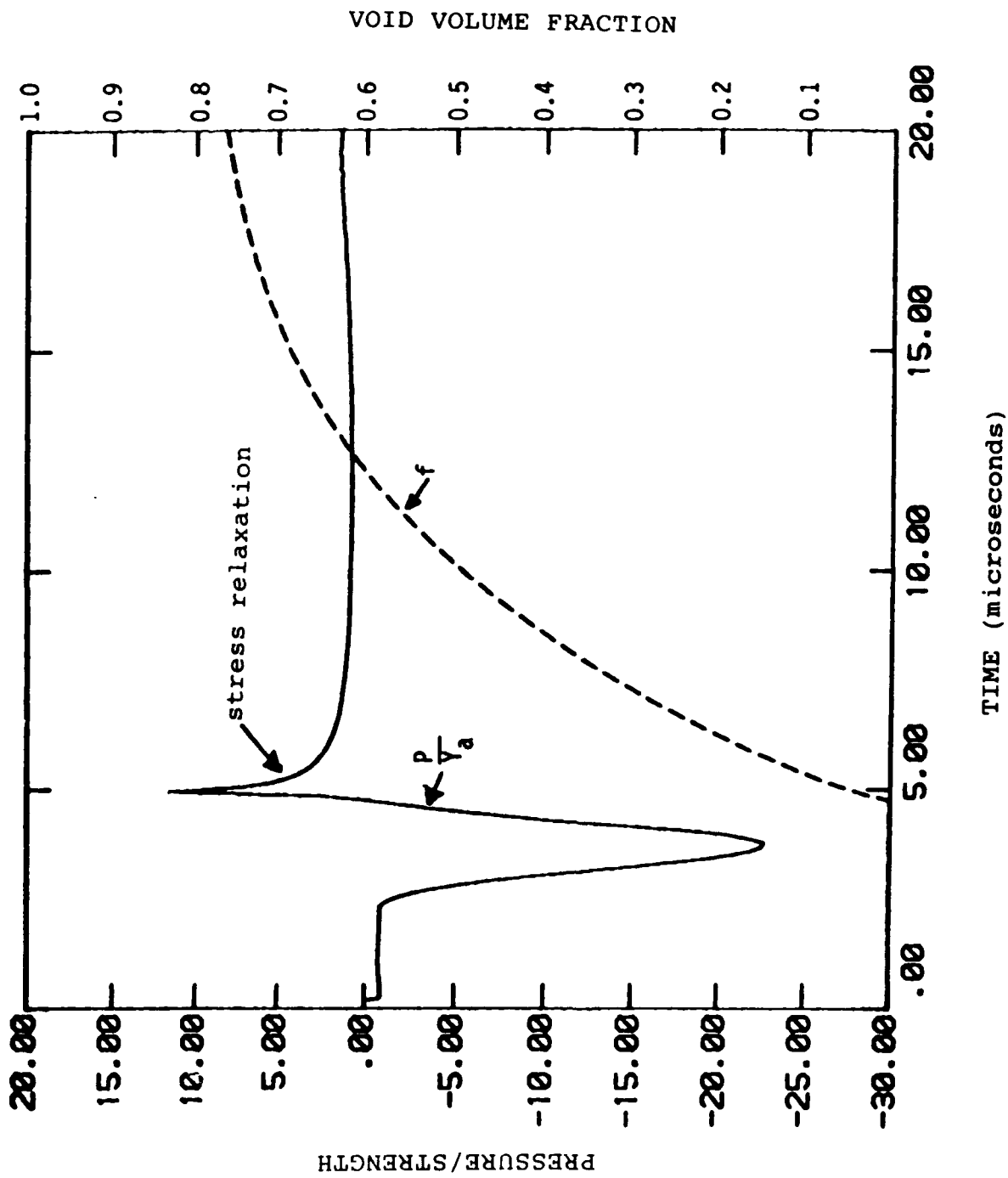


Figure 3.32. Time Histories of Triaxiality (Mean Stress/Aggregate Effective Stress) and Void Volume Fraction for Element 736.

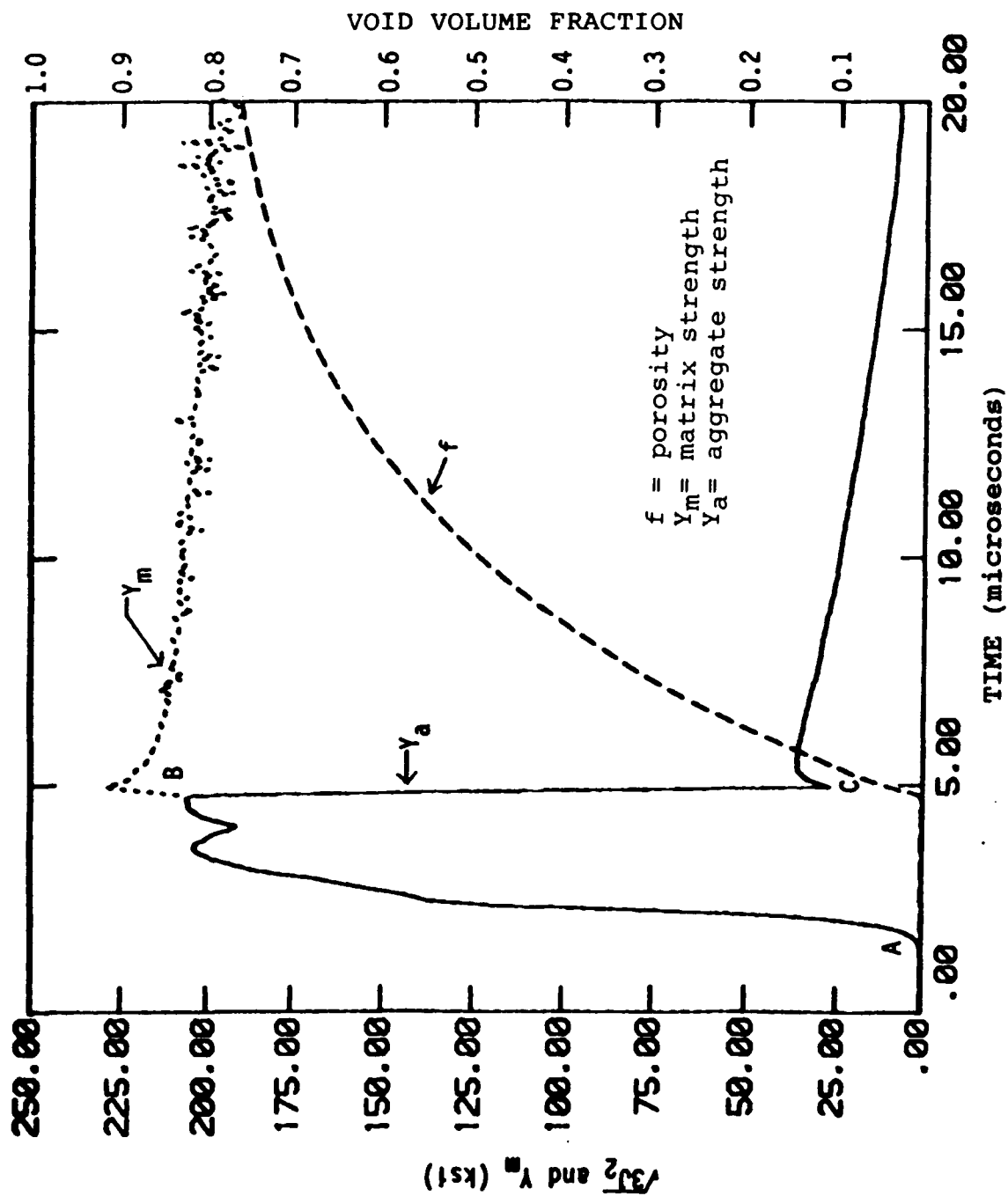


Figure 3.33. Effect of Void Volume Fraction, f (Porosity) on the Aggregate Strength in Element 736. The Matrix Strength (Y_m) is Independent of f .

In Figure 3.34, the loading path in element 736 was plotted with respect to the pressure dependent yield surfaces. Yield surfaces for various values of the void content are indicated by the dashed lines in this figure. These surfaces are generated from the relationship (Equation (1)) between the normalized pressure and normalized effective strength. The pressure and the effective stress are both normalized with respect to the matrix flow strength. Initially, the material is void free and, therefore, the effective stresses (strengths) of the aggregate and the matrix are the same. For this reason, the loading path starts at point *A*, where the value of the normalized effective stress is one. When small amounts of voids ($f < 0.005$) nucleate between points *A* and *B*, the pressure dependence of the yielding makes the aggregate flow strength a function of pressure. The void-containing aggregate strength is lower than the matrix strength, so the ratio between these two strengths becomes less than one. As the loading progresses, rapid void growth occurs between points *B* and *D*. When the void content in element 736 has increased to about 0.02 (at *C*), the aggregate flow strength has dropped to about 60 percent of the original intact material (matrix) strength. Further void growth between points *C* and *D* degrades the aggregate strength to about 10 percent of its original value. Beyond point *D*, the material completely loses its load carrying capacity in tension, and the flow strength, as well as the mean stress (pressure), relaxes to zero.

The RDG model does not include a void coalescence model; however, the void growth model has been formulated in such a manner that rapid void growth occurs at a certain void volume fraction level, indicating void coalescence. This can be clearly seen in Figure 3.34 between points *D* and *F*.

The snapshots in Figure 3.35 illustrate the radial extent of void growth and aggregate strength degradation inside the target at a depth of about 0.8 inches (same as element 736). In this figure, radial distributions of void volume fraction and aggregate strength are plotted for two different times (5 and 20 microseconds). A small number of voids have nucleated and grown at the center of the specimen between *A* and *B* at $t = 5 \mu s$. The corresponding aggregate strength relaxation can be seen between *A'* and *B'*. Beyond a radial distance of 0.5 inches, the material is void-free. By 20 μs , the radial extent of the void distribution has spread to about 1.75 inches (between *C* and *D*). This results in further degradation of the aggregate strength, as indicated by the solid line between *C'* and *D'*.

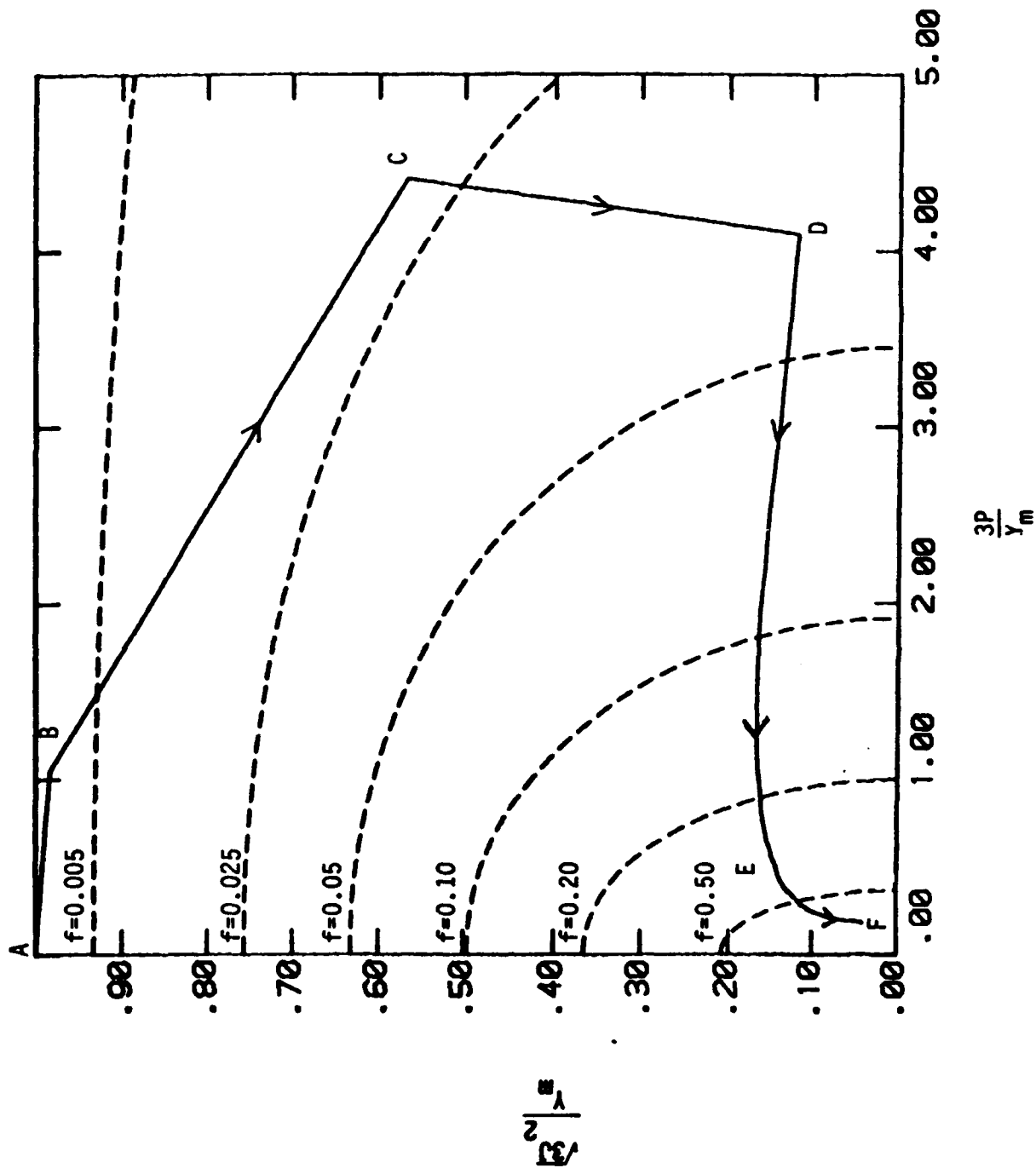


Figure 3.34. The Loading Path (Solid Line) in Element 736, with Respect to the Pressure Dependent Yield Surfaces.

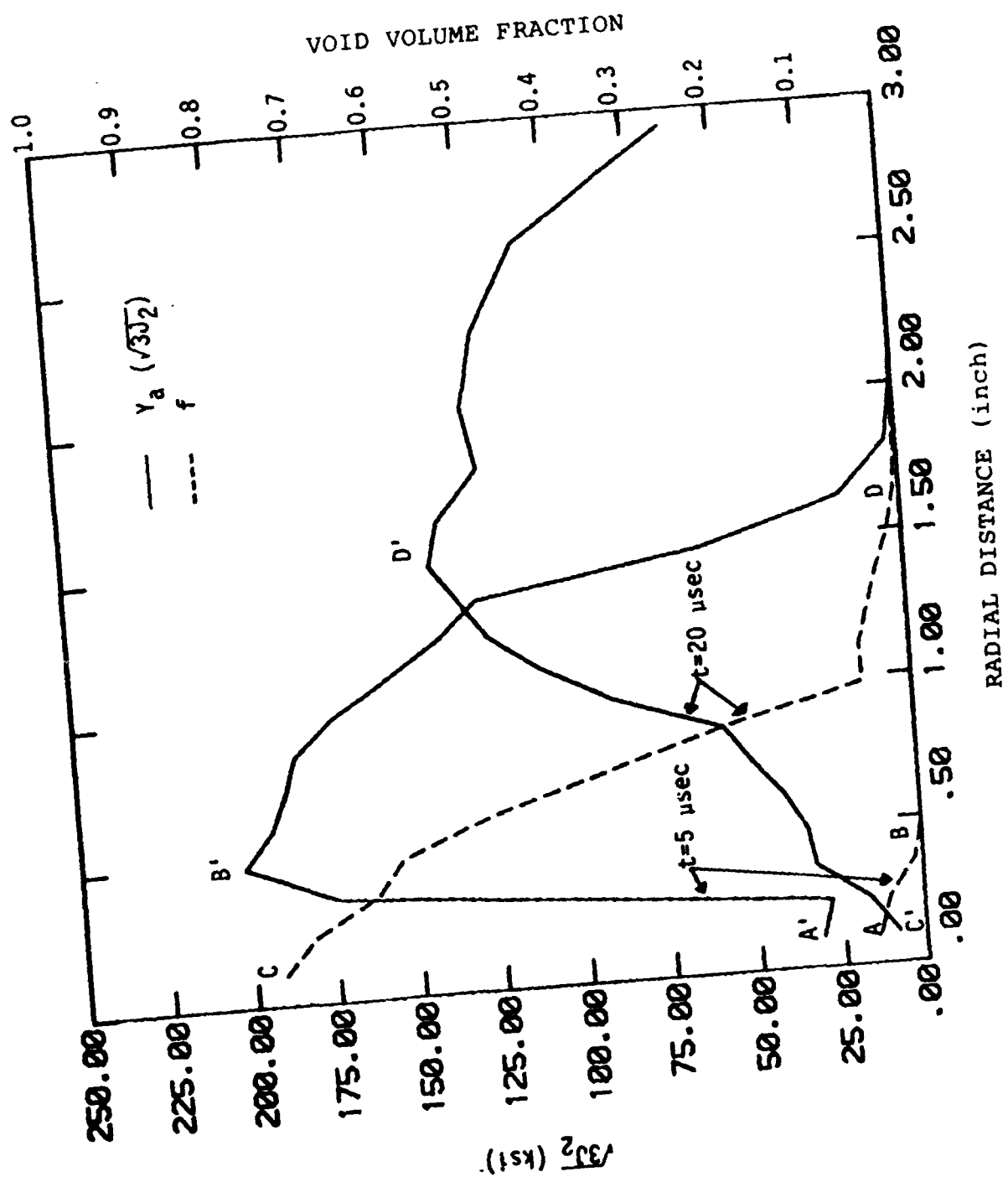


Figure 3.35. Radial Distributions of Aggregate Strength (γ_a) and Void Volume Fraction (f) Inside the Target at a Depth of 0.8 Inches for $t = 5 \mu\text{s}$ and $20 \mu\text{s}$.

The void volume fraction contours for different time intervals are plotted in Figure 3.36. At 5 microseconds, void nucleation and growth has occurred at a distance of 0.9 inches from the top of the target. Since the material in this region experiences relatively large tensile stresses, spall initiates there. The void growth rate is relatively lower outside the region enclosed by the contour in Figure 3.36a. Between 5 and 10 microseconds, the void growth extends to a larger region as shown in Figure 3.36b. At 15 microseconds, the spall process is complete and intense void concentration has occurred. The inner contours in Figure 3.36c represent this intense spall zone. The void volume fraction in this zone was well above 0.5. In a penetration experiment, the material often physically separates and forms stress free fracture surfaces in the target due to void coalescence; in some cases, spall fragments eject out from the back of the target.

For completeness, the case of the rod penetration process without any material degradation was simulated. This calculation did not include the effects of damage or a spall criterion. The material behavior was therefore described by the JC or BP viscoplastic models and without the RDG model. In Figure 3.37, the matrix and aggregate strength time histories from the two analyses, one with material degradation (RDG failure model) and the other without any degradation model, are plotted. Again, these plots are for element 736 of the finite element mesh shown earlier in Figure 3.31. Since the aggregate and matrix strengths are the same in the absence of any porosity, the strength remained high (in the case without voids) as represented by the dashed line in Figure 3.37.

The deformed configurations of the penetrator and the target at time 20 microseconds are compared in Figure 3.38. The target exhibited a relatively larger bulge from enhanced plastic flow due to void softening of the material. Since the damaged target material in front of the projectile allows the projectile to penetrate more easily, the penetration process is accelerated. When there is no material degradation due to void nucleation and growth, the target material is relatively stronger and, therefore, the penetration rate is slower compared to the case in which the material degrades. The differences in the deformed target shapes and the penetration rates demonstrate the importance of an accurate dynamic failure model.

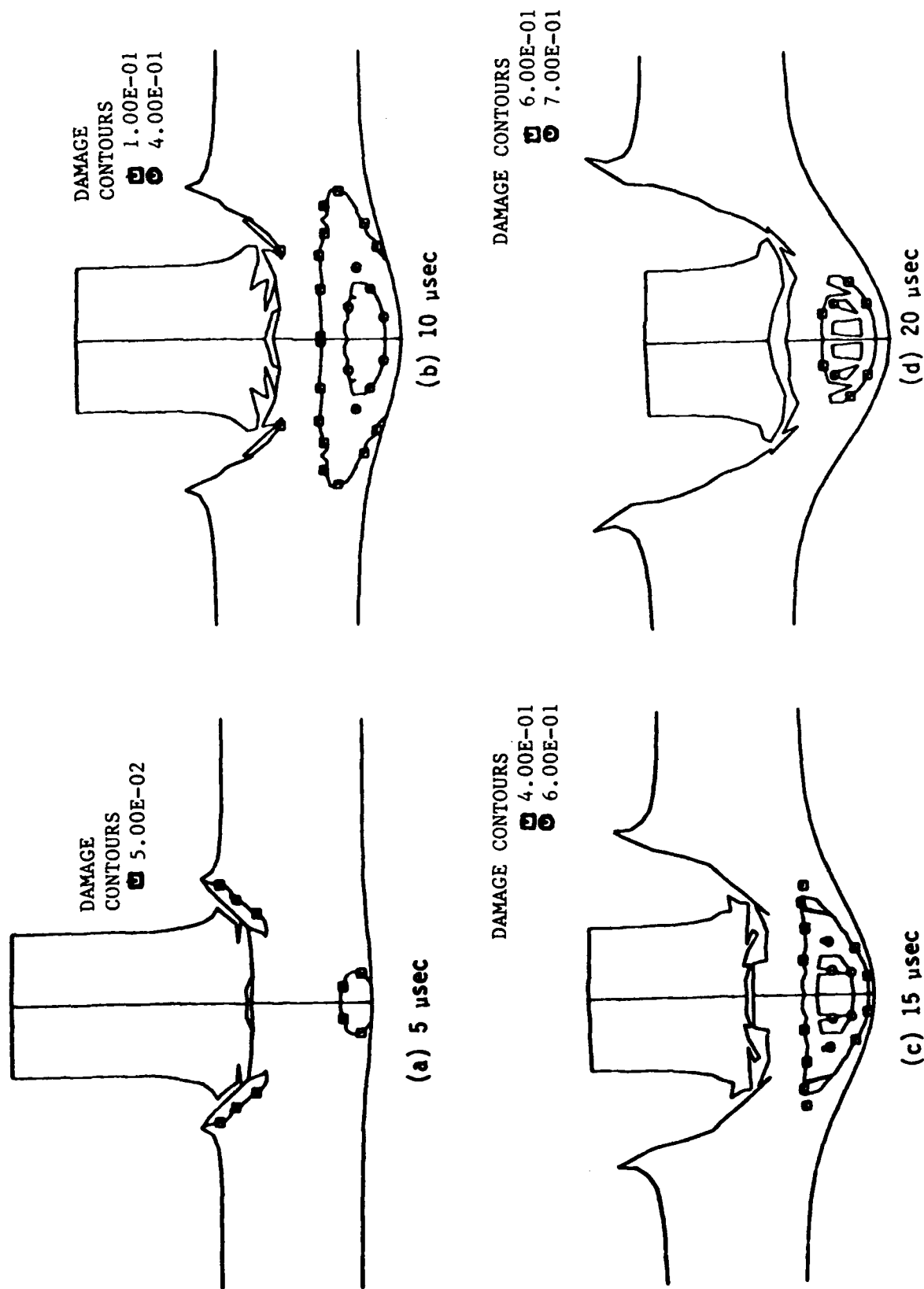


Figure 3.36. Damage Contours at Various Stages in the Rod Penetration.

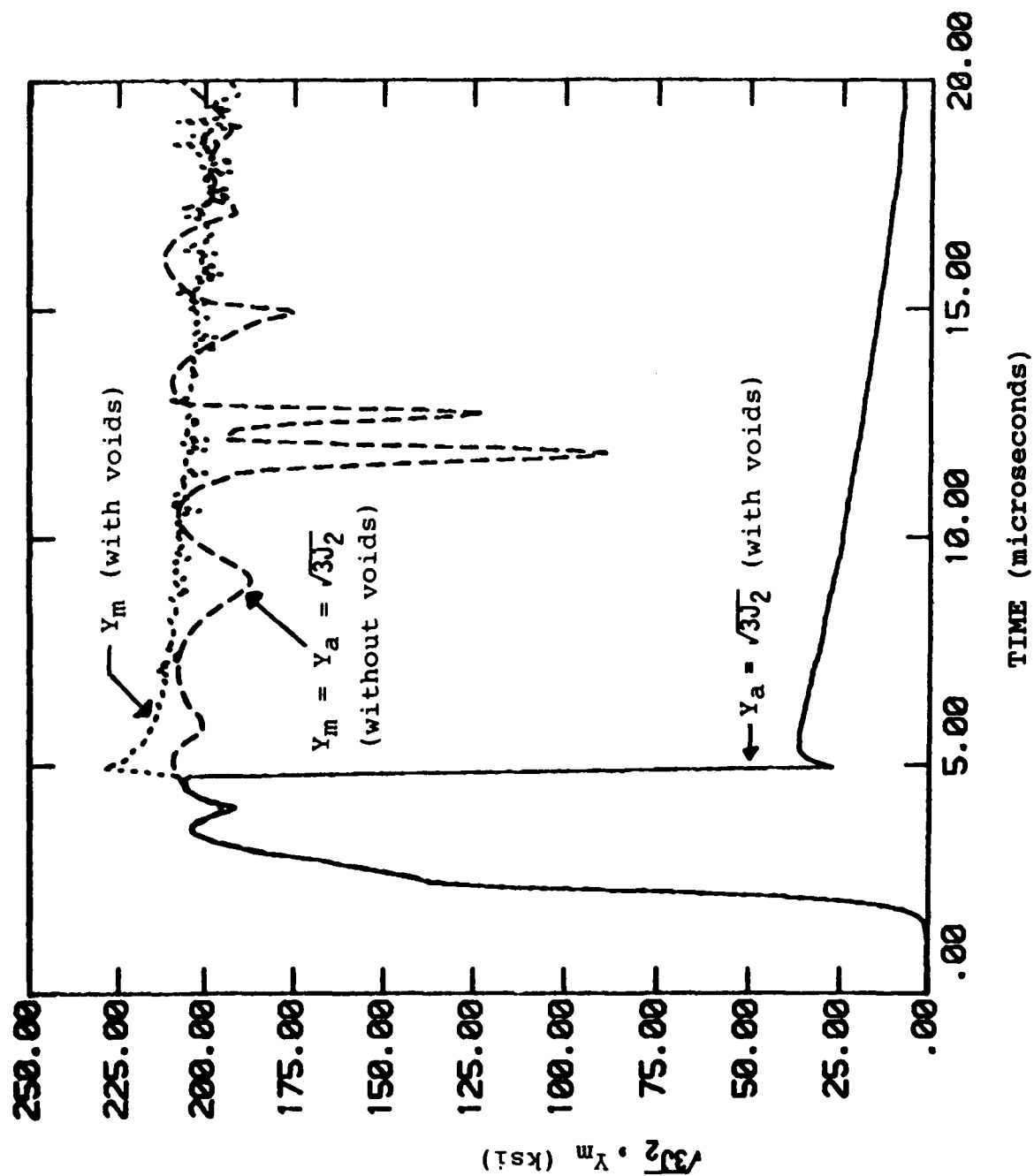


Figure 3.37. Comparison of Aggregate Yield Strengths (Y_a) with and without Voids in Element 736. Y_m is the Matrix Strength of the Void Containing Material. Note that $Y_m = Y_a$ when $f = 0$.

WITHOUT VOIDS

WITH VOIDS

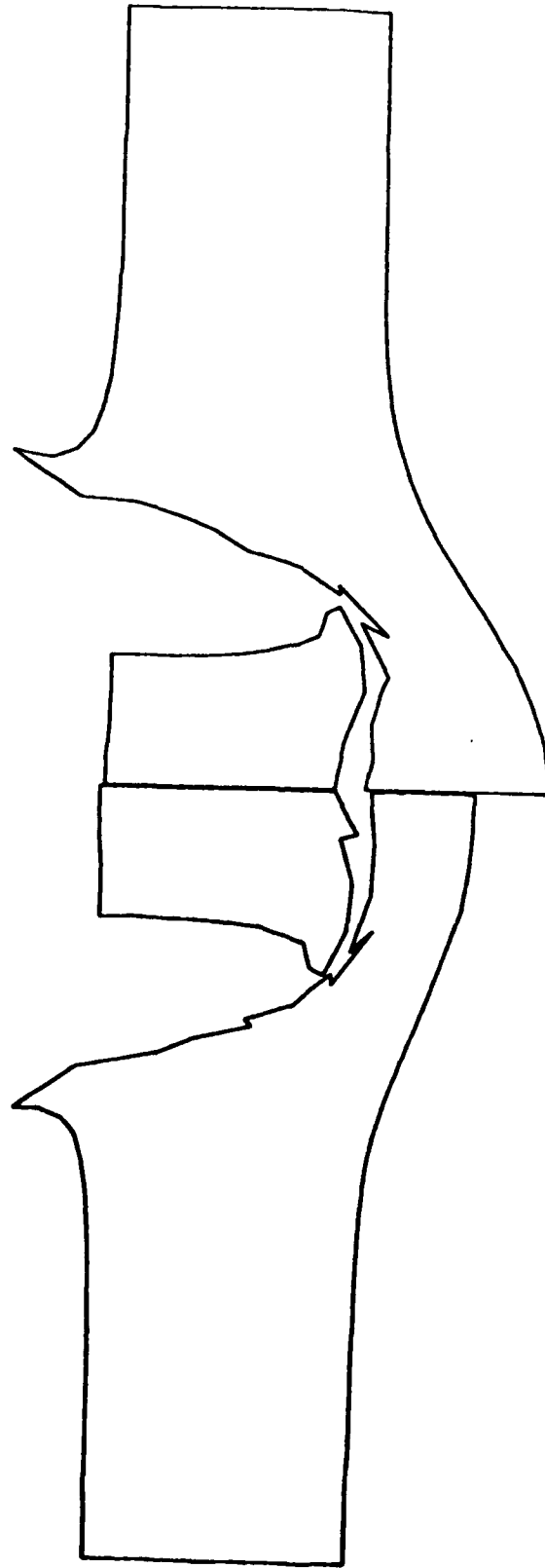


Figure 3.38. Deformed Configurations of the Rod Penetration at 20 μ sec, with and without Void Growth.

3.6.3 Spall in a Solid Cone Target

Spall under a three-dimensional strain state was modeled using the RDG ductile failure model [2,6]. Using this model, we simulated a plate impact configuration in which a flyer plate impacts the base of a solid right circular cone as schematically shown in Figure 3.39a. The main objective of this simulation was to describe spall under a three-dimensional strain state using the RDG model constants determined from a conventional plate impact experiment.

We considered an experimental configuration which involved the impact of a thin circular plate on the base of a right circular cone. The flyer plate was 2 mm thick and 38 mm in diameter, and the cone height was 25 mm. Both the flyer and target were 1020 steel. The experimentally observed spall patterns inside the cone are shown in Figure 3.39b. It can be seen that four separate fracture systems developed in the target. A one-dimensional spall-type fracture developed parallel to the cone surfaces. This fracture was apparently the first one to develop and it is first manifest at about mid-height. The second fracture system consisted of distributed cavities near the axis. The third system below mid height toward the base is roughly a cylindrical failure region about 12 mm in diameter symmetric to the cone axis. The fourth system consisted of radial cracks. This failure is believed to have occurred last, as a result of surface motion induced by wave reflection from the flanks of the cone.

The RDG model constants were calibrated by matching the computed stress history with the plate impact test data as shown earlier in Figure 3.4 for 1020 steel. The cone impact problem was simulated using the EPIC-2 code. The RDG model results showed the evolution of the experimentally observed fracture regions (patterns) as can be seen in Figure 3.40. The spall region parallel to the cone surface evolved clearly in the simulation. The model also reproduced the second region containing the distributed voids. However, the evolution and location of the cylindrical spall zone was not clear.

For further understanding of the code results, we plotted the effective plastic strain contours in Figure 3.41. These contours indicate the evolution of a cylindrical spall plane parallel to the cone's axis. To generate the (physical) spall planes in the code simulation, elements were failed according to a failure strain option in the EPIC-2 code. Using this option, elements that experienced a critical amount of effective plastic strain were removed from the finite element mesh. Figure 3.42 shows the code generated spall plane parallel to the lateral

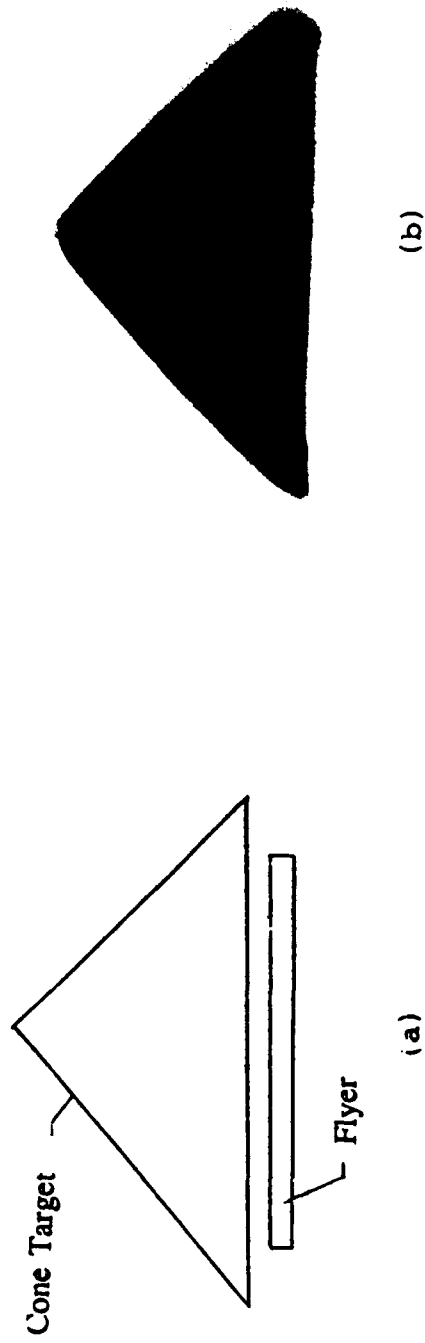


Figure 3.39. (a) Schematic Two-Dimensional Sketch of a Flyer Plate Impact on the Base of a Right Solid Cone.
(b) Recovered and Sectioned Solid Cone Revealing the Complex Spall Zones.

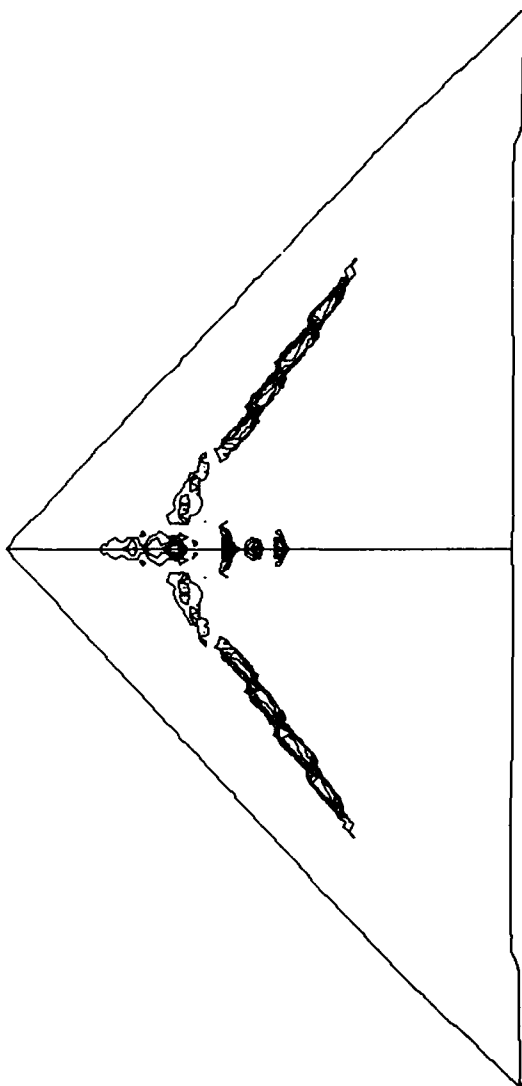


Figure 3.40. Void Contours ($\geq 10\%$) in Cone, from RDG Model Simulation.

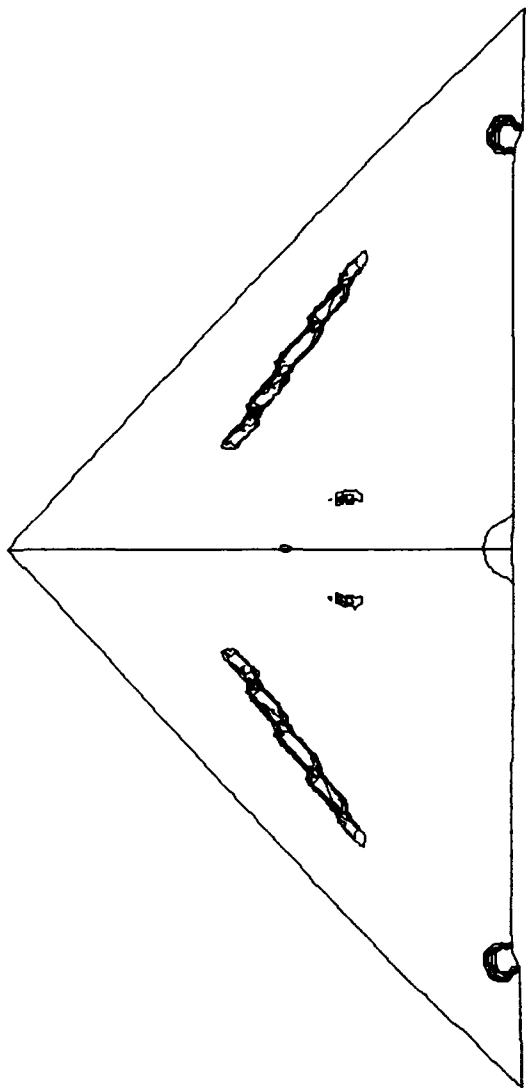


Figure 3.41. Effective Plastic Strain Contours ($\geq 10\%$) in Cone, from RDG Model Simulation.

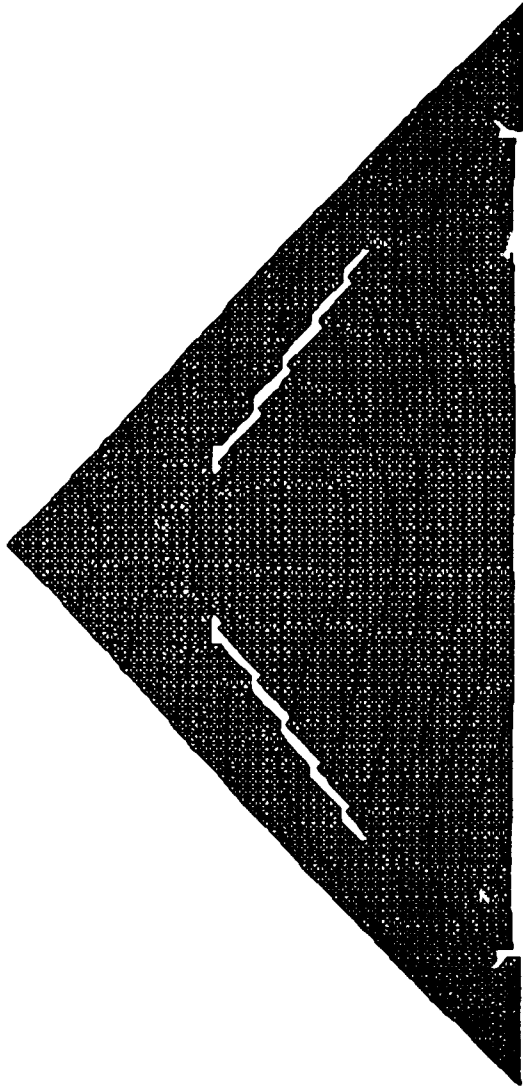


Figure 3.42. Code Generated Spall Planes in Cone, from RDG Model Simulation.

surface, which compares well with the experiment (see Figure 3.39). Even though the cylindrical spall plane did not appear in Figure 3.42, the effective plastic strain contours (Figure 3.41) confirmed the RDG model's ability to predict the development of a cylindrical spall plane. Using a smaller critical failure strain to produce the cylindrical spall plane resulted in excessive failure at the base of the cone.

As a final exercise, this simulation was performed without void nucleation and growth. Figure 3.43 shows the resulting effective plastic strain contours. Comparing Figure 3.43 with Figure 3.41, it is obvious that the void nucleation and growth process has a significant influence on the evolution of plastic strain regions inside the cone. Therefore, to successfully predict spall, it is important to use models that incorporate degradation of stiffness and strength due to void nucleation and growth.

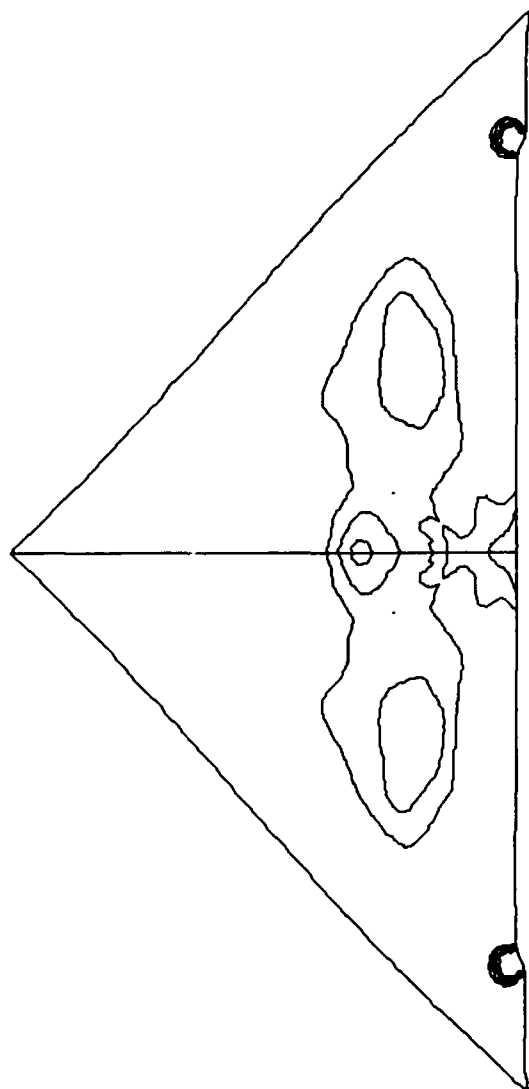


Figure 3.43. Effective Plastic Strain Contours ($\geq 10\%$) in Cone, with Void Growth Suppressed.

Section 4

Impact Damage Model for Ceramics

Ceramic materials exhibit inelastic deformation when shocked above the Hugoniot Elastic Limit (HEL). Due to lack of any strong physical evidence, it can only be speculated that the inelastic deformation is due to either plasticity (dislocations movement) or microcracking or both. The microscopic examination of particle impacted ceramic targets often reveals dislocation controlled plastic flow at the impact site. Such evidence has not been established yet in flyer plate impacted targets, especially at impact velocities above the HEL. However, in a few ceramic materials, microcracks have been observed in targets (plates) impacted below the HEL level. In 1988, Rajendran and Cook [9] summarized a literature review on the impact behavior of ceramics.

When developing the constitutive model to describe the impact behavior of ceramic materials, a microphysical based approach was chosen, instead of an empirical or phenomenological approach, because it seemed best suited for the analysis of both the microcracking and plastic processes. Typically, a microphysical model formulation begins by decomposing the strain into its elastic and inelastic components. Physically motivated equations are then used to relate the inelastic strains to underlying mechanisms such as microcracking and void opening/collapse (plasticity). Since ceramics fail at low stresses under tensile loading, inelastic strains are assumed to be strictly due to microcracking only. The inelastic strains due to dislocation motion can be described by viscoplastic equations.

In the ceramic model developed here, Margolin's equations [12] for a penny shaped crack are used to calculate the inelastic strains due to crack opening and sliding both under tension and shear loading. However, under compression, only the displacement fields due to crack sliding are considered. Therefore, crack opening under compression is not considered in the present formulation. Further, ceramic materials are assumed to contain a large number of closed microflaws and that the microcracks propagate upon shock loading. The model formulation under this assumption eliminates any nucleation model or threshold condition requirements; this

minimizes the number of model parameters. This section presents the mathematical formulation of this microphysical based model for ceramic materials.

4.1 Constitutive Equations

In the case of a ceramic containing microcracks and spherical voids, the total strain may be decomposed into elastic and plastic strains as,

$$\epsilon_{ij} = \epsilon_{ij}^e + \epsilon_{ij}^p \quad , \quad (14)$$

where the elastic strain consists of the matrix elastic strain, the microcrack opening strain, and the elastic strain of the embedded spherical voids,

$$\epsilon_{ij}^e = \epsilon_{ij}^m + \epsilon_{ij}^c + \epsilon_{ij}^v \quad . \quad (15)$$

The matrix elastic strain ϵ_{ij}^m and the microcrack opening strain ϵ_{ij}^c are both proportional to the applied stress field. By definition, the total elastic strains of the spherical voids ϵ_{ij}^v can be expressed as,

$$\epsilon_{ij}^v = e_{ij}^v + \frac{\epsilon_v^v}{3} \delta_{ij} \quad (16)$$

where e_{ij}^v are the elastic deviatoric strains and ϵ_v^v is the elastic volumetric strain associated with the voids. These strains can be defined, using Mackenzie's equations [30], as

$$\epsilon_v^v = \epsilon_v^e - R_k \epsilon_v^e \quad (17)$$

and

$$e_{ij}^v = e_{ij}^e - R_g e_{ij}^e \quad (18)$$

where

$$R_k = \frac{(1-f)}{\left(1 + \frac{3\bar{K}f}{4G}\right)} \quad (19)$$

and

$$R_g = (1 - f) \left(1 - \frac{(6\bar{K} + 12\bar{G})f}{9K + 8G} \right). \quad (20)$$

\bar{K} is the bulk modulus and \bar{G} is the shear modulus of the microcracked material without spherical voids, and f is the void volume fraction related to the amount of volumetric plastic strain. Using Equations (14) through (18), the elastic strains in the cracked "matrix" material may be expressed as,

$$e_v^m + e_v^c = R_k e_v^e = R_k (e_v - e_v^p) \quad (21)$$

and

$$e_{ij}^m + e_{ij}^c = R_g e_{ij}^e = R_g (e_{ij} - e_{ij}^p), \quad (22)$$

where $e_v^p = e_{ii}^p$ and $e_{ij}^p = (e_{ij}^p - e_v^p/3)$ by definition.

A pressure dependent yield function to define plastic flow in the ceramic material is employed. This yield function has an implicit analytic form,

$$\Phi(f, Y_m, \sigma_{ij}) = 0 \quad (23)$$

where f is the void volume fraction, Y_m is the flow stress in the matrix (intact) material, and σ_{ij} are the total stresses. The total plastic strain rates are given by:

$$\dot{e}_{ij}^p = \frac{(1-f) Y_m \dot{D}_m^p \frac{\partial \Phi}{\partial \sigma_{ij}}}{\sigma_{r1} \frac{\partial \Phi}{\partial \sigma_{r1}}} \quad (24)$$

where

$$f = 1 - \exp(-e_v^p) \quad (25)$$

$$\dot{W}_m^p = Y_m \dot{D}_m^p \quad (26)$$

and

$$\dot{D}_m^P = g (Y_m, D_m^P, W_m^P) \quad . \quad (27)$$

In the above equations, Y_m , W_m^P , and D_m^P represent flow stress, plastic work, and equivalent plastic strain, respectively, in the matrix (void-free) material. The value of Y_m is obtained by solving Equation (23), using estimated values of the void volume fraction and the stresses. The plastic strains are obtained from the numerical integration of Equation (24). Equation (25) defines the relationship between the void volume fraction f and the volumetric plastic strain e_v^P . Equation (26) defines the plastic work rate, and Equation (27) is the flow rule for the yield function; either the Johnson-Cook or the Bodner-Partom model can be selected. The details of the Equations (23) through (27) can be found in Appendix C.

To implement the constitutive model in a hydrodynamic code, the stress tensor must be expressed as a direct function of the total strain tensor. First, assume that the elastic strains in the microcracked "matrix" (void-free) material are related to the stress tensor as follows:

$$e_{ij}^m + e_{ij}^c = C_{ijkl} \sigma_{kl} \quad (28)$$

where C_{ijkl} is the effective compliance tensor of the microcracked material. If C_{ijkl} can be analytically inverted to the stiffness tensor M_{ijkl} , the resulting stress state is,

$$\sigma_{ij} = M_{ijkl} (e_{kl}^m + e_{kl}^c) \quad (29)$$

Assuming that the stiffness tensor is isotropic, Equation (29) can be decomposed by standard procedures into pressure and deviatoric stress expressions:

$$P = -\bar{K} (e_v^m + e_v^c) \quad (30)$$

and

$$S_{ij} = 2 \bar{G} (e_{ij}^m + e_{ij}^c) \quad . \quad (31)$$

Substituting Equations (21) and (22) into Equations (30) and (31),

$$P = -R_k \bar{K} (e_v - e_v^P) \quad (32)$$

and

$$S_{ij} = 2 R_g \bar{G} (e_{ij} - e_{ij}^p) . \quad (33)$$

Recall that the total plastic strains are available from Equation (24). The form of Equation (32) suggests that the Hugoniot equation of state in the microcracked void-free material can be approximated by,

$$\bar{P}_H = (\bar{K} / K) P_H \quad (34)$$

where

$$P_H = \beta_1 \mu + \beta_2 \mu^2 + \beta_3 \mu^3 \quad (35)$$

and

$$\mu = \exp [- (\epsilon_v - \epsilon_v^p)] - 1 . \quad (36)$$

Equation (36) defines the elastic compressibility μ as a function of the true elastic volumetric strain. The Mie-Gruneisen adjustment for the shock jump condition within the microcracked material leads to the following equation of state:

$$P = R_k [\bar{P}_H (1 - 0.5 \Gamma \mu) + \Gamma \rho_o (I - I_o)] \quad (37)$$

where Γ is the Mie-Gruneisen parameter, ρ_o is the material's initial density, I_o is the initial value of internal energy, and I is the current internal energy. Note that Equation (37) incorporates Mackenzie's adjustment factor R_k for non-zero values of f . If Γ is zero and the elastic compressibility μ is negligible, Equation (37) reduces to Equation (32). Similarly, if there are no microcracks or voids, Equation (37) reduces to the usual Mie-Gruneisen equation of state for an undamaged, flawless material. The appearance of the internal energy term in Equation (37) requires the numerical integration of the internal energy rate,

$$\rho_o \dot{I} = \frac{-P \dot{\epsilon}_v + S_{ij} \dot{e}_{ij}}{1 + \mu} \quad (38)$$

4.2 Damaged Stiffness Tensor

It is essential that the damaged compliance tensor be analytically invertible for practical use of the model in explicit hydrodynamic codes. This requirement of analytical formulae for the damaged stiffness tensor M_{ijkl} permits only isotropic or orthotropic forms of C_{ijkl} . Because of this, the present ceramic model formulation adopts the elastic moduli of a cracked body proposed by Margolin [12] and by Budiansky and O'Connell [42]. Both of these formulations lead to effective compliance tensors that are isotropic.

For non-interacting, penny-shaped microcracks of various sizes and in random orientations, Margolin provided the following expression for the isotropic elastic moduli:

$$C_{ijkl} = c_1 \delta_{ik} \delta_{jl} + c_2 \delta_{il} \delta_{jk} + c_3 \delta_{ij} \delta_{kl} \quad (39)$$

where

$$c_1 = B_o + \frac{1}{4G} \quad , \quad (40)$$

$$c_2 = D_o + \frac{1}{4G} \quad , \quad (41)$$

and

$$c_3 = A_o - \frac{\nu}{2(1+\nu)G} \quad . \quad (42)$$

In the above equations, G and ν are the shear modulus and Poisson's ratio, respectively, of the undamaged material, while A_o , B_o , and D_o are damage parameters whose values depend on the stress state. To evaluate these parameters, Margolin defined a microcrack density parameter,

$$\gamma^* = \frac{16\gamma}{45E} \quad , \quad (43)$$

where

$$\gamma = \int_0^{a_{\max}} \left(\frac{N_o}{a} \right) \exp\left(-\frac{a}{a}\right) a^3 da = N_o^* a_{\max}^3 \quad . \quad (44)$$

In Equation (43), γ is the microcrack density and E is the Young's modulus of the undamaged material. Equation (44) is the expression for microcrack density that results from assuming an exponential size distribution of microcracks. N_o is the number of microcracks per unit volume, \bar{a} is the average microcrack size, and a_{\max} is the maximum microcrack size in the distribution. Margolin identified the following four cases of stress state in evaluating the damage parameters A_o , B_o , and D_o :

Case 1: $\sigma_1, \bar{\sigma}_2, \bar{\sigma}_3 > 0$

(all principal stresses are tensile)

$$A_o = [(1 - \nu^2) - (1 + \nu)] \gamma^* \quad (45)$$

$$B_o = [(1 - \nu^2) + 4(1 + \nu)] \gamma^* \quad (46)$$

$$D_o = A_o \quad (47)$$

Case 2: $\bar{\sigma}_1, \bar{\sigma}_2, \bar{\sigma}_3 < 0$

(all principal stresses are compressive)

$$A_o = -(1 + \nu) \gamma^* \quad (48)$$

$$B_o = 4(1 + \nu) \gamma^* \quad (49)$$

$$D_o = A_o \quad (50)$$

Equations (48) through (50) will result in the degradation of the shear modulus, but not of the bulk modulus, because under compression only crack movement of the closed microcracks under modes II and III are permitted.

Case 3: $\bar{\sigma}_1, \bar{\sigma}_2 > 0, \bar{\sigma}_3 < 0$

(two principal stresses are tensile, and one principal stress is compressive)

$$A_o = \left[\frac{(5\beta^3 - 3\beta^5)}{2} (1 - \nu^2) - (1 + \nu) \right] \gamma^* \quad (51)$$

$$B_o = \left[\frac{(5\beta^3 - 3\beta^5)}{2} (1 - \nu^2) + 4(1 + \nu) \right] \gamma^* \quad (52)$$

$$D_o = [(6\beta^5 - 5\beta^3) (1 - \nu^2) - (1 + \nu)] \gamma^* \quad (53)$$

where

$$\beta \approx \sqrt{\frac{\bar{\sigma}_1 + \bar{\sigma}_2}{\bar{\sigma}_1 + \bar{\sigma}_2 - 2\bar{\sigma}_3}} \quad (54)$$

Equation (54) is an approximation to Margolin's numerical evaluation of the integral over solid angles (Equation 6.3 in Margolin [12]), assuming an averaged portion of the solid angle is under tensile stress.

Case 4: $\bar{\sigma}_1 > 0, \bar{\sigma}_2, \bar{\sigma}_3 < 0$

(one principal stress is tensile, and two principal stresses are compressive)

$$A_o = \left[\frac{5(1 - \beta^3) - 3(1 - \beta^5)}{2} (1 - \nu^2) - (1 + \nu) \right] \gamma^* \quad (55)$$

$$B_o = \left[\frac{5(1 - \beta^3) - 3(1 - \beta^5)}{2} (1 - \nu^2) + 4(1 + \nu) \right] \gamma^* \quad (56)$$

$$D_o = \{ [6(1 - \beta^5) - 5(1 - \beta^3)] (1 - \nu^2) - (1 + \nu) \} \gamma^* \quad (57)$$

where

$$\beta \approx \sqrt{\frac{\bar{\sigma}_2 + \bar{\sigma}_3}{\sigma_2 + \sigma_3 - 2\sigma_1}} \quad (58)$$

As in Case 3, Equation (58) is an approximation to the numerical solution of the integral over solid angles.

Next, the elements of the stiffness tensor are solved from

$$M_{ijkl} C_{ijkl} = \frac{(\delta_{ik} \delta_{jl} + \delta_{il} \delta_{jk})}{2} \quad (59)$$

with the result

$$M_{ijkl} = m_1 \delta_{ik} \delta_{jl} + m_2 \delta_{il} \delta_{jk} + m_3 \delta_{ij} \delta_{kl} \quad (60)$$

where

$$m_1 = m_2 = \frac{1}{2(c_1 + c_2)} \quad (61)$$

and

$$m_3 = \frac{-c_3}{(c_1 + c_2)(c_1 + c_2 + 3c_3)} \quad (62)$$

The degraded shear and bulk moduli are then given by

$$\bar{G} = m_1 \quad (63)$$

and

$$\bar{K} = m_3 + \frac{2}{3}m_1 \quad (64)$$

Budiansky and O'Connell [42] considered the case where microcracks are randomly oriented, interacting, self-consistent, and subjected to tensile loading. Relating their results to Equation (60), the damaged stiffness tensor solution is given as:

$$m_1 = m_2 = \bar{G} \quad , \quad (65)$$

$$m_3 = \frac{2 \bar{G} \bar{\nu}}{(1 - 2\bar{\nu})} \quad , \quad (66)$$

where

$$\bar{\nu} = \nu \left(1 - \frac{16}{9} \gamma \right) \quad , \quad (67)$$

and

$$\bar{G} = G \left\{ 1 - \left(\frac{32}{45} \right) \frac{(1 - \bar{\nu})(5 - \bar{\nu})}{(2 - \bar{\nu})} \gamma \right\} \quad . \quad (68)$$

In these equations, $\bar{\nu}$ and \bar{G} are the Poisson's ratio and shear modulus, respectively, of the microcrack damaged material. Using m_1 and m_3 from Equations (65) and (66), the degraded bulk modulus can be computed from Equation (64). It is obvious from Equations (65) through (68) that a complete loss of strength is predicted when the microcrack density γ reaches 9/16. For tensile loading conditions, based on comparisons with more detailed models (Nemat-Nasser and Obata [43]), as well as in Margolin's approach, there is no bound on the crack density. However, Budiansky and O'Connell's solution limits the crack density to 9/16. This permits the damage parameter to vary from zero (no damage) to one (fully damaged). Therefore, in the ceramic model, Budiansky and O'Connell's equations are used instead of Margolin's equations for the case when all the principal stresses are positive (Case 1).

4.3 Microcrack Damage Evolution

The microcrack growth mechanism is analyzed using a dynamic linear fracture mechanics theory. This mechanism consists of: (1) nucleating microcracks when the stress state satisfies a generalized Griffith criterion, (2) propagating the cracks at a crack tip speed which is a function of stress intensity factor, and (3) modeling coalescence of the microcracks at some critical crack size. The three stages of microcrack damage (nucleation, growth, and coalescence) occur at

different times within a given elemental volume. Since current experimental diagnostics are incapable of resolving these stages of microcrack damage, incorporating this process into a constitutive theory becomes a challenging task.

4.3.1 Microcrack Nucleation

In brittle materials, such as ceramics, a microcrack starts to grow when the stress field at the crack tip satisfies Griffith's criterion [44]. If the microcracks in a given material have an exponential crack size distribution, then the various microcracks begin to grow at different times as the stress levels increase. At low enough strain rates, the largest microcrack begins to grow first, causing stress relaxation in other zones, thus preventing other microcracks from growing. In dynamic plate impact situations, the strain rates are of order $10^3/\text{sec}$ and higher. At such high strain rates, since the crack tip speed is limited to the Rayleigh velocity, significant stress relaxation will not occur until nearly all the microcracks have begun to propagate. In addition, with the stress intensity factors becoming much higher than the critical value in a very short time, multiple crack branching will occur. Modeling the details of these processes would be an extremely difficult task.

Our simplified approach is the following. Microcracks are considered nucleated (actively growing) when the stress state is such that Griffith's criterion is satisfied for the largest characteristic microcrack. All smaller microcracks are then assumed to propagate at appropriate rates that maintain an exponential size distribution of microcracks (in random orientation). These assumptions permit a straightforward application of linear fracture mechanics concepts with some caveats. For example, because it is endowed with a statistical property, the characteristic microcrack size in the model may not correspond to the true microcrack size in the ceramic. Also, since the actual microcrack size distribution might not fit an exponential distribution, a bias can occur in the characteristic crack size. If the microcracks are oriented in preferred directions, the assumption of randomly oriented cracks could introduce a bias to the damaged moduli. There is the additional problem of examining all crack orientations to determine the highest stress intensity factor (or crack energy release rate) for nucleating the microcracks. All these modeling ambiguities are tolerable when weighed against the requirement to develop analytically tractable solutions for microcrack damage evolution.

To model microcrack nucleation, a generalized Griffith criterion developed by Margolin [12] and Dienes [45] is used for any given crack orientation. For crack surfaces perpendicular to **tensile** normal stresses $\bar{\sigma}_{kk}$, the crack energy release rate for mode I crack opening is

$$G^+ = \frac{4(1-\nu^2)}{\pi E} a_{\max} \left[\bar{\sigma}_{kk}^2 + \frac{2(\bar{\sigma}_{ik}^2 + \bar{\sigma}_{jk}^2)}{2-\nu} \right], \quad i \neq j \neq k \quad (69)$$

where a_{\max} is the size of the largest microcrack, and ν and E are Poisson's ratio and Young's modulus, respectively, in the undamaged material. The repeated index 'k' does not mean summation. The bar over the stress components means stresses in the cracked material. When the crack surfaces are perpendicular to tensile principal stresses $\bar{\sigma}_1$, then Equation (69) is evaluated with $\bar{\sigma}_{kk} = \bar{\sigma}_1$ and $\bar{\sigma}_{ik} = \bar{\sigma}_{jk} = 0$. For crack surfaces perpendicular to **compressive** normal stresses $\bar{\sigma}_{kk}$, Dienes derived the crack energy release rate as

$$G^- = \frac{8(1-\nu^2)}{\pi E(2-\nu)} a_{\max} \left[\sqrt{\bar{\sigma}_{ik}^2 + \bar{\sigma}_{jk}^2} - \tau_o + \omega \bar{\sigma}_{kk} \right]^2, \quad i \neq j \neq k \quad (70)$$

where τ_o is the cohesion stress and ω is the friction coefficient. In this case, only modes II and III are active and the normal stresses serve only to resist the shearing stresses. Defining G_{\max} to be the maximum of all values of G^+ and G^- , microcracks are assumed to have nucleated if G_{\max} exceeds the critical crack energy release rate G_c , where

$$G_c = 2T \quad (71)$$

and

$$T = \frac{K_{IC}^2(1-\nu^2)}{2E} \quad (72)$$

Equation (72) defines the surface tension T as a function of the static fracture toughness (K_{IC}), Poisson's ratio (ν), and Young's modulus (E) in the undamaged material. Note that all three modes of crack opening are considered in this approach.

4.3.2 Microcrack Growth

From the theory of dynamic fracture mechanics [46], the classical solution for the dynamic energy release rate under mode I conditions, G_I , is given by the formula,

$$\frac{\dot{a}}{C_R} = 1 - \frac{G_c}{G_I} \quad (73)$$

where \dot{a} is the microcrack growth rate. C_R is the Rayleigh wave speed, and G_c is the critical crack energy release rate, as defined by Equations (71) and (72). In generalizing Equation (73) for all three modes of microcrack growth, empirical constants to control the limiting crack tip speed were introduced. This also allows a nonlinear dependence on the crack energy release rate. The newly proposed microcrack growth evolution equation is defined as

$$\dot{a}_{\max} = \begin{cases} 0, & G_{\max}^+ \leq G_c \text{ and } G_{\max}^- \leq G_c \\ n_1^+ C_R \left[1 - \left(\frac{G_c}{G_{\max}^+} \right)^{n_2^+} \right], & G_{\max}^+ > G_c \\ n_1^- C_R \left[1 - \left(\frac{G_c}{G_{\max}^-} \right)^{n_2^-} \right], & G_{\max}^+ \leq G_c \text{ and } G_{\max}^- > G_c \end{cases} \quad (74)$$

where G_{\max}^+ is the maximum G^+ calculated from Equation (69) and G_{\max}^- is the maximum G^- calculated from Equation (70). Two distinct sets of microcrack growth constants, one for mode I crack opening (n_1^+ and n_2^+) and one for modes II and III (n_1^- and n_2^-) are considered. The n_1^+ and n_1^- coefficients directly control the limiting crack growth rates for the different modes of crack opening, while the n_2^+ and n_2^- exponents serve to inhibit crack growth during the initial phase. Small positive values ($\ll 1$) of n_2^+ and n_2^- will effectively delay microcrack growth until the critical crack energy release rate G_c has been significantly exceeded. Second order effects on the microcrack growth, such as toughening and crack interactions, are ignored in the model. The microcrack growth rate is ultimately a function of the current stress state and maximum microcrack size. Therefore, the microcrack damage evolution is obtained from the numerical

integration of Equation (74) and the evaluation of the crack density function from Equation (44). Since the damage evolution itself degrades the moduli, the stress levels will relax as the microcracks grow, possibly enough to arrest the crack growth. In some cases, however, the stress relaxation will be gradual enough to result in microcrack coalescence before crack growth arrest can occur.

4.3.3 Microcrack Coalescence

Microcrack coalescence occurs when propagating microcracks intersect each other to the point of pulverization and significant loss of strength. Based on this definition, a reasonable pulverization criterion can readily be derived as follows. If N_o is the number of microcracks per unit volume, then the average spacing between cracks is obtained by inverting Equation (44), i.e.

$$d = N_o^{-\frac{1}{3}} \quad (75)$$

If \bar{a} is the average crack radius, pulverization can be expected to occur when this radius reaches half the average spacing, or

$$\bar{a}_p = \frac{d}{2} \quad (76)$$

This coalescence condition defines a critical value for the microcrack density function as follows. Assuming that the constant ratio $\frac{a_{max}}{\bar{a}}$ is much larger than unity and all the flaws have been transformed to penny shaped microcracks, then a reevaluation of Equation (44) results in the following approximation for γ :

$$\gamma = N_o^* a_{max}^3 \approx 6 N_o \bar{a}^3 \quad (77)$$

Substitution of Equations (75) and (76) into Equation (77) provides the following definition of pulverization in terms of microcrack density:

$$\gamma_p = \frac{3}{4} \quad (78)$$

This criterion is introduced into the ceramic model because Margolin's formulae for the damaged moduli does not include the effects of microcrack interactions. The material is considered to be pulverized when Equation (78) is satisfied ($\gamma \geq \gamma_p$) during a stress state in which at least one of the principal stresses is compressive (Cases 2, 3, or 4 from Section 4.2). At this time, the pulverized bulk and shear moduli, \bar{K}_p and \bar{G}_p , are defined to be the current values of \bar{K} and \bar{G} computed from Equations (63) and (64). Henceforth, the material has no strength in tension, and its compressive strength follows a Mohr-Coulomb law, as in

$$Y = \begin{cases} 0, & P \leq 0 \\ \alpha_p + \beta_p P, & P > 0 \end{cases} \quad (79)$$

where Y is strength, P is pressure, and α_p and β_p are model constants for the pulverized material. The pressure is computed simply from

$$P = \begin{cases} 0, & \epsilon_v^e \geq 0 \\ -\bar{K}_p \epsilon_v^e, & \epsilon_v^e < 0 \end{cases} \quad (80)$$

where ϵ_v^e is engineering elastic volumetric strain and \bar{K}_p is the pulverized bulk modulus. With this approach, each pulverized element in a finite element mesh may have its own distinct values for \bar{K}_p and \bar{G}_p .

4.4 Numerical Solutions of Equations

4.4.1 Uniaxial Stress

A PC based computer program to solve the governing equations under one-dimensional stress conditions was developed. This program generates stress-strain plots for arbitrary strain rate and confining pressure histories. A diagonally implicit Runge-Kutta (DIRK) numerical scheme described in Appendix D was used for the solution of three-dimensional constitutive equations under uniaxial stress conditions. The uniaxial responses of AD-85 ceramic to different strain rates and confining pressures were generated. The porous AD-85 ceramic was analyzed using the proposed ceramic model. The compressive stress-strain curves generated by this model are shown in Figure 4.1. This figure shows the effects of both strain rate and confining pressure. The stress-strain curves that correspond to strain rates of 100 and 2000/sec. exhibit non-linear

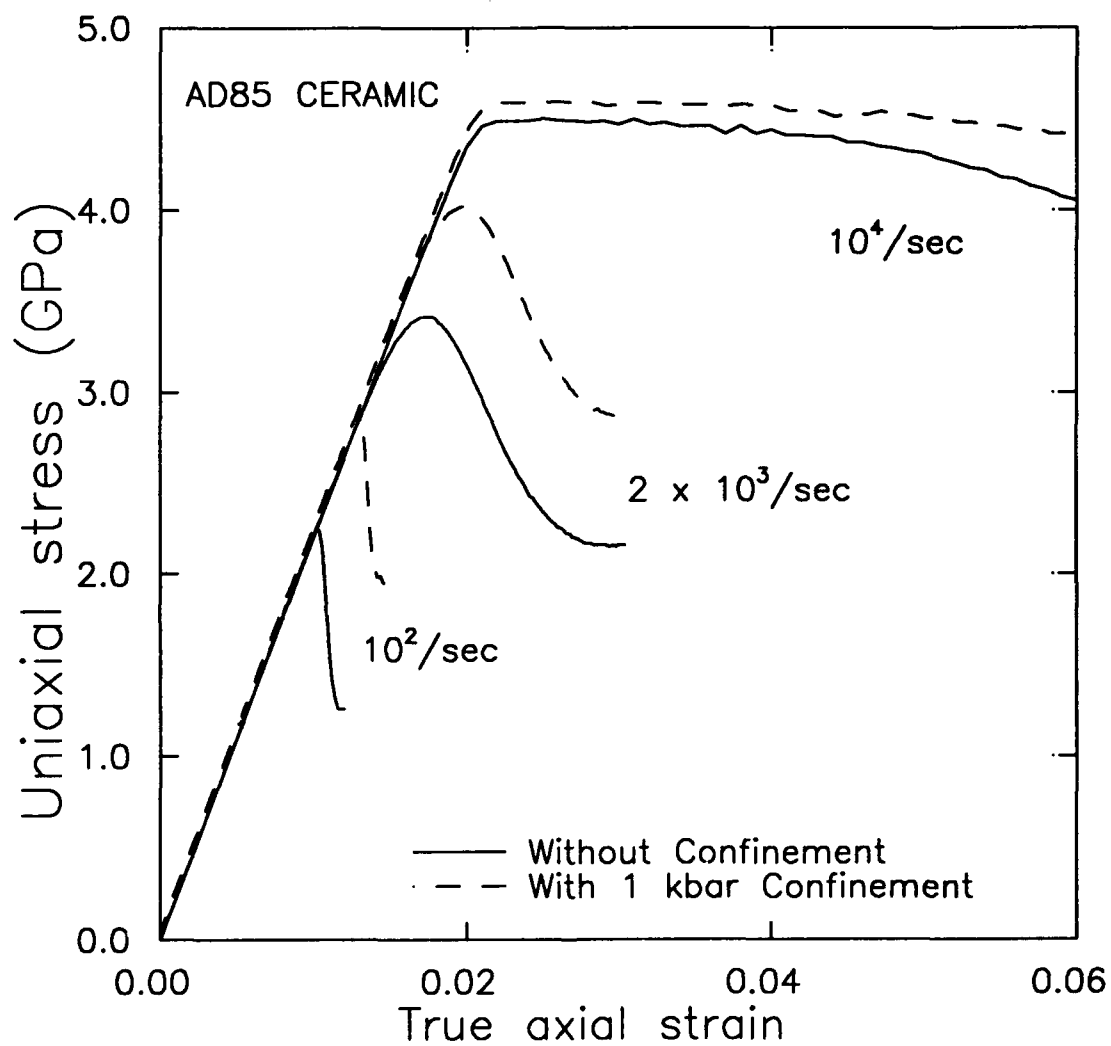


Figure 4.1. Stress-Strain Curves for AD-85 Ceramic at Different Strain Rates and Confining Pressures.

behavior that is due to cracking under compression. At extremely high strain rates, the stress increases sufficiently to satisfy the yield criterion and the behavior becomes dominated by plastic flow. The transition from brittle to ductile behavior as a function of strain rate is illustrated in Figure 4.2. The strength enhancement resulting from increasing strain rates is due to the limiting crack velocity (beginning at a strain rate of about 100/sec.). If viscoplastic flow is suppressed, the strength continues to increase rapidly with strain rate as shown by the solid curve in the figure. When viscoplastic flow is included, the peak stress cannot exceed the flow strength and microcracking becomes less important. Figure 4.3 illustrates the transition from brittle to ductile behavior as a function of confining pressure. Initially, increased confining pressure delays the onset of shear cracking and the strength gradually increases as shown in the figure. This trend continues until the stress state reaches a threshold value for viscoplastic pore collapse. Once this value is attained, the strength becomes more dependent on the viscoplastic properties than the cracking properties.

Figure 4.3 also includes data obtained from uniaxial stress (confined and unconfined) and uniaxial strain experiments. As shown in the figure, the variation of strength as a function of pressure is successfully modeled using the microphysical model. These results are described in detail in Reference [47].

4.4.2 Plate Impact Simulation

In the analysis, plate impact experimental data were used to calibrate the model constants for AD-85 Alumina and for Titanium Diboride [48]. In these experiments, either the velocity history was recorded using a velocity interferometer (VISAR) or the stress history at the interface of the target and back-up PMMA was recorded using a manganin stress gauge. When a flyer plate impacts a target plate at low velocities, fracture is induced in the target by the tension arising from the interaction of reflected waves from the stress-free planes. This interaction leads to growth and coalescence of microcracks, thus spalling the target. At high impact speeds, the damage growth during the initial compression of the target alters the subsequent spallation process.

We considered three different experiments for calibrating and validating the model constants. In the first experiment, the target was AD-85 Alumina and the impact velocity was 570 m/s, which is above the HEL. Upon this high velocity impact, the shock stress in the target

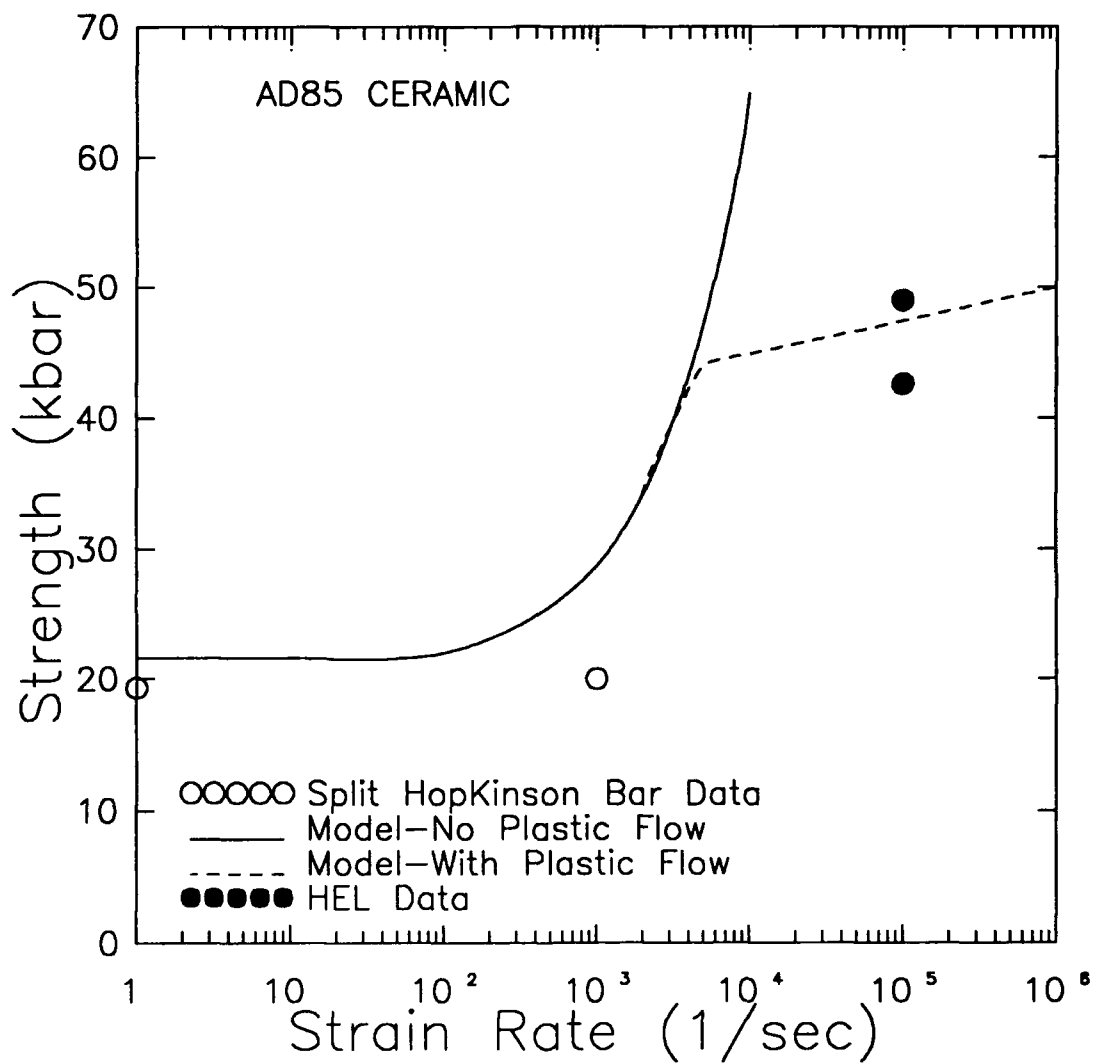


Figure 4.2. Effects of Dynamic Cracking and Viscoplastic Flow on the Compressive Strength of AD-85.

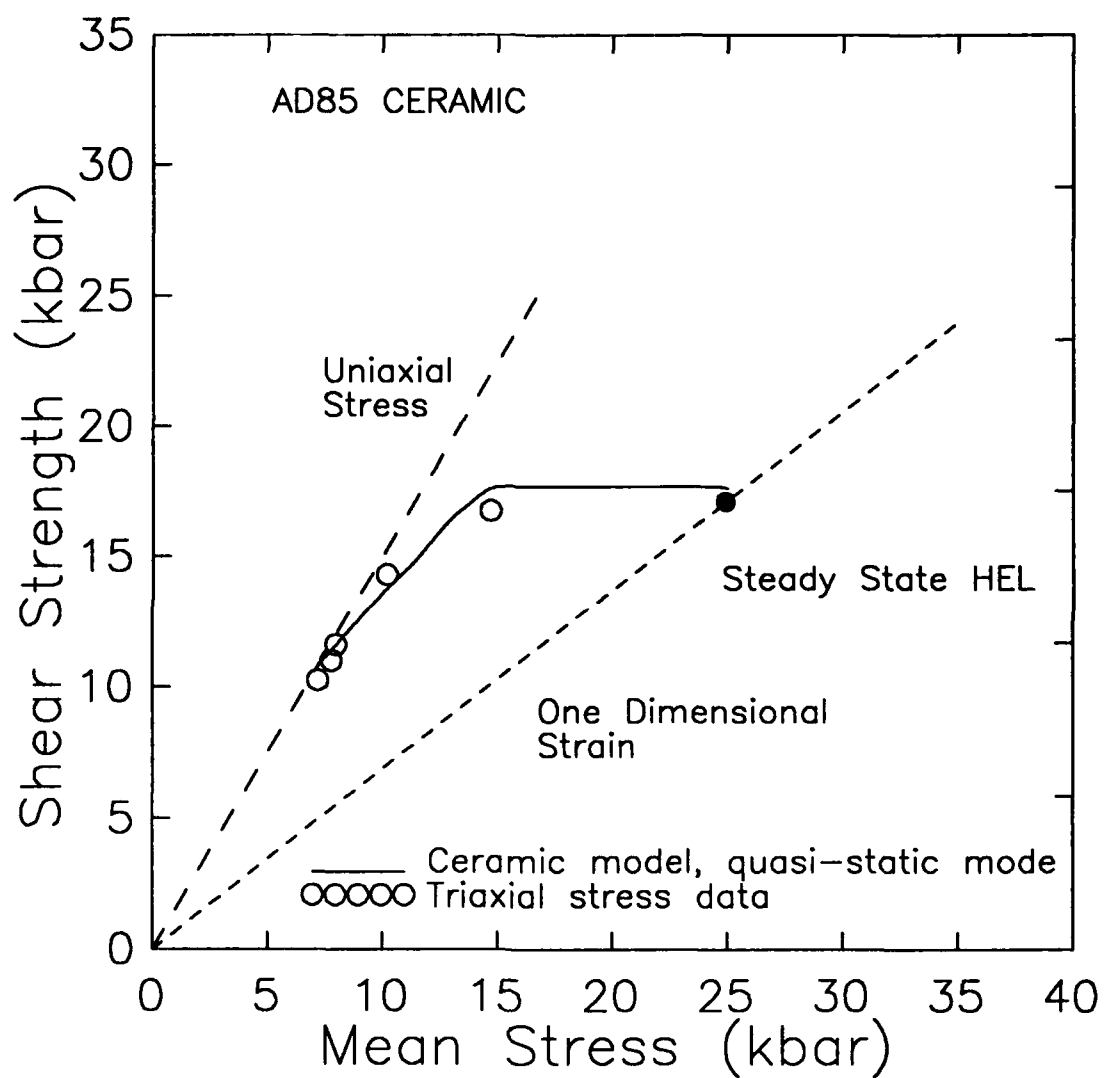


Figure 4.3. Effect of Confining Pressure on Strength of AD-85.

exceeded the Hugoniot elastic limit (HEL) and the corresponding stress signal exhibited a ramping 'plastic' wave as shown in Figure 4.4. Due to lack of any physical evidence, we can only speculate that either pore crushing or strain rate dependent plastic flow could generate such a ramping wave. Pore crushing will lead to randomly oriented microcracks during the initial compression. The EOS and compressive strength constants were obtained from Yaziv [34] and were corrected for the 10% voids in AD-85 with the Mackenzie formulae. Figure 4.4 shows the fit to the data that was achieved with the calibrated model constants. Upon tensile loading, the microcracks in all orientations are sufficiently large to satisfy the Griffith criterion almost simultaneously. This leads to isotropic damaged moduli behavior and rapid microcrack growth to a pulverized state. The model predicted an almost complete pulverization of the target plate by 4 μ s, as verified by post shock observations.

In the second experiment, a double flyer plate impacted an AD-85 Alumina target at a lower velocity of 293 m/s. This impact generated shock stresses well below the HEL. The VISAR data, shown in Figure 4.5, shows a spall signal after the arrival of the release wave, and then a recompaction wave signal from the second flyer. With the isotropic microcrack option we could match the spall signal but could not fit the subsequent recompaction signal. A few simulations with this option indicated that it was not possible to match the entire gauge signal over a wide range of model parameters. The isotropic damage model overpredicted the damage level in the target at velocities below the HEL. However, using a model option in which cracks are allowed to coalesce along the perpendicular to the shock wave propagation direction, we achieved matching of the double flyer plate impact experimental data as shown in Figure 4.5.

The third experiment was a flyer impact on a TiB_2 target plate at a velocity of 719 m/s. The manganin gauge stress history is compared with the simulation results in Figure 4.6. The experiment shows a descending compressive stress as a function of time and then a fairly level spall signal. The growth of randomly oriented microcracks in the non-porous TiB_2 ceramic during both compression and tension is postulated to explain the trend in the data. A fairly good fit was obtained by using the isotropic microcracking option. The Griffith criterion parameters were set close to zero to initiate crack growth upon arrival of the shock wave.

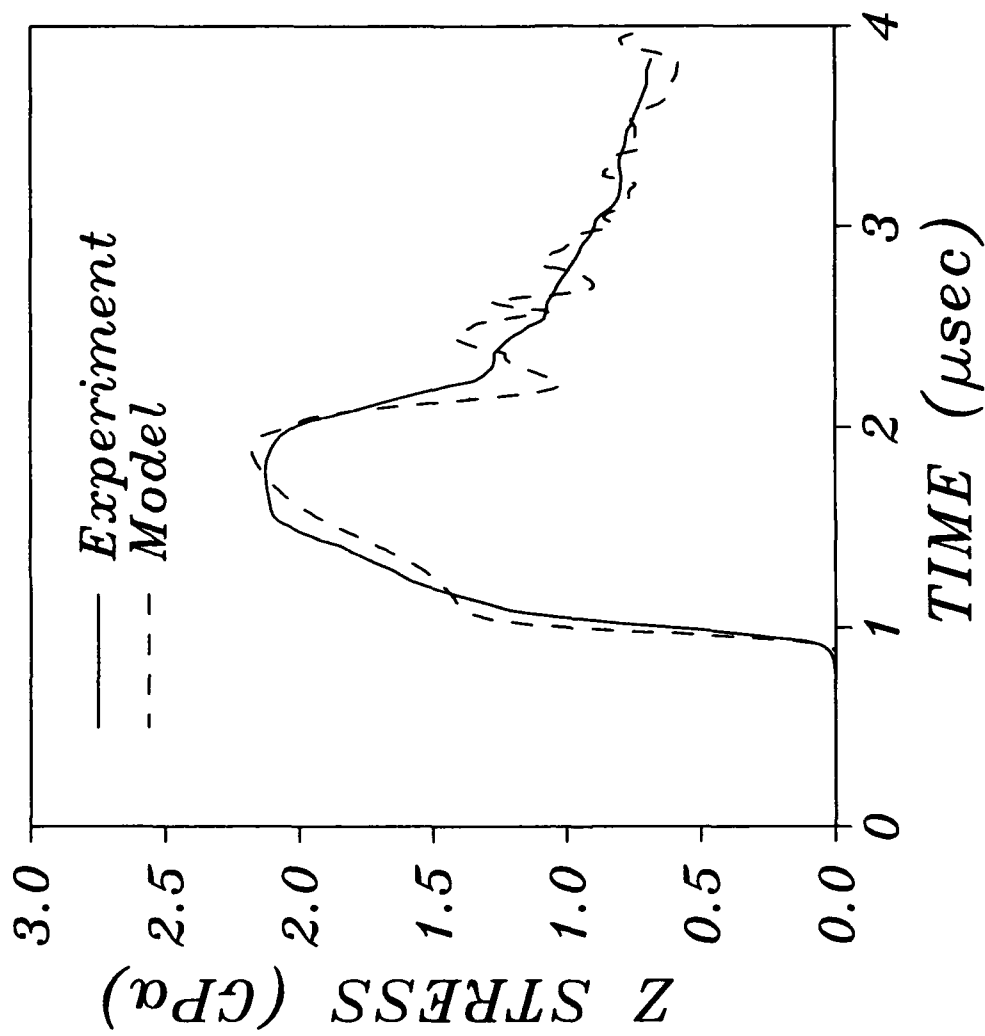


Figure 4.4. Manganin Stress Gauge Data and Model Simulation for Single Flyer Impact on Alumina Plate at Velocity 570 m/sec.

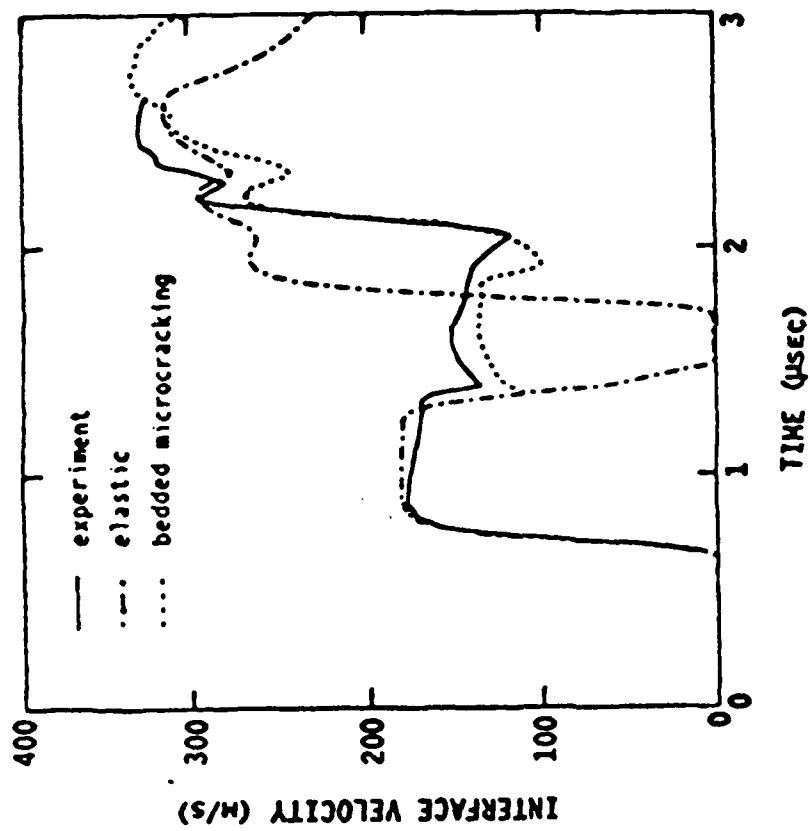


Figure 4.5. VISAR Data and Model Simulation for Double Flyer Impact on Alumina Plate at Velocity 293 m/sec.

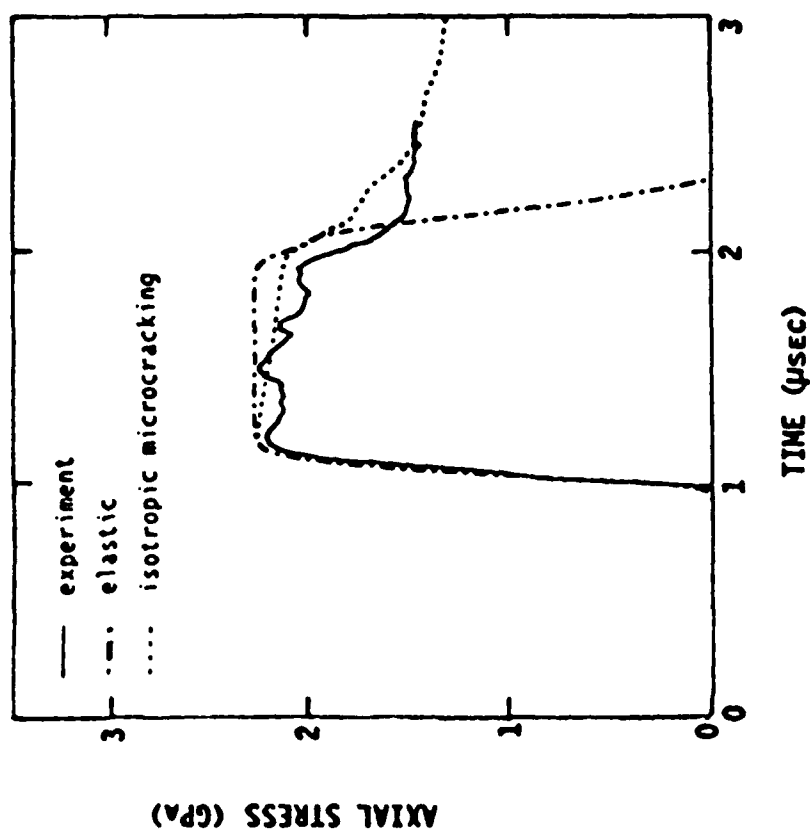


Figure 4.6. Manganin Stress Gauge Data and Model Simulation for Single Flyer Impact on TiB₂ Plate at Velocity 719 m/sec.

We performed several plate impact tests on Silicon Nitride (Si_3N_4) targets and determined the Hugoniot Elastic Limit (HEL) as 12 GPa. For modeling, we considered two different tests at impact velocities 175 m/s and 800 m/s. The stress amplitude (3.0 GPa) in the low velocity test is therefore within the elastic range. Damage under compression is not expected to occur at this stress level. The target fails due to the tensile waves generated due to wave reflections from the stress free back surface of the flyer and the target plates. However, above the HEL stress level, complex inelastic deformations due to microplasticity and microcracking under compressive loading usually occur in the target material. In fact the failure process is almost complete prior to the arrival of any tensile waves.

Rajendran et al. [49] modeled the 'below HEL' and 'above HEL' experiments using the EPIC-2 code. Figure 4.7a compares the model generated stress history with the gauge signal from the low velocity experiment. The flat top (between *A* and *B*) in this figure indicates that there is no microfracturing under compression and the deformation is elastic. However, the target spalled due to the tensile waves as indicated by the signal between *C* and *D*. In the absence of spall, the stress history would continue to decrease, as shown by the dotted line. In Figure 4.7b, the model simulated stress history inside the target is shown. The shock wave arrives at *A* and the material remains in compression until the unloading wave arrives at *C*. Tensile loading begins at *D*, followed by stress relaxation due to tensile damage between *E* and *F*. The dashed line in Figure 4.7b shows the damage evolution inside the target. Complete failure is assumed when damage reaches a value of one.

In ceramics, it is easier to nucleate and propagate microcracks under tension than under compression. Therefore, in tension, n^+ in Equation (74) is assumed to be equal to one. However, in compression, n^- is usually small ($\ll 1$) and is calibrated by matching the gauge signal.

Figure 4.8a compares the model generated stress history with the gauge signal from the high velocity (above HEL) experiment. In this figure, the stress drop between points *A* and *B* signifies compressive damage growth in the target. Figure 4.8b shows the model generated stress and damage histories inside the target. Compressive damage initiation and growth leads to stress relaxation between *B* and *C*. At *C*, the release wave from the flyer unloads the stress. In general, the ability of the model in reproducing the measured stress histories was extremely good.

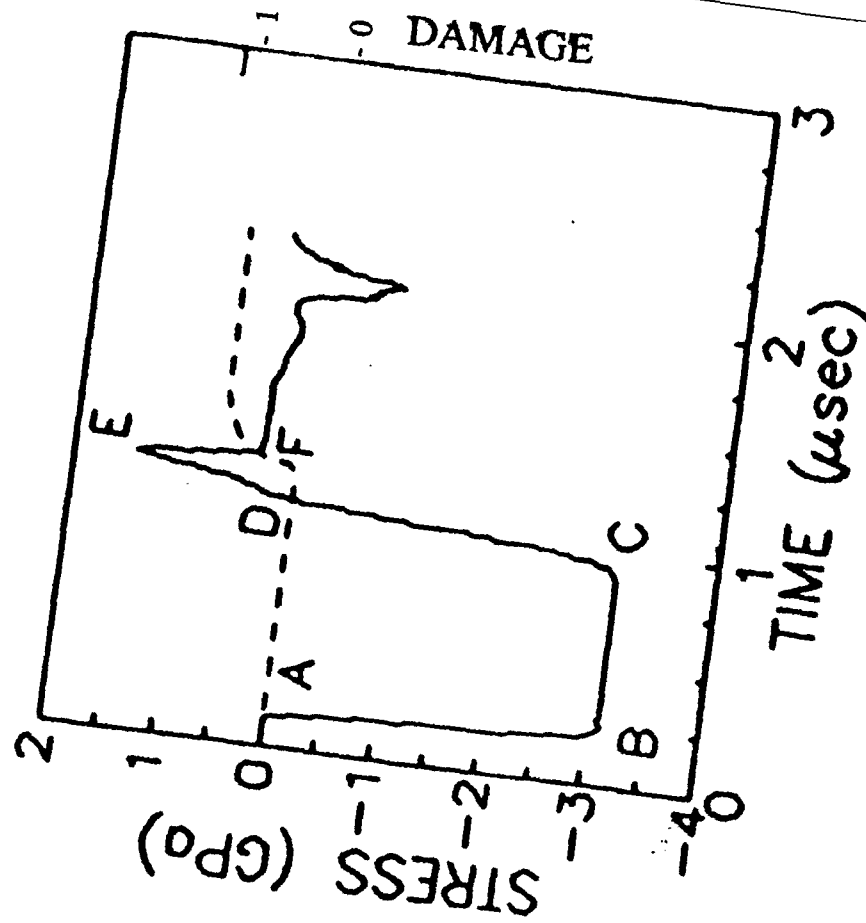
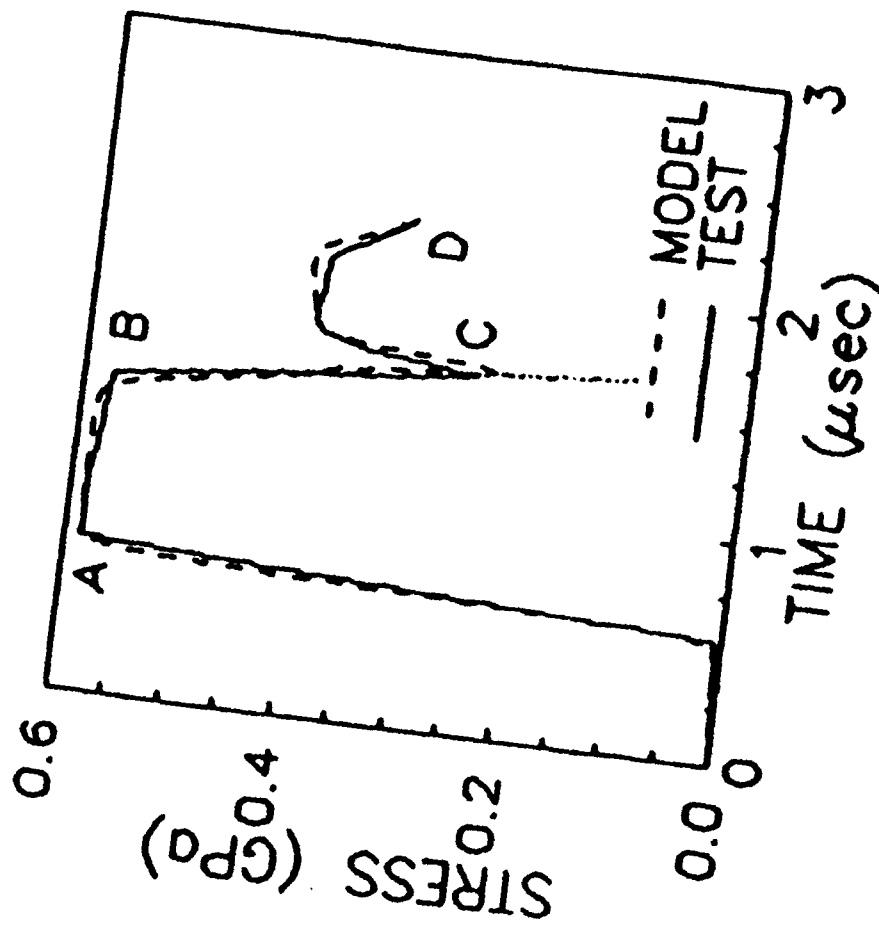


Figure 4.7. Low Velocity (175 m/s) Plate Impact Test with Si_3N_4 Target.
 (a) Comparison Between Model and Gauge Signal.
 (b) Model Generated Stress (Solid Line) and Damage (Dashed Line) Histories Inside the Target.

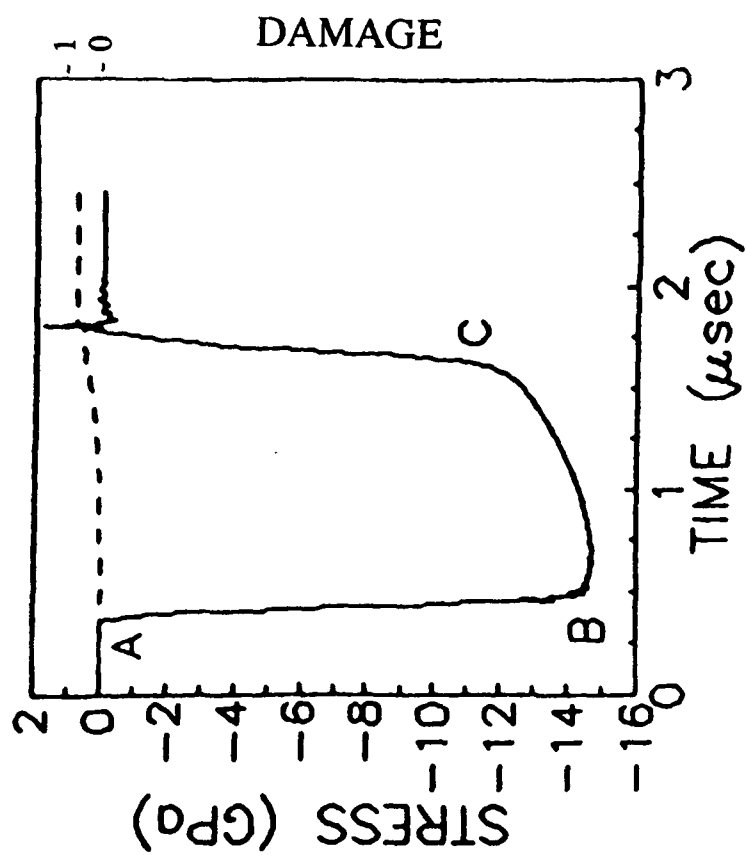
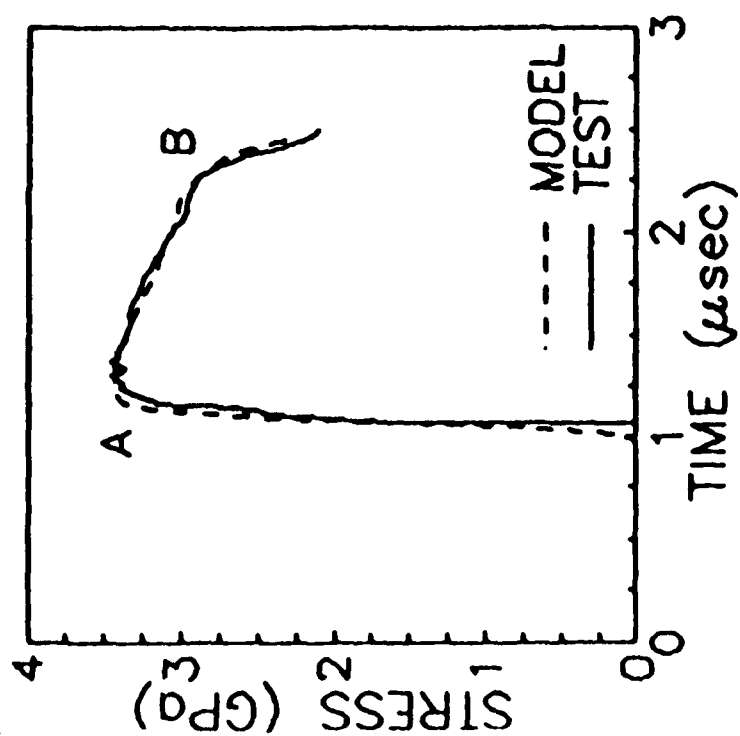


Figure 4.8. High Velocity (800 m/s) Plate Impact Test with Si_3N_4 Target.
 (a) Comparison Between Model and Gauge Signal,
 (b) Model Generated Stress (Solid Line) and Damage (Dashed Line) Histories
 Inside the Target.

4.5 Bar-on-Bar Impact Simulation

The model constants were calibrated using the data from both plate impact and split Hopkinson bar experiments. To further evaluate the model constants, Grove and Rajendran [27] simulated a rod impact experiment, using the EPIC-2 finite element code. The computed stress history was compared with the measured stress history inside the target rod. The model constants required further adjustment to obtain agreement with these experimental data.

An experiment was performed in which a short AD-85 ceramic rod impacted a long AD-85 ceramic rod at a velocity of 110 m/s. The projectile and target rod lengths were 50.8 mm and 152.4 mm, respectively, and both rods were 12.7 mm in diameter. A manganin gauge, embedded 25.4 mm from the free end of the target rod, was used to measure the stress history in the rod. Figure 4.9 illustrates the experimental configuration. Both rods broke into small pieces as a result of the impact.

The rod impact experiment was simulated as an axisymmetric problem using the EPIC-2 finite element code. The AD-85 ceramic was modeled as an elastic-plastic material with 10 percent porosity. The microcrack model constants were derived from split Hopkinson bar data and a plate impact experiment. In the first simulation, damage due to microcracking was suppressed (the ceramic remained intact and elastic) and the results were compared with the experimental stress history. As can be seen in Figure 4.10, the simulated stress history had a higher peak than the measured stress history. The lower stress amplitude in the experiment indicates either degradation of the material or some sort of stress release due to fracture at the impact plane.

In the second simulation, the ceramic was allowed to undergo damage. The microcracking was modeled using the precalibrated model constants. As Figure 4.11 indicates, the computed peak stress was significantly lower than the measured stress. The model apparently overpredicted the damage at the impact end, and release waves from the fractured end reduced the amplitude of the initial shock wave. With lack of any meaningful data for the microcrack propagation rate, the model parameters n_1^+ , n_2^+ , n_1^- , and n_2^- (see Equation (74)) were arbitrarily assumed to be equal to one.

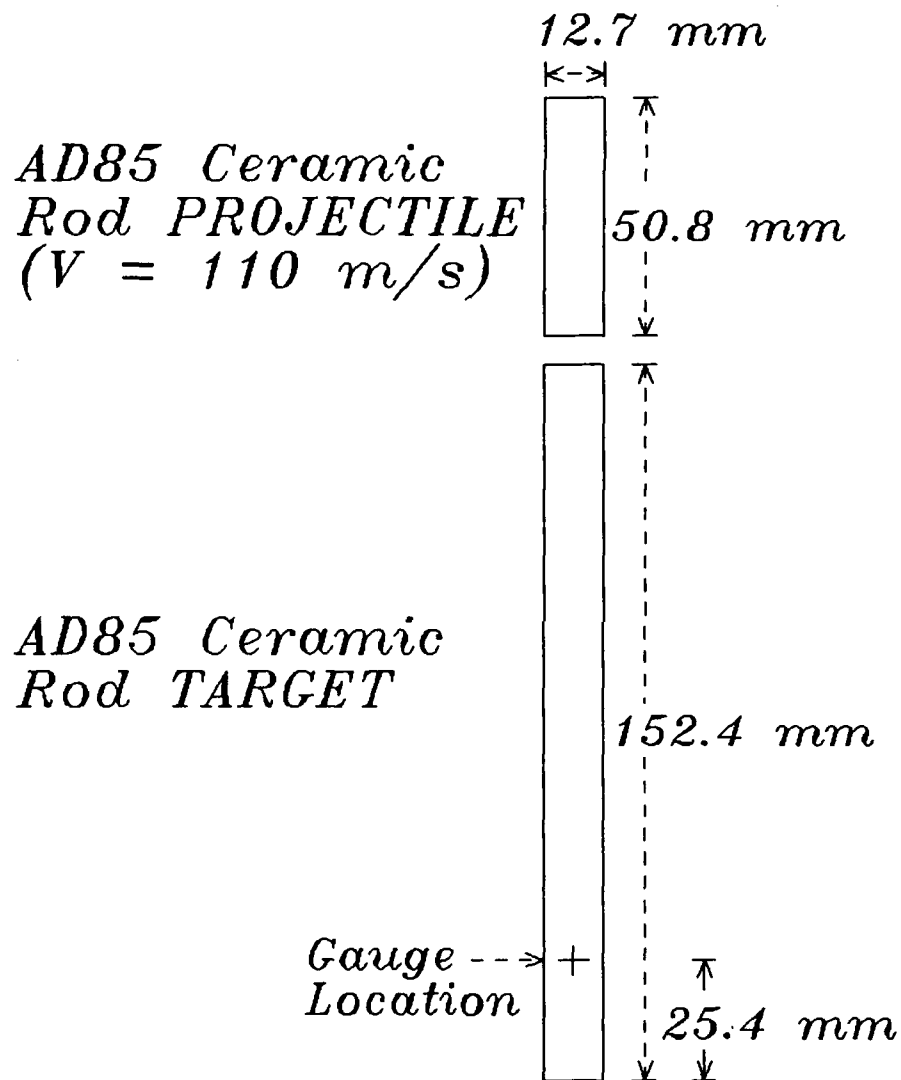


Figure 4.9. Configuration of AD-85 Bar-on-Bar Impact Experiment.

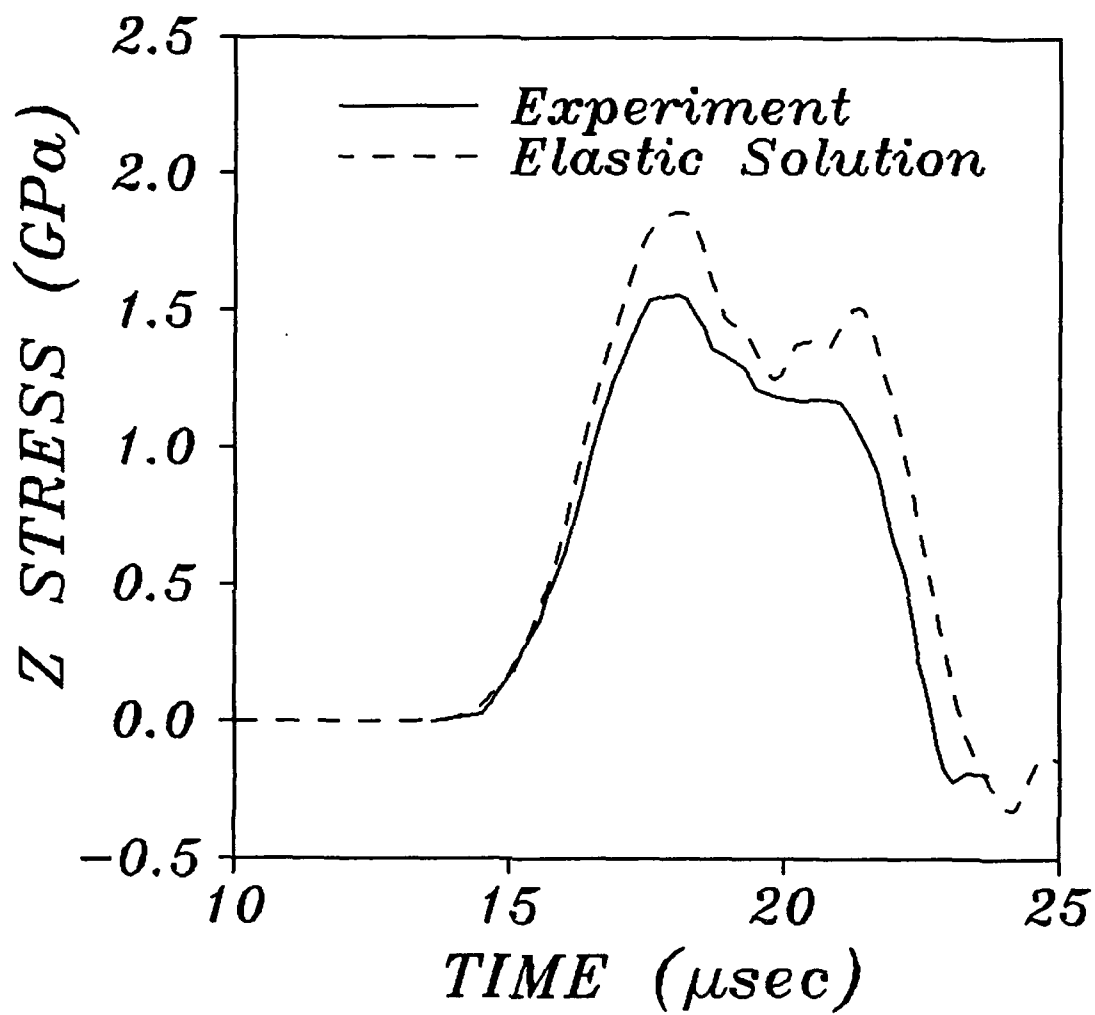


Figure 4.10. Stress History from Elastic (No Microcracking) Simulation of AD-85 Bar-on-Bar Impact Experiment.

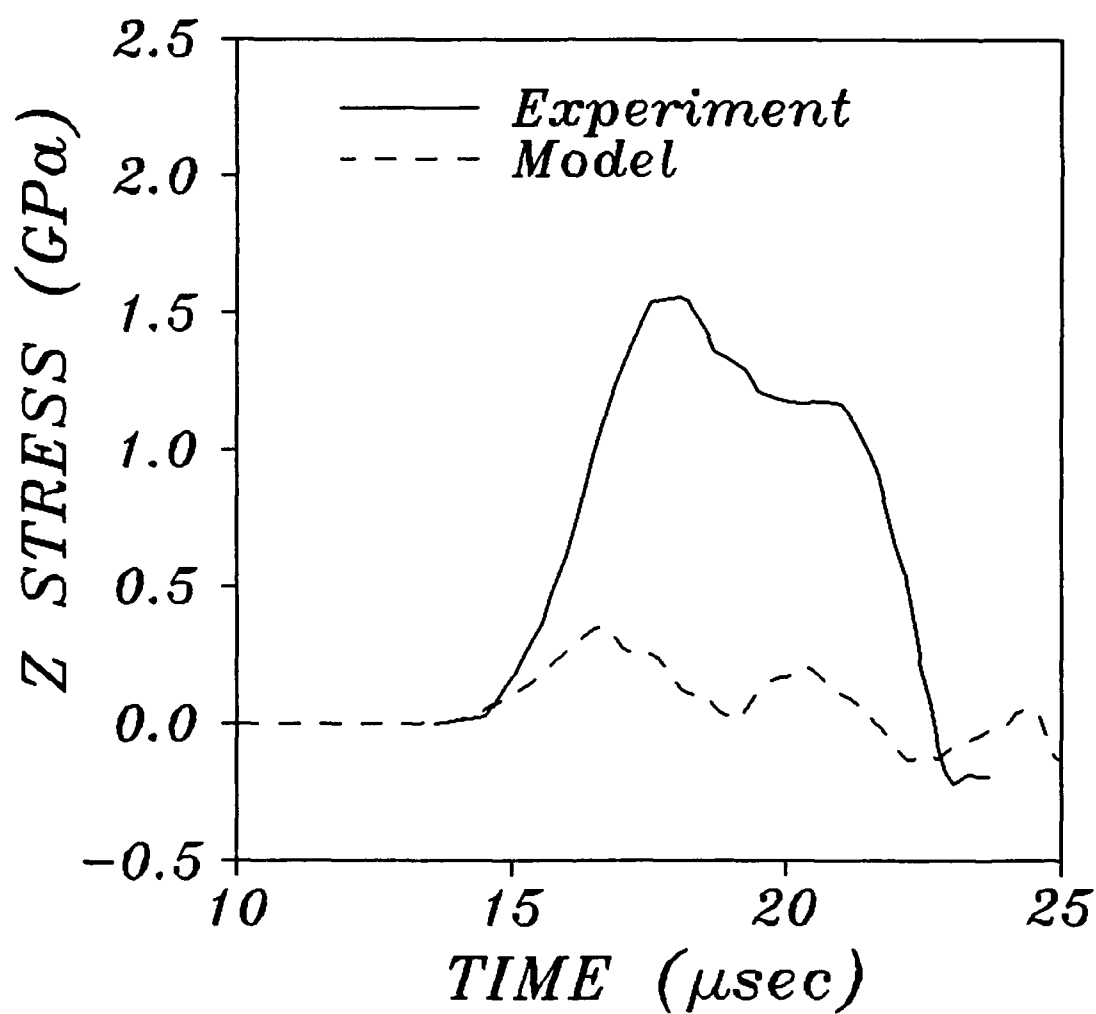


Figure 4.11. Model Generated Stress History with Microcrack Growth Rate Parameters (n_1^+ , n_2^+ , n_1^- , and n_2^-) Equal to 1.0 (Excessive Crack Growth) for AD-85 Bar-on-Bar Impact Experiment.

It was possible to match the experimental stress profile, as shown in Figure 4.12, by adjusting the model constants to limit the microcrack growth rates for both tensile (mode I) and shearing (modes II and III) conditions. The corresponding values for the constants are given in Table 4.1. Using the new model constants, we were still able to match the plate impact and Hopkinson bar experimental results.

TABLE 4.1
MODEL CONSTANTS FOR AD-85 CERAMIC

SYMBOL	VALUE	DESCRIPTION
K_{IC}	$3 \text{ MPa}\sqrt{m}$	Static fracture toughness
μ	0.72	Coefficient of friction
N_o^*	$1.83 \times 10^{10} \text{ m}^{-3}$	Microcrack density coefficient
a_o	$58 \times 10^{-6} \text{ m}$	Initial microcrack size
n_1^+	1.0	Microcrack growth rate constants for mode I
n_2^+	0.07	
n_1^-	0.1	Microcrack growth rate constants for modes II and III
n_2^-	0.07	

4.6 Long Rod Penetration Simulation

To verify the applicability of the microphysical based ceramic model, a hypothetical penetration experiment was simulated. In the simulation, a long rod with an aspect ratio (L/D , L =length, D =diameter) of 8 impacts a 50.8 mm thick ceramic plate which is confined between two 25.4 mm thick steel plates as shown in Figure 4.13.

The EPIC-2 penetration calculation was performed for 25 microseconds. During this time, the projectile nearly penetrated the first steel plate. The main objective of the analysis was to understand the damage evolution inside the ceramic at various locations. Figure 4.14 indicates

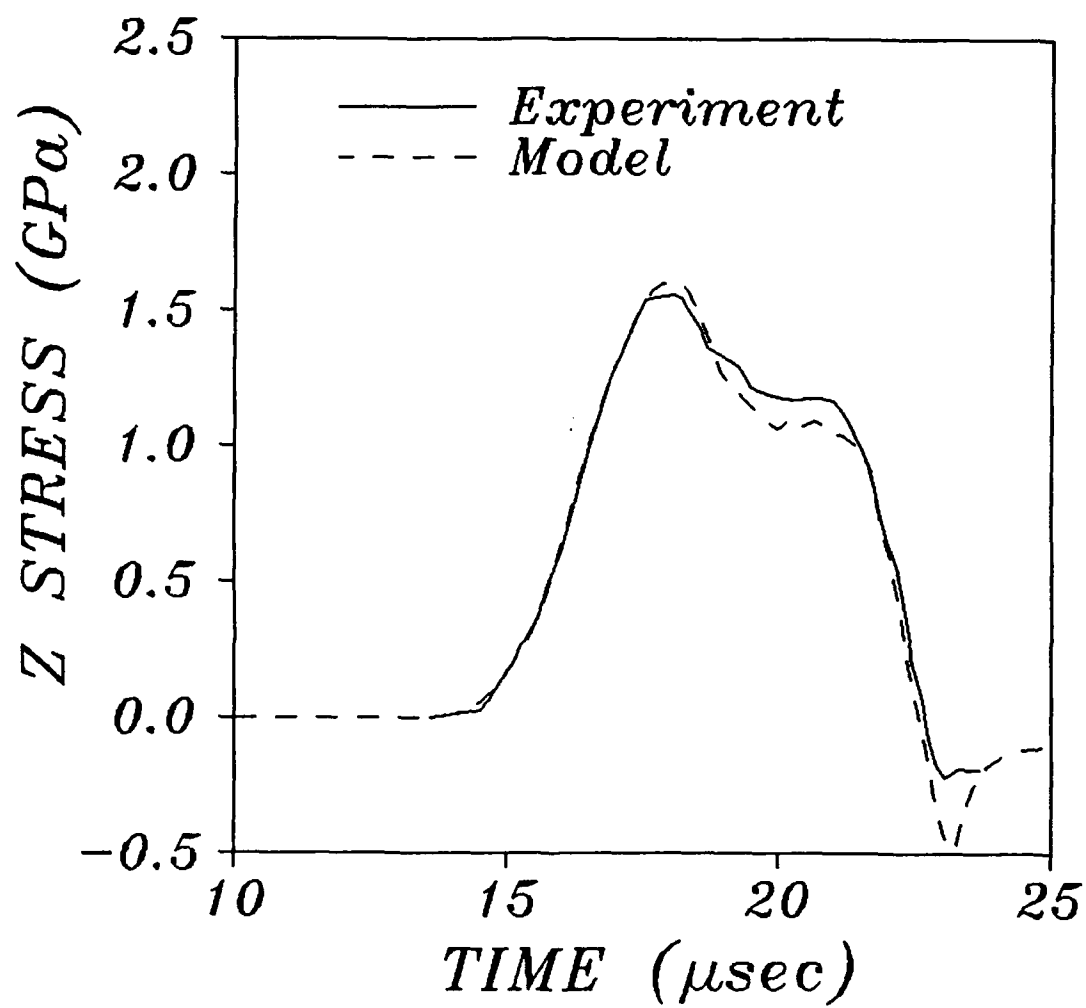


Figure 4.12. Model Generated Stress History with New Set of Constants for AD-85 Bar-on-Bar Impact Experiment.

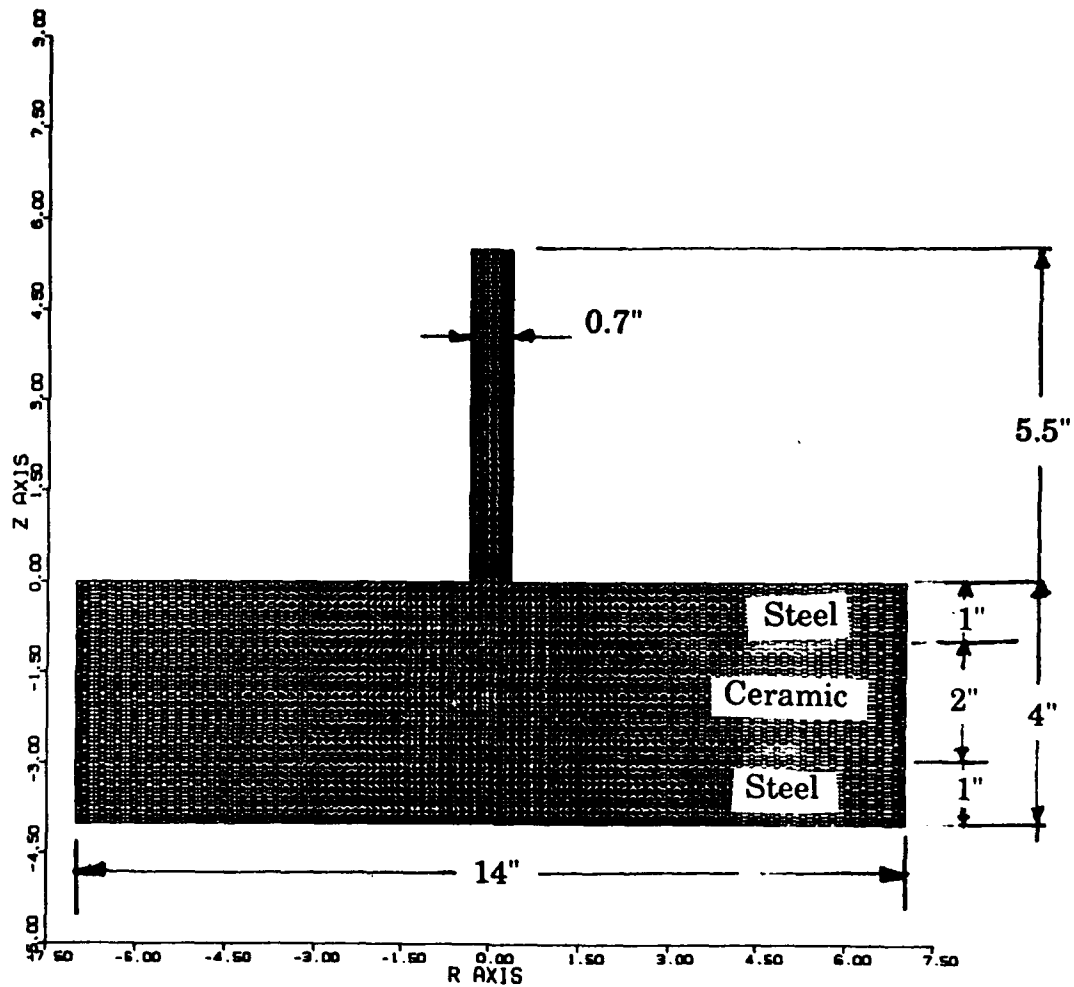


Figure 4.13. A Long Tungsten Rod Penetration into a Confined Ceramic Target.

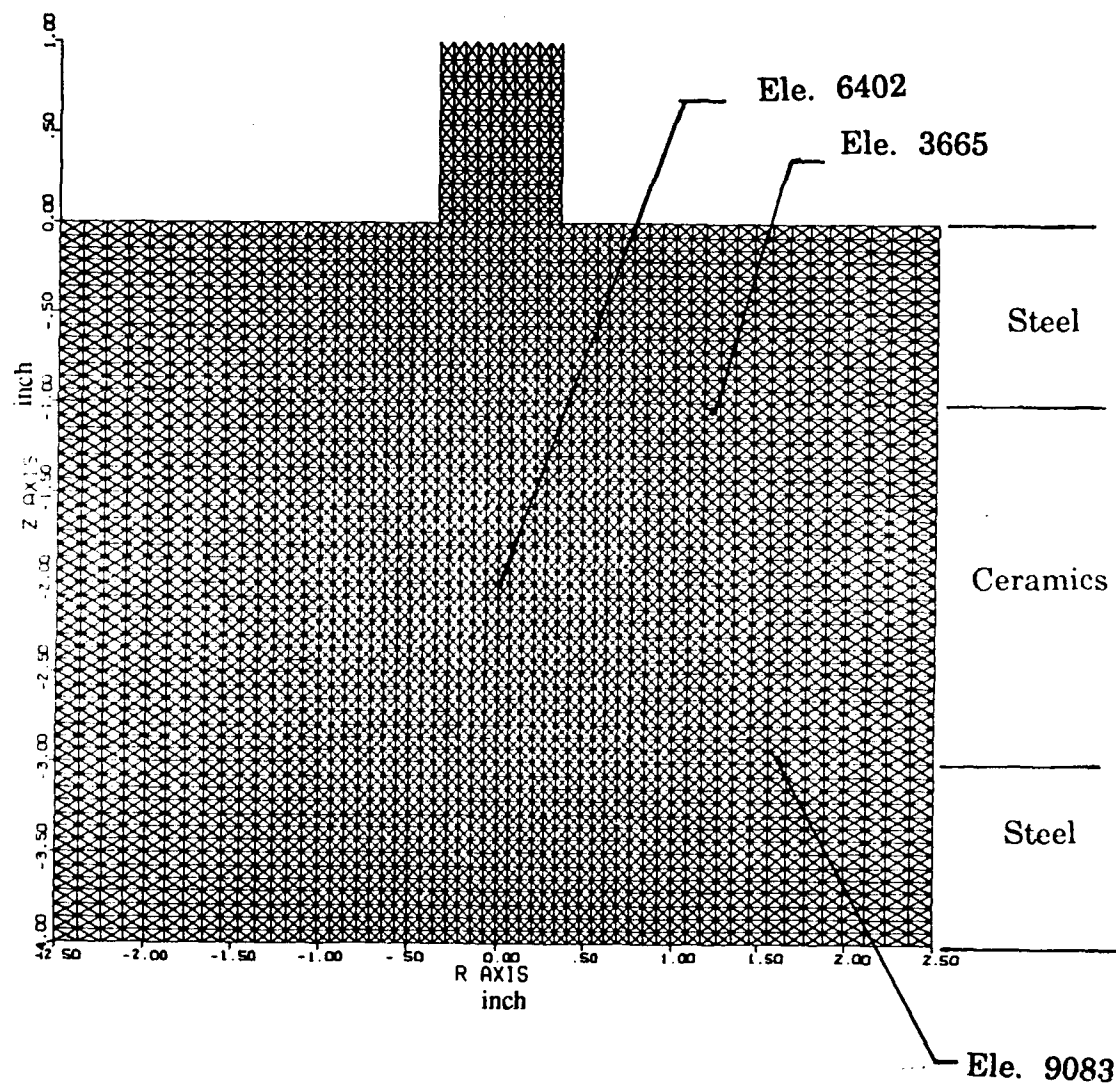


Figure 4.14. Element Locations (Inside Ceramic Plate) in Rod Penetration Simulation.

the locations of the elements in the ceramic plate where time history information was obtained from the simulation. Element 3665 is near the top surface of the ceramic layer (about 30.5 mm from the axis of symmetry), element 6402 is near the center of the ceramic layer (on the axis of symmetry), and element 9083 is near the bottom surface of the ceramic layer (about 40.6 mm from the axis of symmetry). These three elements were selected for the following reasons:

1. Element 3665 is expected to fracture completely due to tensile loading since it is away from the axis of symmetry.
2. Element 6402, on the axis of symmetry, is expected to experience compressive fracture prior to any tensile fracture.
3. Since element 9083 is located at the confined back surface of the ceramic and away from the axis, it is expected to fracture due to combined compressive and tensile loading.

In addition to time history plots, damage contour plots were generated at 8, 10, 12, and 20 microseconds. These plots, shown in Figure 4.15, illustrate the evolution of microcrack damage in the ceramic target plate. Damage initiates at locations near element 3665 (see Figure 4.15a), well before the penetrator makes any contact with the ceramic layer. The brittle fracture of the ceramic occurs as soon as it is loaded in tension due to lateral release waves at 6-8 microseconds. The expanding region between the damage contours in the figure represents the pulverized ceramic material. The damage is progressive as seen by the contours movement in Figure 4.15. A small portion (region A in Figure 4.15c) of the ceramic directly under the penetrator remains intact while the damage that initiated near element 3665 propagates well into the ceramic. At 20 microseconds, the strong compressive loading, induced by the approaching rod, completes the fracturing process. As Figure 4.15d indicates, the ceramic material directly beneath the penetrating rod pulverizes completely before the rod reaches the ceramic. A mesh plot of the fractured ceramic is shown in Figure 4.16; the dark region is the pulverized ceramic.

The time history plots in Figures 4.17 through 4.19 provide information concerning elements 3665, 6402, and 9083. These figures include maximum principal stress, pressure, and damage time-history plots. Elements 3665 and 6402 experience only compressive pressures as can be seen from Figure 4.17a and 4.18a. The compressive pressure is positive in the plots.

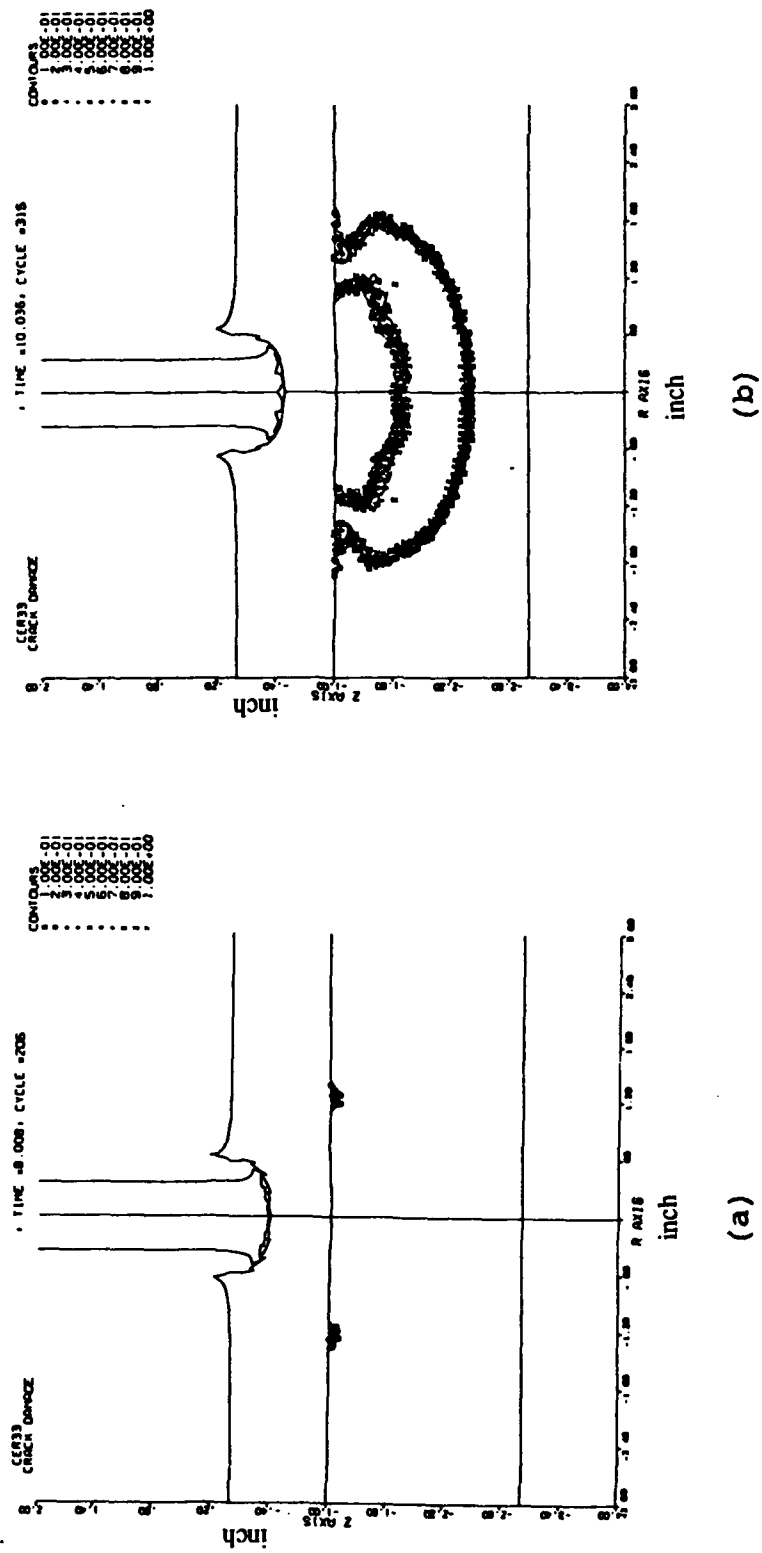
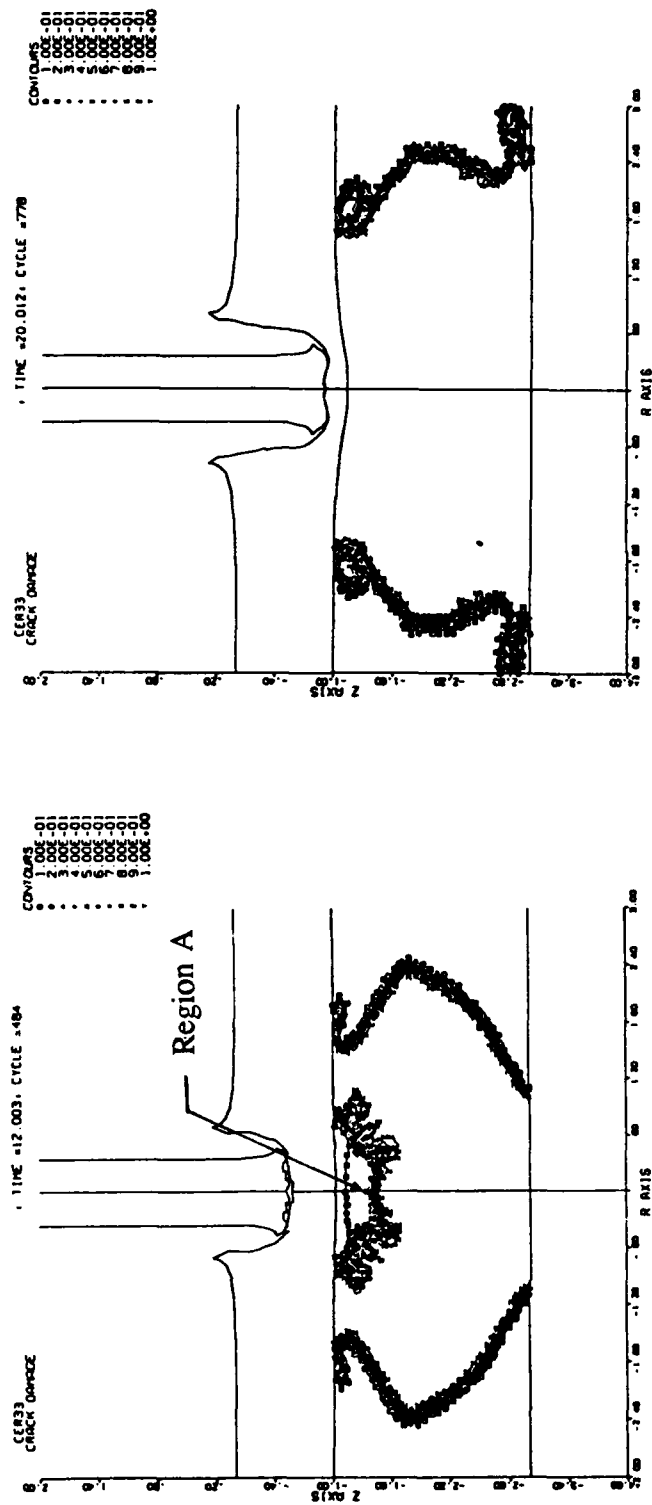
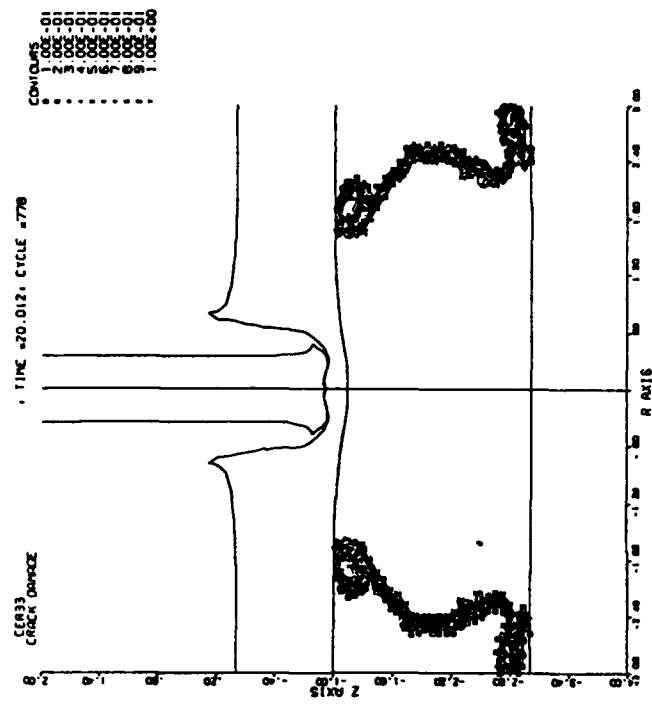


Figure 4.15. Microcrack Damage Contours at (a) 8 μ s, (b) 10 μ s, (c) 12 μ s, and (d) 20 μ s.



(c)



(d)

Figure 4.15. Microcrack Damage Contours at (a) 8 μ s, (b) 10 μ s, (c) 12 μ s, and (d) 20 μ s (concluded).

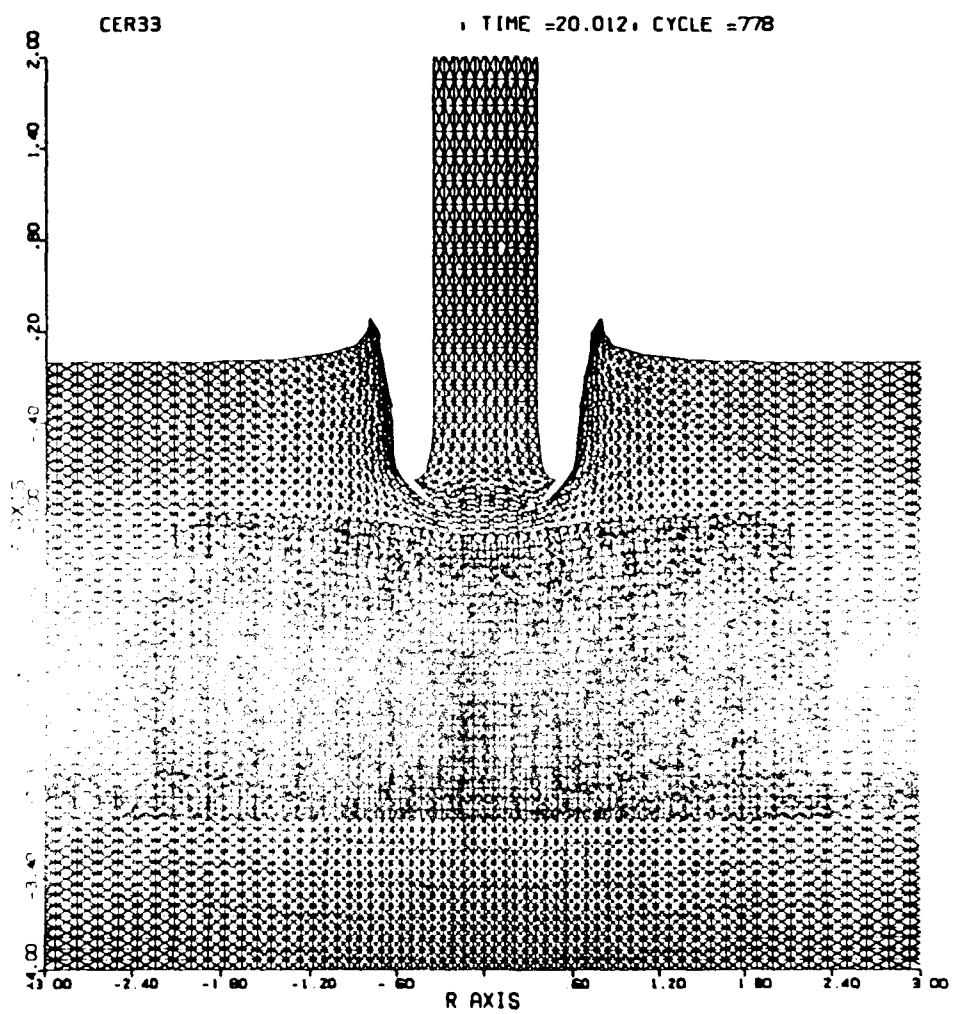


Figure 4.16. Mesh Plot of the Pulverized (Darker Region) Ceramic.

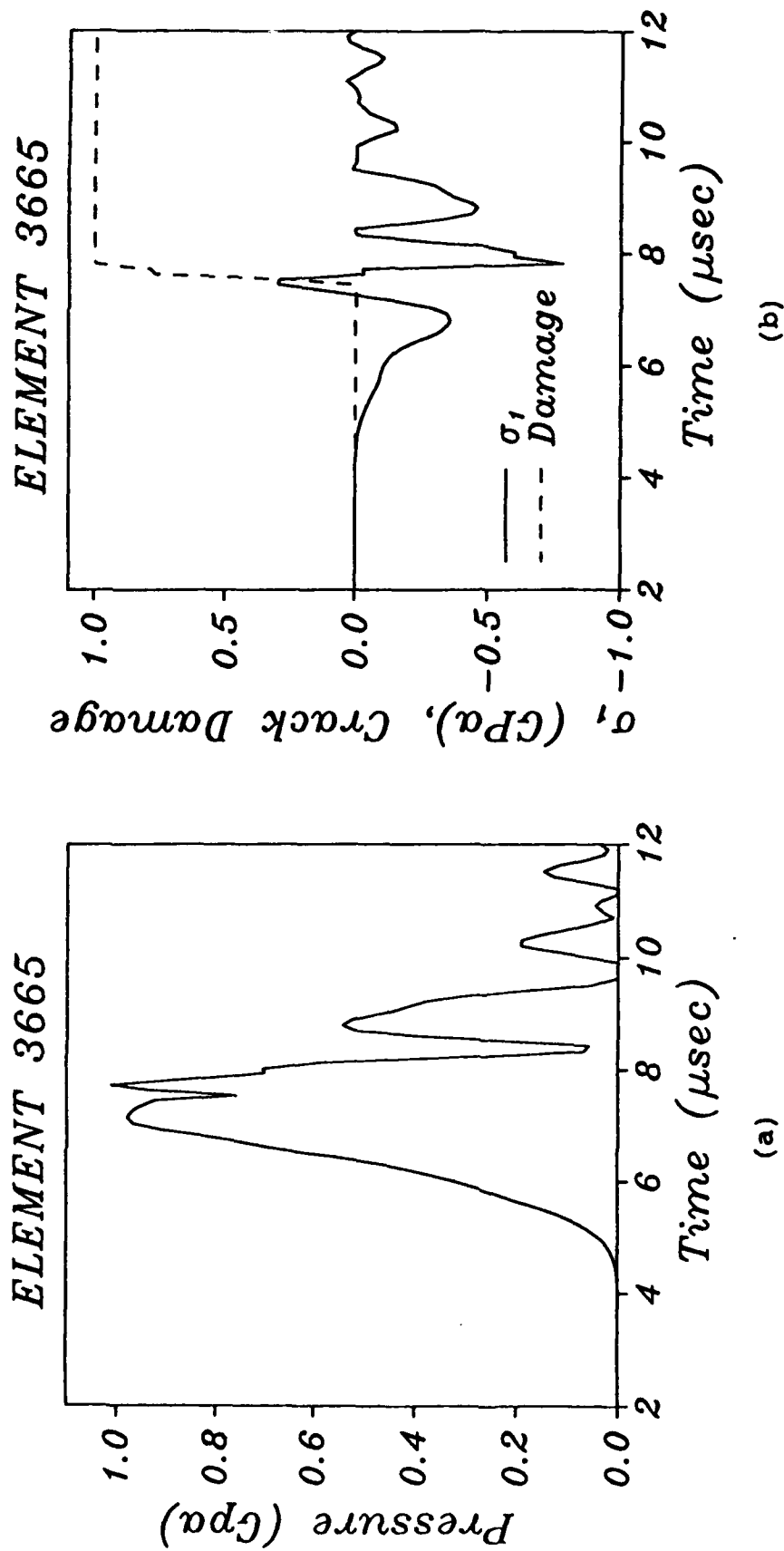


Figure 4.17. Time History Plots for Element 3665: (a) Pressure, and (b) Maximum Principal Stress (Solid Line) and Damage (Dashed Line).

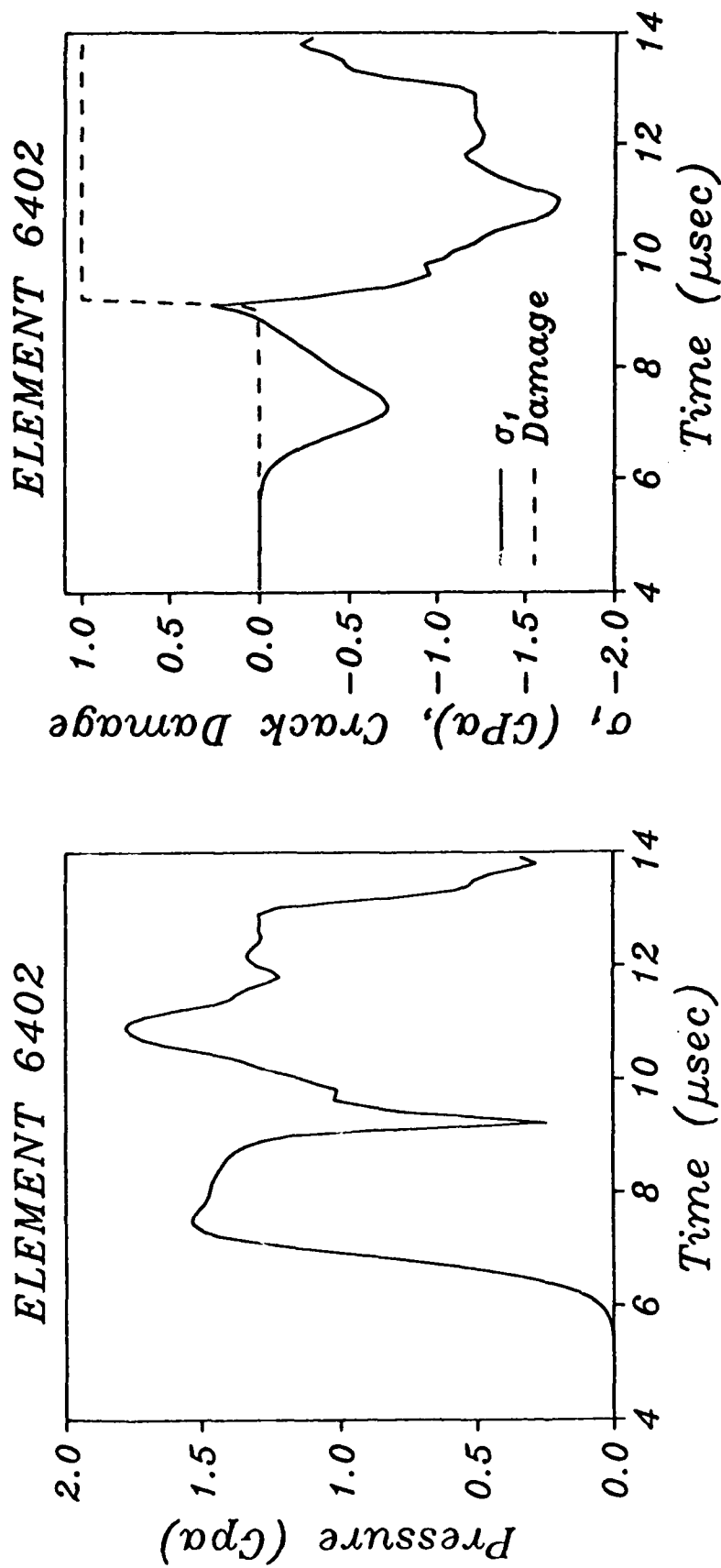


Figure 4.18. Time History Plots for Element 6402: (a) Pressure, and (b) Maximum Principal Stress (Solid Line) and Damage (Dashed Line).

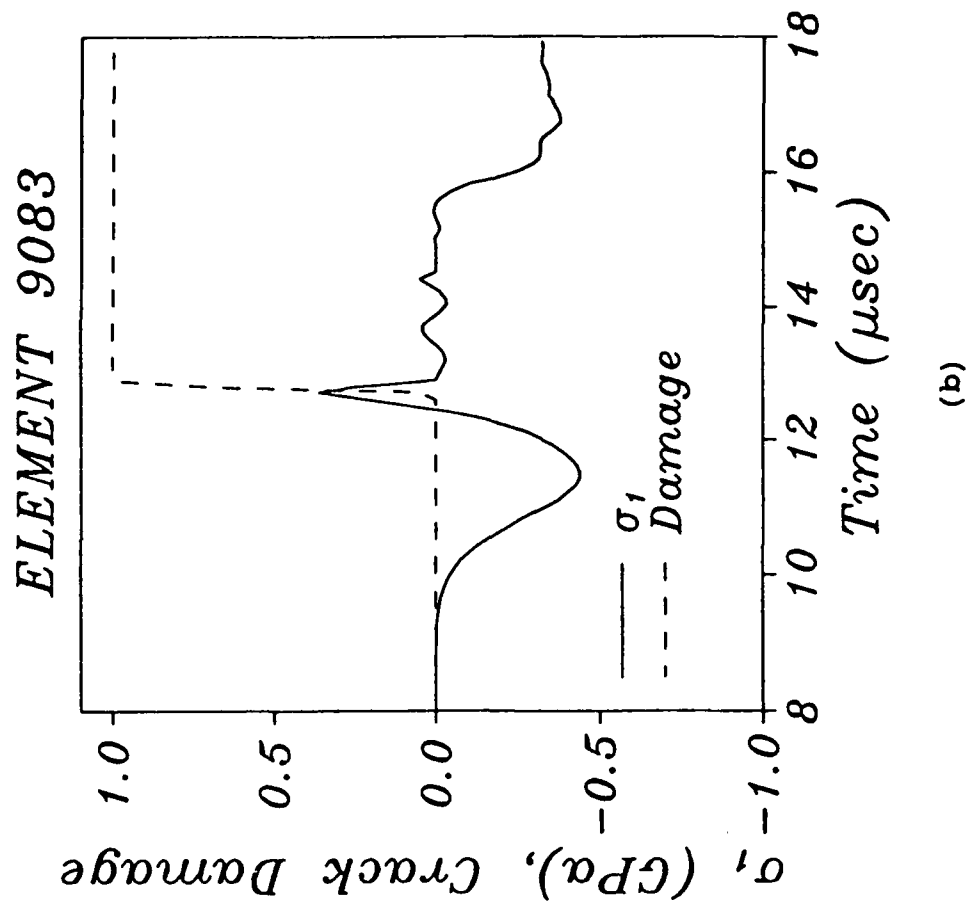
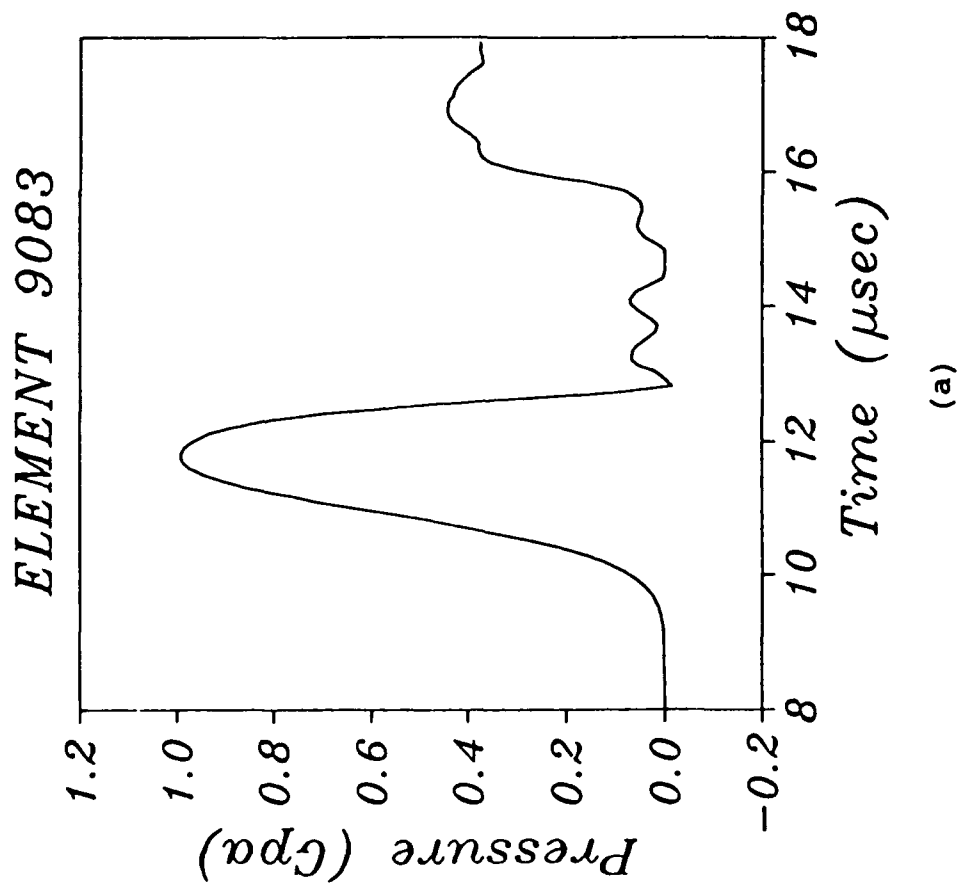


Figure 4.19. Time History Plots for Element 9083: (a) Pressure, and (b) Maximum Principal Stress (Solid Line) and Damage (Dashed Line).

However, element 9083 experiences a small tensile pressure at approximately $t=13$ microseconds, as shown in Figure 4.19.

Plots of principal stress and damage versus time are presented in Figures 4.17b, 4.18b, and 4.19b for elements 3665, 6402, and 9083, respectively. The model restricts the maximum positive (tensile) principal stress to a few kilobars (<3 kbars). This is achieved by the model through stress relaxation due to damage evolution. Element 3665 experienced only Mode I microcrack growth, while the microcracking in element 6402 began in Modes II and III finished in Mode I. However, the crack growth under compression (shear cracking) is relatively small compared to the tensile growth and is not discernable in the figure. Element 9083, like 3665, experienced only rapid Mode I microcrack growth. These time history plots indicate that the model predicted damage evolution in the ceramic according to the generalized Griffith criterion and stress relaxation according to micromechanics. The stress relaxation under tensile loading is clearly demonstrated in the simulation. Unlike models in which damage does not influence the strength, this advanced ceramic model incorporates the effects of damage on both strength and stiffness. Thus, the use of this newly developed ceramic model in penetration-into-ceramic calculations should provide hydrocodes with the necessary predictive capabilities.

Section 5

Summary and Recommendations

The development of advanced constitutive models for use in hydrocode calculations was reported. A ductile failure model (the RDG model) for metals and a microcracking model for ceramics were presented. In the model formulations, the evolution equations were directly related to the physics operating at the microscopic level. One goal in the model development was to describe the physical process with meaningful mathematical expressions. Another important philosophy was to keep the model constants to a minimum.

5.1 RDG Model Summary

The RDG model is a continuum mechanics based ductile failure model. The model formulation is three-dimensional and therefore applicable under a general stress-strain state. The RDG model describes several fundamental aspects of the failure process. When the failure process is initiated due to void nucleation in the material, the plastic flow becomes pressure dependent. Also, under high velocity impact loading, most metals exhibit strain rate dependent behavior. The RDG model includes the effects of pressure and strain rate in the constitutive (strength) model formulation. An important feature of the RDG model is its accurate modeling of the intact material using appropriate viscoplastic equations. The Bodner-Partom (BP) equations were selected for this purpose although we have shown that the Johnson-Cook (JC) equations may also be used. The state variables in the RDG model formulation are the equivalent plastic strain rate in the matrix material and the BP model state variable Z , which describes the loading history effects.

A pressure dependent yield function serves as the plastic potential in the derivation of plastic strain rate for the void contained aggregate. Since the aggregate plastic strain rates are directly related to the equivalent plastic strain rate of the matrix material, the strain rate and loading history effects enter into the failure model formulation through the Bodner-Partom model. The RDG failure model does not require separate loading or unloading conditions. Both elastic and plastic rate components are taken to be always nonzero, and the same relations are intended to hold under loading and unloading conditions as in the Bodner-Partom model. When the

equivalent plastic strain rates are numerically very small ($<0.0001/\text{sec.}$), the deformation is considered to be elastic.

Another appealing feature of the RDG failure model is the void growth law. Assuming that the void volume fraction growth rate is equal to the summation of the normal plastic strain rate components (dilatation) removes the requirement for a new evolution law for the void growth rate. This modeling approach significantly reduces the number of model constants. While the Bodner-Partom model usually requires five constants, the determination of those constants is fairly straight forward and Rajendran et al. [32] reported a procedure to calibrate the constants using data from a limited number of standard impact tests.

In the RDG model, there are three constants for void nucleation, and two constants that control the growth of voids. Model constants can be determined from numerical simulations of a plate impact experiment. The initial value for the void volume fraction and the threshold nucleation stress can be adjusted to match the time of arrival of the experimental spall signal. The standard deviation of the nucleation stress distribution is arbitrarily set to one third or one fourth of this threshold stress. The initial slope and amplitude of the spall signal guides the selection of the void growth (or yield function) constants.

The RDG model was incorporated into the EPIC-2 finite element code. A numerically stable and accurate solution technique based on a diagonally implicit Runge-Kutta (DIRK) method was used to solve the complex and stiff governing differential equations. Various aspects of the numerical scheme were demonstrated in References [1] and [50]. For solving only the Bodner-Partom equations, an iterative radial return scheme has been successfully implemented. The BP model constants had already been determined for these materials and reported by Rajendran et al. [51]. The RDG model accurately matched several of the plate impact experiments. RDG model constants for OFHC copper, tantalum, Armco iron, and 1020, MAR 200, MAR 250, AF1410, C1008, and HY100 steels were determined and are presented in this report.

The capability of the RDG model was extended to multiple impact loading conditions. The model accurately predicted the failure process in a twice-impacted target plate. Both void growth and collapse were modeled in this case. To describe the pore collapse correctly, a critical

value of void volume fraction was calibrated for collapse. For complete spallation, the critical void volume fraction was arbitrarily assumed to be 1.0 for most metals.

We also successfully modeled spallation under a three-dimensional strain state using the RDG model. The model constants were determined from a one-dimensional (strain) plane plate impact test. Using those constants, the RDG model reproduced multiple spall regions in a cone target under a three-dimensional stress-strain state. This demonstration greatly increased our confidence in the generality of this model, even when calibrated with one-dimensional experiments. We also established that the correct spall patterns in the cone can only be obtained by using a void nucleation and growth model such as the RDG model.

5.2 Ceramic Model Summary

Initially, a relatively simple fragmentation based ceramic model (the modified TCK model) was developed and reported in Reference [11]. However, based on the complexity of impact damage evolution under both compressive and tensile loading, an advanced microphysical model was developed. This model is capable of modeling inelastic strains due to pore collapse, plastic flow, and microcracking in ceramics. This advanced model has been incorporated into the EPIC-2 computer code. Plate impact, rod-on-rod impact, and long rod penetration into ceramic target experiments were simulated. In the simulation, when the ceramic material completely pulverizes at impact velocities above the HEL, the isotropic damage model is sufficient to describe the tensile failure. The pore crushing and strain rate dependent plasticity under compression are modeled using the state variable and pressure dependent plastic flow theories.

The EPIC-2 code simulation of a plate impact test on AD85 ceramic using the ceramic model reproduced the measured stress-time history. Since this is a porous ceramic, the inelastic ("plastic") ramping of the stress was modeled through the plastic pore collapse option of the ceramic model. The damage in AD-85 and TiB_2 at impact velocities above HEL was modeled by treating the damage as a randomly oriented scalar variable.

Since microdamage occurs at shock levels well below the HEL, it is important to model fracture initiation under compression. Using the microphysical model which contains this feature, a plate impact test on a silicon nitride target, at a velocity well below the HEL, was successfully

modeled. The model reproduced the spall signals extremely well. We successfully modeled impact damage evolution in silicon nitride under both tensile and compressive loading conditions. The strength and stiffness degradations were modeled through an internal state variable based scalar damage parameter γ representing the crack density in the material. We demonstrated the capabilities of the microphysical model by modeling both 'below HEL' and 'above HEL' plate impact experiments.

A long rod penetration into a confined ceramic target was also simulated using the EPIC-2 code. The impact behavior of the ceramic target was described by the advanced ceramic model. The code analysis showed the details of damage evolution under multi axial loading. Physically meaningful results were obtained from the code simulation. The capability of obtaining realistic solutions from the hydrocode calculations using such physically based models is an important advantage in advanced impact design feasibility studies.

5.3 Recommendations

5.3.1 Metals

The results from the analysis of the application problems suggest the need for additional in-depth analyses supported by experimental data. For example, to substantiate the tensile necking analysis, high speed photographic split Hopkinson bar tests on shallow notch specimens should be conducted. The experimentally determined necking profiles should be compared with the RDG model predictions. For this purpose, selection of a material in which microvoids have been observed under dynamic tensile loading conditions is recommended.

It is desirable to perform instrumented penetration experiments for validating the RDG model prediction. Radiographs of the projectile and target during the penetration, and post-failure analysis on the target would identify additional model requirements. These radiographs are particularly important for verifying the spall fragmentation studies.

5.3.2 Ceramics

The generality of the new ceramic model requires additional validation. Simulations of plate impact tests with different options, such as (1) elastic-cracking, (2) elastic-viscoplastic without pore collapse, (3) elastic-viscoplastic with pore collapse, and (4) elastic-cracking-viscoplastic, should be performed. Since the impact response of ceramics differs significantly

from ceramic to ceramic, it is important that other ceramic materials, such as boron carbide, silicon carbide, aluminum nitride, etc., are also considered in the model evaluation. The effects of pulverization on the stress wave profiles must be investigated.

Additional efforts are required for the bar-on-bar and long rod penetration experiments. Here again, the various options in the ceramic model should be invoked and the corresponding simulation results should be compared. A model constants evaluation scheme needs to be firmly established. The development of a standard procedure is essential so that material constants for various ceramics can be systematically derived.

The ability of the ceramic model to predict the penetration depth of a long rod penetrating both confined and unconfined ceramics must be established. This will require data from diagnostic penetration experiments. In summary, further research is required to validate the newly developed microphysical model.

References

1. Rajendran, A. M., Dietenberger, M. A., and Grove, D. J., "A Void Nucleation and Growth Based Failure Model for Spallation," *J. Appl. Phys.*, **65**, 1521-1527, (1989).
2. Rajendran, A. M., Bless, S. J., and Grove, D. J., "Dynamic Ductile Failure under Multiaxial Loading," Proceedings of Third International Symposium on Plasticity, Grenoble, France, August 1991.
3. Rajendran, A. M., Grove, D. J., and Dietenberger, M. A., "A Dynamic Plasticity Based Failure Model," in 'Advances in Plasticity,' eds. A. S. Khan and M. Tokuda, Proceedings of Plasticity '89, Pergamon Press, (1989).
4. Rajendran, A. M., Dietenberger, M. A., and Grove, D. J., "Results from the Recently Developed Dynamic Failure Model," Shock Compression of Condensed Matter - 1989, eds. S. C. Schmidt, J. N. Johnson, and L. W. Davison, Elsevier Science Publishers, 373-376, (1989).
5. Grove, D. J., Rajendran, A. M., and Dietenberger, M. A., "Numerical Simulation of a Double Flyer Impact Experiment," Shock Compression of Condensed Matter - 1989, eds. S. C. Schmidt, J. N. Johnson, and L. W. Davison, Elsevier Science Publishers, 365-368, (1989).
6. Bar-On, E., Rajendran, A. M., Bless, S. J., and Grove, D. J., "Modeling of Dynamic Fracture in a Solid Cone Target," Shock Compression of Condensed Matter - 1991, Elsevier Science Publishers, (1991).
7. Nicholas, T. and Rajendran, A.M., "Material Characterization at High Strain Rates," Chapter 3 in "High Velocity Impact Dynamics," E. Zukas, J.A., John-Wiley & Sons, pp. 127-296, (1990).
8. Rajendran, A. M. and Nicholas, T., "Dynamic Constitutive/Failure Models," AFWAL-TR-88-4229, Wright-Patterson Air Force Base, OH, December 1988.
9. Rajendran, A. M. and Cook, W. H., "A Comprehensive Review of Modeling of Impact Damage in Ceramics," AFATL-TR-88-143, Air Force Armament Laboratory, Eglin Air Force Base, FL, December 1988.
10. Taylor, L. N., Chen, E. P., and Kuszmaul, J. S., "Microcrack-Induced Damage Accumulation in Brittle Rock under Dynamic Loading," *Computer Methods in Applied Mechanics and Engineering*, **55**, (1986).
11. Rajendran, A. M. and Kroupa, J. L., "Impact Damage Model for Ceramic Materials," *J. of Appl. Physics*, **8**, **66**, 7-20, 3560-3565, (1989).

25. Rosenberg, Z., Brar, N. S., and Bless, S. J., "Elastic Precursor Decay in Ceramics as Determined with Manganin Stress Gauges," *J. de Physique*, 49, C3.707-711, (1988).
26. Brar, N. S. and Bless, S. J., "Dynamic Fracture and Failure Mechanisms of Ceramic Bars," International Conference on Shock-Wave and High-Strain Rate Phenomena in Materials (Explomet 90), San Diego, CA, 12-17 August 1990.
27. Grove, D. J., Rajendran, A. M., and Bless, S. J., "Damage Evolution in a Ceramic Rod," Shock Compression of Condensed Matter - 1991, Elsevier Science Publishers, (1991).
28. Brar, N. S., Bless, S. J., and Rosenberg, Z., "Impact Induced Failure Waves in Glass Bars and Plates," submitted to Appl. Phys. Letters, August 1991.
29. Bless, S. J., Brar, N. S., Kanel, G. I., and Rosenberg, Z., "Failure Waves in Glass," to appear in *J. American Ceramics Society*, (1992).
30. Mackenzie, J. H., "The Elastic Contents of a Solid Containing Spherical Holes," *Proc. Phys. Soc.*, 2, 63, (1950).
31. Johnson, G. R. and Stryk, R. A., "User Instructions for the EPIC-2 Code," AFATL-TR-86-51, Eglin Air Force Base, FL, (1986).
32. Rajendran, A. M., Bless, S. J., and Dawicke, D. S., "Evaluation of Bodner-Partom Model Parameters at High Strain Rate," *J. Eng. Mat. and Tech.*, 108, 75-80, (1986).
33. Johnson, G. R. and Holmquist, T. J., "Evaluation of Cylinder-Impact Test Data for Constitutive Model Constants," *J. Appl. Phys.*, 64, 3901-3910, (1989).
34. Yaziv, D., "Shock Fracture and Recompaction of Ceramics," Ph.D. Thesis, Univ. of Dayton, Dayton, C'I, (1985).
35. Yaziv, D., Bless, S. J., and Rosenberg, Z., "Study of Spall and Recompaction of Ceramics Using a Double-Impact Technique," *J. Appl. Phys.*, 58, 3415-3418, (1985).
36. Hancock, J. W. and Brown, D. K., "On the Role of Strain and Stress State in Ductile Failure," *J. Mech. Phys. Solids*, 31, 1-24, (1983).
37. Norris, D. M., Moran, B., Scudder, J. K., and Quinones, D. F., "A Computer Simulation of the Tension Test," *J. Mech. Phys. Solids*, 26, 1-19, (1978).
38. Kleiber, "On Plastic Localization and Failure in Plane Strain and Round Void Containing Tensile Bars," *Int. J. Plasticity*, 2, 205-221, (1986).
39. Rice, J. R., and Tracey, D. M., "On the Ductile Enlargements of Voids in Triaxial Stress Fields," *J. Mech. Phys. Solids*, 17, 201, (1969).

40. McClintock, F. A., "A Criterion for Ductile Fracture by the Growth of Holes," *J. Appl. Mech.*, 35, 363, (1968).
41. Hancock, J. W. and MacKenzie, A. C., "On the Mechanisms of Ductile Rupture in High-Strength Steel Subjected to Multi-Axial Stress States," *J. Mech. Phys. Solids*, 24, 147, (1976).
42. Budiansky, B. and O'Connell, R. J., "Elastic Moduli of a Cracked Solid," *Int. J. of Solids and Structures*, 12, 81-97, (1976).
43. Nemat-Nasser, S. and Obata, M., "A Microcrack Model of Dilatency in Brittle Materials," *J. Appl. Mech.*, 55, 24-35, March 1988.
44. Griffith, A. A., "The Phenomena of Rupture and Flow in Solids," *Phil. Trans. of Royal Soc. of London*, 221, 163-198, (1920).
45. Dienes, J. K., "Comments on 'A Generalized Griffith Criterion for Crack Propagation,' by L. G. Margolin" - a Technical Note, *Eng. Fracture Mechanics*, 3, 23, 615-617, (1986).
46. Kanninen, M. F. and Popelar, C. H., "Advanced Fracture Mechanics," Oxford Univ. Press, NY, (1985).
47. Dietenberger, M., Antoun, T., and Rajendran, A. M., "Simulation of Uniaxial Stress Behavior for Arbitrary Strain Rate and Confining Stress Histories," *Shock Compression of Condensed Matter - 1991*, Elsevier Science Publishers, (1991).
48. Dietenberger, M. A., Rajendran, A. M., and Grove, D. J., "A Use of Microphysical Fracture Model to Describe Ceramic Material Upon Impact," *Shock Compression of Condensed Matter - 1989*, eds. S.C. Schmidt, J.N. Johnson, and L.W. Davison, Elsevier Science Publishers, 457-460, (1989).
49. Rajendran, A. M., Dietenberger, M. A., and Grove, D. J., "Microphysical Model to Describe Impact Behavior of Ceramics," Constitutive Laws for Engineering Materials, eds. C. S. Desai et al., ASME Press, 609-612, (1991).
50. Cook, W. H., Rajendran, A. M., and Grove, D. J., "An Efficient Implementation of the Bodner-Partom Model in an Explicit Finite Element Code," to appear in *J. of Eng. Fracture Mechanics*, (1992).
51. Rajendran, A. M., Grove, D. J., Dietenberger, M. A., and Cook, W. H., "A Dynamic Failure Model for Ductile Materials," AFATL-TR-90-84, Eglin Air Force Base, FL, (1990).

Appendix A

Split Hopkinson Bar and Plate Impact Data

This section comprises a compendium of experimental data obtained during the course of this investigation. The SHB data are presented in terms of plots of stress versus log strain rate for a given value of strain for several metals. The plate impact data are in terms of plots of measured stress versus time for several metals. Brief descriptions of both these test techniques are also presented in this section.

A.1 Split Hopkinson Bar (SHB)

The SHB apparatus consists of a striker bar that is made to impact end-to-end onto the pressure bar. The impact produces a stress wave in the pressure bar whose duration is twice the acoustic transit time of the striker bar (0.3 ms in the bar used at the University of Dayton Research Institute). The specimen is placed at the other end of the pressure bar (bar 1) as shown in Figure A.1a. The specimen is also connected to the transmission bar (bar 2). The striker, pressure, and transmission bars are all the same material and diameter (12.7-mm diameter Inconel in these experiments). The stress wave that travels down the pressure bar is partially transmitted and partially reflected by the specimen. The reflected and transmitted waves in the bars are detected by strain gauges. Analysis of the strain-gauge signals yields the load and displacement history of the specimen. Detailed discussions on the strain-gauge analysis can be found in References [A.1] and [A.2].

For tensile measurements, a collar is placed around the specimen, and the specimen is screwed into the pressure and transmission bars. (See Figure A.1b.) The initial compression wave is transmitted through the collar, and reflects as a tensile wave. When the tensile wave returns to the specimen, the collar falls away and the specimen sustains the tensile load. The data from the Hopkinson-bar strain gauges are used to calculate engineering stress and strain in the sample, which are converted to true stress and strain until the onset of localized deformation (necking) by using the conventional relationships.

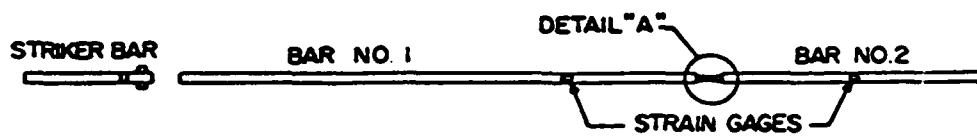


Figure A.1a. A Schematic of the Split Hopkinson Bar Setup.

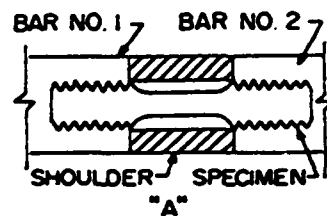


Figure A.1b. SHB Tensile Specimen Configuration.

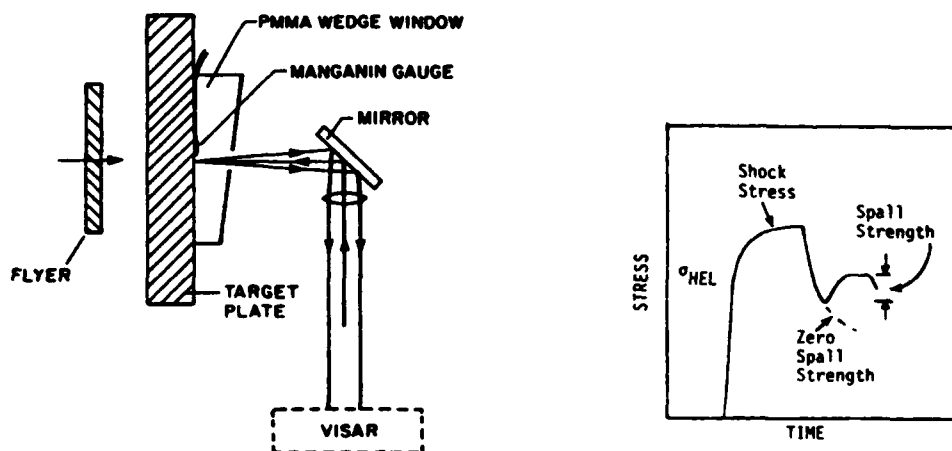


Figure A.2. A Schematic of the Plate Impact Test Configuration

A.2 Plate Impact Experiments

Many discussions of planar impact loading are available (References [A.3] and [A.4]). Plate impact tests provide a loading path that is very different from conventional SHB compression or tension tests. The deformation is that of one-dimensional strain, and the mean stress is generally very high compared to that in SHB tests. Strain rates are 10^5 s^{-1} or higher. The material undergoes compression immediately followed by tension. Thus, plate impact experiments are essential for calibrating and validating high strain rate material models that aspire to general applicability. Specifically, plate impact data may be interpreted to infer compression and tensile yield strengths and failure parameters.

The plate impact tests were conducted with three objectives: (1) determination of Hugoniot Elastic Limit, (2) determination of the unloading path from the free surface velocity history, and (3) determination of the threshold conditions associated with onset of spall fracture.

Impact induces an elastic shock and a plastic shock in the target. The amplitude of the elastic shock is σ_{HEL} . The Hugoniot elastic limit, σ_{HEL} , is the maximum stress for one-dimensional elastic wave propagation. This stress level is a material property, and above this level the material flows plastically. The stress σ_{HEL} can be determined from the experimentally obtained free surface velocity of the target that corresponds to the elastic shock, u_{HEL} .

$$\sigma_{HEL} = \frac{1}{2} \rho c_L u_{HEL} \quad (\text{A.1})$$

where c_L is the elastic sound speed. However, when a stress gauge is used to measure σ_{HEL} we need the impedance match solution to interpret the data. Since the measured stress is the stress that is transmitted into the PMMA wedge window (see Figure A.2), this σ_{HEL}^P of the PMMA must be multiplied by a factor in order to obtain the σ_{HEL} of the target material. The corresponding impedance relationship is,

$$\sigma_{HEL} = \left(\frac{Z_T + Z_P}{2Z_P} \right) \sigma_{HEL}^P \quad (\text{A.2})$$

where Z_T and Z_P are the impedance (ρc) of the target and PMMA, respectively. In our experiments, $Z_P = 33.5 \times 10^5 \text{ Pa-sec/m}$.

A.3 Materials Data

The plots of strength variation with respect to strain rate for several metals are given in Figures A.3 - A.25. This data is presented in terms of effective stress versus strain rate for a given strain level. This data is generated from quasi-static and Split Hopkinson bar terms.

The measured stress versus time histories from plate impact tests for several metals and ceramics are plotted in Figures A.26 - A.45. This data is valuable for material model validation.

A.4 References

- A.1. Nicholas, T., "Tensile Testing of Materials at High Rates of Strain," *Exp. Mech.*, 21, 177-185, (1981).
- A.2. Lindholm, U. S., "Some Experiments with the Split Hopkinson Pressure Bar," *J. Mech. Phys. Solids*, 12, 317-335, (1964).
- A.3. Karnes, C. H., "The Plate Impact Configuration for Determining Mechanical Properties of Materials at High Strain Rates," Mechanical Behavior of Materials under Dynamic Loads, ed. U. S. Lindholm, Springer-Verlag, NY, (1968).
- A.4. Asay, J. R. and Lipkin, J., "A Self Consistent Technique for Estimating the Dynamic Yield Strength of a Shock Loaded Material," *J. Appl. Phy.*, 49, 4242, (1978).

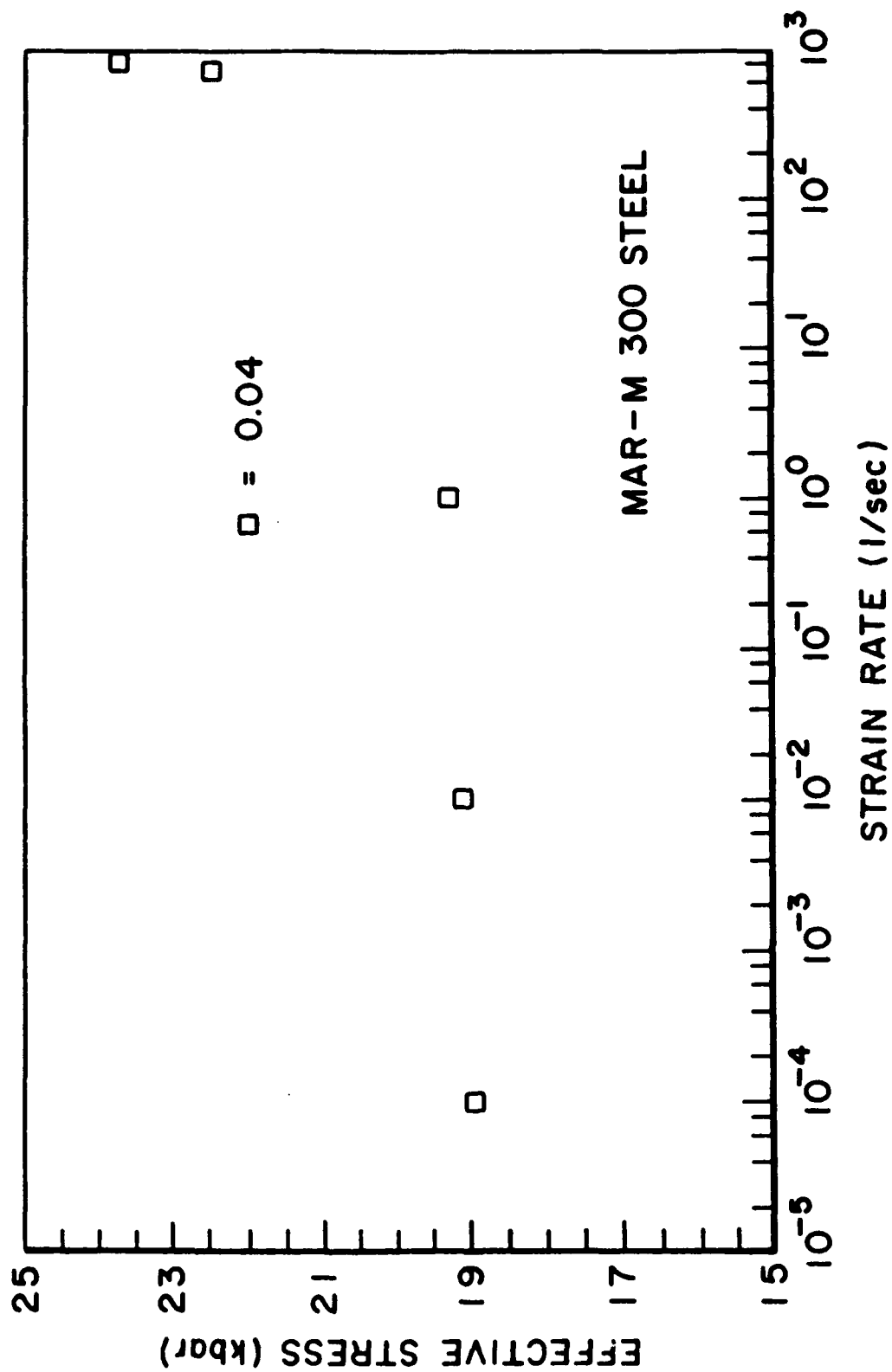


Figure A-3 Stress (strength) versus strain rate for MAR-M 300 Steel

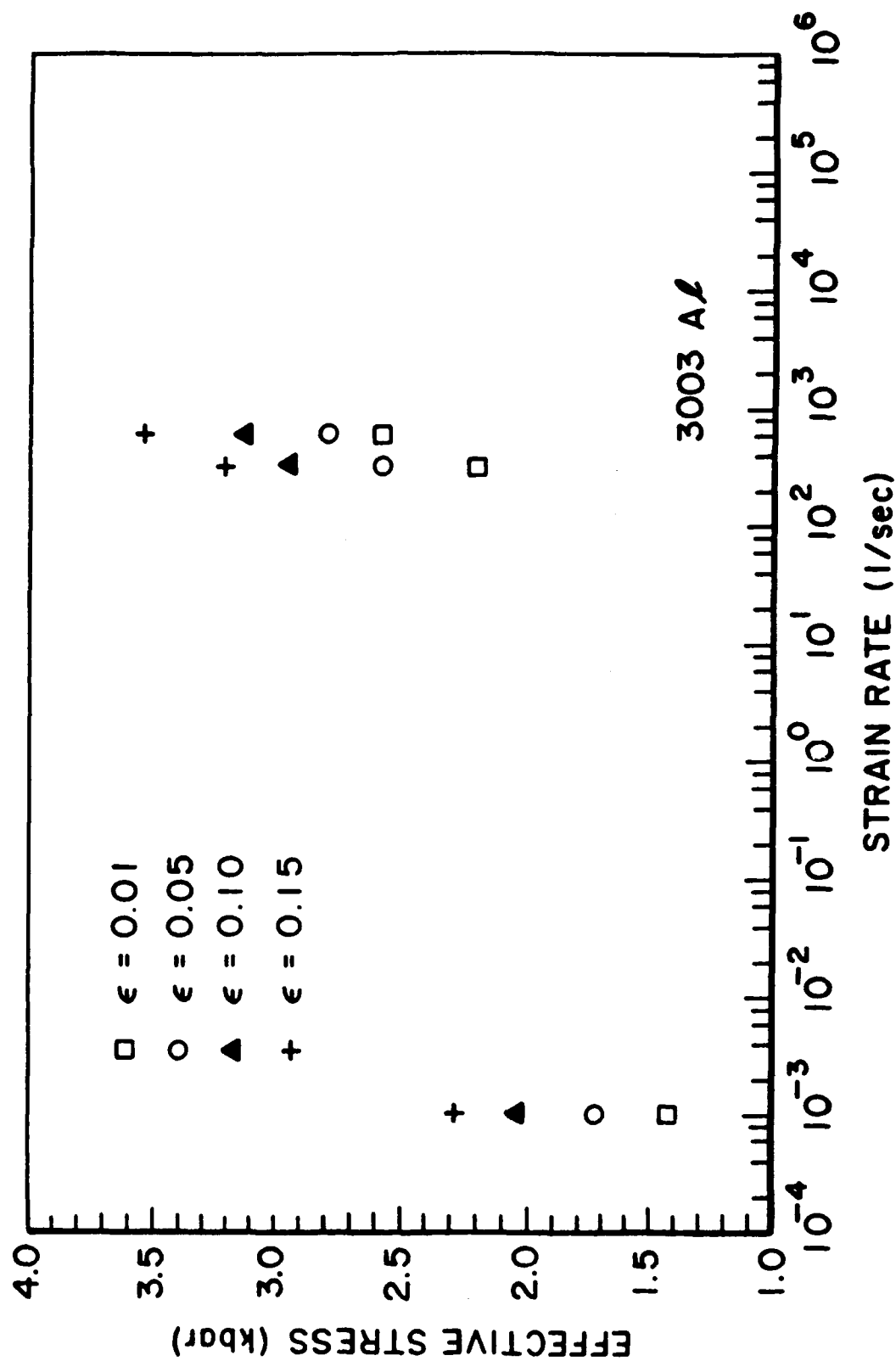


Figure A-4 Stress (strength) versus strain rate for 3003 Aluminum

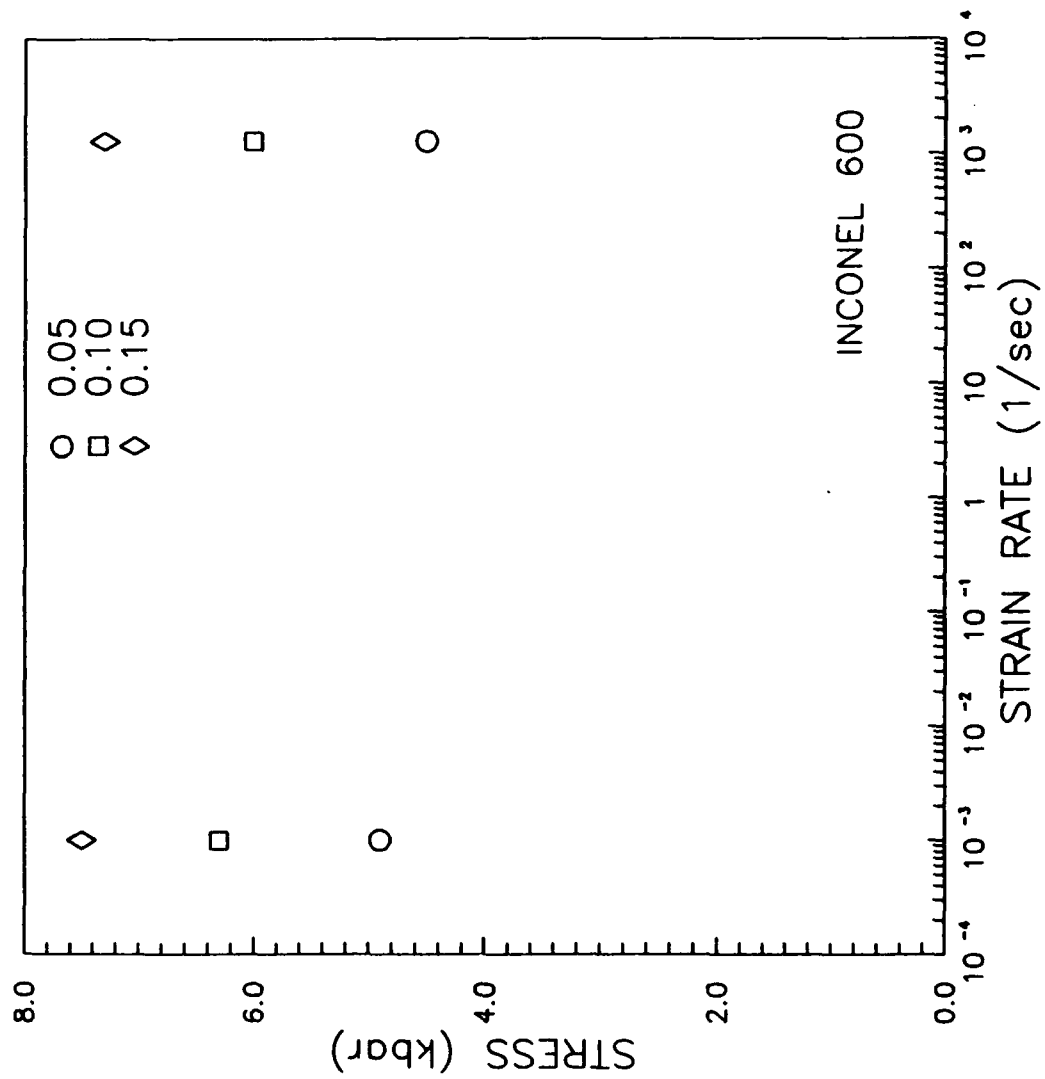


Figure A-5 Stress (strength) versus strain rate for Inconel 600

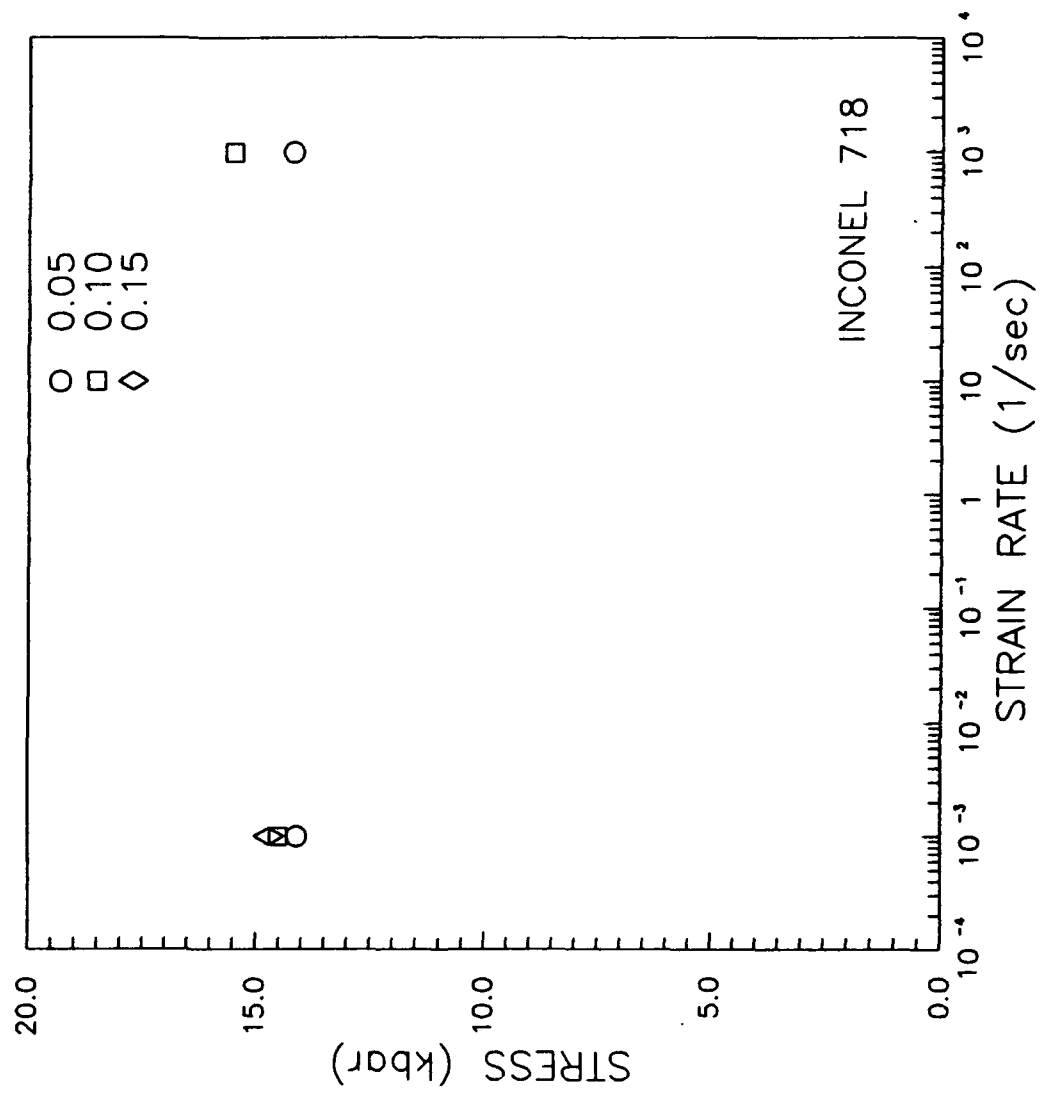


Figure A-6 Stress (strength) versus strain rate for Inconel 718

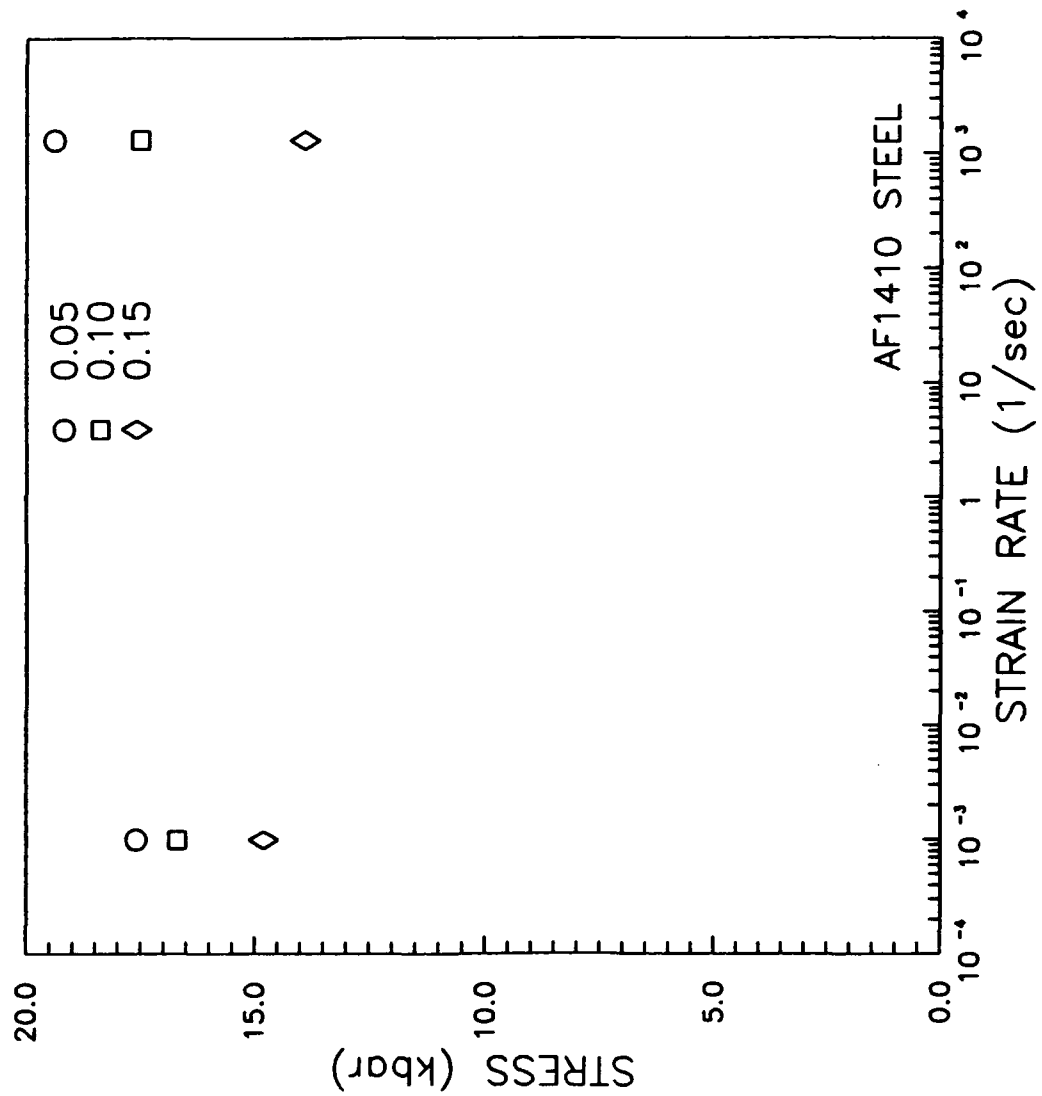


Figure A-7 Stress (strength) versus strain rate for AF1410 Steel

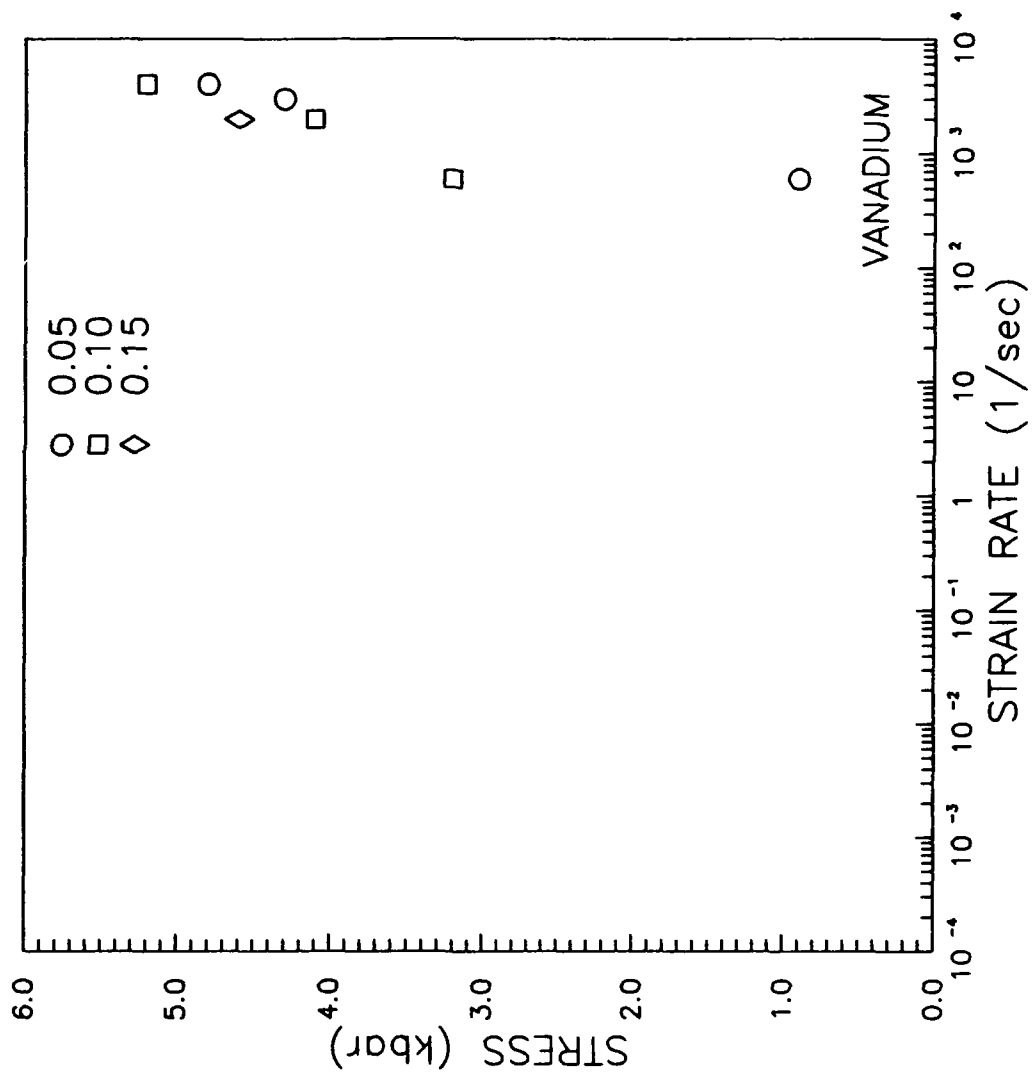


Figure A-8 Stress (strength) versus strain rate for Vanadium

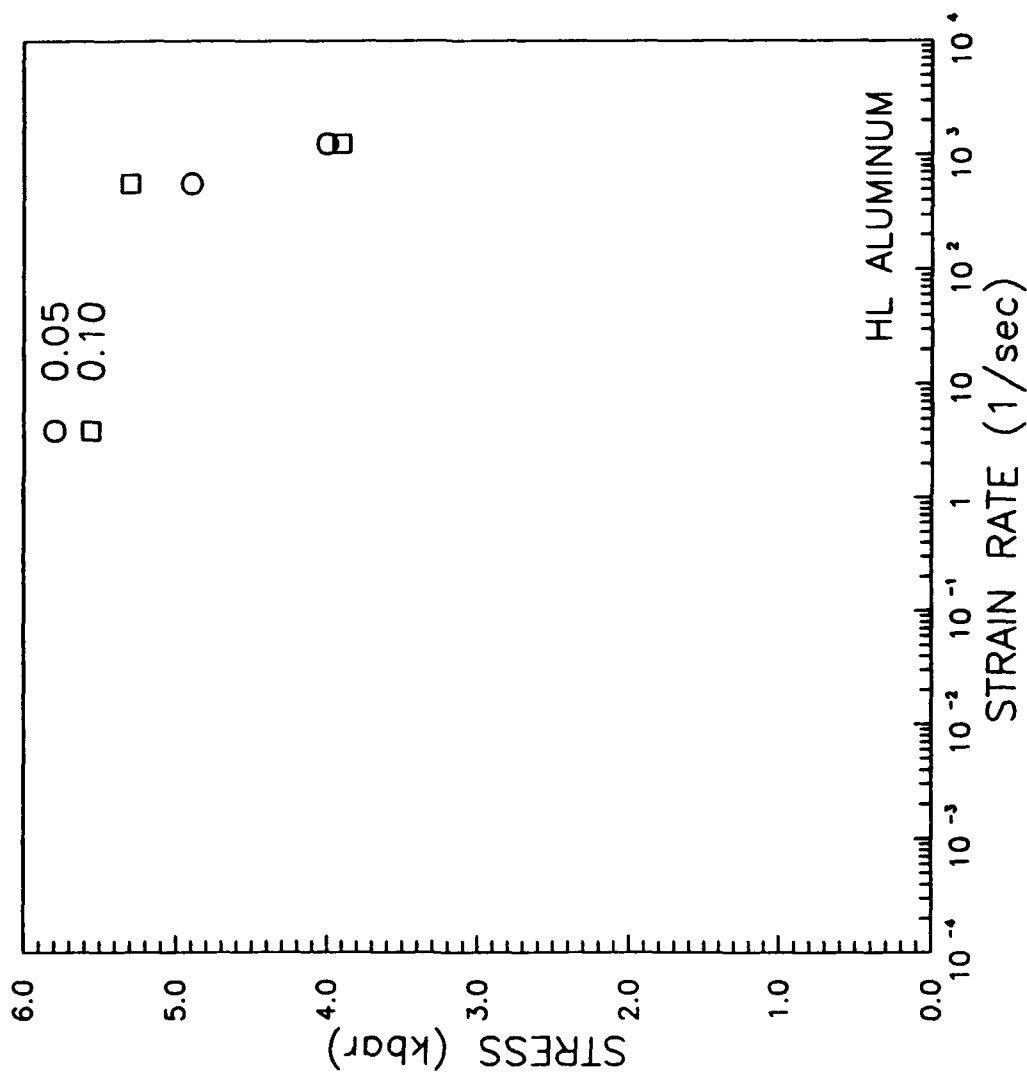


Figure A-9 Stress (strength) versus strain rate for HL Aluminum

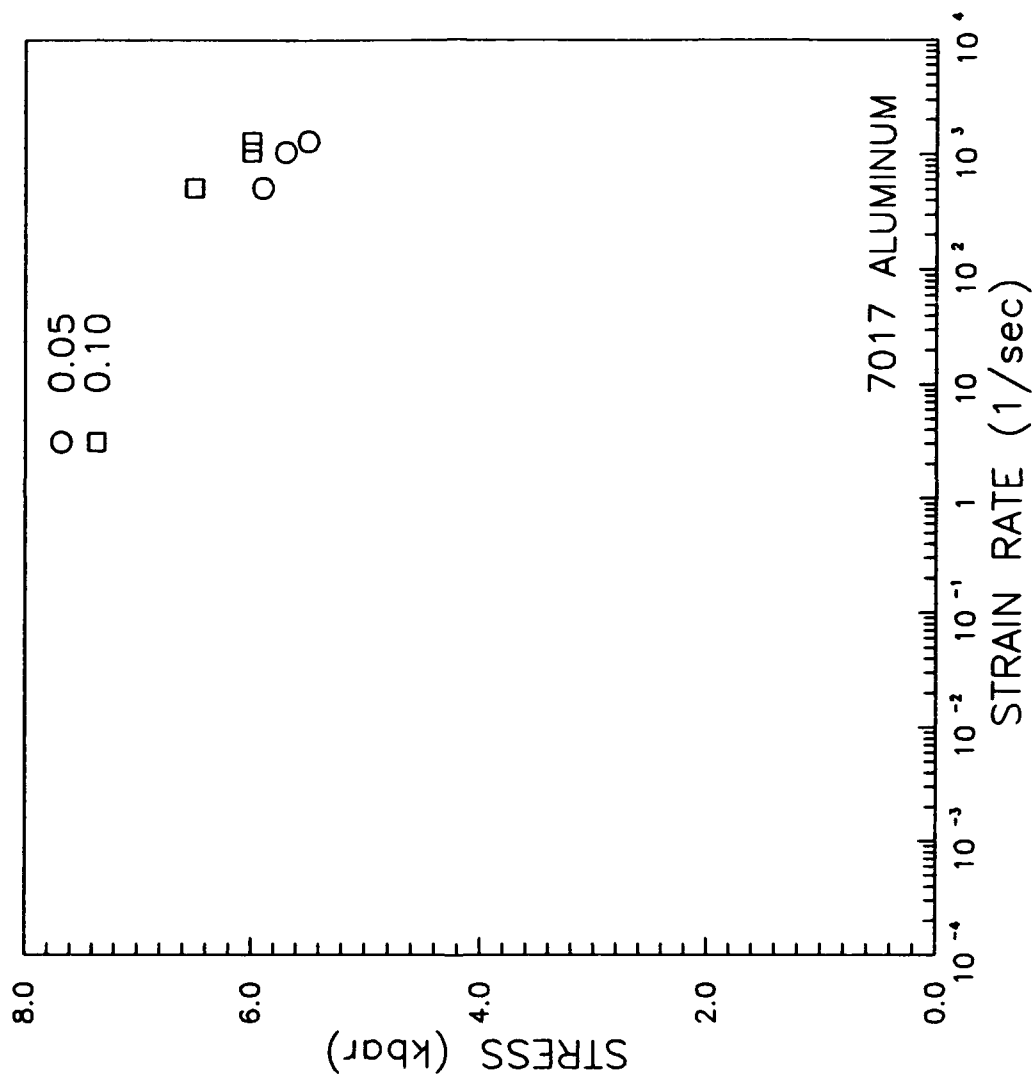


Figure A-10 Stress (strength) versus strain rate for 7017 Aluminum

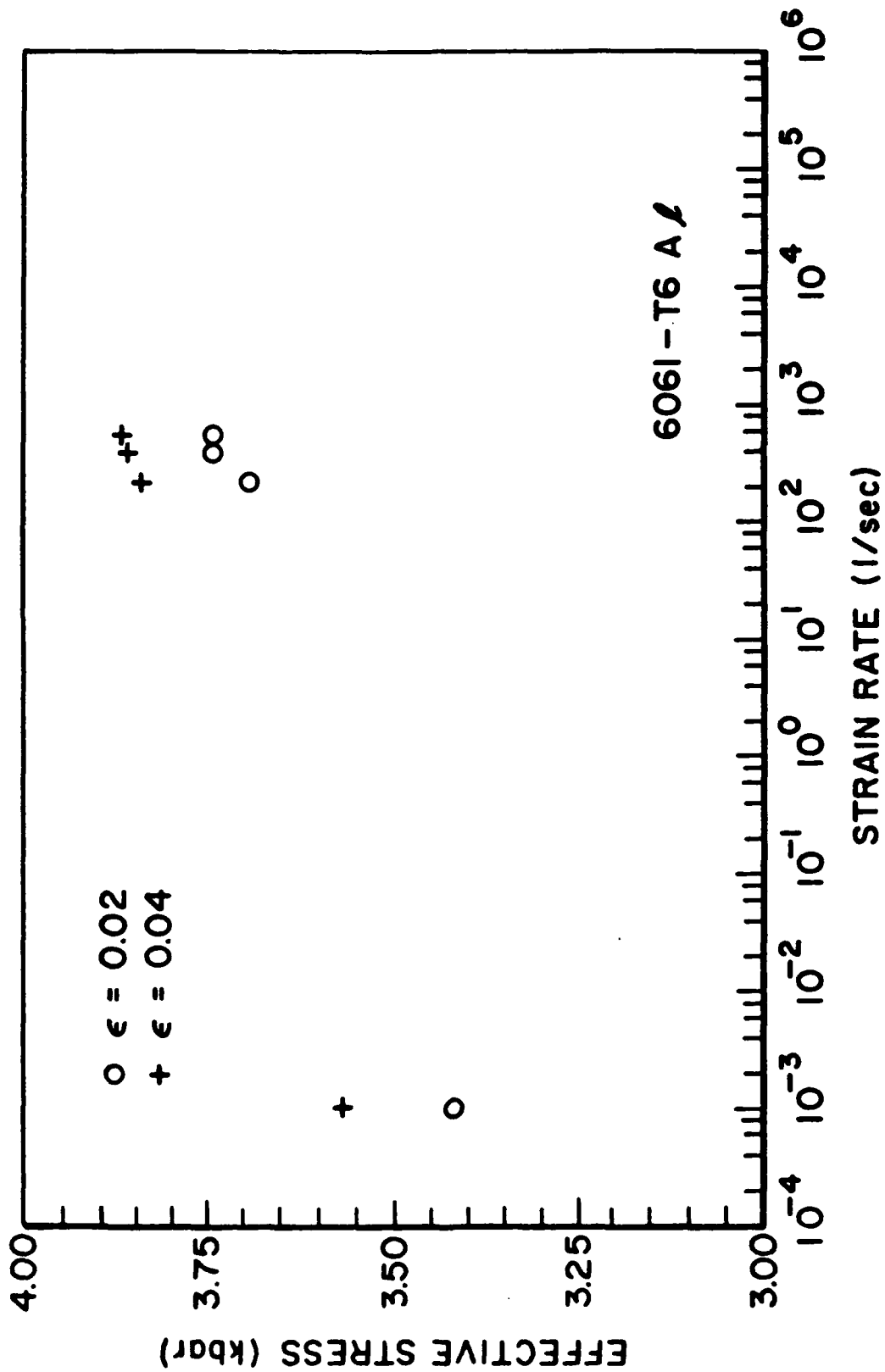


Figure A-11 Stress (strength) versus strain rate for 6016-T6 Aluminum

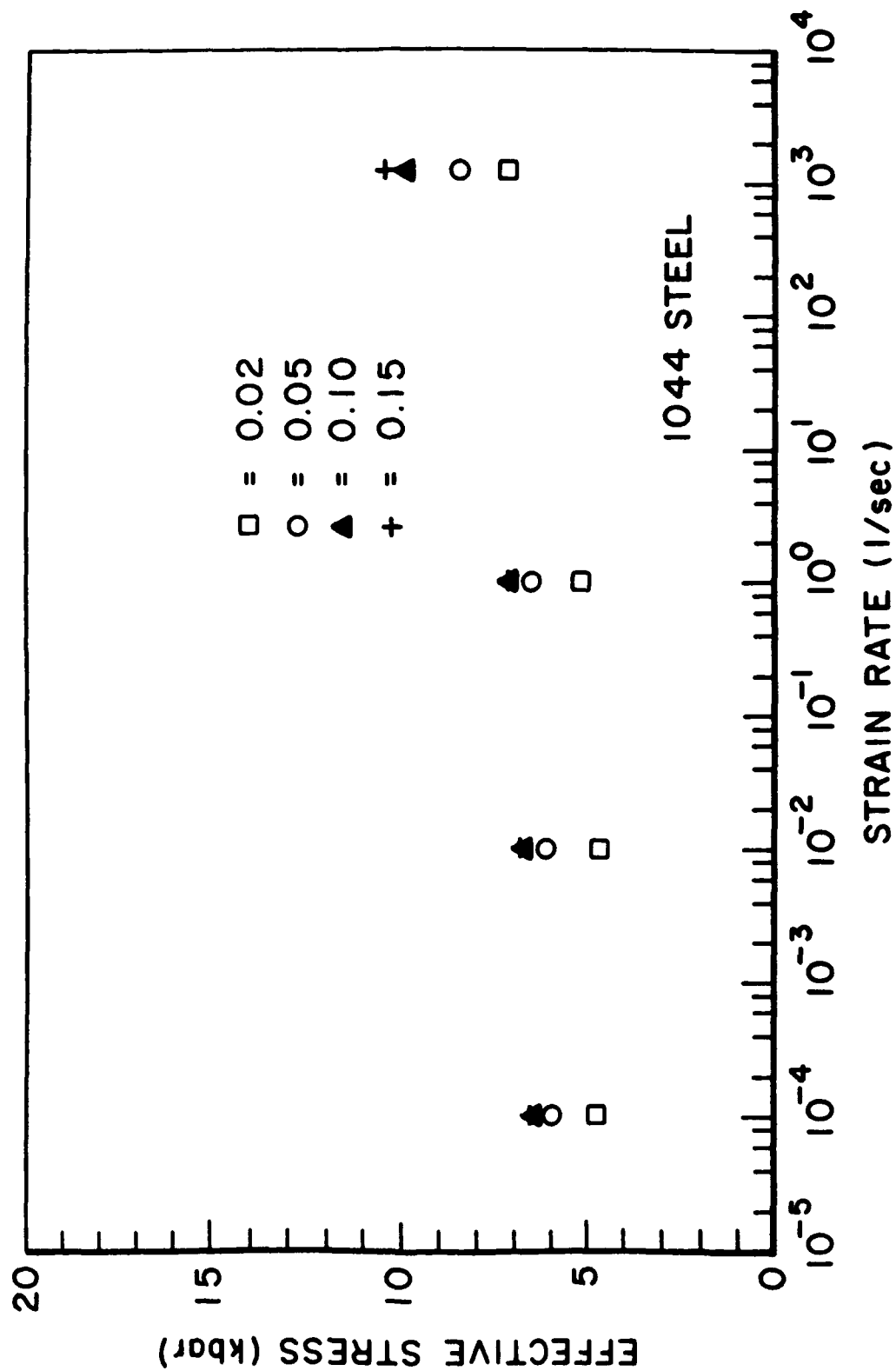


Figure A-12 Stress (strength) versus strain rate for 1044 Steel

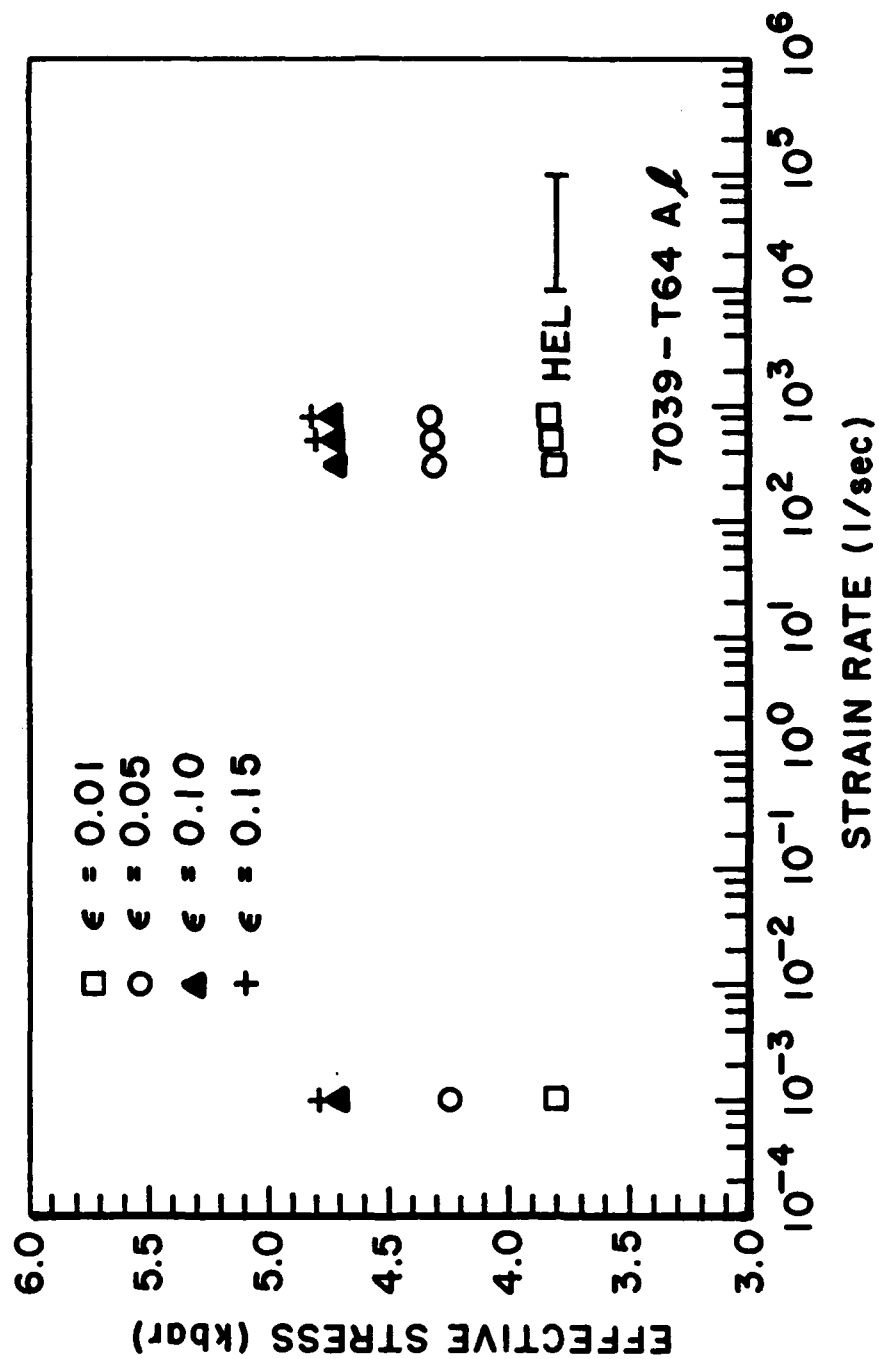


Figure A-13 Stress (strength) versus strain rate for 7039-T64 Aluminum

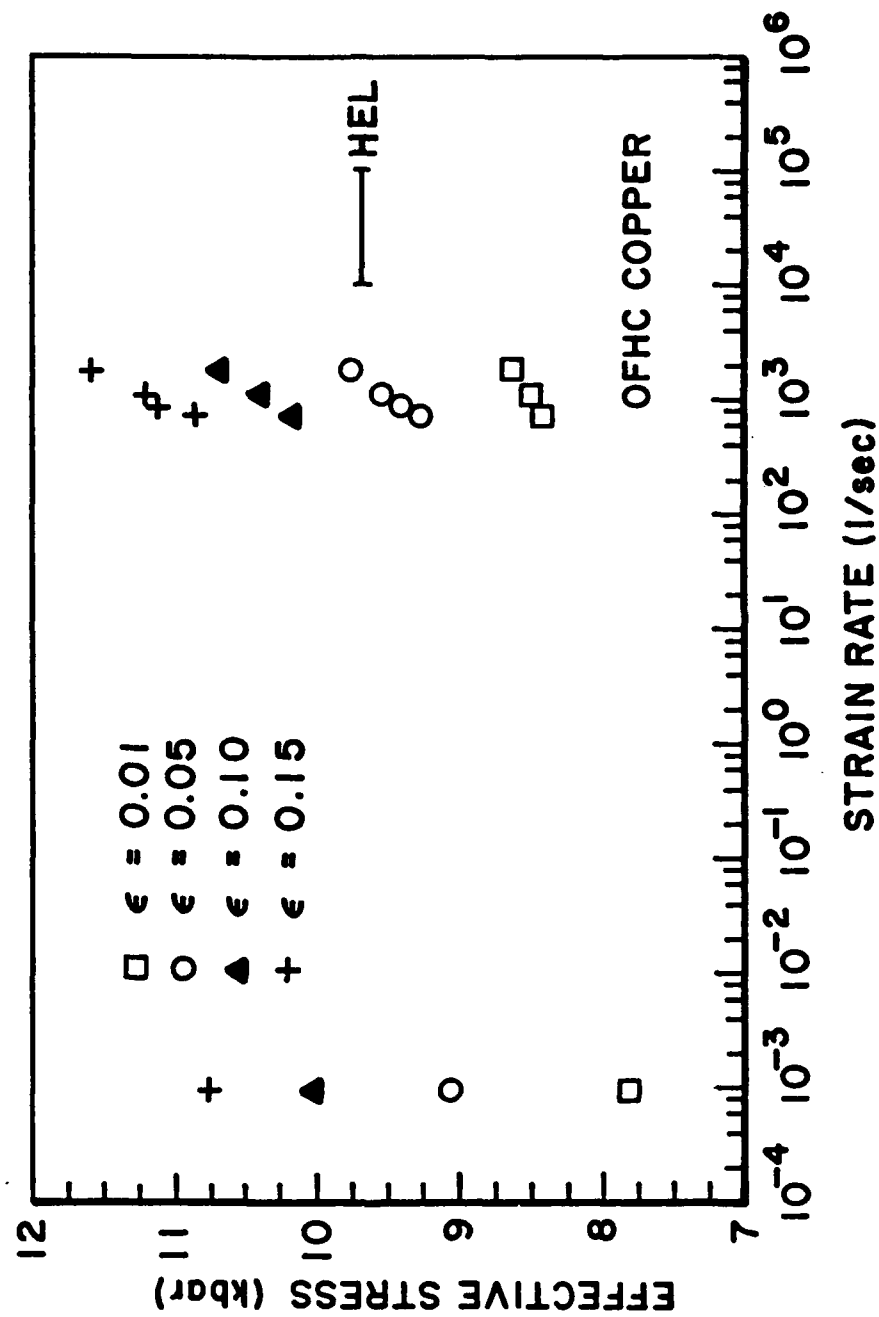


Figure A-14 Stress (strength) versus strain rate for OFHC Copper

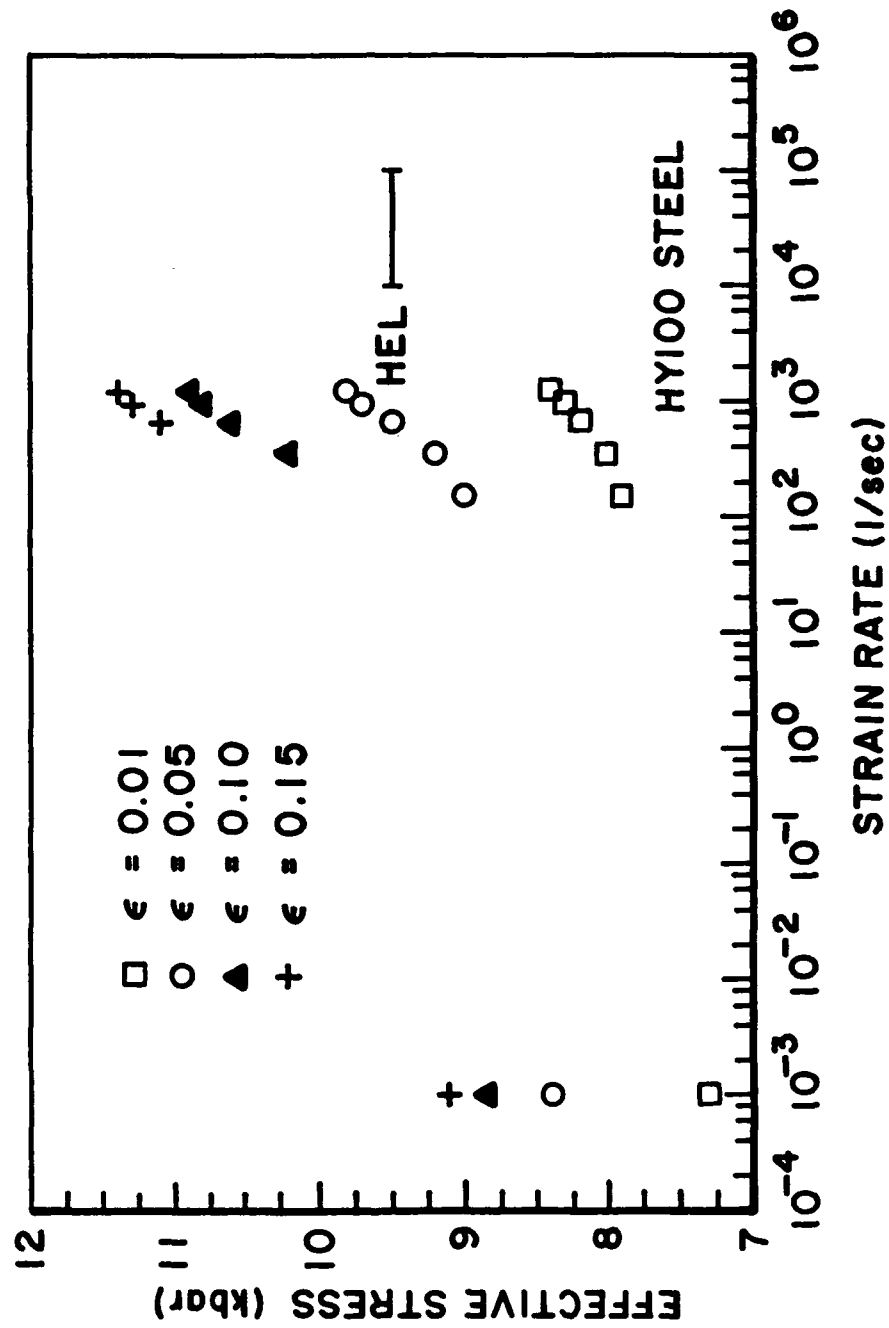


Figure A-15 Stress (strength) versus strain rate for HY100 Steel

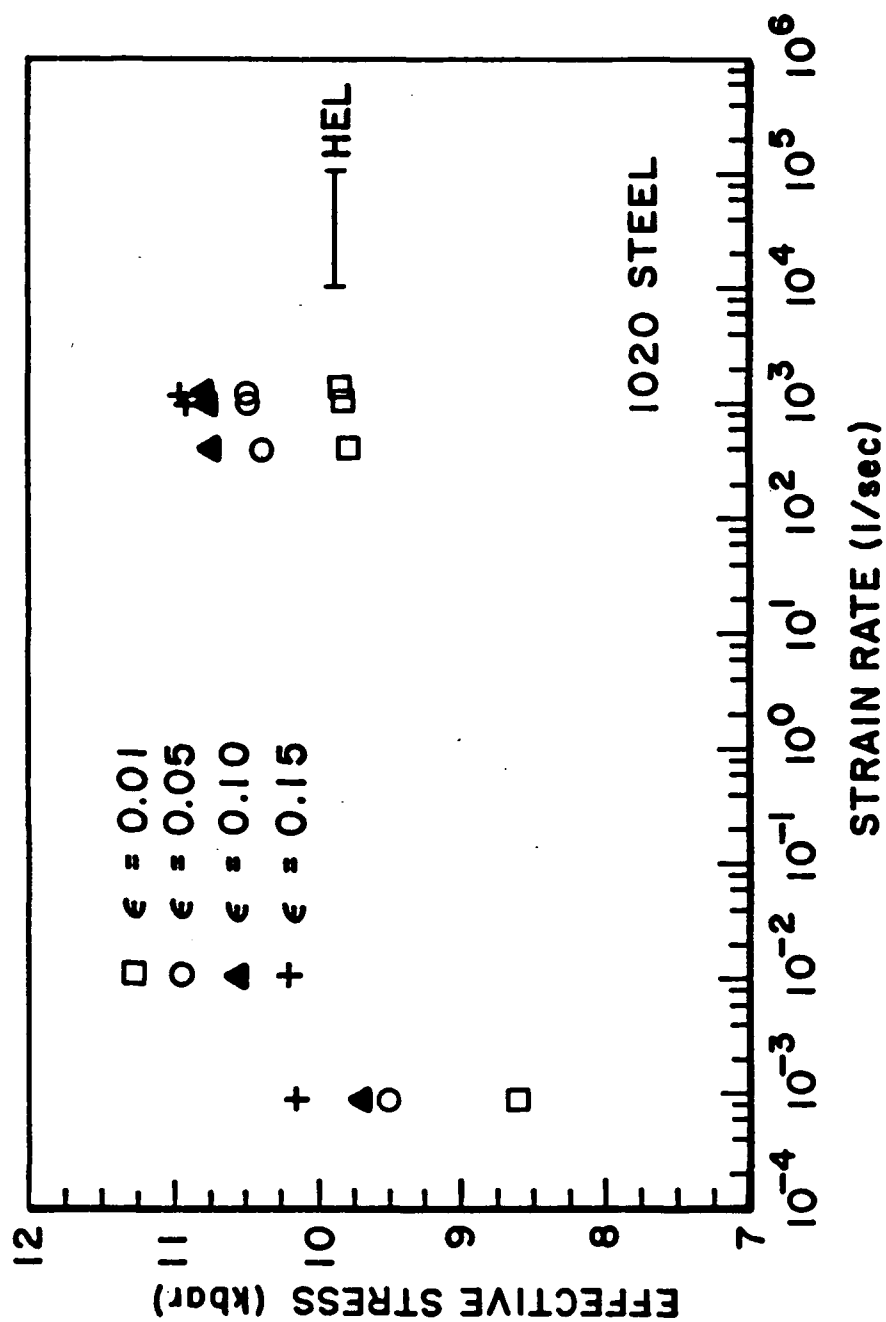


Figure A-16 Stress (strength) versus strain rate for 1020 Steel

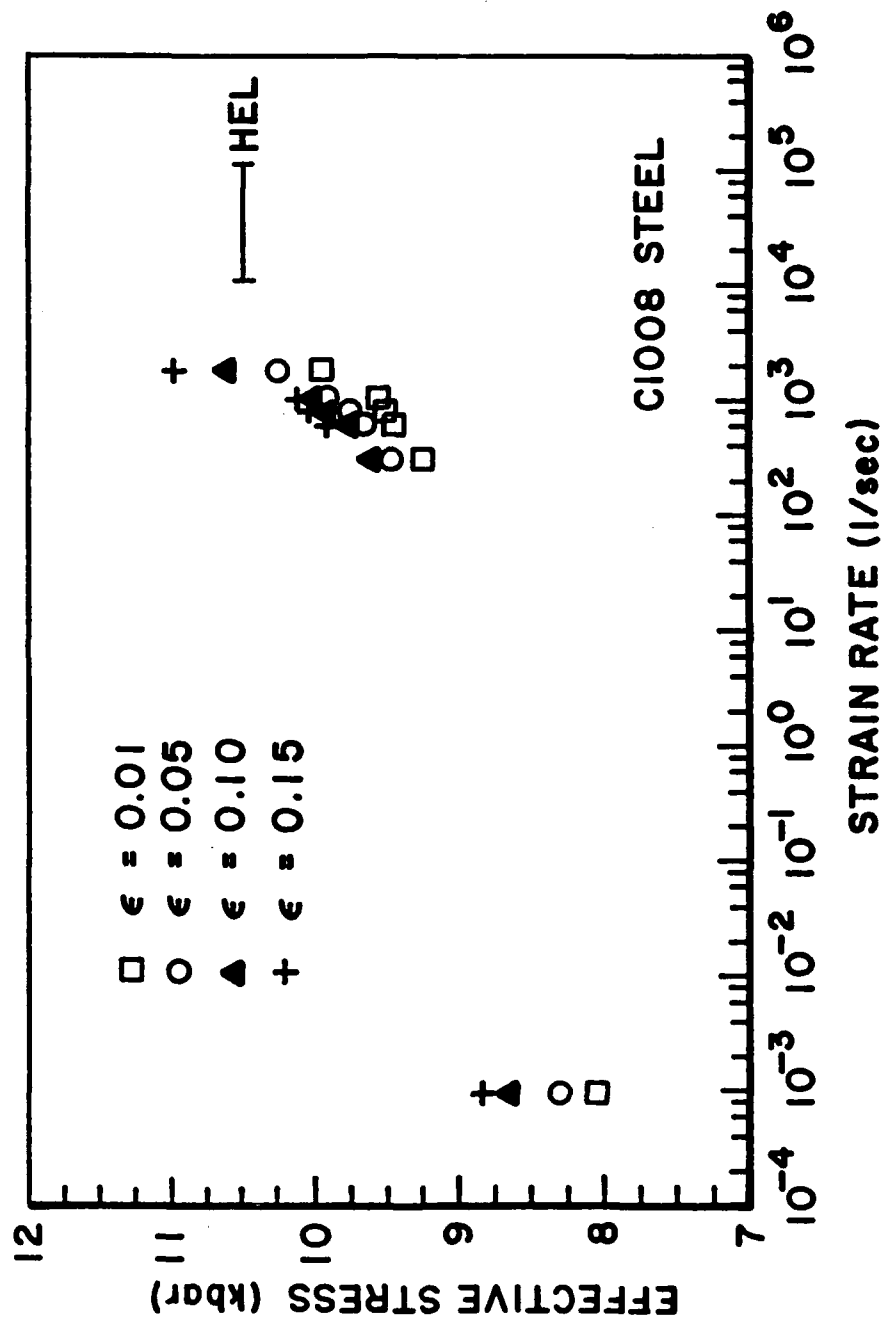


Figure A-17 Stress (strength) versus strain rate for C1008 Steel

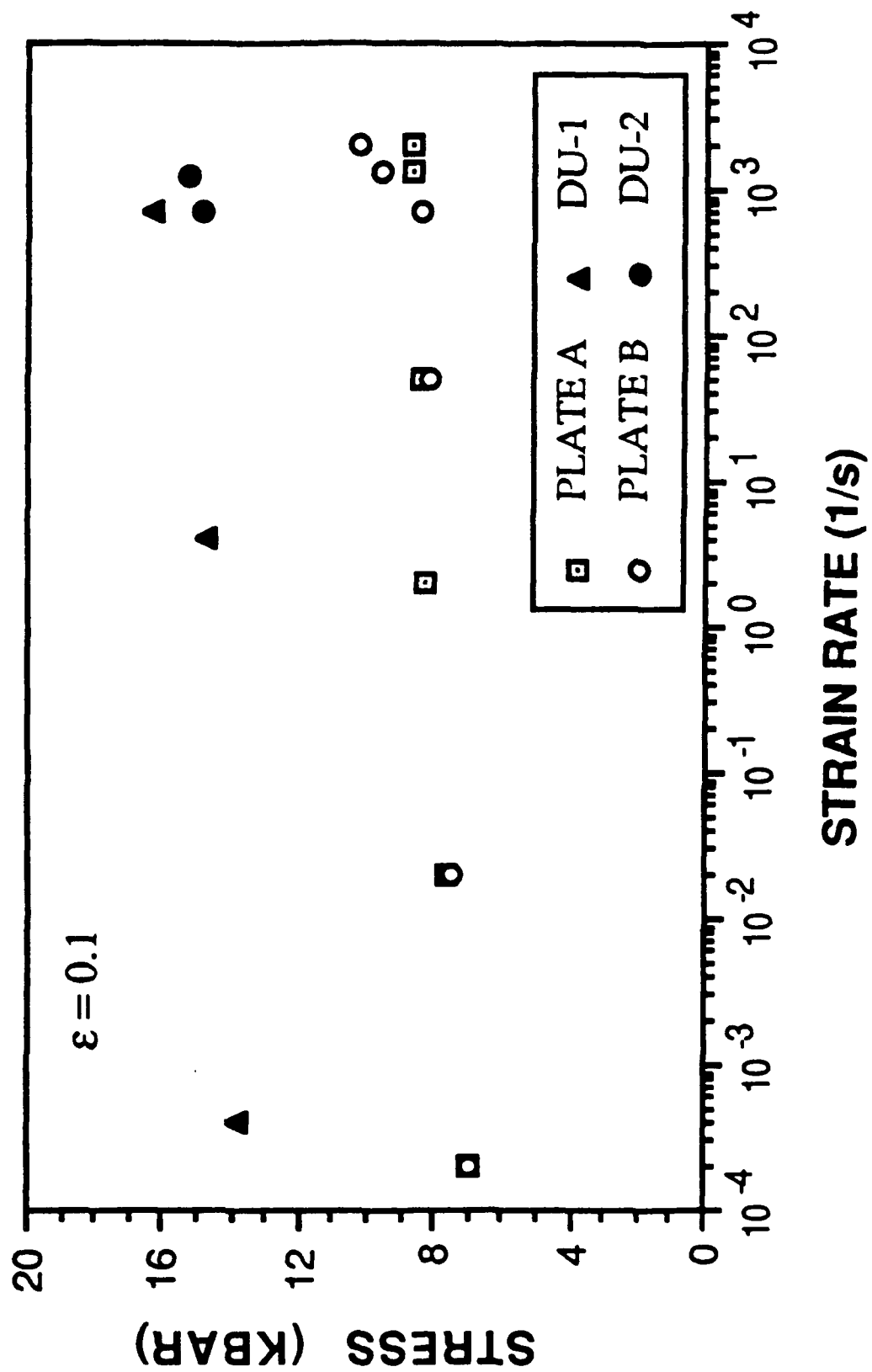


Figure A-18 Stress (strength) versus strain rate for Plate A and B, DU1 and DU2

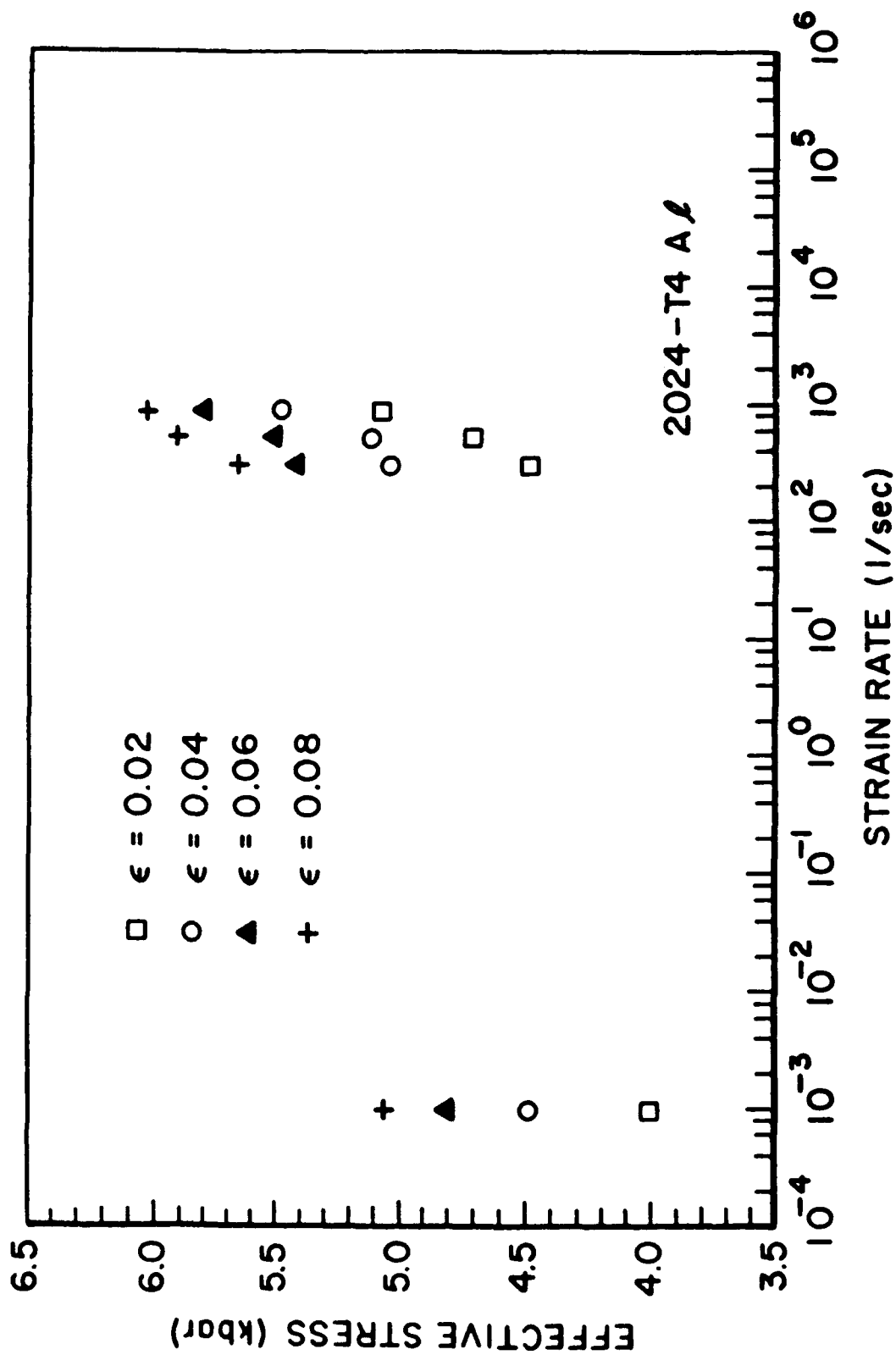


Figure A-19 Stress (strength) versus strain rate for 2024-T6 Aluminum

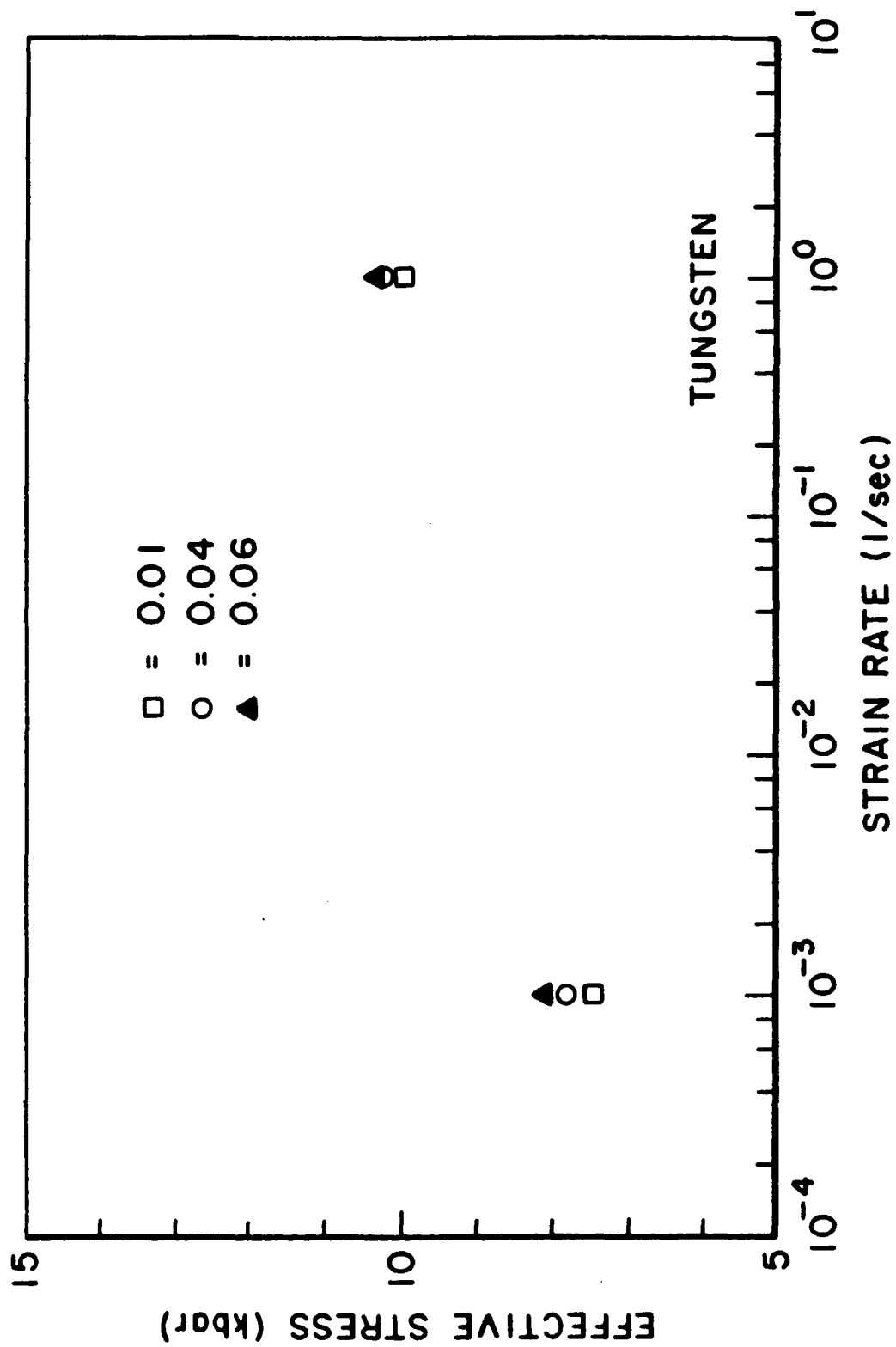


Figure A-20 Stress (strength) versus strain rate for Tungsten

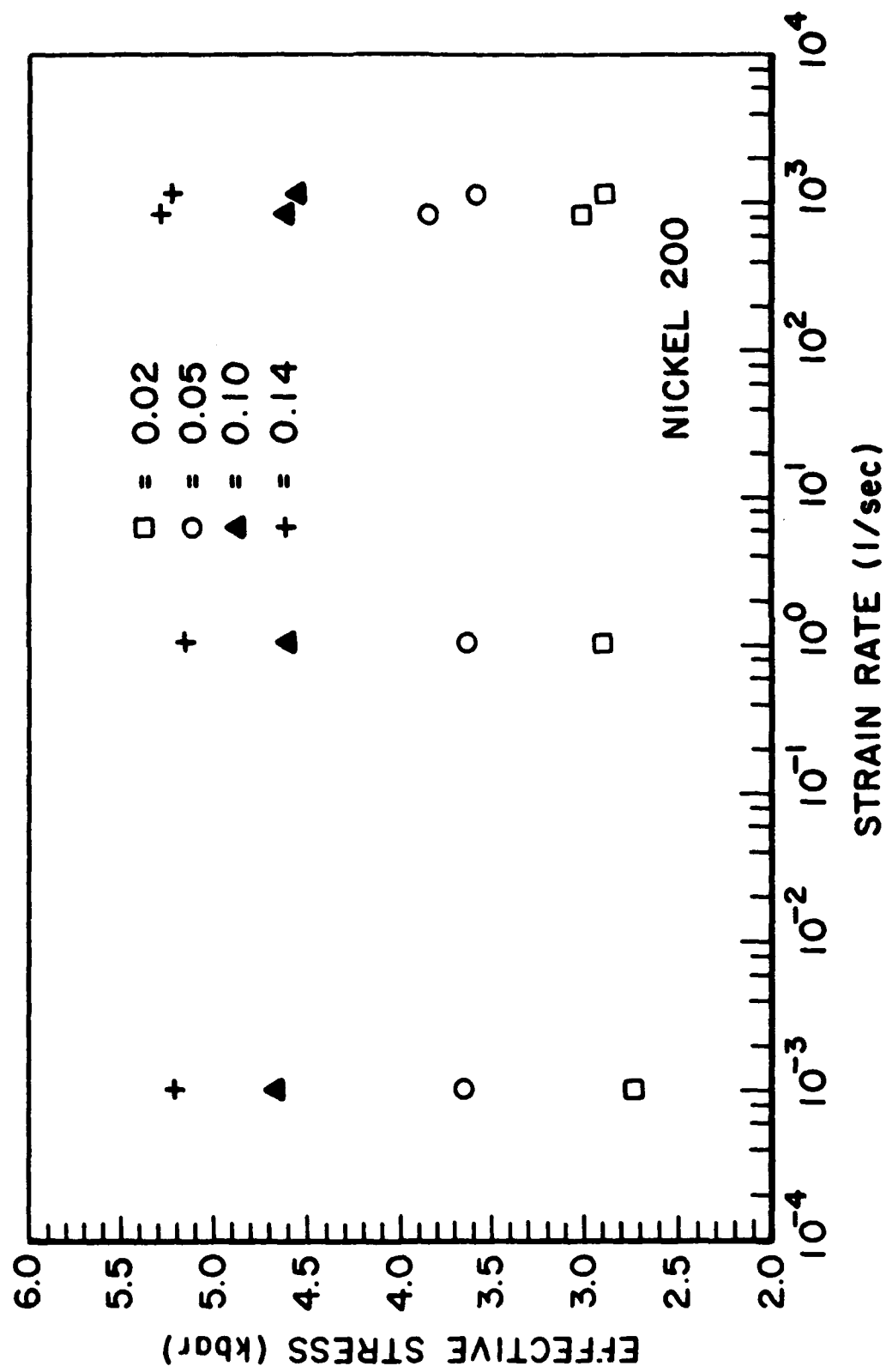


Figure A-21 Stress (strength) versus strain rate for Nickel

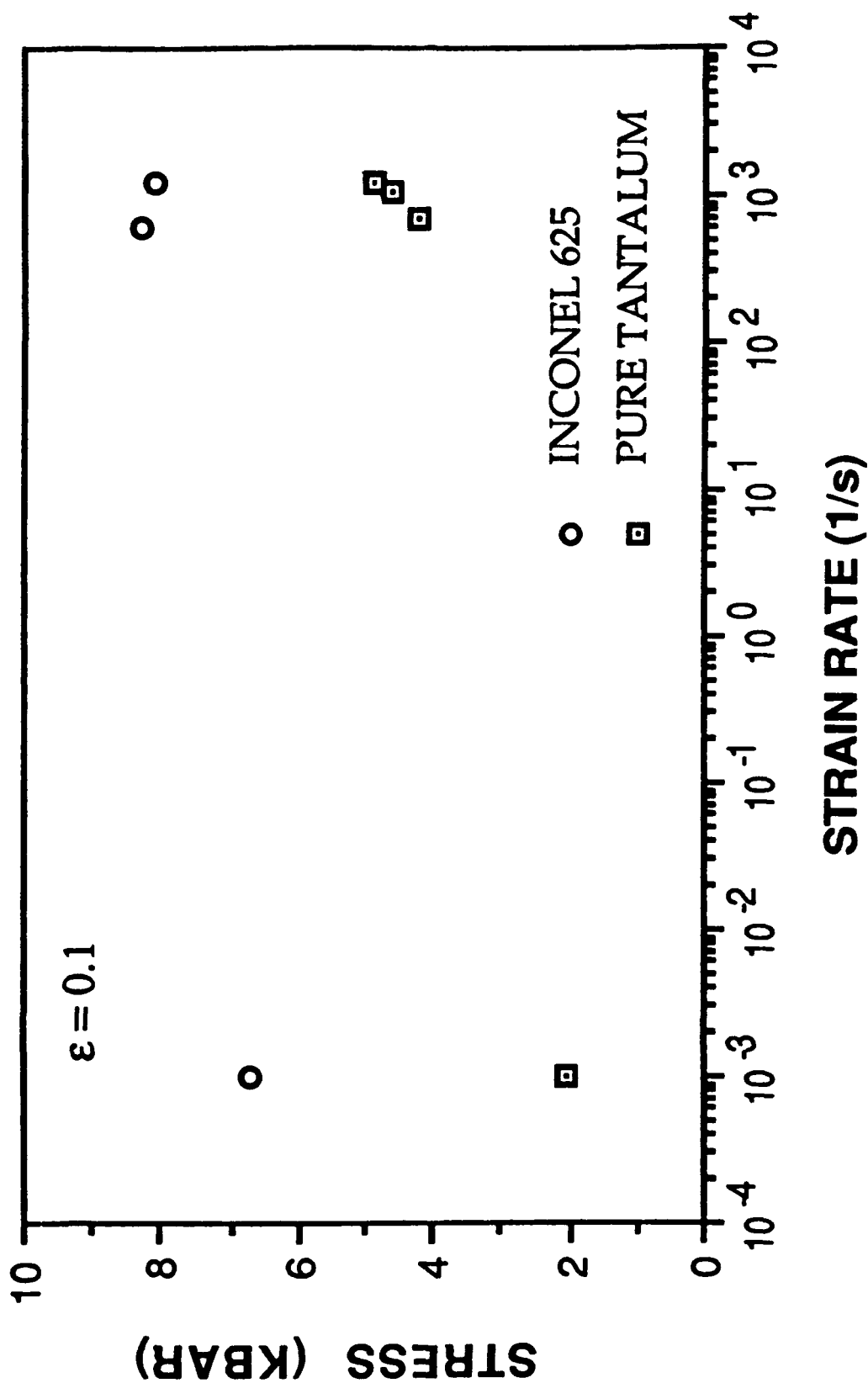


Figure A-22 Stress (strength) versus strain rate for Inconel 625 and pure Tantalum

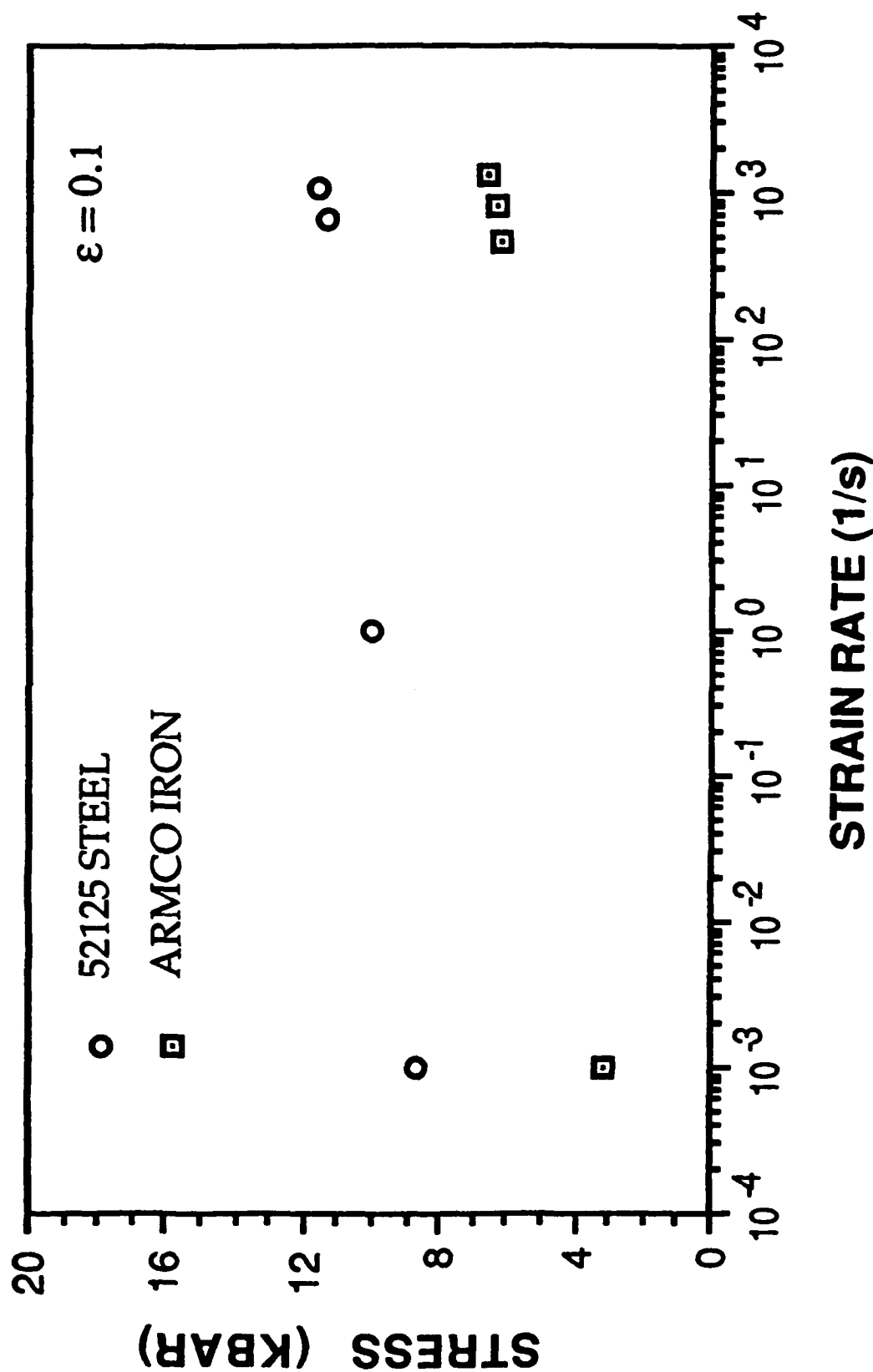


Figure A-23 Stress (strength) versus strain rate for 52125 Steel and Armco Iron

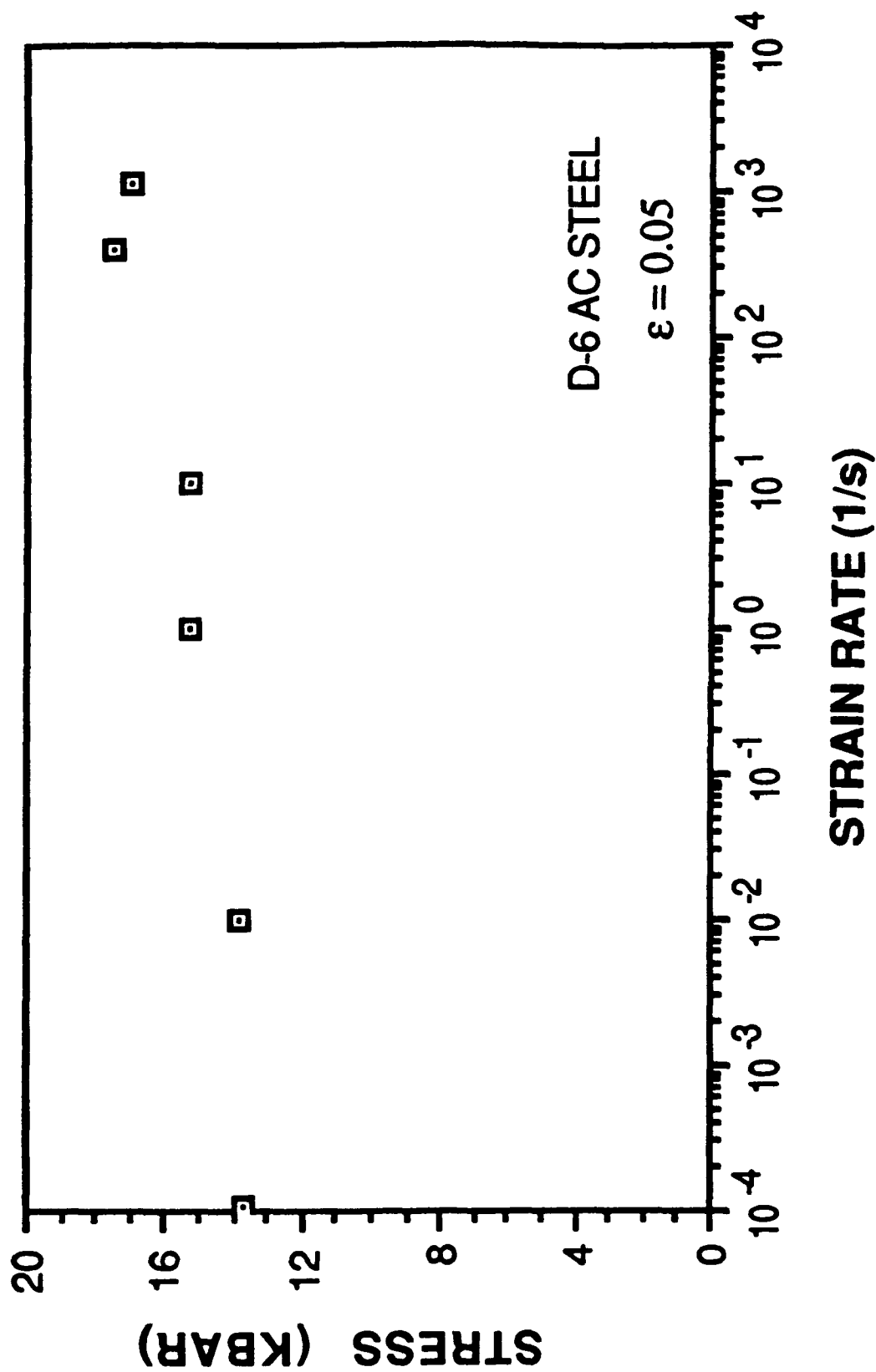


Figure A-24 Stress (strength) versus strain rate for D-6AC Steel

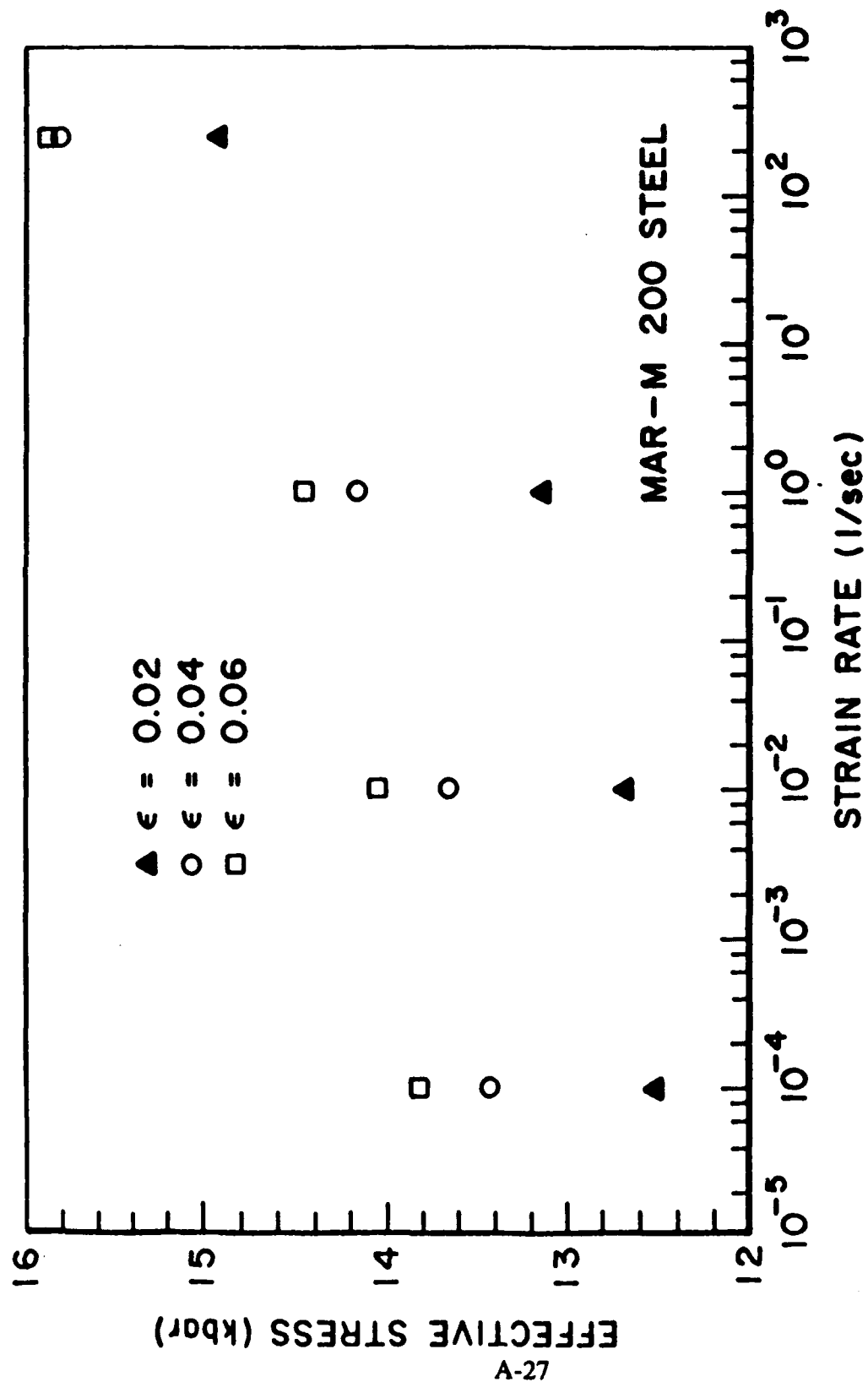


Figure A-25 Stress (strength) versus strain rate for MAR-M 200 Steel

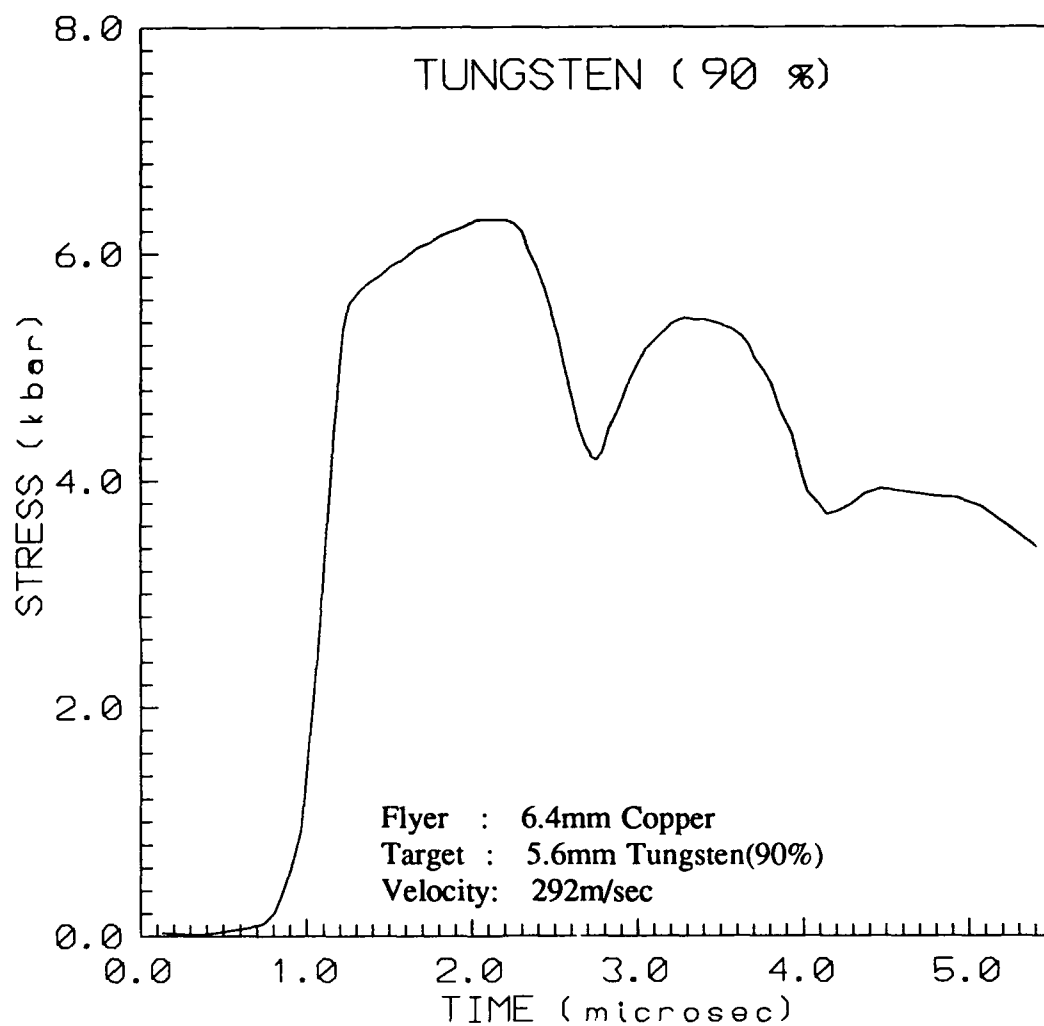


Figure A-26 Gage stress-time history for Tungsten (90%) plate impact test

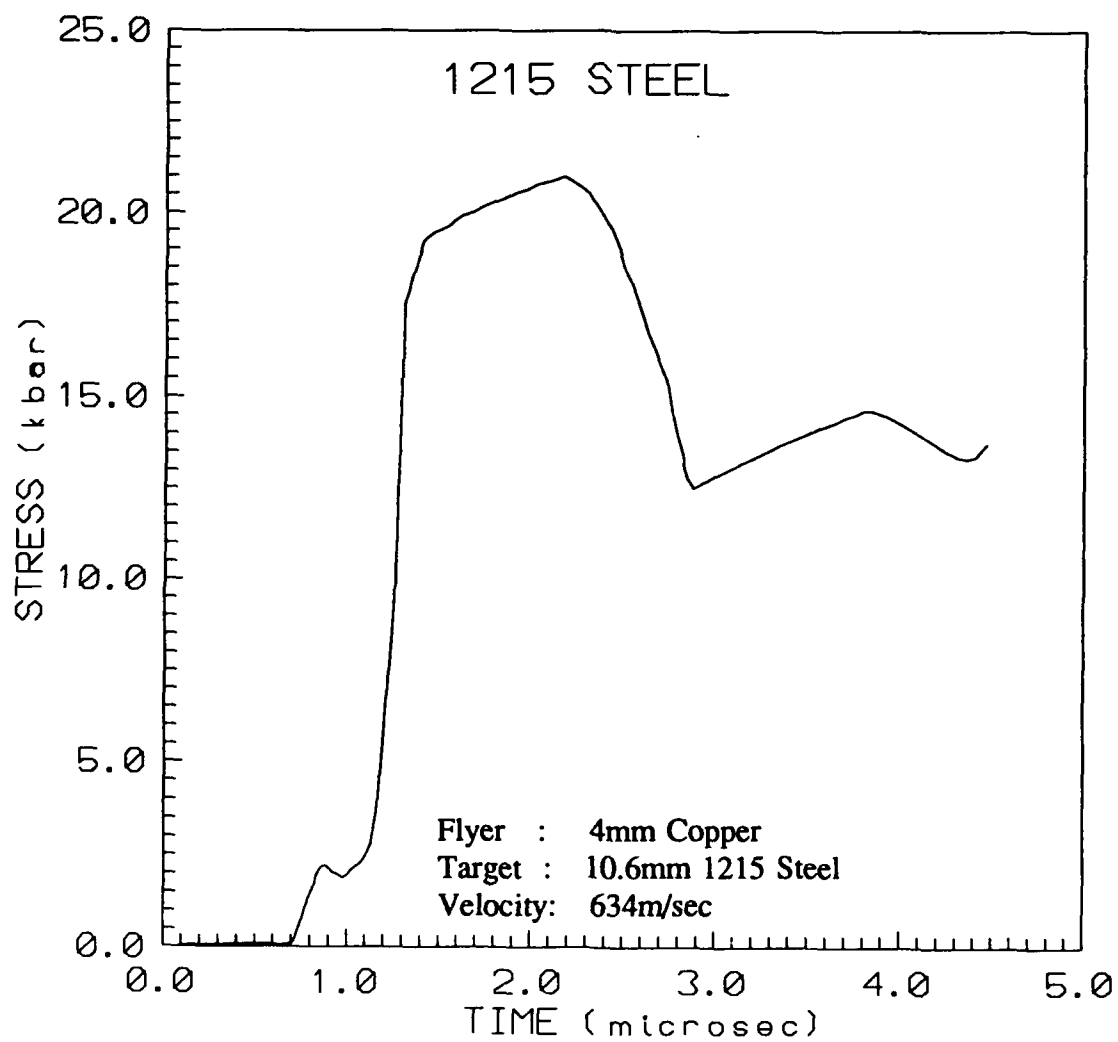


Figure A-27 Gage stress-time history for 1215 Steel plate impact test

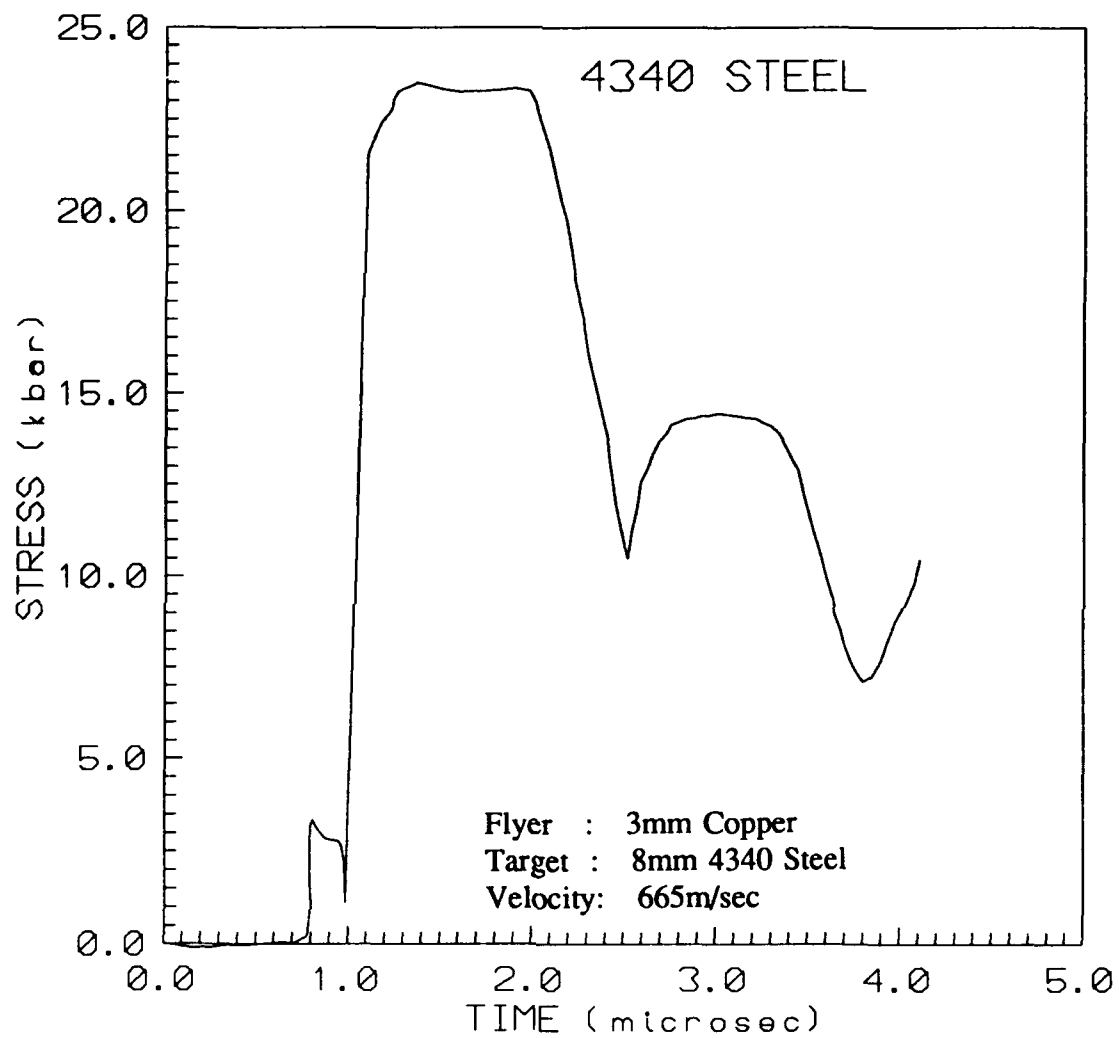


Figure A-28 Gage stress-time history for 4340 Steel plate impact test

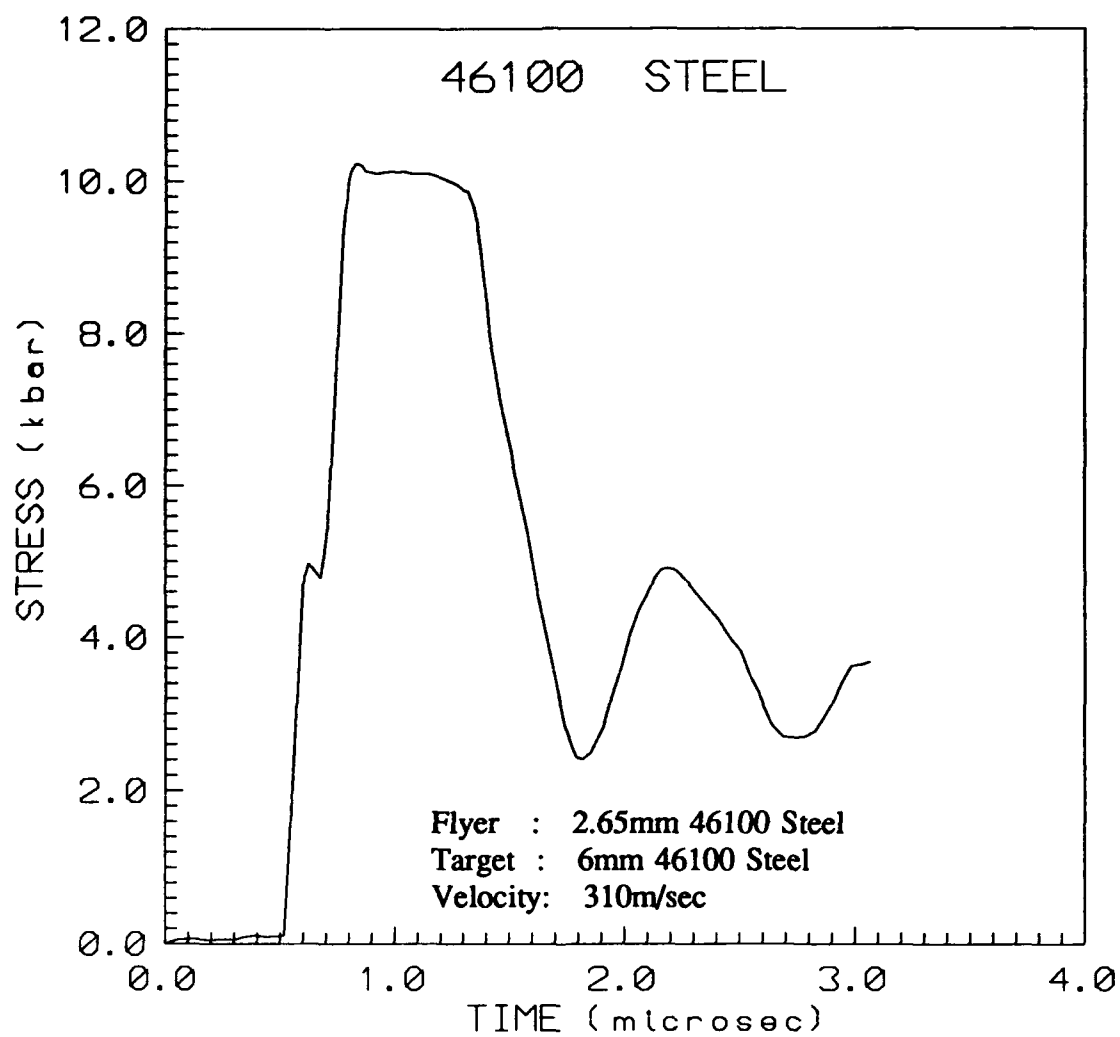


Figure A-29 Gage stress-time history for 46100 Steel plate impact test

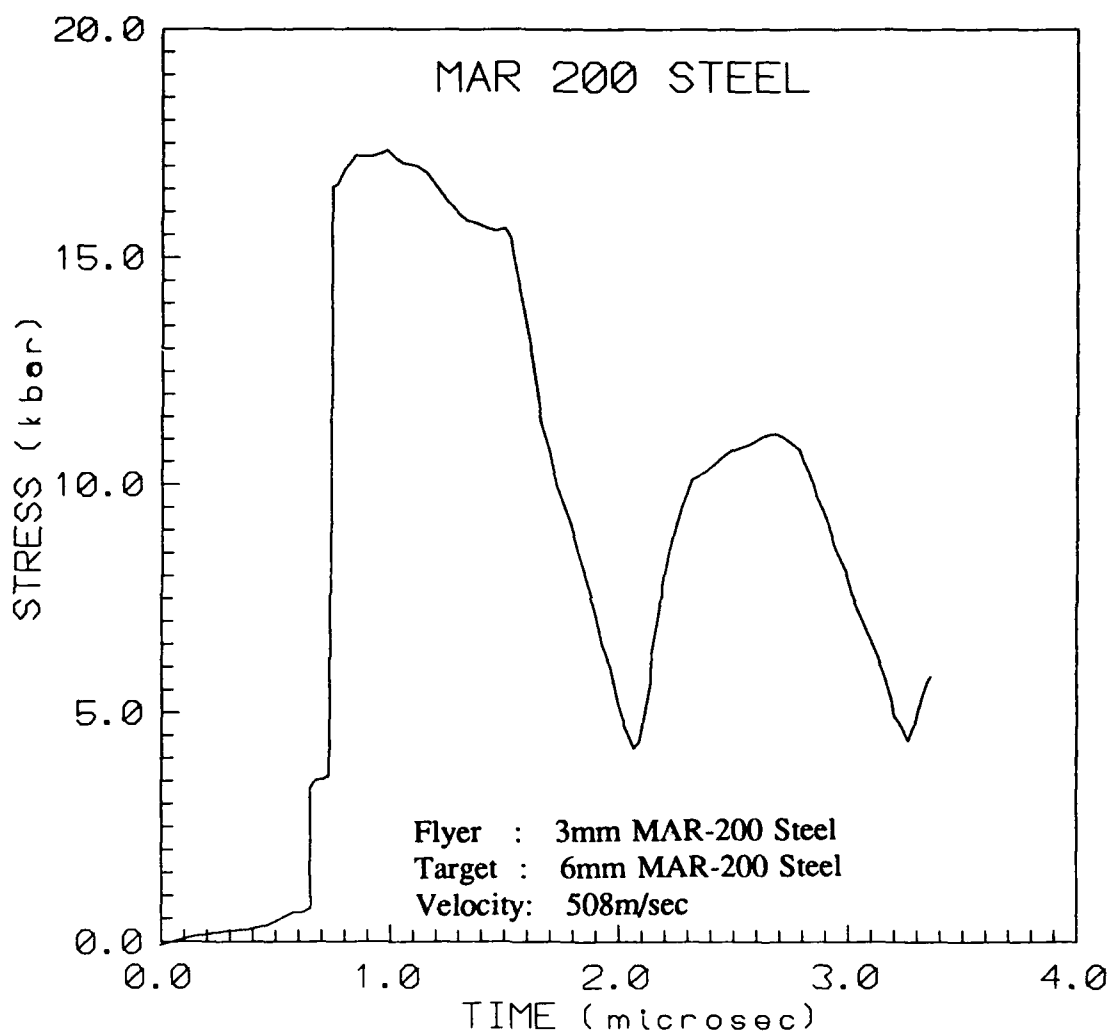


Figure A-30 Gage stress-time history for MAR 200 Steel plate impact test

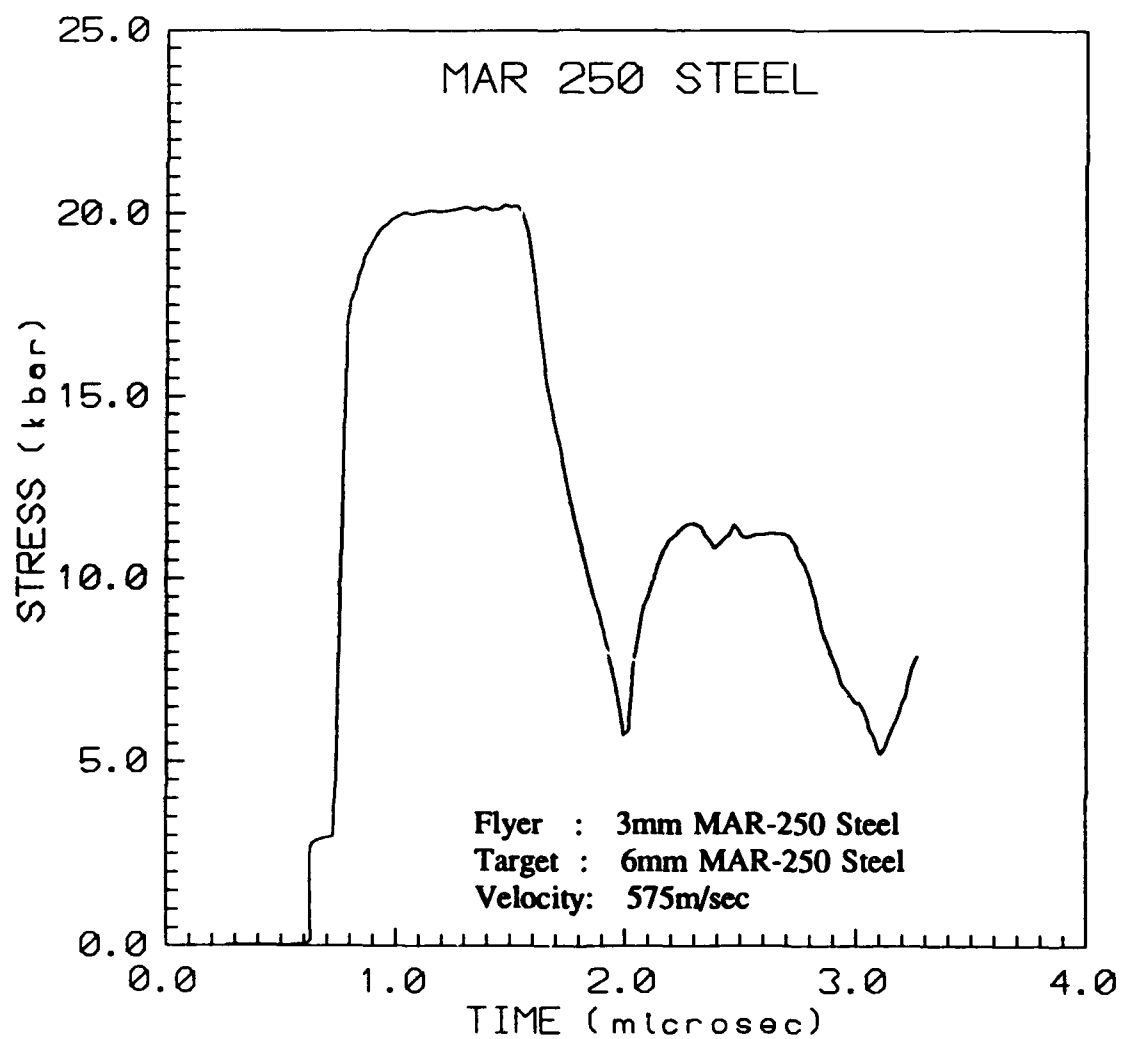


Figure A-31 Gage stress-time history for MAR 250 Steel plate impact test

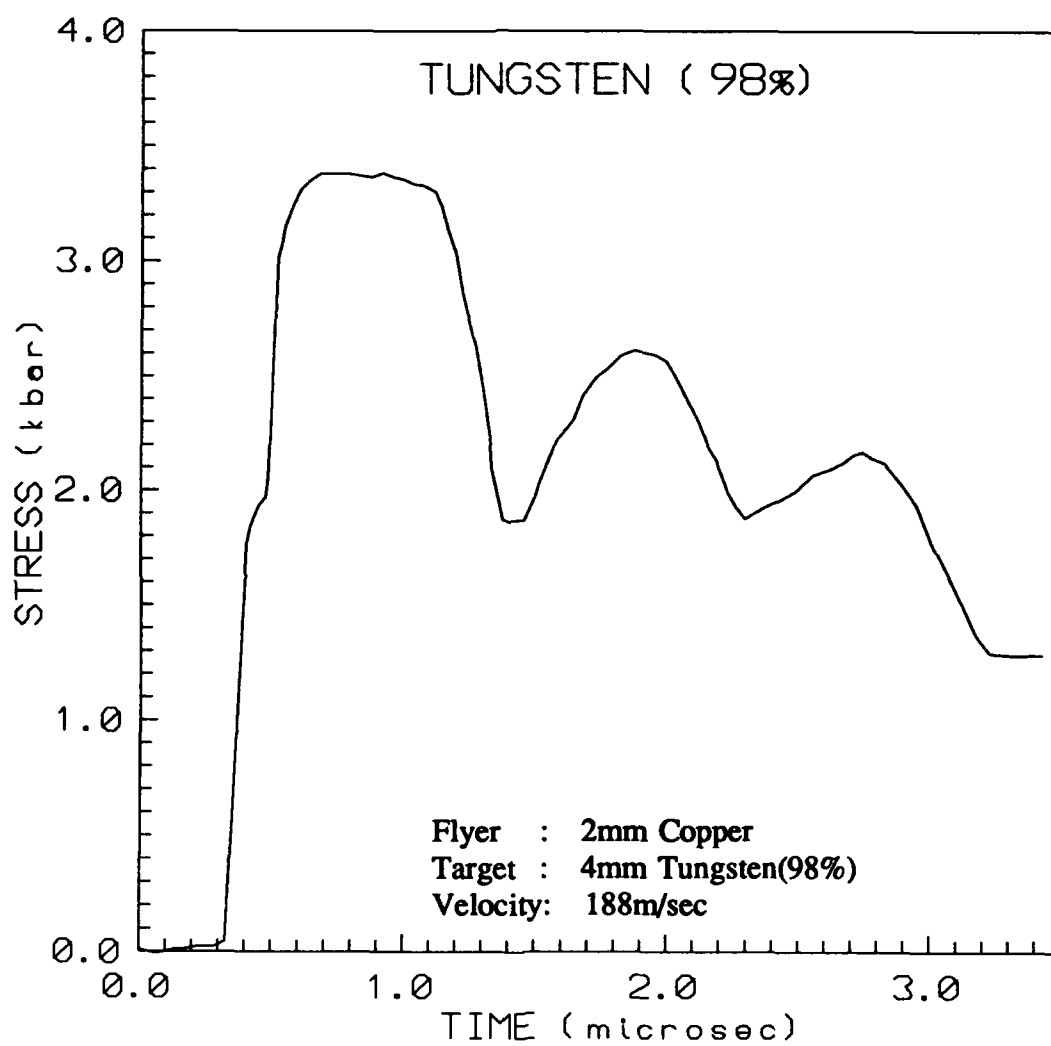


Figure A-32 Gage stress-time history for Tungsten (98%) plate impact test

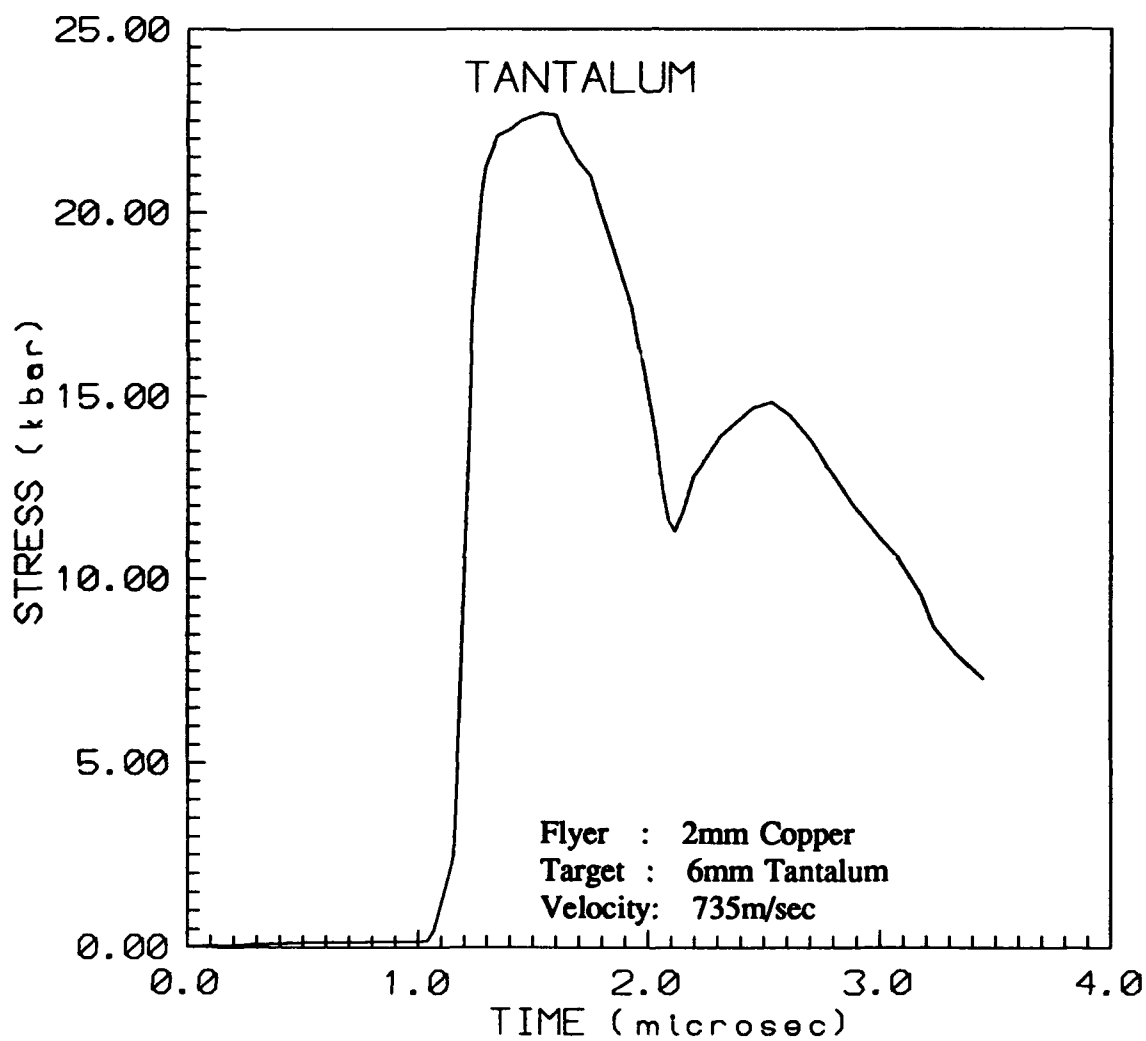


Figure A-33 Gage stress-time history for Tantalum plate impact test

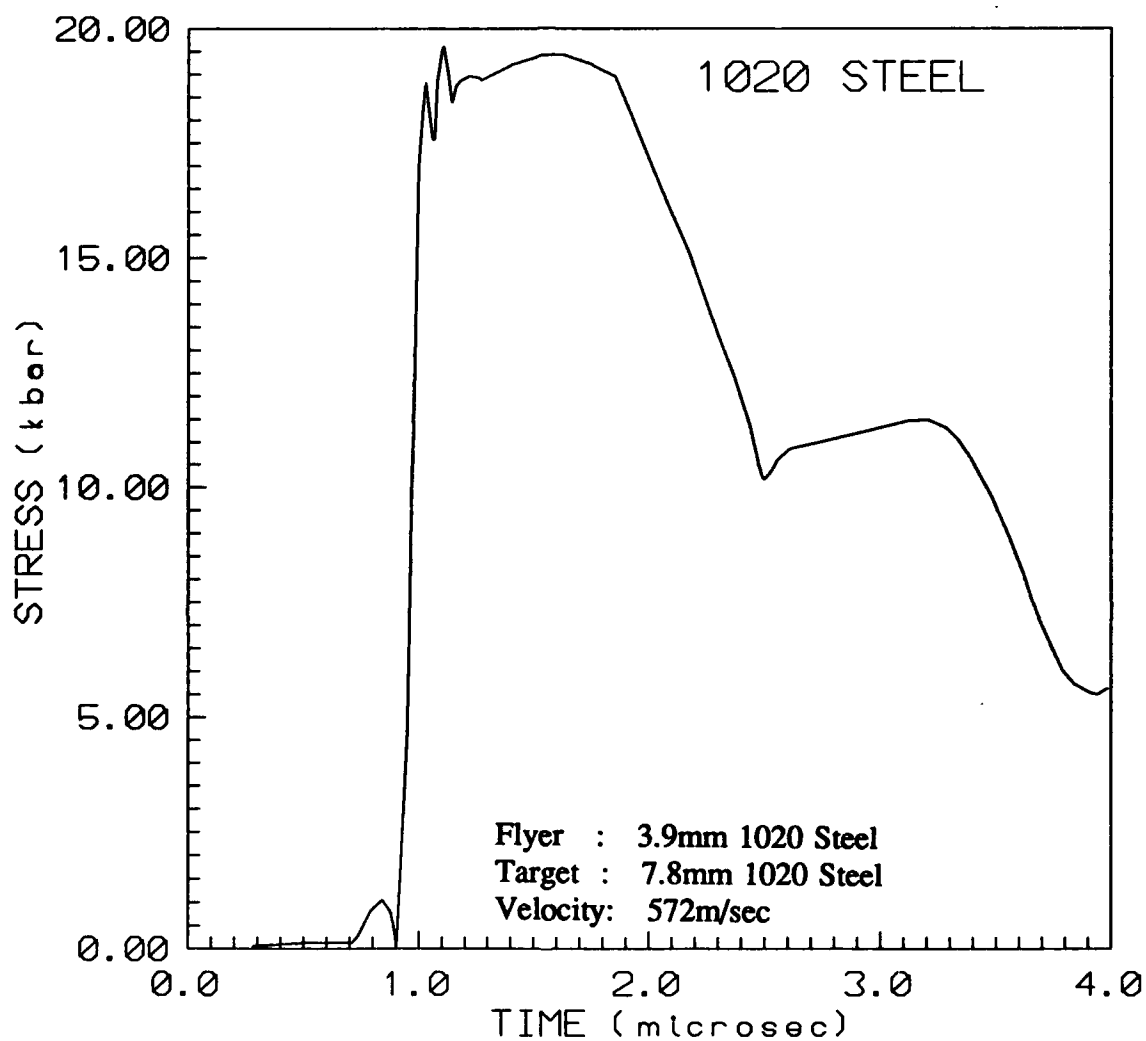


Figure A-35 Gage stress-time history for 1020 Steel plate impact test

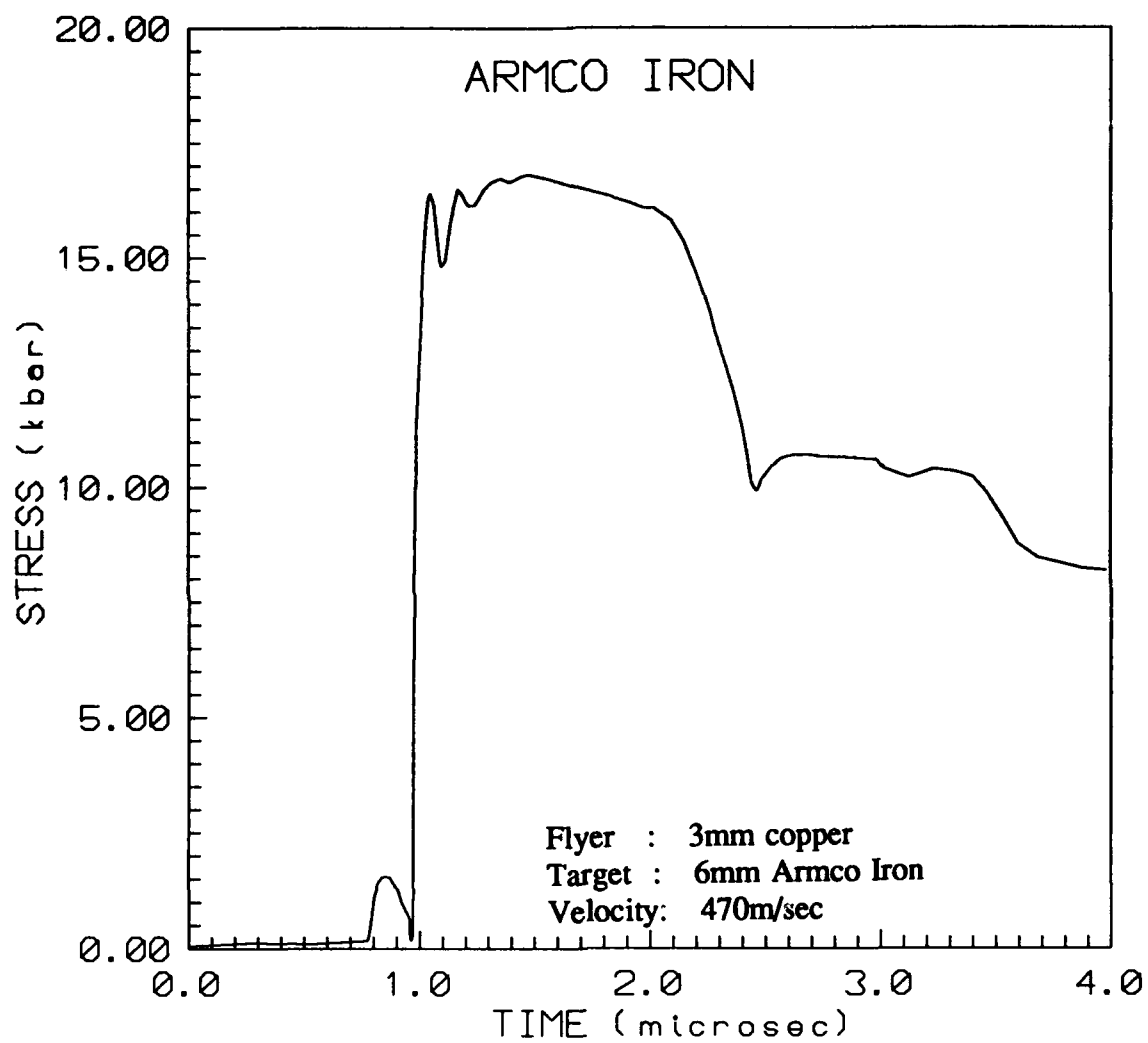


Figure A-36 Gage stress-time history for Armco Iron plate impact test

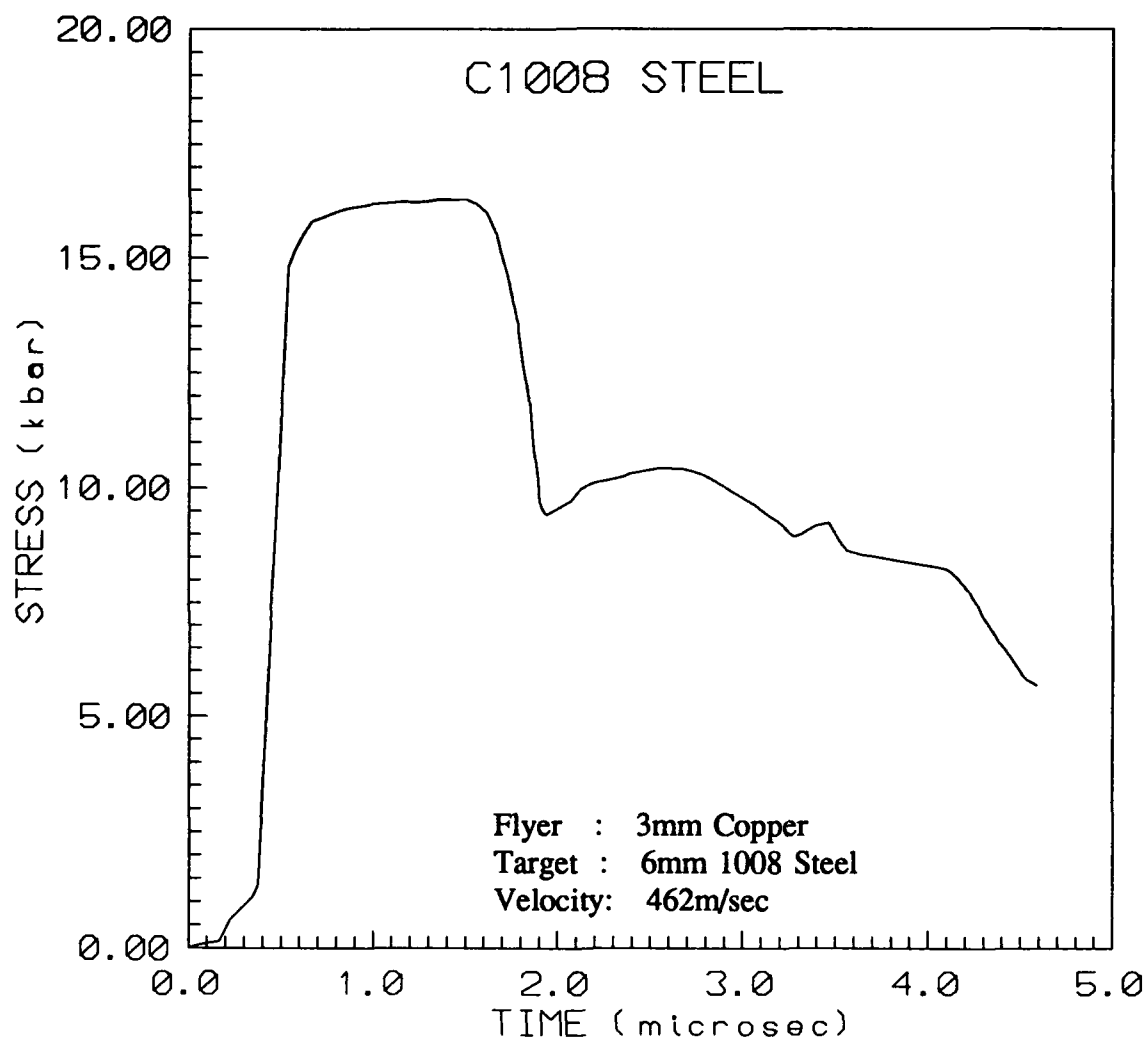


Figure A-37 Gage stress-time history for C1008 Steel plate impact test

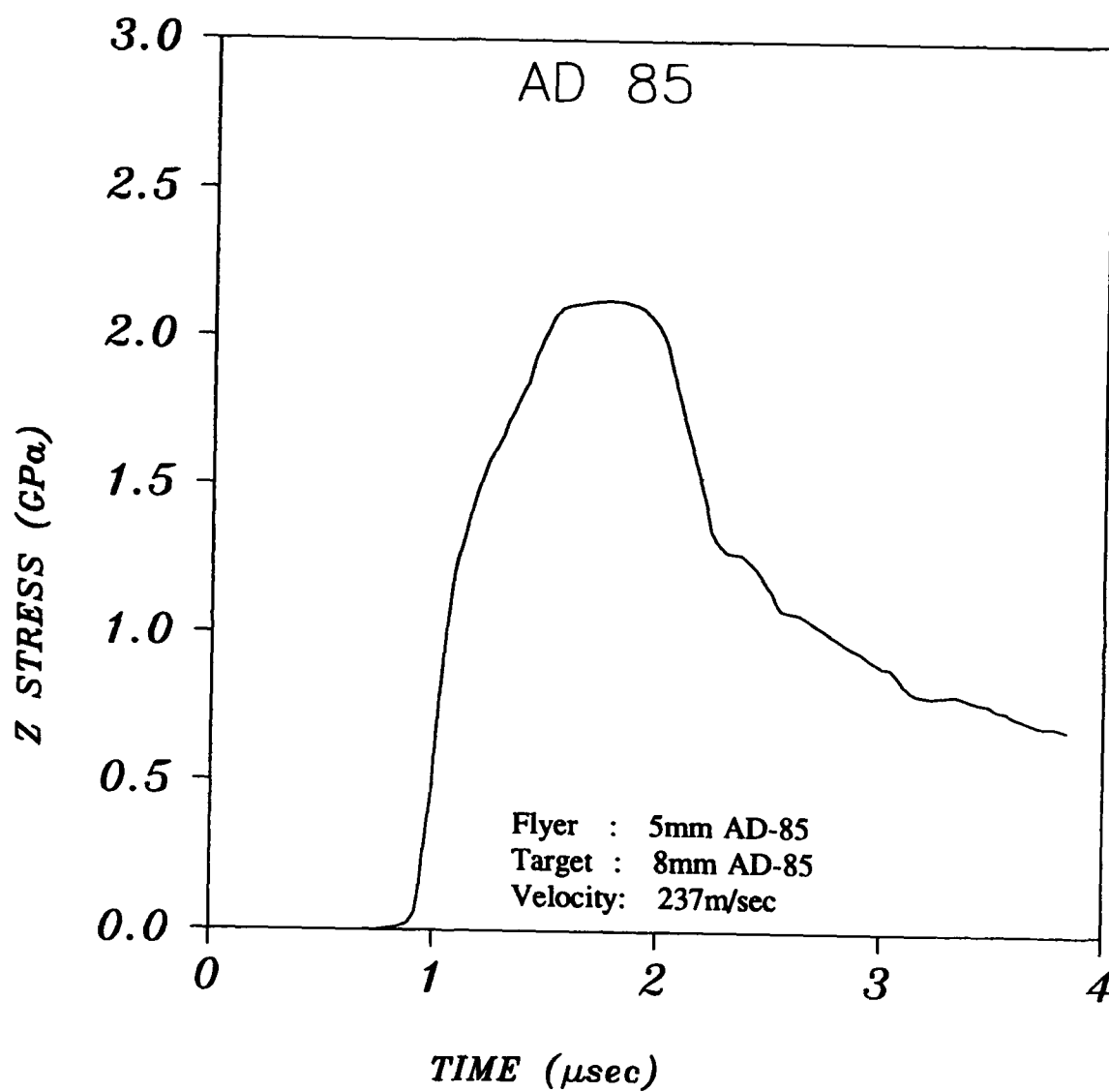


Figure A-38 Gage stress-time history for AD-85 plate impact test

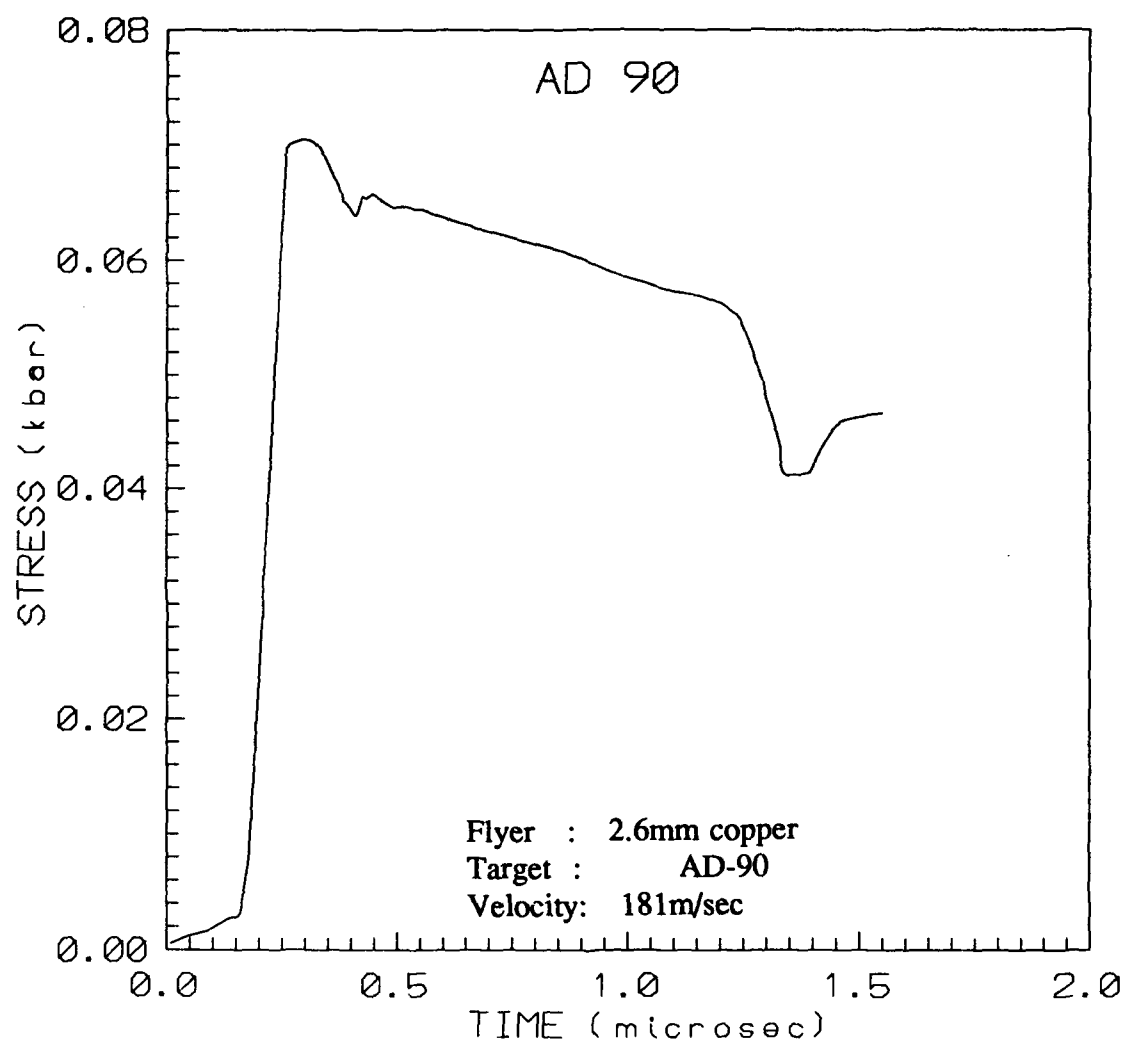


Figure A-39 Gage stress-time history for AD-90 plate impact test

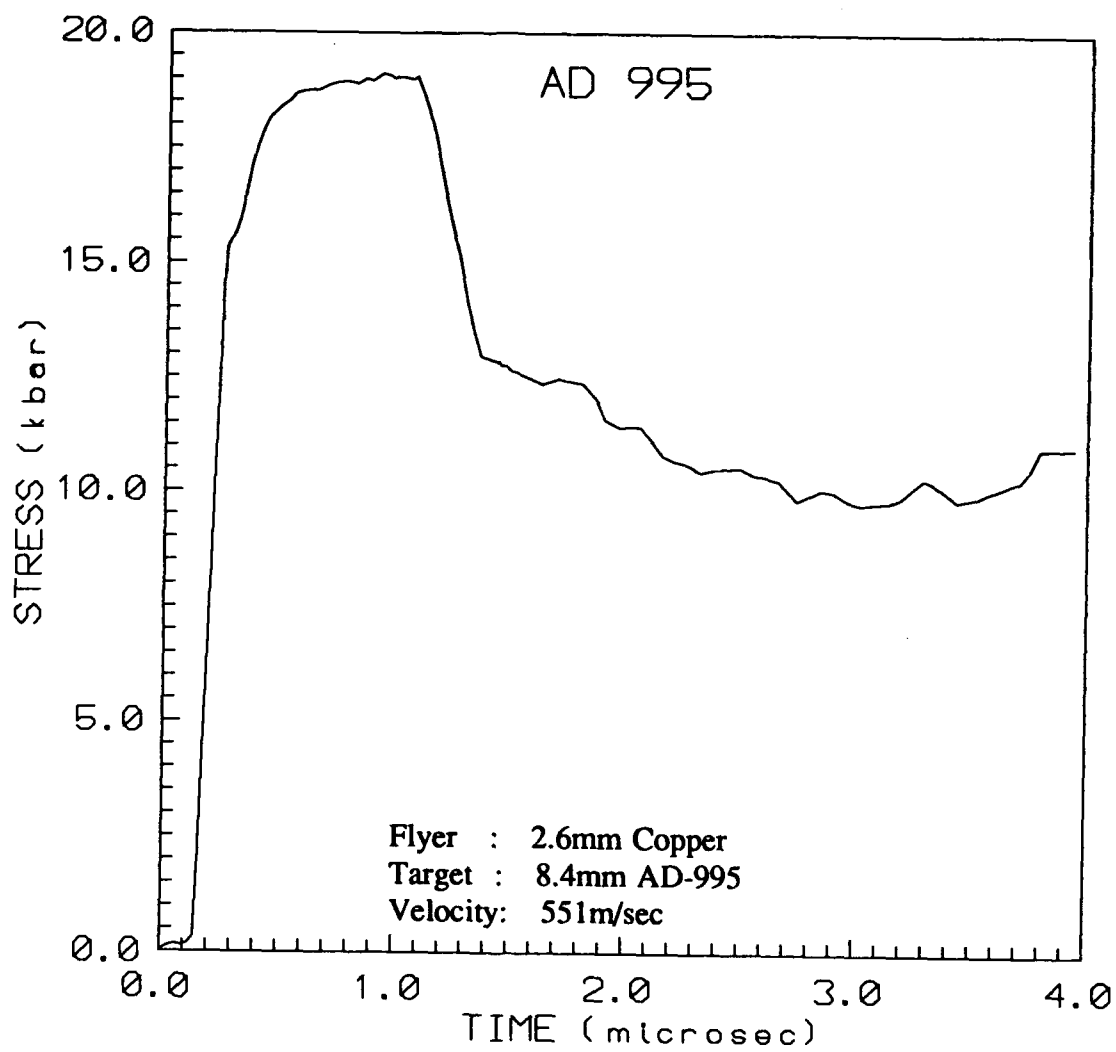


Figure A-40 Gage stress-time history for AD-995 plate impact test

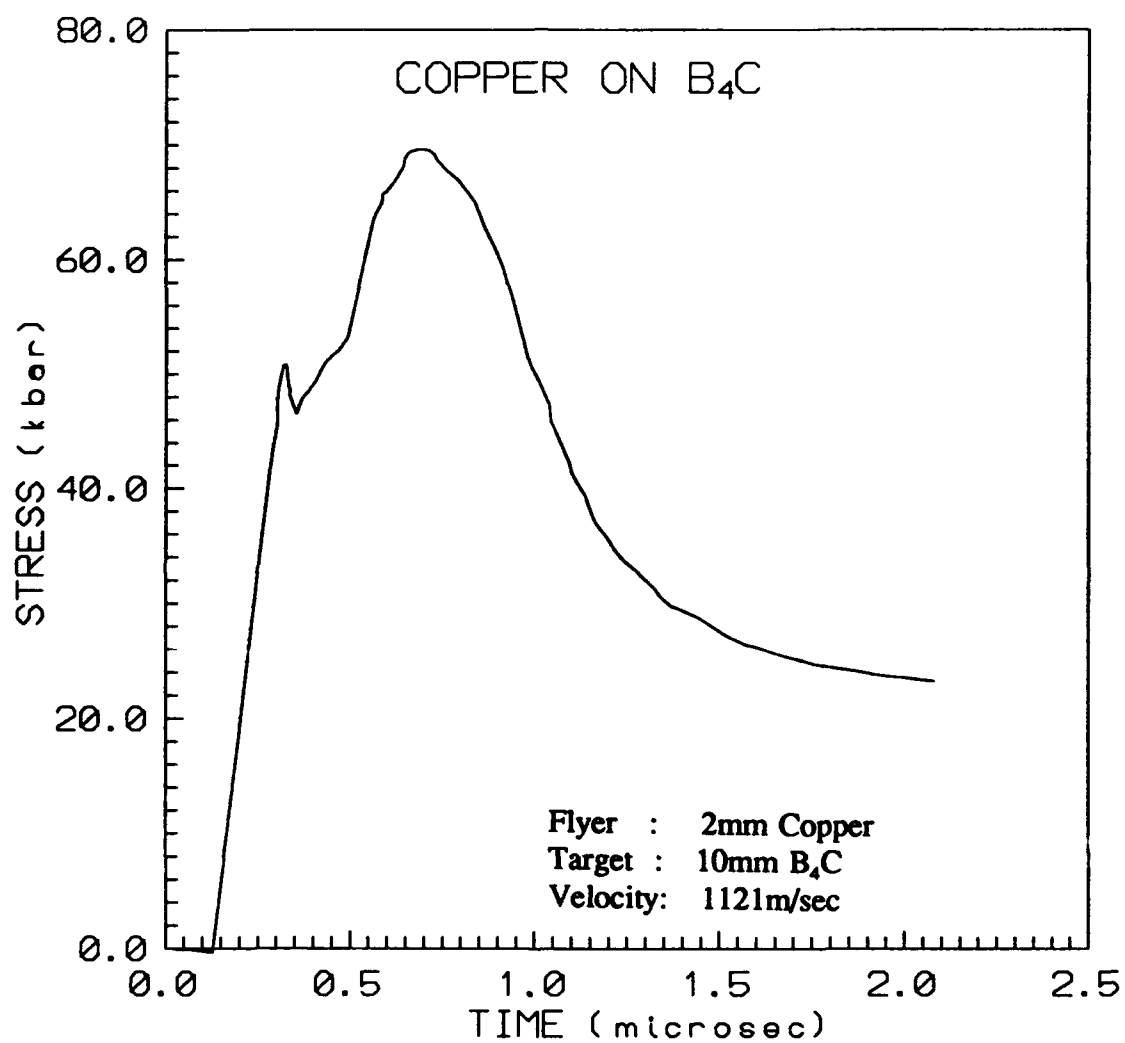


Figure A-41 Gage stress-time history for Boron carbide plate impact test

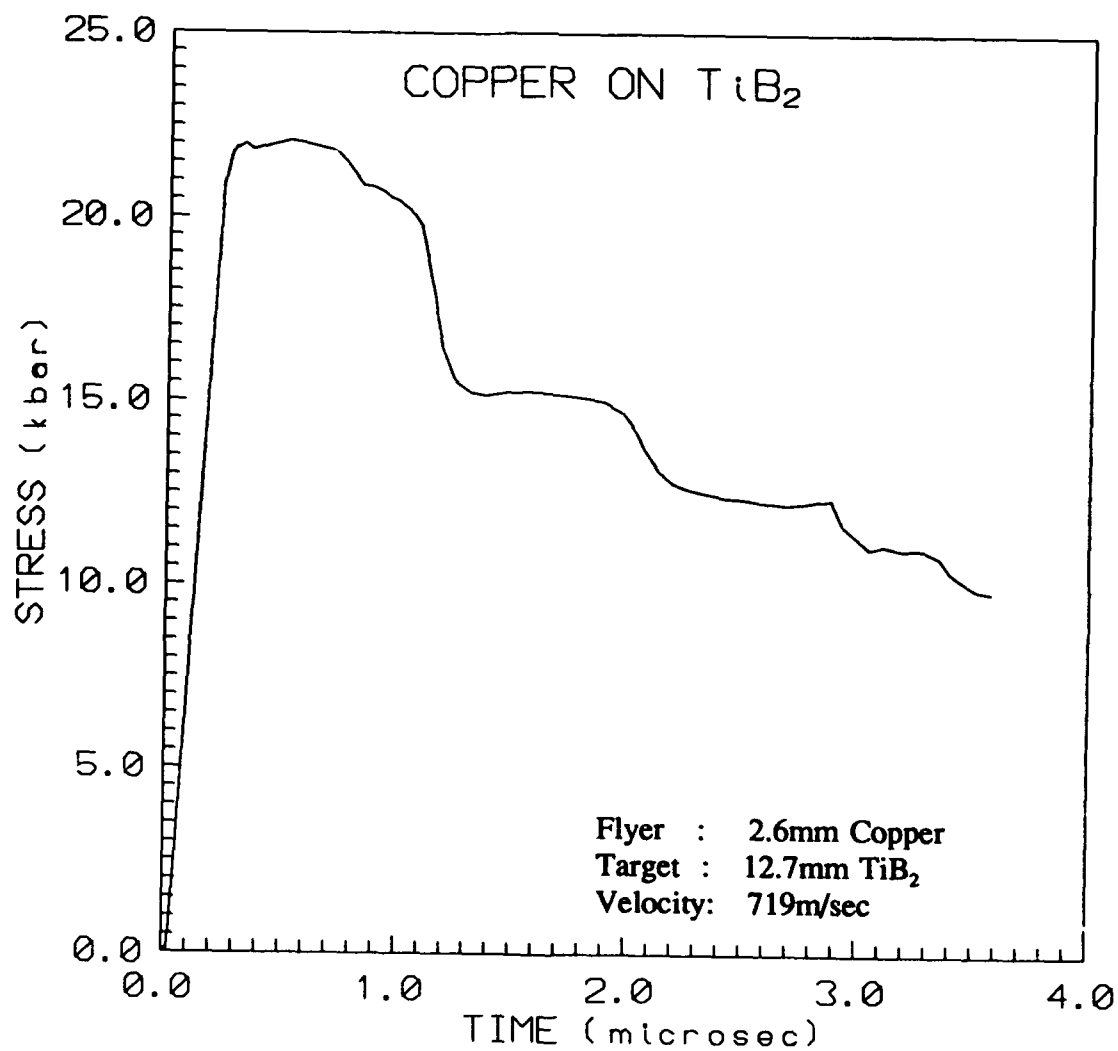


Figure A-42 Gage stress-time history for Titanium diboride plate impact test

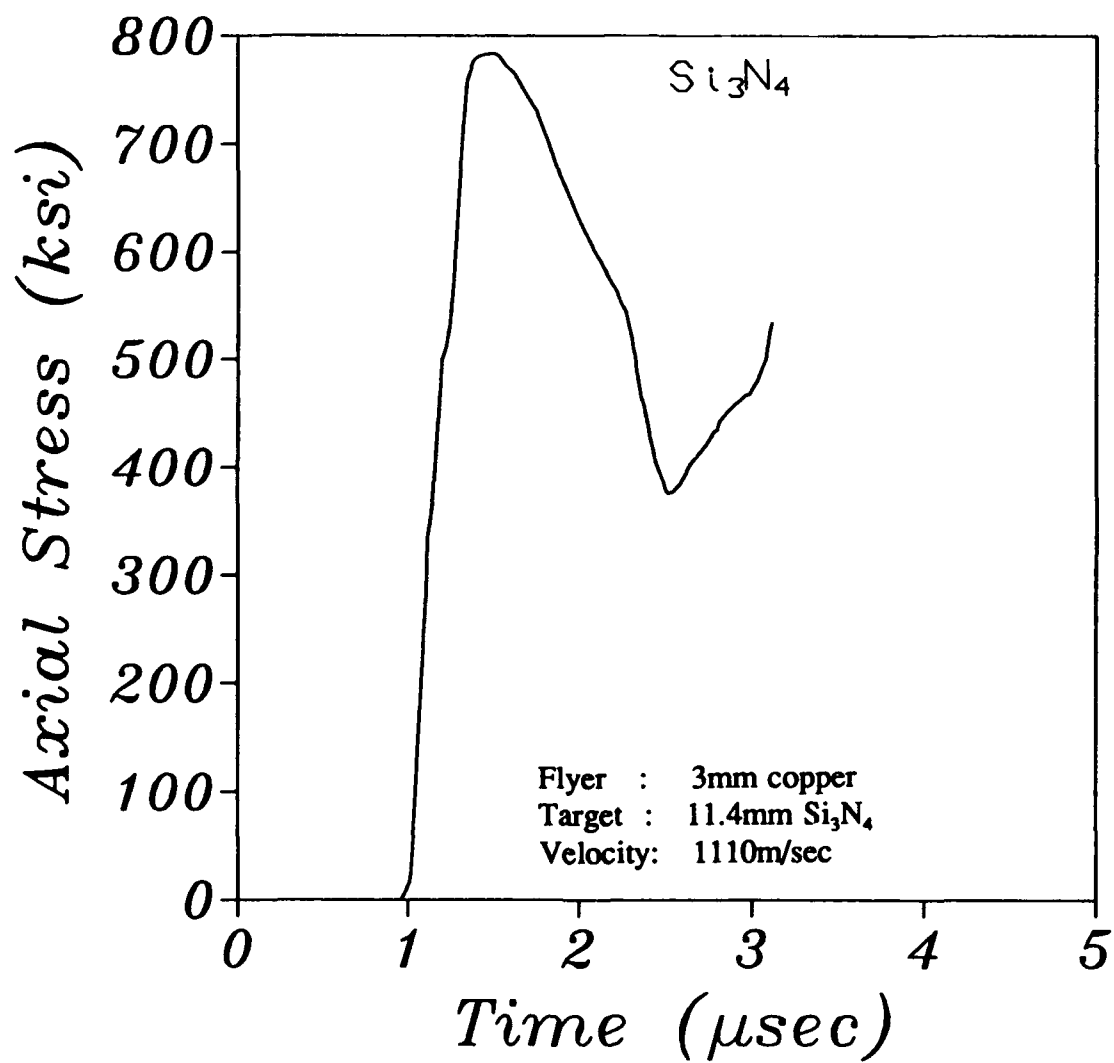


Figure A-43 Gage stress-time history for Silicon nitride plate impact test

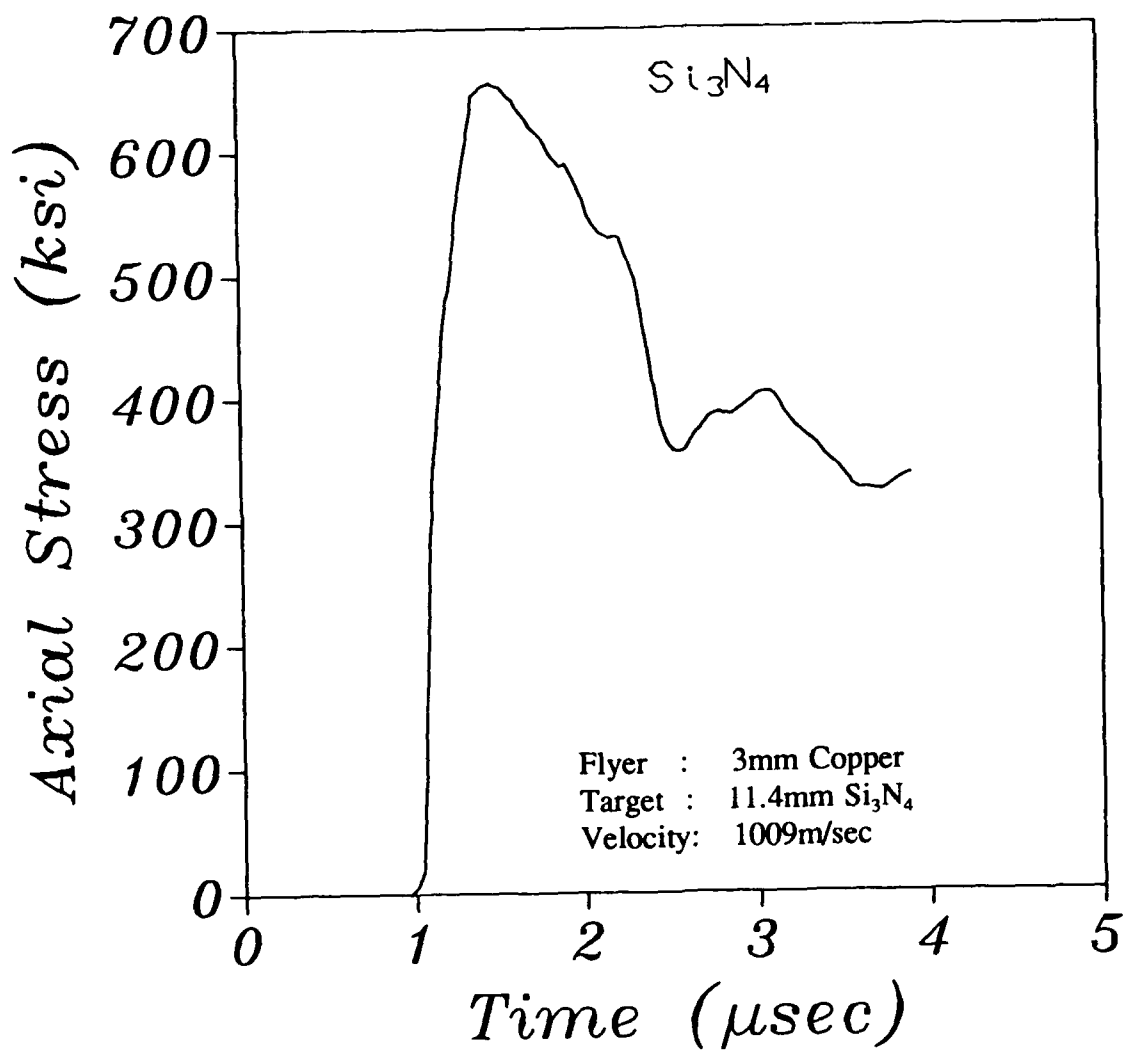


Figure A-44 Gage stress-time history for Silicon nitride plate impact test

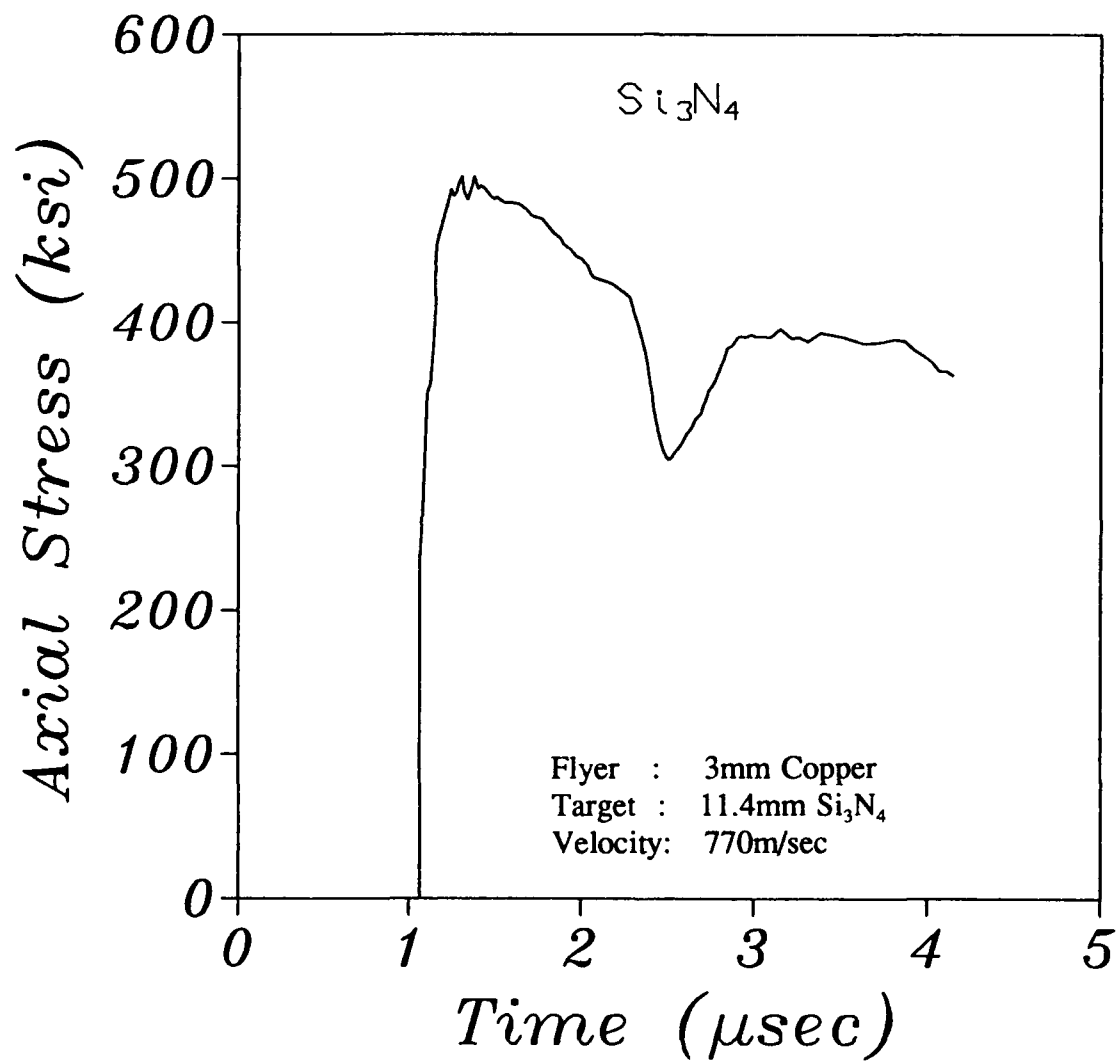


Figure A-45 Gage stress-time history for Silicon nitride plate impact test

Appendix B

Johnson-Cook and Bodner-Partom Models

B.1 Johnson-Cook Model

The Johnson-Cook constitutive model [B.1] provides realistic solutions to hydrocode simulations of a broad class of applications to dynamic events such as impact, penetration, and explosive acceleration of metals. The Johnson-Cook model has the form:

$$Y = [A + B \bar{\epsilon}^n] [1 + C \ln \dot{\epsilon}^*] [1 - T^{*M}] \quad (\text{B.1})$$

$$T^* = \frac{T - T_{room}}{T_{melt} - T_{room}} \quad (\text{B.2})$$

where: Y is the flow strength, $\bar{\epsilon}$ is effective plastic strain, $\dot{\epsilon}^*$ is non-dimensional (effective plastic) strain rate (normalized by 1/sec), T^* is homologous temperature, T_{melt} is the temperature at melting, and T is the applied temperature. The five material constants are defined as follows: A is the static yield strength, B is the work hardening coefficient, n is the work hardening exponent, C is the strain rate coefficient, and M is the thermal softening exponent. In Table B.1, the values of these constants are tabulated for various metals.

The JC model solution scheme in the EPIC code is based on a radial return method. The model constants A , B , and n are determined from quasi-static stress-strain data either from tensile or compressive tests. The strain rate dependent constant C is determined from the slope of the stress vs. strain rate plot. The temperature constant M is estimated from the stress vs. temperature plot. In the code analysis, for a given strain, strain rate, and temperature, the von Mises yield radius is calculated from the JC equation. The von Mises stress, $\sqrt{3J_2}$ is given by,

$$\sqrt{3J_2} = \sqrt{\frac{3}{2} S_{ij} S_{ij}} \quad (\text{B.3})$$

where the J_2 is the second invariant of the stress deviators, S_{ij} .

TABLE B.1
STRENGTH MODEL CONSTANTS FOR JOHNSON-COOK MODEL

MATERIAL	A MPa	B MPa	C	n	M	REMARKS
OFHC Copper	89.63	291.64	0.025	0.31	1.09	800°F, Anneal/60 min.
Cartridge Brass	111.69	504.69	0.009	0.42	1.68	1000°F, Anneal/60 min.
Nickel 200	163.40	648.10	0.006	0.33	1.44	1300°F, Anneal/30 min.
Armco Iron	175.12	3799.90	0.06	0.32	0.55	1700°F, Anneal/60 min.
Carpenter Electric Iron	289.58	338.53	0.055	0.40	0.55	1000°F, Anneal/60 min.
1006 Steel	350.25	275.00	0.022	0.36	1.00	
2024-T351 Aluminum	264.75	426.09	0.015	0.34	1.00	
7039 Aluminum	336.46	342.66	0.01	0.41	1.00	
4340 Steel	792.19	509.51	0.014	0.26	1.03	
S-7 Tool Steel	1538.89	476.42	0.012	0.18	1.00	
Tungsten	1505.79	176.50	0.016	0.12	1.00	7% Ni, 3% Fe
Depleted Uranium	1079.01	1119.69	0.007	0.25	1.00	0.75 Ti
Tantalum	140.00	300.00	*	0.30	0.70	[ref. Lips et al. (1987)]

*not provided

B.2 Bodner-Partom Model

We present the major features of the Bodner-Partom model [B.2] here, as well as an extension of the model for extreme work hardening materials, as proposed earlier by Bodner and Merzer [B.3].

The total strain rate is assumed to be decomposable into elastic and inelastic components.

$$\dot{\epsilon}_{ij} = \dot{\epsilon}_{ij}^e + \dot{\epsilon}_{ij}^p \quad (\text{B.4})$$

Both are nonzero for all loading/unloading conditions. The elastic strain rate is related to the stress rate by the elastic constants (Hooke's Law). The inelastic strain rate is assumed to be a function of stress, σ_{ij} , a state variable, Z , and to follow the Prandtl-Reuss flow rule

$$\dot{\epsilon}_{ij}^p = \dot{\epsilon}_{ij}^p = \lambda S_{ij} \quad (\text{B.5})$$

where $\dot{\epsilon}_{ij}^p$ are the deviatoric plastic strain rates. Squaring Equation (B.5) gives

$$D_2^p = \lambda^2 J_2 \quad (\text{B.6})$$

where D_2^p is the second invariant of the plastic strain rate.

$$D_2^p = D_0^2 \exp \left[- \left(\frac{Z^2}{3J_2} \right)^n \left(\frac{n+1}{n} \right) \right] \quad (\text{B.7})$$

where D_0 is the limiting value of the plastic strain rate in shear, and n is a parameter that is mainly related to strain rate sensitivity. Z is a measure of the overall resistance of the material to plastic flow, and it depends on the loading history.

The plastic strain rate can be expressed in the following form by regrouping Equations (B.5) through (B.7):

$$\dot{\epsilon}_{ij}^p = D_0 \exp \left[- \left(\frac{n+1}{2n} \right) \left(\frac{Z^2}{3J_2} \right)^n \right] \frac{S_{ij}}{\sqrt{J_2}} \quad (\text{B.8})$$

It is assumed that Z is a function of the plastic work, W_p :

$$\dot{Z} = m(Z_1 - Z) \dot{W}_p \quad (\text{B.9})$$

where $\dot{W}_p = \sigma_{ij} \dot{\epsilon}_{ij}^p$. Integration of Equation (B.9) leads to:

$$Z = Z_1 - (Z_1 - Z_0) e^{-mW_p} \quad (\text{B.10})$$

Z_0 is the initial value of Z , Z_1 is the maximum value that Z can attain, and m is a parameter that describes the strain hardening behavior of the material.

To describe extreme strain hardening material behavior, m can be assumed to take the following form:

$$m = m_0 + m_1 e^{-\alpha W_p} \quad (\text{B.11})$$

The expression for Z is obtained by combining Equations (B.9) and (B.11) and integrating,

$$Z = Z_1 - (Z_1 - Z_0) e^{-\left[\frac{(m_0 + m_1 - m)}{\alpha} + m_0 W_p \right]} \quad (\text{B.12})$$

The additional constants, m_0 and m_1 , replace the original m . We also need α to model the extreme strain hardening behavior of a material like annealed OFHC copper [B.4].

The effect of temperature on the flow stress is included through the parameter n . Based on quasi-static experimental evidence, the parameter n is assumed to vary as an inverse function of absolute temperature (T):

$$n = A + \frac{B}{T} \quad (\text{B.13})$$

where A and B are model parameters and T is expressed in either degrees Rankine or degrees Kelvin. Thus the BP model contains five principal material parameters D_0 , Z_0 , Z_1 , m , and n that have to be evaluated from high strain-rate experiments under room temperature for most metals. The two secondary work hardening constants α and m_1 are used to describe highly strain hardening materials like OFHC copper. In high strain rate applications, the limiting strain rate

D_0 has been assumed to be $10^8/\text{sec}$ for metals. This eliminates the task of determining one more model constant. Therefore, the BP model generally requires only 4 material model constants for room temperature applications. However, for high temperature applications, one additional constant is required.

Rajendran and Geers [B.5] developed a user interactive program called BPSOLVE for the determination of the first four constants described above, based on at least three tensile tests at different strain rates. The temperature related material constants can be determined iteratively using high temperature SHB test data. Rajendran et al. [B.6,B.7] determined model parameters for several metals using the BPSOLVE program. The corresponding model constants are given in Table B.2.

In the BP model, the plastic strain rates are expressed as a function of stress components, state variable Z , and the second invariant of the stress deviator. Therefore, expressing the strength Y in terms of strain rate and state variables (as in the JC model) is not a straightforward task. In hydrocodes, calculation of the deviatoric stresses requires an iterative scheme when implementing the BP model (or similar constitutive relationships). Initially, the plastic strain rates are estimated using the deviatoric stresses calculated from elastic equations as,

$$\dot{S}_{ij} = 2G \left(\dot{e}_{ij} - \dot{e}_{ij}^p \right) \quad (\text{B.14})$$

The plastic strain rate expressions [B.8] of the Bodner-Partom model make these ordinary differential equations stiff under certain conditions. Computation of the deviatoric stresses requires plastic strain rate estimates, while computation of the plastic strain rates requires deviatoric stress estimates. Therefore, the stress calculation requires an iterative scheme in the numerical implementation of the BP model. Several articles on the results from using the BP model in hydrocodes can be found in References [B.8] through [B.13].

B.3 References

- B.1. Johnson, G. R. and Cook, W. H., "Fracture Characteristics of Three Metals Subjected to Various Strains, Strain Rates, Temperatures and Pressures," *Eng. Fracture Mech.*, 21, 31-48 (1985).
- B.2. Bodner, S. R. and Partom, Y., "Constitutive Equations for Elastic-Viscoplastic Strain Hardening Materials", *J. of Appl. Mech.*, 42, 385-89 (1975).

TABLE B.2
BODNER-PARTOM MODEL CONSTANTS

Material	Z_0 (GPa)	Z_1 (GPa)	n	m_0 GPa ⁻¹	m_1 GPa ⁻¹	α GPa ⁻¹	A	B
C1008 Steel	5.5	7.0	0.4	15	0	0	0.245	46
HY100 Steel	2.4	3.6	1.2	10	0	0	NA	NA
1020 Steel	0.64	0.93	4.0	30	0	0	NA	NA
MAR-200 Steel	2.2	2.4	4.0	5	0	0	NA	NA
Armco Iron	2.65	4.2	0.58	56	0	0	NA	NA
OFHC Copper	0.8	6.6	0.4	11	150	1500	NA	NA
6061-T6 Aluminum	0.45	0.55	4.0	120	0	0	-2.86	2343
7039-T64 Aluminum	0.56	0.76	4.0	28	0	0	NA	NA
Pure Tantalum	1.3	3.1	0.74	20	0	0	NA	NA
W-2 Tungsten	8.75	10.0	0.58	150	0	0	0.166	134
Nickel 200	0.32	0.82	4.0	40	0	0	NA	NA
MAR-250 Steel	2.5	2.7	5.0	20	0	0	NA	NA
AF1410 Steel	2.4	2.75	5.0	15	0	0	NA	NA

NA -- The high temperature constants are "Not Available"

- B.3. Bodner, S. R. and Merzer, A., "**Viscoplastic Constitutive Equations for Copper with Strain Rate History and Temperature Effects**," *ASME J. Eng. Mat. and Tech.*, 100, 388-94, (1978).
- B.4. Rajendran, A. M. and Bless, S. J., "**High Strain Rate Material Behavior**," AFWAL-TR-85-4009, Wright-Patterson Air Force Base, OH, (1985).
- B.5. Rajendran, A. M. and Geers, E., "**BPSOLVE - A Program to Determine Bodner-Partom Model Parameters**," UDR-TR-86-95, University of Dayton Research Institute, Dayton, OH, (1986).
- B.6. Rajendran, A. M., Bless, S. J. and Dawicke, D. S., "**Evaluation of Bodner-Partom Model Parameters at High Strain Rate**," *ASME J. Eng. Mat. and Tech.*, 108, 75-80, (1986).
- B.7. Rajendran, A. M. and Bless, S. J., "**Plastic Flow and Failure Modeling under High Strain Rate Loading**," AFWAL-TR-87-4134, Wright-Patterson Air Force Base, OH, (1988).
- B.8. Rajendran, A. M. and Grove, D. J., "**Bodner-Partom Viscoplastic Model in STEALTH Finite Difference Code**", AFWAL-TR-86-4098, Materials Laboratory, WPAFB, OH, (1987).
- B.9. Cook, W. H., "**Applications of the Bodner-Partom Model**," Dynamic Constitutive/Failure Models, eds. A. M. Rajendran and T. Nicholas, AFWAL-TR-88-4229, Wright-Patterson Air Force Base, OH.
- B.10. Rajendran, A. M., Dietenberger, M. A. and Grove, D. J., "**A Void Nucleation and Growth Based Failure Model for Spallation**," *J. of Appl. Phys.*, 65, 1521-27, (1989).
- B.11. Rajendran, A. M., Grove, D. J., Dietenberger, M. A., and Cook, W. H., "**A Dynamic Failure Model for Ductile Materials**," AFATL-TR-90-84, Eglin Air Force Base, FL, (1990).
- B.12. Bodner, S. R., "**A Review of Unified Elastic-Viscoplasticity Theory**," *Unified Constitutive Equations for Creep and Plasticity* (Chapter 6), ed. A. K. Miller, Elsevier Applied Science, Pub. England, (1987).
- B.13. Cook, W. H., Rajendran, A. M., and Grove, D. J., "**An Efficient Implementation of the Bodner-Partom Model in an Explicit Finite Element Code**," to appear in *J. of Eng. Fracture Mechanics*, (1992).

Appendix C

Solution Scheme

C.1 Numerical Solution of the Governing Equations in Sections 3 and 4

The governing equations described in Sections 3 and 4 are rearranged and numerically integrated. A detailed description can be found in Reference [C.1]. For stability, accuracy, and uniqueness of the solution, a second order diagonally implicit Runge-Kutta (DIRK) method was considered for integrating the system of stiff ordinary differential equations. The DIRK scheme is outlined in Appendix D. The DIRK variables are integrated using the estimated rates for the current time.

The EPIC-2 code calculates the current strain rates in each material element. Before any void nucleation occurs, the volumetric strains of the matrix and the aggregate are the same. However, once void nucleation occurs in an element, the incremental volumetric strain of the aggregate, ϵ_v , is the sum of the incremental elastic volume change, ϵ_v^e , in the aggregate (in the same sense as Mackenzie's) and the incremental volume change due to the viscoplastic growth of voids, ϵ_{ii}^p . This relationship can be related directly to the aggregate elastic compressible strain, μ_{ag} , from Equation (13) as follows. The relationship between the true volumetric strain and the compressible strain is, by definition,

$$1 + \mu = e^{-\epsilon_v} \quad (C.1)$$

The relationship between the true plastic dilatation and the void volume fraction is given by the direct integration of Equation (9) as,

$$1 - f = e^{-\epsilon_{ii}^p} \quad (C.2)$$

where the plastic dilatation, ϵ_{ii}^p , is zero at $f = 0$. Substituting Equations (C.1) and (C.2) into Equation (13), the following relationships were obtained:

$$\mu_{ag} = e^{-\epsilon_v^e} - 1 \quad (C.3)$$

and
$$\epsilon_V^e = \epsilon_V - \epsilon_{ii}^P . \quad (C.4)$$

where ϵ_V^e is the true elastic dilatation strain of the aggregate. This development suggests that the plastic strain rates, $\dot{\epsilon}_{ij}^P$, should be numerically integrated instead of integrating Equation (4). The aggregate pressure, P, is evaluated by using Equation (C.3) and the procedure outlined in Section 3. The true elastic deviatoric strains of the aggregate are given by the equation,

$$e_{ij}^e = e_{ij} - \left[\epsilon_{ij}^P - \left(\frac{\epsilon_{kk}^P}{3} \right) \delta_{ij} \right] . \quad (C.5)$$

The aggregate deviatoric stresses can then be determined from:

$$S_{ij} = 2 \bar{G} e_{ij}^e , \quad (C.6)$$

where \bar{G} is the degraded shear modulus, as defined by Equation (11).

One numerical bonus of the above approach is that the use of Equation (C.2) to calculate f avoids numerical integration of the stiff differential Equation (9). Equations (4), (B.8), and (B.9) lead to stiff differential equations; therefore, the DIRK scheme permits extremely small time steps to maintain solution stability and accuracy. For numerical efficiency (i.e. to avoid extremely small time steps), Equations (B.9) and (6) were analytically integrated to derive the following equations for the BP model loading history parameter (Z) and the void volume fraction due to nucleation of voids (f_n):

$$Z = Z_1 - (Z_1 - Z_0) e^{-\left[\frac{(m_0 + m_1 - m)}{\alpha} + m_0 W_P \right]} \quad (C.7)$$

$$f_n = \left(\frac{f_1}{2} \right) \left[\operatorname{erf} \left(\frac{P + Y_m - \sigma_N}{\sqrt{2} s_1} \right) - \operatorname{erf} \left(\frac{-\sigma_N}{\sqrt{2} s_1} \right) \right] + \left(\frac{f_2}{2} \right) \left[\operatorname{erf} \left(\frac{D_m^P - e_N}{\sqrt{2} s_2} \right) - \operatorname{erf} \left(\frac{-e_N}{\sqrt{2} s_2} \right) \right] \quad (C.8)$$

Using Equation (C.8) eliminates the need to evaluate the effective matrix stress rate, \dot{Y}_m , as was

required in Equation (6). The value of the effective matrix stress can be obtained from the yield function (Equation (1)):

$$Y_m^2 = \frac{(2+\rho^2) J_2 + \frac{1-\rho^2}{3} I_1^2}{\delta(\rho)} \quad (C.9)$$

The yield function described by Equation (1) is treated as a plastic potential. Implicitly assumed is that the loading and unloading are controlled by the BP model through the matrix equivalent plastic strain.

Examination of Equation (B.7) shows that $D_2^P (\equiv \frac{3}{4} (\dot{D}_m^P)^2)$ is ultimately a function of the same four integration variables (the variables input from EPIC are considered constant during the EPIC time step). The BP state variable Z is only a function of w_p through Equation (C.7), and the term $3J_2 (\equiv Y_m^2)$ is a function of f , P , and S_{ij} through Equation (C.9). The variables f , P , and S_{ij} are in turn functions of ϵ_{ij}^P through Eqs. (24) to (26) and Eqs. (C.2) to (C.6). Since the variables P and S_{ij} are also direct functions of f_n (through the degraded modulus), and the f_n is in turn a function of P and S_{ij} through Equations (C.8) and (C.9), an efficient convergent iterative scheme was developed to solve f_n simultaneously with P and S_{ij} . Since the temperature (T) in Equation (B.13) and the pressure (P_s) in Equation (12) are both direct functions of the internal energy, Equation (38) must also be integrated.

This rearrangement of the governing equations has resulted in fewer differential equations which are relatively less stiff. Thus, the numerical integration problem was reduced to the solution of the rate equations for D_m^P , w_p , I , and ϵ_{ij}^P . The corresponding rate equations were solved using the DIRK scheme. The solution stability, accuracy, and uniqueness, with respect to different finite element mesh sizes and time steps, were demonstrated through one-dimensional plate impact solutions in Reference [C.1] and through two-dimensional solutions of several application problems.

C.2 References

- C.1. Rajendran, A. M., Grove, D. J., Dietenberger, M. A., and Cook, W. H., "A Dynamic Failure Model for Ductile Materials," AFATL-TR-90-84, Eglin Air Force Base, FL, 1990.

Appendix D

Diagonally Implicit Runge Kutta Scheme

The diagonally implicit Runge-Kutta integration is given by the formula [D1],

$$K_i^{(n)} = f(t_n + c_i h, y_n + h \sum a_{ij} K_j^{(n)}), \quad i=1(1)q \quad (\text{D.1})$$

$$y_{n+1} = y_n + h \sum b_i K_i^{(n)} \quad (\text{D.2})$$

$$\left(\frac{dy}{dt}\right)_n = f(t_n, y_n) \quad (\text{D.3})$$

h is the time step and y_n is the vector of the integrated variables at time, t_n . Note that K_i is also a function of itself, which requires an iterative corrector procedure. That is, the calculated value of K_i is re-substituted into the nonlinear equation (D.1) until convergence is achieved within an error tolerance. If convergence is not achieved after a certain number of re-substitutions of K_i , then the time step, h , is reduced. Convergence of K_i is assured if a small enough time step is chosen. In the RDG model implementation, if convergence is achieved within a very small error tolerance, the time step h is gradually increased to improve computation time. This scheme was implemented into the shock wave propagation, finite element code, EPIC-2.

The EPIC-2 host code is based on the time-centered integration approach with the time step controlled by the Courant stability criterion; therefore, the time steps usually remain small. Thus, the lowest order DIRK, ($q=1$), will be adequate for stable and accurate solutions. For the values, $q=1$, $a_{11}=1/2$, $b_1=1$, and $c_1=1/2$, the DIRK method becomes second-order accurate. This special case is equivalent to Bass and Oden's [D2] recommendation of their Euler predictor-trapezoidal corrector scheme. Saliba [D3] has effectively proved this special case as stable and accurate in conjunction with the mechanical equilibrium equations for quasi-static problems.

With the DIRK method applied to the ODE of any viscoplastic formulation, a single corrector step was found sufficient for accurate calculations most of the time. However, during the stiff phase of the solutions, such as the unloading, the DIRK time steps require significant

reduction even with several re-substitutions of K_i . Maximum efficiency during the stiff phases was achieved as follows. If after three re-substitutions of K_i the relative error is not within two percent, the DIRK time step is reduced by one-tenth. The process continues until the two percent error is obtained. If, however, after three re-substitutions of K_i the relative error is within two-tenth of a percent, the DIRK time step is increased in an arbitrary manner by 33% for the next time step. This process continues until the end of the EPIC time step is reached.

D.1 References

- D.1. Al-Rabeh, A. H., "Embedded DIRK Methods for the Numerical Integration of Stiff Systems of ODEs," *Int. J. Comp. Math.*, 21, 65-84, (1987).
- D.2. Bass, J. M. and Oden, T. T., "Numerical Solution of the Evolution Equations of Damage and Rate-Dependent Plasticity," *Int. J. Eng. Sci.*, 26, 713-740, (1988).
- D.3. Saliba, J. E., "Numerical Stability of Implicit Integration Schemes in Nonassociated Viscoplasticity," *Comp. & Struct.*, 31, 693-698, (1989).

Appendix E

Modified TCK Model for Ceramic Materials

The following pages were published as a journal article entitled, "Impact Damage Model for Ceramic Materials," *J. Appl. Phys.*, Vol. 66, No. 8, 15 October, 1989.

Impact damage model for ceramic materials

A. M. Rajendran and J. L. Kroupa

Structural Integrity Division, University of Dayton Research Institute, Dayton, Ohio 45469

(Received 9 February 1989; accepted for publication 5 July 1989)

The fracture process in ceramic materials upon impact loading is complex in nature. Most often, the brittle ceramic deforms inelastically due to microcracking under shock (compression) loading. At high-velocity impact, the shock generated microcracks rapidly open and extend under subsequent tension (due to the release waves from the stress-free boundaries) leading to complete pulverization of the ceramic materials. The main objective of this paper is to model the damage process in ceramics due to impact loading. A computationally oriented continuum damage-based constitutive model is considered. Several modifications incorporating strain rate and damage effects on the compressive strength have been introduced into the model. Results are presented in terms of numerical simulations of a plate-impact test configuration. Effects of the model parameters on the compressive strength and spall strength are described. The proposed damage model has been used successfully to match the measured stress history from a plate-impact experiment on AD-85 (85% aluminum oxide) ceramic target material.

1. INTRODUCTION

Ceramic materials usually exhibit very large compressive strength when compared to metals. The compressive strength is found to increase significantly under dynamic loading conditions. The increase in strength is usually attributed to the combined effects of confining pressure and strain rate. Due to their high strength and enhanced high-temperature properties, ceramic materials have often been employed as armor elements and turbine engine components, respectively. The increased use of ceramic as armor material necessitates a thorough understanding of ceramic material behavior under impact loading conditions. Initially, in armor design, the response of the ceramic armor or target was interpolated or sometimes even extrapolated from empirical curves constructed from experimental data. With the advent of increasing computer capabilities, the experimental design and armor material selection are often guided by computer simulations of the impact situations. General purpose shock-wave-propagation finite-element-difference codes have been widely used in the initial estimations of the armor performance. The accuracy and predictability of the numerical calculations depend on the realistic description of the ceramic material through appropriate constitutive and damage models in the code.

Several investigators¹⁻⁸ have modeled the behavior of rock-type brittle solids. In these models, the effects of damage on the constitutive behavior were introduced through degraded elastic moduli. Costin and Stone² and Horii and Nemat-Nasser³ developed constitutive models for brittle materials under static loading conditions where strain-rate effect on the damage process is not considered. These models are capable of modeling different failure modes, such as the faulting and splitting, and describe damage-induced anisotropic material behavior. In general, these models are computationally demanding and mathematically complex, especially the model by Horii and Nemat-Nasser. The microphysical model of Margolin⁴ considers both frictional

effects due to closed cracks and strain-rate effects. This model treats damage as a scalar variable and is based on degraded elastic moduli. Recently, Taylor, Chen, and Kuszmaul⁵ presented a constitutive or damage model to describe the behavior of oil shale under explosive loading conditions. Following the approach of Grady and Kipp,¹ this relatively simple model incorporates strain-rate effects for tensile loading. The inelastic response of rocks under shock (compression) loading is treated simply as an elastic-perfectly-plastic response. The compressive strength Y is treated as a constant independent of damage, pressure, and strain rate. Rajendran, Kroupa, and Brar⁹ implemented the model by Taylor, Chen, and Kuszmaul (TCK model) in a two-dimensional finite-element code, EPIC-2, and simulated a plate-impact experimental configuration using this model. Recently, Rajendran and Cook,¹⁰ in a review report, cited several experimental results that show the effects of pressure and strain rate on the compressive strength of various ceramics.

Hence, several modifications to the original model are required for a realistic description of ceramic-type brittle materials. In the present paper, the application of the modified TCK model to describe ceramic material behavior under impact loading conditions is considered. In the next section, the original TCK model is described. A strain-rate and damage-dependent compressive strength model is proposed and incorporated into the constitutive formulation. For tensile loading, the original TCK model is retained, except that the unloading and reloading paths are different in the present approach. Since the proposed model for ceramic materials is useful for computer code applications, we used an improved and efficient numerical algorithm for solving the governing constitutive equations. A second-order diagonally implicit Runge-Kutta (DIRK) method is employed in the numerical solution. The effects of time step and grid sensitivity on the stability and accuracy of the solutions are verified. Using the proposed constitutive or damage model the response of AD-85 (85% aluminum oxide) ceramic under plate-impact loading (uniaxial strain) conditions was mod-

eled. The experimentally determined stress history matched extremely well with the numerical simulation.

II. TAYLOR-CHEN-KUSZMAUL MODEL

Under dynamic compressive loading conditions, rock- and concretelike materials deform inelastically similar to ceramic materials. The inelastic response of these brittle materials is usually attributed to the nucleation, growth, and coalescence of microcracks. The original TCK model⁵ treats the inelastic behavior under compression as an elastic-perfectly-plastic response. This elastic-perfectly-plastic assumption simplifies the model formulation for compressive loading, and therefore a Prandtl-Reuss or Prandtl-Mises incremental-plasticity-theory-based model is adequate to describe the inelastic behavior.

A crack-growth-based damage model has been used to describe the inelastic behavior under tension. The damage-model formulation considers the growth and interaction of randomly distributed penny-shaped microcracks. The damage nucleation is treated by a Weibull distribution. The number of cracks that nucleate upon loading is given by

$$N = k\epsilon_v^m, \quad (1)$$

where N is the number of flaws per unit volume, k and m are model parameters, and ϵ_v is the volumetric strain. The above equation can be written in terms of pressure by replacing ϵ_v by $P/3K$, where P is the pressure, and K is the bulk modulus.

The growth and coalescence of microcracks degrade the bulk and shear moduli or the Poisson's ratio (ν). To describe the effects of crack volume (or damage) on these elastic moduli, the derivation of Budiansky and O'Connell¹¹ was employed. The corresponding expressions are

$$\frac{\bar{K}}{K} = 1 - \frac{16}{9} \left(\frac{1 - \bar{\nu}^2}{1 - 2\bar{\nu}} \right) C_d, \quad (2)$$

$$\bar{\nu} = \nu(1 - \frac{1}{3}C_d). \quad (3)$$

The above expression for $\bar{\nu}$ is a simplified equivalent form of Budiansky and O'Connell. \bar{K} and $\bar{\nu}$ are the degraded elastic properties and C_d is a crack density parameter. Equations (2) and (3) are not sufficient to determine the three unknowns, $\bar{\nu}$, \bar{K} , and C_d . We need an additional equation and this can be obtained from the definition of crack density, C_d .

The crack density C_d represents the volume fraction of penny-shaped voids. The average crack density is defined by the product of the number of cracks per unit volume (N) and the average volume of the cracks ($\sim a^3$), and is given by

$$C_d = \beta Na^3, \quad (4)$$

where " β " is a crack geometry parameter.

Taylor and co-workers⁵ assumed that the average crack size β is proportional to the size of the average fragments, and utilized the expression derived by Kipp and Grady¹² for fragmentation. The corresponding expression for the crack size is

$$a = \frac{1}{2} \left(\frac{\sqrt{20}K_{IC}}{\rho c \dot{\epsilon}_{max}} \right)^{2/3}, \quad (5)$$

where ρ is the density of the material, K_{IC} is the static fracture toughness, c is the sound speed, and the $\dot{\epsilon}_{max}$ is the

applied strain rate at fracture. By combining Eqs. (1)–(5), the expression for C_d is

$$C_d = \frac{5}{2} \frac{k}{(3K)^m} \left(\frac{K_{IC}}{\rho c} \right)^2 P^m \dot{\epsilon}_{max}^{-2}. \quad (6)$$

Model formulation will be completed once an expression for damage is obtained. The following relationship between damage and the bulk modulus is assumed:

$$\bar{K} = K(1 - D). \quad (7)$$

The bulk modulus is assumed to degrade linearly with increasing damage. Also, by comparing Eqs. (2) and (7), we can describe damage in terms of the crack density as

$$D = \frac{16}{9} \left(\frac{1 - \bar{\nu}^2}{1 - 2\bar{\nu}} \right) C_d. \quad (8)$$

The original bulk modulus K is reduced with respect to damage in a linear manner as shown in Eq. (7). When there is no damage ($D = 0$) the bulk modulus remains the same and $\bar{K} = K$. Upon total damage ($D = 1$) the material can no longer carry any tensile loading due to the complete loss of stiffness. The constitutive equation for the brittle material can now be written as sum of the bulk and deviatoric parts of the stress components,

$$\sigma_{ij} = 3K(1 - D)e_{kk}\delta_{ij} + 2G(1 - D)e_{ij}, \quad (9)$$

where e_{ij} are the deviatoric part of the strain components. When $D = 0$, the Hook's law for linear elastic behavior is recovered from Eq. (9). The rate equations for D and C_d can be derived from Eqs. (6) and (7). The six components of the stress tensor, damage parameter D , and the density parameter C_d are the unknowns in the model formulation. These eight unknowns can be determined by solving the eight rate equations incrementally.

III. NUMERICAL SIMULATIONS

The TCK model was implemented into the EPIC-2 finite-element code.¹³ Initially, we developed a fourth-order Runge-Kutta scheme to solve the governing equations incrementally. However, an improved scheme based on a second-order implicit Runge-Kutta method was developed later for numerical stability and accuracy. For model validation, a plate-impact test on a ceramic target was considered.

A. Plate-impact test description

A schematic representation of the plate-impact test is shown in Fig. 1. A copper flyer disk of 50 mm diameter and 2.5 mm thickness impacts a AD-85 ceramic plate of thick-

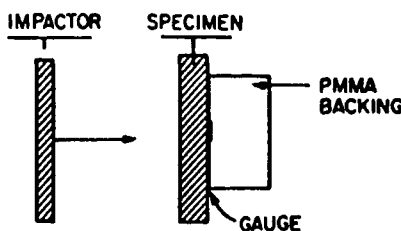


FIG. 1. A schematic representation of the plate-impact experiment.

ness 8.8 mm. The ceramic plate was backed by a 12-mm-thick PMMA (polymethyl methacrylate). The stress history at the interface of AD-85 and PMMA was recorded using a Manganin gauge. For an impact velocity of 570 m/s, the stress-time profile from the Manganin gauge is shown in Fig. 2. The interpretation of this stress profile is as follows: The point "A" on the profile corresponds to the elastic strength of AD-85 under one-dimensional strain condition and it is known as Hugoniot elastic limit (HEL) of the material. The profile between A and the peak stress indicated by point B represents the inelastic (some call it "plastic") part of the stress wave. Point C corresponds to the arrival of the release wave which originated at the rear surface of the flyer. The profile between points C and D is due to elastic unloading of the stress release. The release characteristics are quite complex to interpret. Unlike in metals, most ceramics exhibit a lack of a deterministic spall signal, and therefore some kind of qualitative interpretations only can be made. The slow stress release in steps between points D and E indicates zero spall strength of the material. The interpretations of stress gauge profiles from plate-impact tests on ceramic materials were reviewed in detail by Bless.¹⁴

B. Effect of time step

In the next stage, we simulated the plate-impact test configuration using the EPIC-2 code and the TCK model. A one-dimensional strain condition is assumed in the simulation. The stress history at the interface between the ceramic target and the PMMA (backup) plate was obtained from the numerical simulation. Several computer runs were made with different time steps in each run. The stress histories from these runs are compared in Fig. 3. It can be seen that the time step had no influence on the stress between points A and E in the figure. This is because the constitutive model for compression follows a simple elastic-plastic approach without any damage calculation and no unloading is involved. However, beyond point E, the stress calculations involve

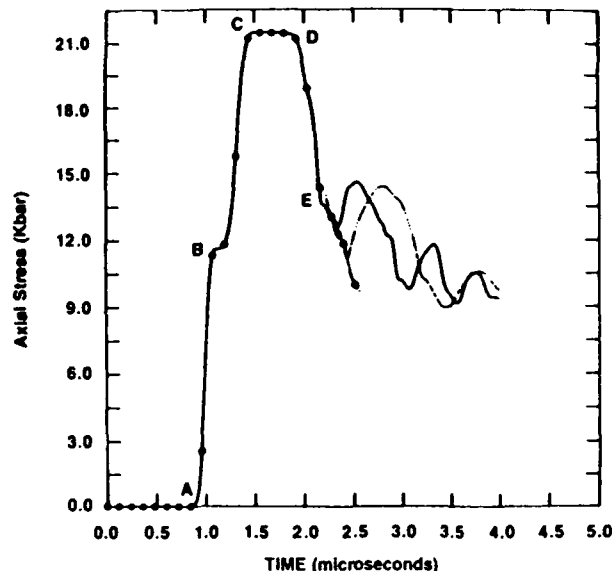


FIG. 3. The effect of time step on the numerical solutions.

damage nucleation, growth, and degradation of stiffness and strength leading to target spallation. The numerical solution exhibited both grid and time-step dependency, indicating nonunique and unstable solution, during the stress release (due to spallation). To investigate this aspect further, the unloading and reloading nature of the model formulation was critically evaluated. We simulated the hypothetical loading, unloading and reloading conditions shown in Fig. 4. In the TCK model, unloading is along the undamaged modulus (between points A and B) while reloading (between points B and C) is along the damaged modulus as shown in the figure. When reloading occurs at different points (B', B'') the pressure reaches different levels for the same strain, indicating nonunique solutions. Brittle solids usually do not exhibit any gross plastic deformation, and therefore strains

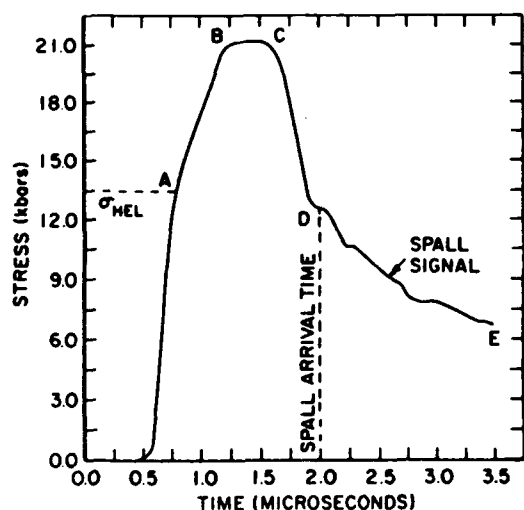


FIG. 2. Stress history in PMMA from the plate-impact test on AD-85.

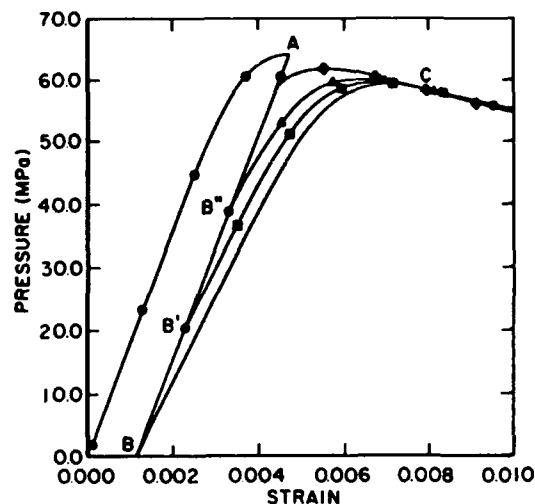


FIG. 4. Nonunique solutions due to unloading along the undamaged modulus and reloading along the damaged modulus.

are not accumulated upon unloading. The unloading occurs along the degraded modulus toward the origin of the uniaxial stress-strain curve. Therefore, in the model, we implemented unloading and reloading along the current damaged modulus until damage reinitiated for further analysis. Additional plate-impact test simulations were conducted with this feature. The solutions obtained using different time steps yielded almost the same stress history as can be seen from Fig. 5.

C. Effects of model parameters

There are four model parameters (without including the bulk and shear moduli of the intact ceramic): the nucleation parameters k and m , the fracture toughness K_{IC} , and the compressive yield strength Y . The compressive yield strength can be directly obtained from the stress (σ_{HEL}) at HEL. The corresponding relationship between Y and σ_{HEL} is given by

$$Y = \frac{\sigma_{HEL}}{K/2G + 3} \quad (10)$$

The values of k and m have to be calibrated based on the model's ability to reproduce the experimental stress history. A value for K_{IC} can be determined from a standard fracture toughness test. However, for better understanding of these three parameters and their effects on the spall signal (between points D and E of Fig. 2) of the stress history, several numerical simulations were carried out by varying one parameter at a time.

In Fig. 6, the effects of the damage nucleation parameter " k " are shown for $m = 6$ and $K_{IC} = 3.0 \text{ (MPa)} \sqrt{m}$. The stress histories at the stress gauge location for $k = 10^{20}$, 10^{27} , and 10^{34} are plotted. For $k < 10^{20}$, the damage (microcracks) level is relatively low and in the simulation the ceramic target did not fracture. The stress history follows the

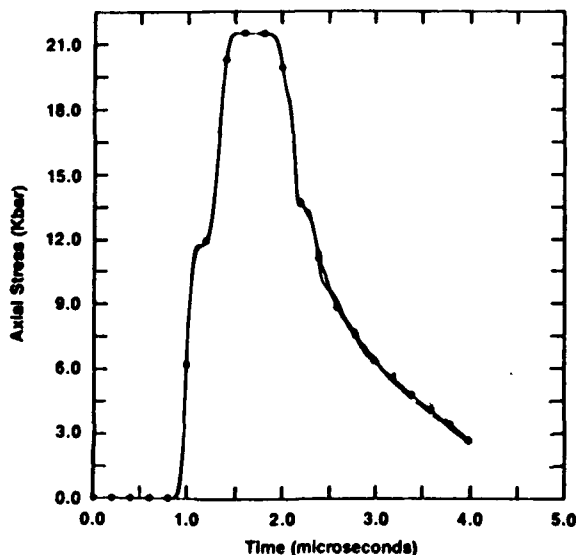


FIG. 5. Effect of time step on the stable numerical solutions due to unloading and reloading along the damaged modulus.

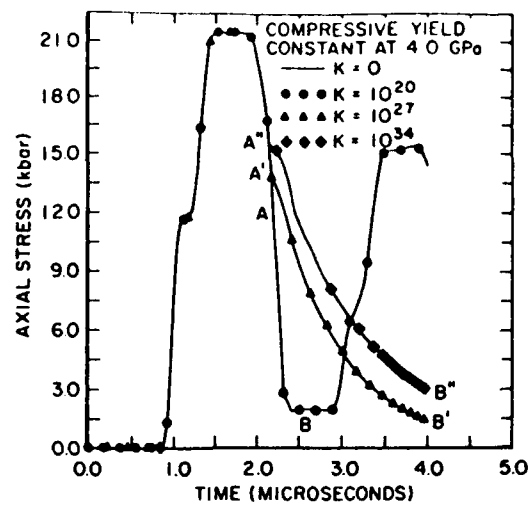


FIG. 6. Effect of damage nucleation parameter k on the spall signal.

solid line AB , which indicates complete unloading of the stress due to the release wave from the back surface of the flyer plate. When the value of k is increased to 10^{27} and 10^{34} , the ceramic target fractured by spalling and the slow step release of stress between $A'B'$ or $A''B''$ clearly shows the salient features of an experimentally obtained stress history (see Fig. 2). A higher value of k represents a larger number of cracks nucleating, and therefore earlier arrival (at point A'') of the spall signal.

Figure 7 demonstrates how m also controls the damage nucleation level. In these simulations, a value of 10^{27} for k and $3.0 \text{ (MPa)} \sqrt{m}$ for K_{IC} are employed. Stress histories were obtained for $m = 4, 5, 6$, and 7 . When the value of m was higher, the damage nucleation was lower [note that in Eq. (1), $e_v \ll 1$], and therefore the spall signal arrival occurred at a later time. For values of m less than 5, the spall signal was relatively unaffected, indicating complete pulverization of the target. Unlike in metals where the spall is limit-

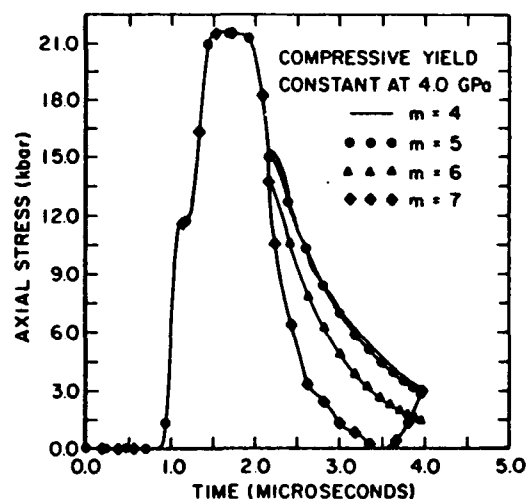


FIG. 7. Effect of the damage nucleation parameter m on the spall signal.

ed to a single plane, in ceramics spall occurs over a zone as can be clearly seen from this figure. This is confirmed by the experimental observation of spall zones in polycrystalline ceramics by Bless, Yaziv, and Rosenberg.¹⁵ Most of the target experienced a critical damage level indicating pulverization. It is clear from these simulations (effects of k and m on the spall signal) that the spall arrival time in the experiment can be used to estimate the values of k and m . An arbitrary value of 6 for m seems to work well in the experimental calibration. The value of k can be adjusted to match the spall arrival time.

As a final exercise, the value of K_{IC} was varied ($m = 6$ and $k = 10^{27}$) and stress history at the gauge location was calculated. The results indicated less-pronounced effects of the fracture toughness on the spall processes as can be seen from Fig. 8. Shock loading induces microcracks in most ceramics. These microcracks often nucleate from preexisting flaws, thus degrading subsequent tensile properties. Therefore, a small tensile load is sufficient to propagate the cracks. Hence K_{IC} may not have significant effect on the spall release.

D. Modeling of AD-85 ceramic

We modeled the plate-impact experiment described earlier in this section. The target was AD-85 ceramic. The following values of the model parameters were used: $K_{IC} = 3.0(\text{MPa})\sqrt{m}$, $k = 10^{27}$, $m = 6$, $Y = 4000 \text{ MPa}$. Note that the value of K_{IC} is obtained from open literature as the fracture toughness value for AD-85.

A comparison between the stress history calculated in the simulation and the experiment is shown in Fig. 9. It can be seen that the stress profile between points *A* (at HEL) and *B* (the peak stress) does not match well. The ramping nature of the stress versus time curve between these two points in the experiment may be speculated as due to some sort of microdamaging mechanism which is a rate-controlled process. In metals, this ramping is usually attributed to the

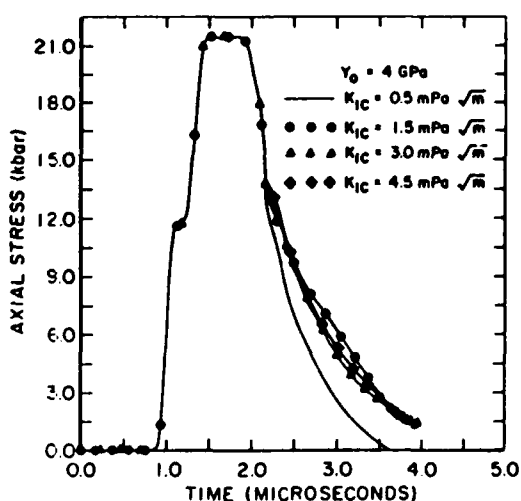


FIG. 8. Effect of K_{IC} on the spall signal.

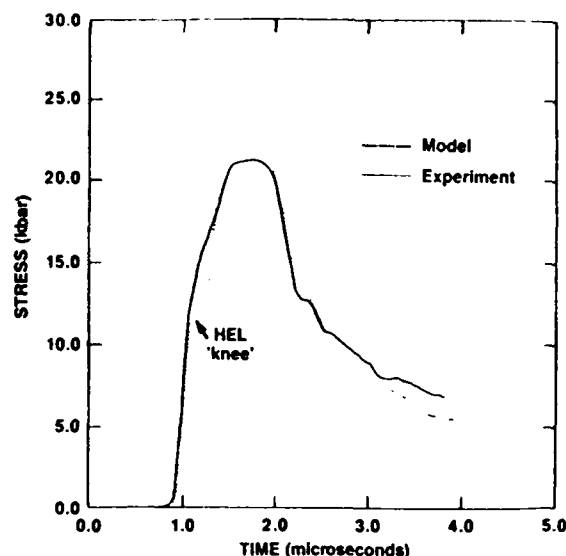


FIG. 9. Calculated stress history using a strain-rate-independent model for compression.

visco-plasticity (strain-rate sensitivity of the flow stress). The behavior of ceramic under compression is assumed to be elastic-perfectly-plastic in the numerical simulation using the original TCK model. Since the strain-rate dependency was absent, the simulated stress history showed the typical "knee" at the HEL. The "plastic" wave profile was without any ramping which is typically observed in strain-rate-independent metals.

For improved modeling of the behavior of ceramic under compression, the following form for the compressive strength is considered¹⁰:

$$Y = Y_s(1 + B \ln \dot{\epsilon})(1 - D), \quad (11)$$

where Y_s is the static strength and B is the strain-rate sensitivity parameter. $\dot{\epsilon}$ is the equivalent plastic strain rate and D is the damage. The damage growth is assumed to be zero under compression. However, the compression strength is reduced after accumulating damage under tension. We incorporated this compression model into the formulation and resimulated the plate-impact experiment. The value of Y_s is determined from static compressive strength as 2000 MPa. By knowing the Y that corresponds to the HEL, a value of 0.175 was obtained for the parameter B . The calculated stress history at the gauge location, based on the new model, compared extremely well with the experimental data as can be seen from Fig. 10.

IV. SUMMARY

In general, the behavior of ceramic under impact loading conditions is complex. Since a recovery test on ceramic is difficult to perform especially at high-velocity impact (above the HEL), many of the deformation and damage mechanisms are speculative in nature. The free-surface velocity history of a ceramic target and the stress history at the interface of ceramic plate and the backup plate are the only measured quantities which we rely upon in the ceramic material modeling. At present, the capabilities of any advanced

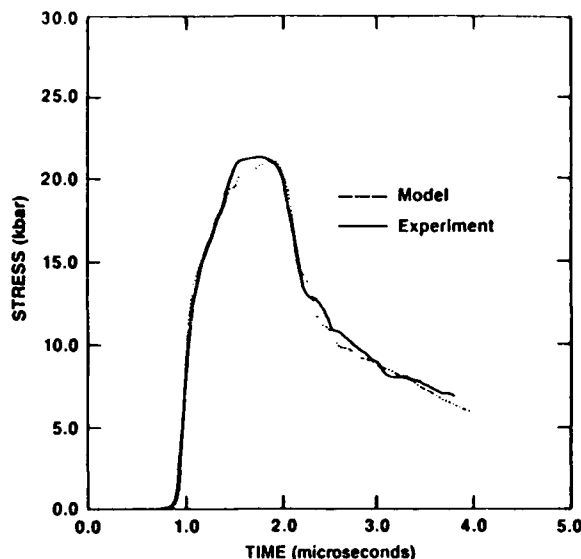


FIG. 10. Comparison between the experimental and the modified TCK model.

engineering or physically based model are validated only through the model's ability to match the various salient features of the experimentally measured data.

A constitutive or damage model for ceramic material under impact loading conditions was presented. This model employed strain-rate-dependent equations for describing the inelastic behavior of ceramic under both compression and tension. The tension model was originally developed for describing fragmentation of rocks and oil shale. A more realistic description of unloading and loading paths was incorporated in the model for unique and stable solutions. The model was then implemented into a shock-wave propagation, finite-element code. The stability of the numerical solution was demonstrated. A model parameter evaluation scheme is presented in terms of the sensitivity study. We have successfully matched the experimental stress history obtained from a plate-impact test on a AD-85 ceramic. The

impact behaviors of different ceramics can be, in general, very different. Depending on the impact velocity and ceramic constituents, deformation and fracture mechanisms can vary significantly from one ceramic to another. The capabilities of the proposed model to describe other ceramic materials are yet to be validated.

ACKNOWLEDGMENTS

This work was performed under the U. S. Air Force Contract No. F33615-86-C-5064. The project monitor was Dr. T. Nicholas, Air Force Wright Aeronautical Laboratories, Wright Patterson Air Force Base, Ohio. Partial support was provided by W. H. Cook, Air Force Armament Laboratory, Eglin Air Force Base, Florida. We express our appreciation to Mark A. Dietenberger and David J. Grove for assisting in the software development. The experimental data were provided by Dr. S. J. Bless and Dr. N. S. Brar.

- ¹D. E. Grady and M. E. Kipp, *Int. J. Rock Mech., Min. Sci. Geomech.* **17**, 147 (1980).
- ²L. S. Costin and C. M. Stone, in *Constitutive Laws for Engineering Materials: Theory and Applications*, edited by C. S. Desai (Elsevier, New York, 1987).
- ³H. Horii and S. Nemat-Nasser, *J. Mech. Phys. Solids* **31**, 155 (1983).
- ⁴L. G. Margolin, *Int. J. Fract.* **22**, 65 (1983).
- ⁵L. N. Taylor, E. P. Chen, and J. S. Kuszmaul, *Comput. Meth. Appl. Mech. Eng.* **55**, 301 (1986).
- ⁶R. Ilankamban and D. Krajcinovic, *Int. J. Solids Struct.* **23**, 1521 (1987).
- ⁷J. C. Simo and J. W. Ju, *Int. J. Solids Struct.* **23**, 821 (1987).
- ⁸J. C. Simo and J. W. Ju, *Int. J. Solids Struct.* **23**, 841 (1987).
- ⁹A. M. Rajendran, J. L. Kroupa, and N. S. Brar, University of Dayton Report No. UDR-TM-87-32, 1987.
- ¹⁰A. M. Rajendran and W. H. Cook, Air Force Armament Technological Laboratory Report No. AFATL-TR-88-1433, Eglin Air Force Base, FL, 1988.
- ¹¹B. Budiansky and R. J. O'Connell, *Int. J. Solids Struct.* **12**, 81 (1976).
- ¹²M. E. Kipp and D. E. Grady, *J. Mech. Phys. Solids* **33**, 399 (1985).
- ¹³G. R. Johnson and R. A. Stryk, Air Force Armament Technological Laboratory Report No. AFATL-TR-86-51, Eglin Air Force Base, FL, 1986.
- ¹⁴S. J. Bless, Report No. AFWAL-TR-88-4229, Wright-Patterson Air Force Base, OH, 1988.
- ¹⁵S. Bless, D. Yaziv, and Z. Rosenberg, *Proceedings of the Fourth APS Topical Conference on Shock Waves in Condensed Matter*, Spokane, WA, 1985, edited by Y. M. Gupta (Plenum, New York, 1986).